DISSERTATION

STRONG FULLERENE AND POLYCYCLIC AROMATIC HYDROCARBON ELECTRON ACCEPTORS WITH PERFLUORINATED SUBSTITUENTS

Submitted by

Long K. San

Department of Chemistry

In partial fulfillment of the requirements

For the Degree of Doctor of Philosophy

Colorado State University

Fort Collins, Colorado

Summer 2015

Doctoral Committee:

Advisor: Steven H. Strauss

Charles Henry
Thomas Borch
Grzegorz Szamel
Qiang Wang

ABSTRACT

STRONG FULLERENE AND POLYCYCLIC AROMATIC HYDROCARBON ELECTRON ACCEPTORS WITH PERFLUORINATED SUBSTITUENTS

The world energy consumption is increasing at an alarming rate and only 10% comes from renewable energy resources. Harnessing the potential energy provided by the sun would provide enough energy to meet the world energy demands and more. One method to improve the collection of solar power is to provide materials that are lightweight, flexible, robust, and low manufacturing costs. The focus of this dissertation include the molecular design of novel materials to be used as organic semiconductors in a variety of applications such as organic photovoltaic and organic light emitting diodes. One very important aspect of these organic electronics is the electron acceptors employed in such devices. The need for strong electron acceptors and higher stabilities under thermal and oxidative stress were investigated by the perfluoroalkylation and perfluorobenzylation of fullerenes and polycyclic aromatic hydrocarbons.

The first chapter of this dissertation demonstrates the novel fullerene derivative (nicknamed faux hawk) that possesses physicochemical properties suitable for use in organic photovoltaics. In fact, an organic photovoltaic figure of merit ($\varphi\Sigma\mu$, yield of free charge carriers × sum of the charge carrier mobilities) determined from time resolved microwave conductivity measurements showed that faux hawk is comparable to that of the most studied fullerene electron acceptor, PCBM. Other properties are compared between faux hawk and PCBM. Mechanistic insight revealed, for the first time in fullerene chemistry, the formation of a carbon–carbon bond via a

carbanion from the fullerene cage. The second chapter of this dissertation investigates novel polycyclic aromatic hydrocarbons containing fluorine withdrawing functional groups via perfluoroalkylation and, for the first time, perfluorobenzylation. These fluoromodifications have profound influences on the physicochemical and electronic properties that are all important for designing new electron acceptors. For example, the perfluorobenzylation greatly affects the π-π intermolecular interactions and is more electron withdrawing than the trifluoromethyl group. Often times a bulky functional group is desired to promote certain properties (i.e., fluorescence).

Several analytical methodologies including ^{19}F and ^{1}H NMR spectroscopy, absorption and emission spectroscopy, mass spectrometry, cyclic voltammetry, gas-phase electron affinity, low-temperature photoelectron spectroscopy, X-ray diffraction, and DFT calculations are used to characterize the compounds discussed. These fundamental studies allow for future molecular engineering and design of even stronger electron acceptors. At the same time, the organic semiconductor library is expanding for use in optoelectronics.

ACKNOWLEDGMENTS

I would like to start off by thanking the past and present Strauss/Boltalina research group members for their support, assistance, and scientific discussions as my colleagues and friends. Specifically, Eric V. Bukovsky and Tyler C. Clikeman for their proficiencies in X-ray crystallography and determining the several structures described in this dissertation. I don't think "*are those new slacks?*" or "*I make noise*" will ever get old. I would also like to thank Karlee Castro, Amanda M. Pluntze, Dr. Igor V. Kuvychko, Dr. Bryon W. Larson, and Dr. James B. Whitaker for making graduate school a great experience, the great celebrations, and the fun group dynamics.

Next, collaborative research is a step towards successful science. I would like to thank Dr. Alexey A. Popov for his work on theoretical calculations. It was great meeting you in Dresden, Germany; Dr. Xue-Bin Wang for the low temperature photoelectron spectroscopy measurements at Pacific Northwest National Laboratory; Dr. Yu-Sheng Chen for X-ray data collection at the Advanced Photon Source; Prof. Konrad Seppelt for the opportunity to perform research in Berlin, Germany; and Dr. Marina Petrukhina for the supply of corannulene.

My deepest gratitude is for my advisors Prof. Steven H. Strauss and Dr. Olga V. Boltalina. Thank you for the support, guidance, mentorship, expertise, scientific discussions, challenges, friendship, and allowing me to make mistakes in order to become a better scientist. The opportunity given to me to travel abroad and work with collaborators will be some of the most memorable moments of my graduate school career. I am honored to have worked for you both.

I would like to thank my family for their continued support. They have shaped me into the person I am today and have taught me that through perseverance and hard work, I can achieve

anything that I set my mind to. I always considered their opinions and thoughts when I needed advice.

Last, but not least, I would like to thank my fiancée Cindy Hoang for the love and support you have given me not only through graduate school, but throughout our relationship. You were always there to celebrate the successes and to help me overcome failures, provided advice, and you always reminded me that hard work pays off. The time and effort you put into listening to my presentations and reading my work even when you didn't understand it helped me become a better scientist.

TABLE OF CONTENTS

LIST OF TABLES

LIST OF FIGURES

LIST OF ACRONYMS AND ABBREVIATIONS

acronym/abbreviation	full name
HPLC	high performance liquid chromatography
t_R	retention time
NI APCI MS	negative ion atmospheric pressure chemical ionization mass spectrometry
UV-vis	ultraviolet-visible
NMR	nuclear magnetic resonance
$E_{1/2}$	reduction potential
TRMC	time resolved microwave conductivity
o-DCB	1,2-dichlorobenzene
PS	proton sponge
DBU	1,8-diazabicycloundec-7-ene
DFT	density functional theory
CV	cyclic voltammetry
SWV	square-wave voltammetry
LT PES	low temperature photoelectron spectroscopy
EA	electron affinity
OPV	organic photovoltaic
S_NAr	nucleophilic aromatic substitution
AIBN	Azobisisobutyronitrile
P3HT	poly-3-hexylthiophene
PFAF	Perfluoroalkylfullerene
PCBM	phenyl-C_{61}-butryic acid methyl ester
ICMA	mono-indene-C_{60}
FCMA	1,9-C_{60}(*cyclo*-CF_2(2-C_6F_4)); "faux hawk-C_{60} mono adduct"
FCBA	C_{60}(*cyclo*-CF_2(2-C_6F_4)$_2$); "faux hawk-C_{60} bis adduct"
FCTA	C_{60}(*cyclo*-CF_2(2-C_6F_4)$_3$); "faux hawk-C_{60} tris adduct"
Bn_F	$CF_2C_6F_5$
Ph_F	C_6F_5
PAH	polycyclic aromatic hydrocarbon
NAPH	Naphthalene
ANTH	Anthracene
TETR	Tetracene
PHTZ	Phenothiazine
ACRD	Acridine
CORA	Corannulene

Introduction

Background & Motivation

The total world energy consumption was estimated to be ca. 6.3×10^{20} J in the year 2013 and is predicted to increase to ca. 8.4×10^{20} J by the year 2040.[1] Approximately 90% of the energy consumption is provided by the burning of fossil fuels; however, two inherent issues are present: 1) the combustion of fossil fuels produces a variety of gaseous side products besides water and carbon dioxide and 2) the supply of fossil fuel is finite. These are two reasons in which clean and sustainable energy must be used to meet the demand of the world energy use. The other 10% of the energy consumption is provided from various renewable energy sources. In Table I.1, the total available energy of five renewable energy sources is listed. Amazingly, the total available solar energy (7400×10^{20} J) would be sufficient to supply the world energy needs even if a fraction was captured and utilized. One method of harnessing the solar energy is by the use of photovoltaics (solar cells).

While inorganic photovoltaics, mainly silicon wafer-based, currently dominate the industry with their high efficiencies (up to 25% power conversion efficiencies[2]) and long lifetimes, it is doubtful whether they will be able to meet the demand for low module manufacturing cost. The cost in fabrication and the necessity for high purity silicon are key components in the high costs of inorganic photovoltaics. In contrast, solution-processed organic photovoltaics (OPVs) might offer significant manufacturing cost reduction as they are based on thinner active layers (i.e., reduce quantity of materials used), use earth-abundant and non-toxic elements and can be deposited onto a wide range of surfaces, such as glass and plastic substrates, using atmospheric pressure roll-to-roll methods avoiding high temperature and vacuum processes.[3-5] Some other

advantages of OPVs include being lightweight, being flexible, and the high absorption coefficients of organic semiconductors.[6]

Significant progress of OPVs has transpired from the 1992 report of photoinduced electron transfer from the *p*-phenyl vinylene (PPV) based polymer MEH-PPV, as the electron donor, onto the fullerene C_{60}, as the electron acceptor.[7] Shortly thereafter, the fullerene derivative PCBM was synthesized which has become one of the most studied OPV electron acceptor.[8] Researchers achieved power conversion efficiencies (PCEs) nearing 3% with PPV-based conjugated polymers.[9] In search of new electron donor materials to combat the low hole mobility and narrow light absorption band of PPV-based polymers, the poly(3-hexylthiophene) (P3HT) polymer was synthesized and has become one of the most studied OPV electron donors due to its higher hole mobility and improved light absorption characteristics.[10,11]

OPV devices containing blends of P3HT and PCBM have reported PCEs approaching 5%.[12,13] The low exciton (a coulombically bound electron/hole pair) diffusion length of ca. 10 nm in organic semiconductors requires an intimate mixture of the electron donor and electron acceptor for efficient exciton dissociation into free charge carriers.[14] The subsequent extraction of the free charge carriers is dependent on the continuous percolation pathways within the photoactive layer. The physical arrangement of the electron donor and electron acceptor in the photoactive layer, referred to as the morphology, is an important aspect in determining the OPV device performance. Several methodologies have been utilized to control the morphologies such as thermal annealing,[15,16] solvents used for the deposition of photoactive materials,[17,18] solvent additives,[19] and growth of nanowires all which are implemented to improve the PCEs.[20,21]

The bulk heterojunction (BHJ) device architecture has been commonly used for device fabrication and is the base device structure in today's state-of-the-art OPV devices.[22] The BHJ

device architecture consists of the light absorbing photoactive layer, which includes the electron donor and electron acceptor, sandwiched between two electrodes with proper work functions as shown in Figure I.1. The photoactive layer is often deposited from solution by either spin-casting or drop-casting. These outdated deposition techniques, which are still used extensively, are being replaced by other solution processing methodologies such as blade coating or slot-die coating.[23,24] The anode typically consists of a transparent layer, such as indium tin oxide (ITO), which allows light to pass through towards the photoactive layer and to collect holes. Often times, a layer of PEDOT:PSS is deposited between the anode and photoactive layer to promote the conduction of holes generated throughout the device. The cathode, often times silver, calcium, or magnesium, is then deposited by thermal evaporation completing the OPV device. LiF has also been used as an electron conductor and hole blocking layer when deposited between the photoactive layer and the cathode.[25]

A general charge generation schematic is shown in Figure I.2. The process begins with the OPV device absorbing light which excites an electron from the highest occupied molecular orbital (HOMO) to the lowest occupied molecular orbital (LUMO) of the electron donor creating an exciton. This exciton migrates towards the electron donor and electron acceptor interface where dissociation into free charge carriers occur (i.e., the excited electron in the LUMO of the electron donor is injected into the LUMO of the electron acceptor). The free charge carriers then migrate towards their respective electrodes and are collected.

The choice of materials used in OPV device fabrication is often based on the electronic properties. The opportunity to tune the energy levels (i.e., the HOMO and LUMO) is driven by the synthetic modification of existing electron donors and electron acceptors to optimize OPV device performance. A recent publication examined ca. 150 BHJ devices and concluded that

energy level alignment of the materials used in device fabrication do not have, in general, a strong correlation with device efficiencies. Control of the morphology by devising new processing methodologies will have significant impact on OPV device performance.[26]

The research presented in this dissertation focuses on organic semiconductors with fluorinated substituents and their potential applications in OPVs as electron acceptors and organic light emitting diodes (OLEDs). Some of the properties that are of interest are solution redox potentials (as measured by cyclic voltammetry) and gas-phase electron affinities (as measured by photoelectron spectroscopy). Often times, Density Functional Theory (DFT) calculations are performed to corroborate experimental results.

Cyclic Voltammetry. The most common electrochemical technique used in this dissertation to measure the solution redox potentials is cyclic voltammetry,[27] which will be the only technique discussed. Briefly, the electrochemical cell setup used consists of a three electrode system which allows for the simultaneous measurement of the change in potential and change in current. The platinum working electrode is responsible for the reduction and oxidation events of the electrochemically active analytes. The change in current is measured between the platinum auxiliary electrode, which does not react with the bulk solution, and the working electrode. The change in potential is measured between the silver reference electrode and the working electrode. During an experiment, the potential at the working electrode is increase linearly versus time (also known as the scan rate) to a set potential. Once this potential is reached, the potential is ramped in the opposite direction back to its initial potential. A cyclic voltammogram is constructed by plotting the measured current and the applied potential.

Figure I.3 shows the fundamental processes of reduction and oxidation that occurs. In general, when the potential of the working electrode becomes more negative, the energy of the

electron can increase high enough to transfer into the LUMO of the analyte (reduction current) as shown in Figure I.3a. If the opposite is performed, lowering the working electrode towards more positive potentials, the electron from the analyte in solution may find the energy at the electrode more favorable and transfer from the HOMO (oxidation current) as shown in Figure I.3b. This cyclic nature of voltammetry can provide insight into electron transfer kinetics and mechanisms of electrochemically active species.

Photoelectron spectroscopy. To measure the gas-phase electron affinities for the discussed compounds in this dissertation, a low-temperature photoelectron spectrometer developed by collaborators at the Pacific Northwest National Laboratory was used.[28] Photoelectron spectrometry measurements provide electronic information of the analyte of interest by measuring the kinetic energy distribution of emitted electrons. The complication of solvent interactions with the analyte in solution provides a challenge of understanding the intrinsic molecular properties; thus, the gas-phase experiments eliminate any solvent effects. In addition, the introduction of low-temperature (12 K) capabilities provides better resolution by reducing or eliminating various vibrational "hot band" energy levels that are present at room temperature. The gas-phase electron affinity values are determined from the 0–0 transition in the photoelectron spectroscopy spectra of the reduced analyte.

The low-temperature photoelectron spectroscopy experiment begins with a syringed dilute solution of analyte and ionized via electrospray ionization or chemically by TDAE. The anions produced are desolvated, mass selected through a quadruple mass filter, collected in a cryogenic cooled ion trap, and directed towards the time-of-flight mass spectrometer. Mass selected anions are intersected by a photodetachment laser beam which the ejected electrons from the anions are directed towards the magnetic-bottle photoelectron energy analyzer. The photoelectron time-of-

flight spectra are converted into kinetic energy spectra and used to calculate the electron binding energy.

Density Functional Theory. Density Functional Theory (DFT), successor to Hartree-Fock theory,[29,30] was first introduced by the seminal work of Kohn et al. and has been utilized to understand the electronic properties of materials based on electron density probability.[31,32] Some early inherent shortcomings of Hartree-Fock theory are that it assumes the wavefunction can be represented by one Slater determinant and that each electron interacts with the average charge distribution cloud due to other electrons. DFT is an approximate way to incorporate these electron correlations making it a valuable research tool to validate empirical conclusions or to suggest other possible conclusions. Modern DFT incorporate two theories: 1) the ground state electron density determines the properties of a system and 2) the energy of an electron distribution can be described as a functional of the electron density. DFT has been applied in the field of computational chemistry to predict various molecular properties, molecular structures (such as bond lengths), vibrational frequencies, atomization energies, ionization energies, reaction pathways, electron affinity, etc.

Gas-phase electron affinity and solution redox potentials are calculated from collaborators at Leibniz Institute for Solid State and Materials Research in Dresden, Germany. For gas-phase electron affinity values, the difference in calculated energies for the optimized neutral and anionic species provides is determined. For solution redox potentials, the solvation energies are computed using polarizable continuum model[33,34] in addition to the electron affinity. This approximates electrostatic contribution to solvation energy. The solvent used is a polarizable medium with specific dielectric constants.

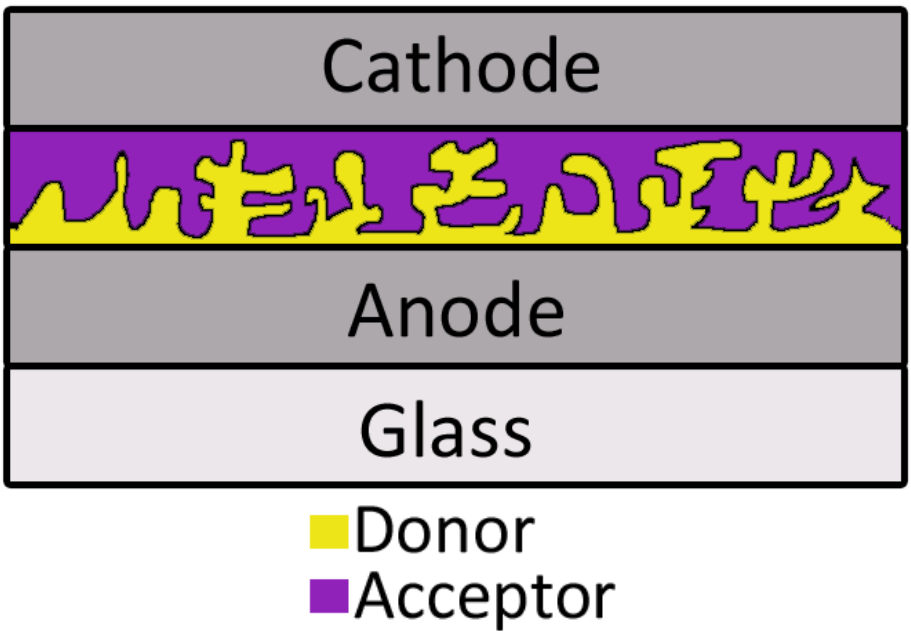

Figure I.1. Schematic diagram of a bulk heterojunction OPV. The yellow represents the electron donor and the purple represents the electron acceptor.

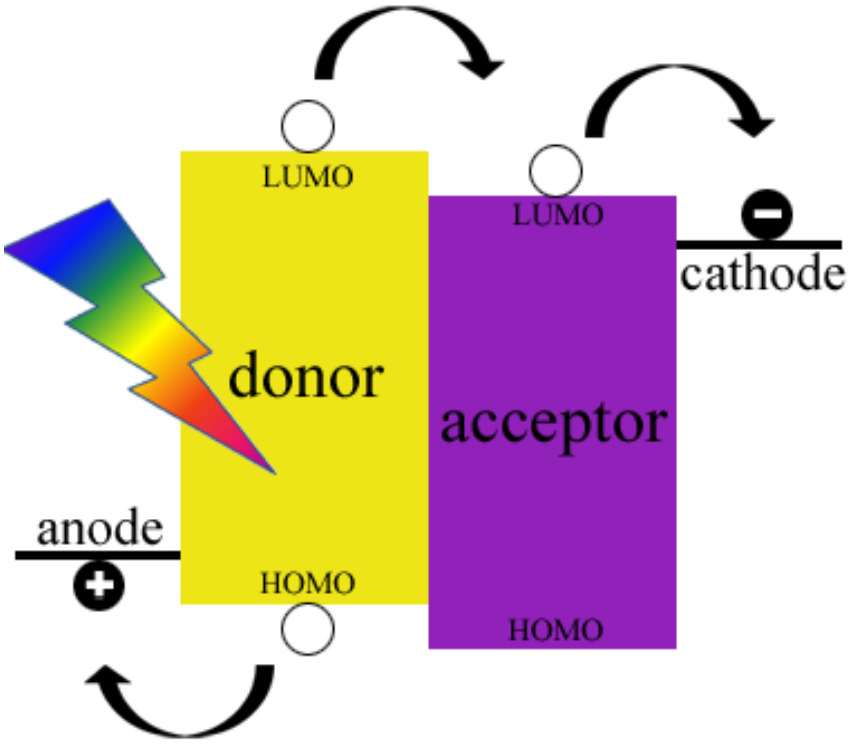

Figure I.2. Energy band diagram of charge transfer in a bulk heterojunction OPV. The OPV device is irradiated with light, which generates an exciton that diffuses towards the donor/acceptor interface. The dissociation of the exciton creates free charge carriers (i.e., holes and electrons) which migrate towards their respective electrodes.

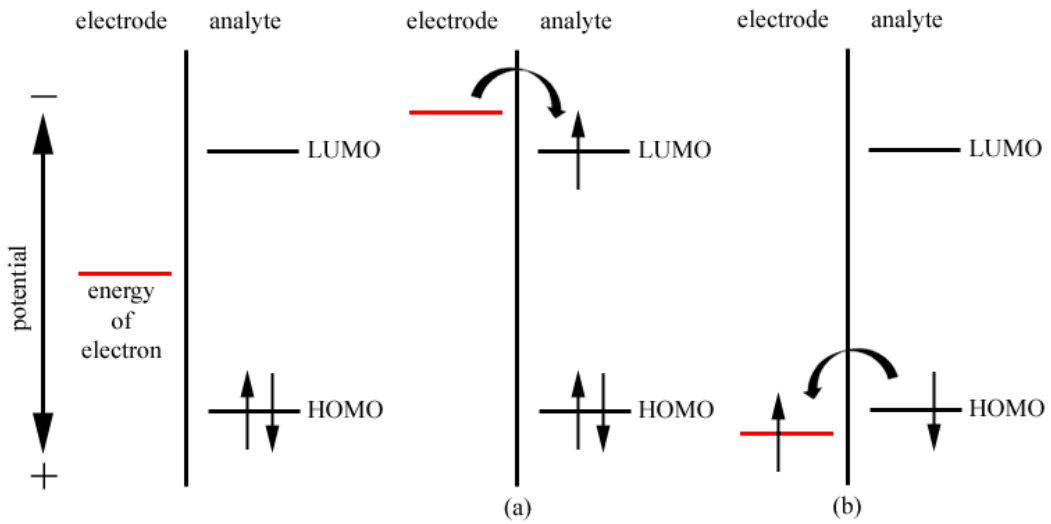

Figure I.3. Energy level diagram demonstrating the reduction (a) and oxidation (b) processes. The red line indicates the energy level of an electron on the electrode.

Table I.1. Total available energy (J) of different renewable energy resources.

source	**available energy (10^{20} J)**
geothermal	0.6
hydro	1.1
biomass	2.1
wind	21
solar	7400

Introduction References

(1) www.eia.gov.

(2) Green, M. A.; Emery, K.; Hishikawa, Y.; Warta, W.; Dunlop, E. D. *Prog. Photovolt: Res. Appl.* **2013**, *21*, 827.

(3) Brabec, C. J.; Durrant, J. R. *MRS Bull.* **2008**, *33*, 670.

(4) Machui, F.; Hösel, M.; Li, N.; Spyropoulos, G. D.; Ameri, T.; Søndergaard, R. R.; Jørgensen, M.; Scheel, A.; Gaiser, D.; Kreul, K.; Lenssen, D.; Legros, M.; Lamaitre, N.; Vilkman, M.; Välimäki, M.; Nordman, S.; Brabec, C. J.; Krebs, F. C. *Energy Environ. Sci.* **2014**, *7*, 2792.

(5) Krebs, F. C. *Sol. Energy Mater. Sol. Cells* **2009**, *93*, 394.

(6) Zhokhavets, U.; Erb, T.; Gobsch, G.; Al-Ibrahim, M.; Ambacher, O. *Chem. Phys. Lett.* **2006**, *418*, 347.

(7) Sariciftci, N. S.; Smilowitz, L.; Heeger, A. J.; Wudl, F. *Science* **1992**, *258*, 1474.

(8) Hummelen, J. C.; Knight, B. W.; LePeq, F.; Wudl, F.; Yao, J.; Wilkins, C. L. *J. Org. Chem.* **1995**, *60*, 532.

(9) Brabec, C. J.; Shaheen, S. E.; Winder, C.; Sariciftci, N. S. *Appl. Phys. Lett.* **2002**, *80*, 1288.

(10) Chen, J.; Cao, Y. *Acc. Chem. Res.* **2009**, *42*, 1709.

(11) Sirringhaus, H.; Brown, P. J.; Friend, R. H.; Nielsen, M. M.; Bechgaard, K.; Langeveld-Voss, B. M. W.; Spiering, A. J. H.; Janssen, R. A. J.; Meijer, E. W.; Herwig, P.; de Leeuw, D. M. *Nature* **1999**, *401*, 685.

(12) Reyes-Reyes, M.; Kim, K.; Carroll, D. L. *Appl. Phys. Lett.* **2005**, *87*, 083506.

(13) Kim, Y.; Cook, S.; Tuladhar, S. M.; Choulis, S. A.; Nelson, J.; Durrant, J. R.; Bradley, D. D. C.; Giles, M.; McCulloch, I.; Ha, C.-S.; Ree, M. *Nature Mater.* **2006**, *5*, 197.

(14) Shaw, P. E.; Ruseckas, A.; Samuel, I. D. W. *Adv. Mater.* **2008**, *20*, 3516.

(15) Kim, H.; So, W.-W.; Moon, S.-J. *Sol. Energy Mater. Sol. Cells* **2007**, *91*, 581.

(16) Yang, X.; Uddin, A. *Renew. Sust. Energy Rev.* **2014**, *30*, 324.

(17) Gadisa, A.; Tumbleston, J. R.; Ko, D.-H.; Aryal, M.; Lopez, R.; Samulski, E. T. *Thin Solid Films* **2012**, *520*, 5466.

(18) Hoppe, H.; Niggemann, M.; Winder, C.; Kraut, J.; Hiesgen, R.; Hinsch, A.; Meissner, D.; Sariciftci, N. S. *Adv. Funct. Mater.* **2004**, *14*, 1005.

(19) Ren, G.; Ahmed, E.; Jenekhe, S. A. *Adv. Energy Mater.* **2011**, *1*, 946.

(20) Kim, F. S.; Jenekhe, S. A. *Macromolecules* **2012**, *45*, 7514.

(21) Kim, F. S.; Ren, G.; Jenekhe, S. A. *Chem. Mater.* **2011**, *23*, 682.

(22) Yu, G.; Gao, J.; Hummelen, J. C.; Wudl, F.; Heeger, A. J. *Science* **1995**, *270*, 1789.

(23) Tsai, P.-T.; Yu, K.-C.; Chang, C.-J.; Horng, S.-F.; Meng, H.-F. *Org. Electron.* **2015**, *22*, 166.

(24) Liu, F.; Ferdous, S.; Schaible, E.; Hexemer, A.; Church, M.; Ding, X.; Wang, C.; Russell, T. P. *Adv. Mater.* **2015**, *27*, 886.

(25) Gao, D.; Helander, M. G.; Wang, Z.-B.; Puzzo, D. P.; Greiner, M. T.; Lu, Z.-H. *Adv. Mater.* **2010**, *22*, 5404.

(26) Jackson, N. E.; Savoie, B. M.; Marks, T. J.; Chen, L. X.; Ratner, M. A. *J. Phys. Chem. Lett.* **2015**, *6*, 77.
(27) Kissinger, P. T.; Heineman, W. R. *J. Chem. Educ.* **1983**, *60*, 702.
(28) Wang, X.-B.; Wang, L.-S. *Rev. Sci. Instrum.* **2008**, *79*, 073108.
(29) Slater, J. C. *Phys. Rev.* **1951**, *81*, 385.
(30) Slater, J. C. *Phys. Rev.* **1930**, *35*, 210.
(31) Hohenbern, P.; Kohn, W. *Phys. Rev.* **1964**, *136*, B864.
(32) Kohn, W.; Sham, L. J. *Phys. Rev.* **1965**, *140*, A1133.
(33) Cossi, M.; Rega, N.; Scalmani, G.; Barone, V. *J. Comp. Chem.* **2003**, *24*, 669.
(34) Tomasi, J.; Mennucci, B.; Cammi, R. *Chem. Rev.* **2005**, *105*, 2999.

Chapter 1.

Functionalization and Characterization of Perfluoroarylated Fullerenes

The contents in this dissertation chapter include the manuscript of a full article published in *Chemical Science* **2015**, DOI: 10.1039/c4sc02970d. This chapter discusses two new compounds 1,9-$C_{60}(CF_2C_6F_5)H$ (**1**) and 1,9-C_{60}(*cyclo*-CF_2(2-C_6F_4)) (**2**). Conversion of **1** into **2** can be realized by the addition of Sn_2(*n*-Bu)$_6$, proton sponge (PS), or cobaltocene ($CoCp_2$). DFT calculations indicate that when **1** is deprotonated, the anion $C_{60}(CF_2C_6F_5)^-$ can undergo facile intramolecular S_NAr annulation to form **2** with concomitant loss of F^-. The gas-phase electron affinity (EA) of **2** was determined to be 2.805(10) eV, higher than the EA of PCBM (phenyl-C_{61}-butyric acid methyl ester) by 0.18(1) eV. In contrast, the $E_{1/2}(0/-)$ values of **2** and PCBM are −0.01(1) and −0.09 V, respectively. TRMC charge-carrier yield × mobility values for organic photovoltaic active-layer-type blends of **2** and P3HT were comparable to those for equimolar blends of PCBM and P3HT. The structure of solvent-free crystals of **2** was determined by single-crystal X-ray diffraction. The number of nearest-neighbor fullerene–fullerene interactions is significantly greater for **2** (10 nearest neighbors) than for solvent-free crystals of PCBM (7 nearest neighbors). Finally, the thermal stability of **2** was found to be far greater than that of PCBM.

The author of this dissertation performed all of the synthetic and S_NAr reactions, all of the spectroscopic measurements except for the LT-PES, which was performed by Dr. Shihu H. M. Deng and Dr. Xue-Bin Wang, and grew single crystals of **2**. Eric V. Bukovsky solved and refined the X-ray structure of **2** under the supervision of Dr. Yu-Sheng Chen. Dr. Bryon W.

Larson performed the TRMC and device measurements at NREL under the supervision of Dr. Nikos Kopidakis and Dr. Garry Rumbles. Dr. James B. Whitaker performed the initial electrochemical measurements on **1** and **2**. Dr. Alexey A. Popov performed all of the DFT calculations. Dr. Brian Newell determined the unit cell parameters of **2** at 120 K.

Project supervision by Prof. Steven H. Strauss and Dr. Olga V. Boltalina.

1.1. Introduction

The Strauss/Boltalina research group[1] and others[2] have been investigating homoleptic perfluoroalkylfullerenes (PFAFs) such as 1,7-$C_{60}(R_F)_2$ (R_F = CF_3, C_2F_5, *n*-C_3F_7, *i*-C_3F_7, *n*-C_4F_9, 2-C_4F_9, and *n*-C_8F_{17}),[3,4] $C_{74}(CF_3)_{12}$,[5] $C_{84}(CF_3)_{12}$,[2,6,7] 7,24-$C_{70}(C_2F_5)_2$,[8] and C_3-C_{60}(*i*-$C_3F_7)_6$[9] since 2003. This very large class of fullerene$(X)_n$ derivatives has fostered an understanding of the relationships between fullerene addition patterns, LUMO shapes and relative energies, perfluoroalkyl chain lengths, and electrochemical/electron affinity properties[4,10,11] and has afforded a range of structurally similar PFAFs with $E_{1/2}(0/-)$ values that vary by as much as 0.5 V to be used for fundamental organic photovoltaic (OPV) active-layer studies.[12] We have recently turned our attention to (i) fullerenes with perfluoroaryl derivatives (e.g., perfluorobenzyl)[13] and (ii) hydro-PFAFs with one or more H atom substituents,[14,15] the latter so that their deprotonation and subsequent treatment with electrophiles E^+ would result in a variety of fullerene$(E)(R_F)_{n-1}$ derivatives for fundamental and applied studies.

The synthesis of 1,9-$C_{60}(CF_2C_6F_5)H$ (**1**), shown in Figure 1.1, and its unexpected transformation upon deprotonation or one-electron reduction to the exocyclic "fullerene with a faux hawk" product 1,9-C_{60}(*cyclo*-CF_2(2-C_6F_4)) (**2**), also shown in Figure 1.1 is discussed. The reaction sequence for the transformation **1** → **2** + HF is supported by DFT calculations. The gas-phase electron affinities, solution reduction potentials, thermal stabilities, X-ray diffraction

molecular structures, and solid-state packing in solvent-free crystals of **2**, PCBM (phenyl-C_{61}-butyric acid methyl ester), and C_{60} are compared and contrasted. Finally, the OPV active-layer thin films made from blends of **2** with poly-3-hexylthiophene (P3HT), when studied using time-resolved microwave photoconductivity, exhibit photoinduced charge-carrier yield × mobility figures of merit that rival the OPV active-layer standard blend of PCBM with P3HT, which demonstrates the potential of **2** as an electron acceptor in OPV and other optoelectronic devices.

1.2. Results and Discussion

1.2.1. Synthesis of 1,9-C_{60}($CF_2C_6F_5$)H (1) and 1,9-C_{60}(cyclo-CF_2(2-C_6F_4)) (2). In 1996 Yoshida, Suzuki, and Iyoda reported that the reaction of C_{60}, perfluoroalkyliodides (R_FI), (*n*-Bu)$_3$SnH, and a catalytic amount of the radical initiator AIBN in refluxing benzene for 30 h produced 1,9-C_{60}(R_F)H derivatives in moderate yields depending on the ratio of the reagents.[16] For example, with 12 equiv. *n*-$C_6F_{13}I$, 5 equiv. (*n*-Bu)$_3$SnH, and 0.1 equiv. AIBN (based on C_{60}), the yield of 1,9-C_{60}(*n*-C_6F_{13})H was 31% and 64% of the original C_{60} was recovered. With 12 equiv. *n*-$C_{12}F_{25}I$, 14 equiv. (*n*-Bu)$_3$SnH, and 0.1 equiv. AIBN, the yield of 1,9-C_{60}(*n*-$C_{12}F_{25}$)H was 26% and 67% of the original C_{60} was recovered. However, no fullerene products containing R_F groups were obtained in the absence of AIBN.[16]

No AIBN was necessary to prepare **1** when the solvent was 1,2-$C_6H_4Cl_2$ (*o*-DCB) and the temperature was 160 °C. Furthermore, reaction times of only 1 or 2 h were sufficient to form appreciable amounts of **1**, as shown in Figure 1.2 and Table 1.1. This is probably due to the higher temperature for the reaction and a lower C–I bond energy for $C_6F_5CF_2I$ than for *n*-$C_6F_{13}I$ or *n*-$C_{12}F_{25}I$, both of which will result in more $C_6F_5CF_2$• radicals present than the number of R_F• radicals in the reactions of Yoshida et al. The mol% values in Table 1.1 are based on HPLC peak

relative integrations and are only approximate. They are listed so that trends in product ratios at various reaction temperatures, reaction times, and reagent mole ratios can be easily understood.

The formation of **1** from $C_6F_5CF_2I$ and $(n\text{-Bu})_3SnH$ in *o*-DCB at elevated temperatures is best represented by the following balanced equation ($Bn_FI = C_6F_5CF_2I$; R = *n*-Bu):

$$C_{60} + Bn_FI + R_3SnH \rightarrow 1,9\text{-}C_{60}(Bn_F)H\ (\mathbf{1}) + \tfrac{1}{2}\ I_2 + \tfrac{1}{2}\ Sn_2R_6$$

At 100 °C and C_{60}:R_FI: R_3SnH reagent mole ratios of 1:1:2 (HPLC trace **a** in Figure 1.2), compound **1** and C_{60} were virtually the only fullerene species present in the reaction mixture after 2 h. The same amount of unreacted C_{60} was also present with the same reagent ratios when the temperature was 160 °C for 1 h (HPLC trace **b**, dotted line), but in this case both **1** and **2** were present (in a ca. 2:1 mol ratio). After 2 h (trace **b**, solid line), significantly less **1** and significantly more **2** were present (now in a ca. 1:5 mol ratio). The HPLC traces labeled **c** and **d** show the results of changing the reagent mole ratios for 1 h (dotted lines) and 2 h (solid lines) reactions. HPLC traces **d** indicate that a large excess of R_3SnH produces many other fullerene derivatives (presumably various hydrofullerenes) and much less **1** and **2** than when less R_3SnH was used. It is concluded that **1** is an intermediate in the formation of **2** under the reaction conditions. It is possible that R_3Sn• radicals are involved, as shown in the following *speculative* balanced equation, but R_3SnF has not been positively identified:

$$1,9\text{-}C_{60}(Bn_F)H\ (\mathbf{1}) + 2\ R_3Sn\bullet \rightarrow 1,9\text{-}C_{60}(\textit{cyclo}\text{-}CF_2(2\text{-}C_6F_4))\ (\mathbf{2}) + R_3SnH + R_3SnF$$

HPLC trace **e** in Figure 1.2 represents a compromise set of reaction conditions that produced significant amounts of **1** and **2**, relatively less unreacted C_{60}, and relatively small amounts of the other fullerene byproducts. This reaction resulted in a 35% isolated yield of **1** and a 7% isolated yield of **2** after HPLC purification (both yields based on C_{60}). These thermal reactions were also

performed using chlorobenzene as the reaction solvent at reaction temperatures of 140 °C to 150 °C. Lower C_{60} conversion and reduced time required for reaction work up were observed.

An alternate synthesis of **2** is the reaction of **1** with excess Proton Sponge (PS, 1,8-bis(dimethylaminonaphthalene)) in CH_2Cl_2 at 23(1) °C for 24 h. Proton Sponge was chosen due to its solubility in organic solvents and high basicity. The above reaction, which resulted in a 76% isolated yield of **2** based on **1**, will be discussed in detail in Section 1.2.7. The formation of **1** and **2** can also be realized by photoirradiation from a high-pressure mercury-arc lamp of the reaction mixture containing C_{60}, Bn_FI, and $(n\text{-}Bu)_3SnH$. When this reaction was performed at room temperature for 24 hours (Figure 1.3**a**) or 48 hours (Figure 1.3**b**), it produced **1** with high selectivity. At a longer photochemical reaction time of one week (Figure 1.3**c**) or even under ambient light (Figure 1.3**d**), high selectivity of **1** was also achieved while only trace amounts of **2** was observed in both cases. These photolysis reactions demonstrated that the formation of **1** can be achieved without applying harsh conditions even though the disadvantage was longer reaction times.

1.2.2. Synthesis of $C_{70}(CF_2C_6F_5)H$ (3) and C_{70}(cyclo-$CF_2(2\text{-}C_6F_4)$) (4) The chemistry described in Section 1.2.1 could be applicable towards other fullerene substrates. The next largest, most abundant, and stable fullerene is C_{70}. Unlike the I_h symmetry of C_{60}, C_{70} is slightly elongated in one axis giving rise to its D_{5h} symmetry and has been demonstrated to absorb more of the visible spectrum making C_{70} a better candidate for use in OPVs.[17] For example, when the donor P3HT polymer was blended with $PC_{60}BM$ or $PC_{70}BM$ in bulk heterojunction solar cells, the measured power conversion efficiencies were 2.6% and 3.3%, respectively.[18]

As one should expect, the additional 10 carbon atoms and lower symmetry of C_{70} should result in lower selectivity producing multiple products. Indeed, this was true when a *o*-DCB

solution containing C_{70} was heated at 160 °C in the presence of 20 equiv. of $C_6F_5CF_2I$ and 10 equiv. of $(n\text{-Bu})_3SnH$ for 2 h. The compounds $C_{70}(Bn_F)H$ (**3**), $C_{70}(cyclo\text{-}CF_2(2\text{-}C_6F_4))$ (**4**), and unreacted C_{70} were isolated from the crude reaction product using HPLC (Figure 1.4) while other minor $C_{70}(Bn_F)_nH_m$ compounds were not identified. When chlorobenzene was used as the reaction solvent heated at temperatures between 140 °C to 150 °C, as with the above C_{60} reactions, higher C_{70} conversion was observed and complex mixture of $C_{70}(Bn_F)_nH_m$ was formed. Its separation has not been undertaken. The reactions performed in *o*-DCB had lower C_{70} conversion and formed compounds **3** and **4** in higher yields in comparison to reactions performed in chlorobenzene where higher C_{70} conversion was observed.

1.2.3. Formation of C_{60} and C_{70} bis/tris-faux hawk adducts. Fullerene derivatives bearing two or three of the same adducts have been shown to perform better in organic photovoltaic devices which have been attributed to an increase in open-circuit voltage and decrease in electron affinity. To realize this, two synthetic routes for the addition of multiple adducts of the faux hawk moiety onto C_{60} was achieved by reacting Bn_FI and $(n\text{-Bu})_3SnH$ with (i) compound **1** or (ii) compound **2**. In both routes, a follow up deprotonation and/or one electron reduction with $CoCp_2$ may be required. When 10 equiv. of Bn_FI and 5 equiv. of $(n\text{-Bu})_3SnH$ was heated in a *o*-DCB solution containing **1**, compound **2** was not observed after 1 h for route (i); however, after 2 h of heating, compound **2** was observed along with C_{60} and a mixture of products containing $C_{60}(Bn_F)_2H_2$. Subsequent treatment of the crude reaction mixture with PS produced a mixture of $C_{60}(cyclo\text{-}CF_2(2\text{-}C_6F_4))_2$, $C_{60}(cyclo\text{-}CF_2(2\text{-}C_6F_4))_3$, and $C_{60}(cyclo\text{-}CF_2(2\text{-}C_6F_4))_2(Bn_F)H$ as observed by APCI-MS.

The purification of a single isomer of bis/tris-faux hawk compounds was expected to be difficult. For instance, bis-adducts of PCBM[19] and ICMA[20] contain multiple isomers which

requires extensive HPLC separation. All of the double bonds in I_h-C_{60} are equal resulting in the single isomer of the mono-adduct. After the first addition to C_{60}, the 29 remaining double bonds are available for the second adduct; however, they are all unequal due to the presence of the first adduct. This renders eight different possible isomers for the bis-adducts. Indeed, several isomers of bis-adducts of C_{60} and C_{70} were formed.

It turns out that bis/tris-faux hawk compounds are also formed during the synthesis of compound **1** (Figure 1.2, HPLC trace **e**, peaks with t_R < 8 minutes). Using the HPLC separation scheme in Figure 1.5, an isomeric mixture of bis- and tris-faux hawk compounds can be obtained. The fact that bis/tris-faux hawks can be isolated from compounds **1** and **2** circumvents the need for sequential reactions; thus, allowing for efficient preparation and separation of the C_{60} faux hawk family. The formation and separation of bis/tris-C_{70} faux hawks are still being investigated.

1.2.4. Characterization of C_{60} and C_{70} faux hawk derivatives. The negative-ion (NI) APCI mass spectrum of **1** exhibited an *m*/*z* species at 937, which is consistent with $C_{60}(CF_2C_6F_5)^-$, or [**1** − H]$^-$. The UV-vis spectrum of **1** (Figure 1.6) exhibited absorption maxima at 324, 431, and 698 nm. The 431 nm band in particular is characteristic of 1,9-$C_{60}X_2$ or 1,9-C_{60}XY derivatives.[21] In contrast, C_{60}XY derivatives with the substituents on the *para* positions on a C_{60} hexagon (i.e., 1,7-C_{60}XY) generally exhibit a prominent band at 450 nm.[4] A singlet at δ 7.2 in the ^{1}H NMR spectrum of **1** in $CDCl_3$ is characteristic of a C_{60}–H species[22-24] (cf δ 6.65 for 1,9-$C_{60}(CH_2C_6H_5)H$[24]).

The NI-APCI mass spectrum of **2** exhibited an *m*/*z* species at 918, which is consistent with the formula $C_{60}(CF_2C_6F_4)^-$. The UV-vis spectrum of **2** (Figure 1.6) exhibited bands at 331, 430,

and 687 nm, which supports a 1,9- addition pattern for this compound as well (verified by X-ray crystallography). No resonance was observed in a ^{1}H NMR spectrum of **2**, as expected.

The structure of **2**, determined by X-ray diffraction, is shown in Figure 1.1. The five-membered carbocycle substituent is essentially planar, with out-of-plane displacements (OOPs) for C1, C2, C7, C8, and C9 that range from 0.003 Å to 0.066 Å (average ±0.042 Å). In fact, C1, C9, and all seven of the perfluorinated substituent's C atoms are also co-planar (the nine OOPs range from 0.003 to 0.089 Å and average ±0.032 Å). The long C1–C9 bond distance of 1.611(3) Å is typical of C_{60} derivatives with 3-, 4-, 5-, and 6-membered exocyclic rings.[25,26]

On a side note, the structure of **4** was determined by the preliminary X-ray diffraction study and will only be used to determine its structure. The analysis of the X-ray diffraction study confirms that the faux hawk substituent is attached to the C_{70} fullerene cage similarly to the faux hawk substituent in compound **2** at the 6,6 hexagon junction. No other X-ray crystallography details about compound **4** will be further discussed.

Compound **2** has idealized C_s symmetry, with the essentially planar faux hawk substituent nearly perpendicular (i.e., 84°) to a plane tangent to the idealized fullerene surface at the C1–C9 midpoint (the two C2–C1–C_{cage} angles only differ by ca. 2°; the same is true for the two C8–C9–C_{cage} angles). This gives the molecule its "faux hawk hairstyle" appearance, as shown in Figure 1.1. In the OLYP DFT-optimized structure of **2**, the faux hawk substituent is rigorously planar (except for F1 and F2) and rigorously perpendicular to the C_{60} surface. See Table 1.2 for a comparison of relevant interatomic distances and angles for the X-ray and OLYP DFT-optimized structures of **2** and Figure 1.7 for a side-by-side comparison of the two structures. Note that the faux hawk substituent in **2** is attached to the type of C_{60} C–C bond that is common to two hexagons. Table 1.2 also includes the distances and angles for the OLYP DFT-optimized

structure of the isomer with the faux hawk substituent attached to a C_{60} C–C bond that is common to a pentagon and a hexagon, showing that the faux hawk substituent is sterically congruent in both isomers. Nevertheless, the DFT-predicted relative energy of the unobserved alternate isomer is 62 kJ mol^{-1} above the energy of the observed isomer. This difference is, therefore, fullerene based and not faux hawk-substituent based. As indicated above, the faux hawk substituent in the unobserved and observed isomers is attached to a 5,6 pentagon–hexagon and a 6,6 hexagon–hexagon C_{60} edge, respectively. Attachment of substituent atoms to a 5,6 edge of C_{60} introduces two C=C double bonds in pentagons, each of which is predicted to raise the energy of the C_{60} core by 33.5 ± 4.2 kJ mol^{-1}.[27]

There are several other examples of C_{60} derivatives with five-membered carbocyclic rings (these are formed by 3+2 cycloadditions of trimethylenemethanes to C_{60}),[28,29] but **2** is the only structurally characterized example in which the carbocycle contains a C=C double bond and is therefore planar. It is also the only example in which the carbocycle is perfluorinated.

Fluorine-19 NMR spectra of **1** and **2** are shown in Figures 1.8 and 1.9, respectively. Chemical shifts and coupling constants are listed in Table 1.3. The *J*(FF) coupling constants were determined by simulating the experimental spectra using the program MestReNova 8.1.1. The free rotation about the $F_2C–C_{ipso}$ bond in **1** and the presumed time-averaged C_s symmetry of **2** render the F atoms in the CF_2 moiety magnetically equivalent in both compounds. The aromatic moieties in **1** and **2** exhibited bb'cc'd and bcde patterns, respectively (the notation here conforms to the F atom labels in Figures 1.8 and 1.9).

There are distinct similarities between the C_{60} and C_{70} hydrofullerene (**1** and **3**, respectively), and between the C_{60} and C_{70} mono-adduct faux hawk (**2** and **4**, respectively). For instance, four resonances are observed in the ^{19}F NMR spectrum of **3** in a 2:2:1:2 ratio (t, δ −97.53; qt, δ

−137.13; m, δ −149.78; m, δ −161.87) in $CDCl_3$. Meanwhile, a singlet at δ 7.9 ppm was observed in the ^{1}H NMR spectrum, approximately 0.7 ppm shifted downfield in comparison to **1**. Five resonances was observed in compound **4** in a 2:1:1:1:1 ratio (d, δ −74.71; m, δ −139.14; m, δ −141.27; dt, δ −148.01, dt, δ −152.22) in 60/40 (v/v) $CS_2/CDCl_3$. The noticeable difference in solubility between **2** and **4** required the use of CS_2 for NMR analysis.

The *meta* coupling constants $J(F_bF_{b'})$, $J(F_cF_{c'})$, and $J(F_{bb'}F_d)$ in **1** and $J(F_bF_d)$ and $J(F_cF_e)$ in **2** are all 5–6 Hz. The *ortho* values, $J(F_bF_c)/J(F_{b'}F_{c'})$ and $J(F_{cc'}F_d)$ in **1** and $J(F_bF_c)$, $J(F_cF_d)$, and $J(F_dF_e)$ in **2**, are, as expected,[30] significantly larger, 18–26 Hz. The *para* coupling constants, however, are substantially different for the two compounds; $J(F_bF_{c'}) = J(F_{b'}F_c)$ is 7 Hz in **1** and $J(F_bF_e)$ is 23 Hz in **2**. The 7 Hz value for **1** is the same as the ca. 7 Hz coupling constants for F atoms *para* to one another in perfluorophenyl groups.[31] The 23 Hz value for **2** can be compared with the 18–26 Hz range for F atoms *para* to one another in tri- and tetrafluorobenzo[b]thiophenes,[32] the 14–19 Hz range in polyfluoroindenes,[33] and the 12–16 Hz range in tetrafluorobenzo[b]thiazoles,[34] compounds that, like **2**, have a polyfluorobenzo moiety fused to a coplanar five-membered ring. The origin of the difference in magnitude for *para* J(FF) values for polyfluorophenyl vs. polyfluorobenzo compounds is not well understood.

On the other hand, the substantial difference in $^4J(F_aF_{bb'})$ in **1** and $^4J(F_aF_b)$ in **2**, 30 Hz and 5.5 Hz, respectively, has a compelling explanation (the $^4J(F_aF_{bb'})$ value for $C_6F_5CF_2I$ is also 30 Hz). In both cases the F atoms are separated by a C(sp^2)–C(sp^3) single bond as well as a C(sp^2)–C(sp^2) bond, and the ^4J(FF) values are almost certainly dominated by Fermi-contact through-space interactions,[35-44] which are strongly dependent on the F···F distance, the F–C···C(F) angle, and the F–C···C–F torsion angle. The two $F_a\cdots F_b$ distances in the X-ray structure of **2** (these are F1···F6 and F2···F6 in Figure 1.1) are 2.998(6) and 3.151(6) Å, respectively, near the limit of ca.

3.2 Å for observable Fermi-contact through-space coupling between proximal F atoms (the corresponding distances in the C_s-symmetric DFT-optimized structure of **2** are 3.088 Å).[35-44] In contrast, the short $F_a\cdots F_b$ distances in the C_s-symmetric lowest-energy DFT-optimized structure of **1** are both 2.587 Å, a distance which is comparable to the 2.60–2.65 Å F···F distances in compounds previously shown to exhibit ^4J(FF) values of 19, 25, 27, or 48 Hz depending on the aforementioned angles.[43]

The gas-phase electron affinity (*EA*) of **2** was determined to be 2.805(10) eV by low-temperature photoelectron spectroscopy (LT-PES) of the $\mathbf{2}^-$ radical anion, as shown in Figure 1.10 (cf. 2.683(8) eV for C_{60}[45] and 2.63(1) eV for PCBM[46]). Therefore, **2** is a stronger electron acceptor (in the gas phase) than C_{60} and PCBM by 0.12(1) and 0.18(1) eV, respectively. We attribute this to the strong electron-withdrawing nature of the faux hawk moiety. The LT-PES spectrum of $\mathbf{1}^-$ could not be observed because of the rapid loss of the H atom to form the closed-shell species $[\mathbf{1} - H]^-$ (i.e., $C_{60}(CF_2C_6F_5)^-$). Photodetachment of an electron from this anion allowed the 3.75(3) eV *EA* of the neutral radical $C_{60}(CF_2C_6F_5)$• to be determined, but the *EA* of **1** remains unknown. It is well known that the *EA* values for fullerene radicals are ca. 1–2 eV higher than for closed-shell fullerene derivatives of similar composition. For example, the *EA* values for closed-shell $C_{60}F_{46}$, the $C_{60}F_{47}$• radical, and closed-shell $C_{60}F_{48}$ are 4.06(25),[47] 5.66(10),[48] and 4.06(30) eV,[47] respectively.

Square-wave and cyclic voltammograms (SWVs and CVs, respectively) of **1**, **2**, C_{60}, and PCBM were recorded under identical conditions in *o*-DCB containing 0.1 M N(*n*-Bu)$_4$BF$_4$ and Fe(Cp)$_2$ as an internal standard. In all cases the reduction potentials determined by SWV and by CV were the same within the ±0.01 V uncertainty of the individual measurements. The potentials are listed in Table 1.4 along with $E_{1/2}(0/-)$ values for the related compounds 1,9-$C_{60}H_2$,[49,50] 1,9-

$C_{60}(CH_3)_2$,[51] and 1,9-C_{60}(*cyclo*-C_2F_4).[52] Our $E_{1/2}(0/-)$ values for C_{60} and PCBM were first reported in 2013 in the same paper reporting the EA of PCBM.[46] The CVs for **1**, **2**, and C_{60} are shown in Figure 1.11. The similarity of $E_{1/2}(0/-)$ values for **2** and C_{60} is at odds with the 0.12(1) eV difference in their EAs. However, differences in $E_{1/2}(0/-)$ values for fullerene derivatives are generally smaller, and sometimes much smaller, than the corresponding differences in their EAs.[4,11]

Removing one of the double bonds of C_{60} by addition of substituents or a cycloadduct to C1 and C9 generally lowers the $E_{1/2}(0/-)$ by ca. 0.1 V. For example, $E_{1/2}(0/-)$ values for 1,9-$C_{60}(CH_2C_6H_5)H$,[24] PCBM,[46] 1,9-$C_{60}(CH_3)_2$,[51] and 1,9-$C_{60}H_2$,[50] are −0.08, −0.09, −0.12, and −0.13 V vs. $C_{60}^{0/-}$, respectively (in each case the comparison with C_{60} was made under the same conditions of solvent, electrolyte, and temperature). If the cycloadduct is fluorinated and therefore electron withdrawing, as in **2** and 1,9-C_{60}(*cyclo*-C_2F_4), the $E_{1/2}(0/-)$ values, −0.01 and 0.03, respectively, have increased by ca. 0.1 V from PCBM-like potentials, resulting in C_{60}-like potentials. The $E_{1/2}(0/-)$ values of **2** and C_{60} are the same because the offsetting effects of (i) reducing the fullerene π system by one double bond and (ii) changing the substituent(s) from hydrocarbyl groups or a hydrocarbyl cycloadduct to a perfluorocarbon cycloadduct cancel each other in this case.

The foregoing analysis is the reason that the three $E_{1/2}$ values for **1** and **2** are so similar. The expected $E_{1/2}(0/-)$ value for **1** should be ca. halfway between 0.03 and −0.13 V based on the $E_{1/2}(0/-)$ values in Table 4, but clearly this is not the case (an ^{19}F NMR spectrum of **1** in the electrolyte solution used for the CV experiments, to which 10% C_6D_6 was added, verified that **1** does not react with the electrolyte solution on the timescale of the CV experiment). Compound $\mathbf{1}^-$ was expected to undergo loss of the H atom to form $[\mathbf{1} - H]^-$, as it did in the LT-PES

experiment discussed above and in the **1** + $CoCp_2$ reaction. Furthermore, hydrofullerenes such as 1,9-$C_{60}H_2$,[49,50] 1,9-$C_{60}(CH_2C_6H_5)H$,[53] and isomers of $C_{70}(CH_2C_6H_5)H$[54] are known to undergo observable H-atom loss upon one-electron reduction unless the CV scan speed is extremely high or the solution is cooled to a low temperature. Nevertheless, in the absence of additional electrochemical experiments, the redox potentials for **1** listed in Table 1.4 are correctly assigned.

It has been shown that the second and third addition of the indene moiety to ICMA significantly shifts the $E_{1/2}(0/-)$ cathodically by 40 mV and 240 mV, respectively.[20] A similar trend was observed for the bis/tris-C_{60} faux hawk compounds albeit smaller shifts. The cyclic voltammograms shown in Figure 1.12 depict cathodic shifts of 22 mV and 82 mV in $E_{1/2}(0/-)$ from **2** suggesting that the electron withdrawing abilities of the faux hawk moiety is much stronger than the indene moiety even though the bis- and tris-adducts contain the same number of π electrons remaining on the fullerene cage.

1.2.5. Thermal stability comparison of 2 and PCBM. It was recently shown that PCBM undergoes substantial decomposition in only 20 min at 340 °C.[55] An HPLC trace of 340 °C-treated PCBM, taken from a figure in reference 55, is shown in Figure 1.13. Part of the 340 °C-treated PCBM sample was a charred residue that did not dissolve in toluene. Of the portion of the sample that did dissolve, only ca. 22% was intact PCBM. The most abundant decomposition product was identified as a new five-membered ring cycloadduct isomer of PCBM and that is virtually a hydrocarbyl equivalent of **2**.[55] Quantum chemical calculations predict iso-PCBM to be ca. 43 kJ mol^{-1} more thermodynamically stable than PCBM due to the isomerization from a three-membered cyclopropyl adduct to a five-membered cyclopentyl adduct.[55]

In contrast, the HPLC trace of 340 °C-treated **2**, also shown in Figure 1.13, shows no evidence of decomposition unless the traces are vertically expanded 100 times. In the expanded

trace, the unambiguous presence of one yet-unidentified new species with an abundance of ca. 0.6 mol% based on HPLC relative intensities can be seen. In addition, no new peaks were observed in the ^{19}F NMR spectrum of 340 °C-treated **2**. Based on the signal/noise ratio of that spectrum, the upper limit of any fluorine-containing compound other than **2** is ca. 0.5 mol%. Significantly, there was no insoluble residue after **2** was heated at 340 °C. It is hypothesized that the thermal stability of **2** is a result of the strong C–F bonds and the already present five-membered cyclopentyl adduct.

These results are important because post-fabrication thermal annealing of fullerene-containing OPV devices can, in some cases, improve device efficiency and therefore have become common practice in OPV research[56,57] and because thin films of PCBM or similar fullerene derivatives used for photophysical or electronic property investigations were prepared by high-temperature vacuum sublimation[58-60] (see additional references cited in reference 61). It is possible that the thin films and other materials/devices studied in the papers just cited contained iso-PCBM as well as PCBM and possibly other PCBM thermal decomposition products. How well faux hawk fullerene **2** performs not only in OPV but in other organic electronic applications, especially those that involve thermal annealing and/or thermal evaporation at temperatures up to and including 340 °C, remains to be seen.

1.2.6. Solid-state packing of 2 and comparison with PCBM. There are two solvent-free X-ray structures of PCBM: a single-crystal structure determined using data collected at 100(2) K[62] and a structure determined by powder X-ray diffraction data collected at 298(2) K.[63] Both have the same space group, the same nearest-neighbor crystal packing (see Figure 1.14), and, despite the difference in temperature, have densities (i.e., unit cell volumes) that differ by only 0.64(3)%. This is somewhat surprising because most organic crystals exhibit a larger percentage-increase in

density between 300 and 100 K, typically 3–6%.[64] For example, the density increases over this temperature range for benzene, naphthalene, and the *F*3*m*3 polymorph of C_{60} are 5.1, 7.8, and 2.0%, respectively.[64] This may indicate that solvent-free PCBM is packed as tightly as possible at room temperature, even more so than C_{60}.

The molecular structures of **2** and the 100 K single-crystal structure PCBM[62] are shown side-by-side in Figure 1.15. The two substituents have nearly the same number of non-hydrogen atoms, 13 for **2** and 14 for PCBM, but the faux hawk substituent is clearly the more compact. The 1.632(2) Å C1–C9 bond in PCBM is only marginally longer than the 1.610(5) Å distance in **2**, and fullerene cage atoms C1 and C9 are only slightly less pyramidalized in PCBM (POAV θ_p = 17.1° × 2) than in **2** (θ_p = 18.9 and 19.1°).

The solvent-free solid-state packing of **2** and PCBM[62] are shown in Figures 1.16 and 1.17, respectively. In both cases the C_{60} cage centroids (⊙) form rigorously-planar layers that are stacked in the third dimension. (In the structure of **2**, the stacking direction is parallel to the crystallographic *c* axis, as shown in Figure 1.18.) Significantly, the numbers of nearest neighbor molecules in the two structures are different. There are only seven (7) nearest neighbor fullerene molecules in crystalline solvent-free PCBM, with ⊙···⊙ distances of 9.95–10.28 Å. The mean and median distances are 10.17 and 10.24 Å, respectively. On the other hand, there are ten (10) nearest neighbors in the structure of **2**, with ⊙···⊙ distances of 9.74–10.34 Å. The mean and median distances are 10.09 and 10.05 Å, respectively. The result is that the density of crystalline **2**, 1.885 g cm^{-3}, is 15.6% higher than the 1.631 g cm^{-3} density of solvent-free PCBM, even though the molar masses of the two compounds, 918.67 g mol^{-1} for **2** and 910.83 g mol^{-1} for PCBM, differ by only 1.1%. Although the diffraction data reported here for **2** were collected at 15(2) K, unit cell parameters were also determined at 120(2) K, and the unit cell volume was

only 0.64% larger than at 15(2) K. If the 120 K density is considered, then the density of crystalline **2** is 14.8% higher than crystalline solvent-free PCBM at 100 K. This result should not come at a surprise because of the electron-withdrawing nature of the faux hawk moiety, the dipole moment of **2** is expected to be greater than PCBM; thus, allowing for stronger intermolecular electrostatic attractive forces to bring molecules of **2** closer to each other.

It is widely believed that the aggregation behavior of OPV acceptor fullerenes in the solid state, especially the number of electronically coupled nearest neighbors and their three-dimensional arrangement, are among the key factors that determine charge transport properties in the fullerene domains in Type II heterojunction solar cells.[20,62,63,65-71] Accordingly, the determination of the number of nearest neighbor fullerenes is important, and it depends on the choice of the maximum relevant ⊙···⊙ distance beyond which fullerene–fullerene electronic coupling is probably negligible. After the seven closest PCBM molecules surrounding each molecule of PCBM in the solvent-free structure,[62] shown in Figure 1.17, the two next shortest ⊙···⊙ distances are 11.61 and 13.23 Å. On what basis did we decide whether or not the 11.61 Å molecule should be considered to be an electronically-relevant nearest neighbor? The following criterion is proposed. The 11.61 Å distance to is too long for effective electronic coupling because the closest $C_{cage}\cdots C_{cage}$ distance between these two PCBM molecules is 5.03 Å (and these two C_{cage} atoms are close to lying on the ⊙···⊙ vector). In contrast, the closest $C_{cage}\cdots C_{cage}$ distances for PCBM molecules with ⊙···⊙ separations of 10.28 and 10.24 Å are 3.23 and 3.32 Å, respectively, approximately the same as the 3.35 Å interplanar separation in graphite.[72] For **2**, the closest C···C distance between two molecules with separations of 10.34 Å is 3.38 Å, and the next closest ⊙···⊙ distances are 14.00 Å. Therefore, the two centroids that are 10.34 Å from the

central centroid in Figure 1.16 belong to faux hawk molecules counted among the ten nearest neighbors around each faux hawk molecule.

Interestingly, the perpendicular spacings between the rigorously-planar layers of centroids are smaller, in the structure of solvent-free PCBM, 5.89 and 6.46 Å, than in the structure of **2**, 6.96 and 8.71 Å. Due to offsets of the C_{60} centroid layers relative to one another, the interlayer spacings are not an important metric from the standpoint of electron mobility. The ⊙···⊙ distances and their three-dimensional arrangement are important.

It may come as a surprise to many readers that the ⊙···⊙ distances in PCBM crystals containing solvent molecules can be, on average, shorter, than in the solvent-free structure discussed above, *even when there are as many PCBM nearest neighbors*. In the 123 K single-crystal structure of PCBM·0.5CS_2,[67] seven ⊙···⊙ distances span the range 9.86–10.27 Å and average 10.08 Å. There are two unique PCBM molecules in the 90 K structure of PCBM·0.5C_6H_5Cl, they both have seven nearest neighbors, and the mean ⊙···⊙ distances are 10.01 and 10.02 Å (the two ranges are 9.84–10.14 and 9.95–10.06 Å, respectively).[70] In the 123 K structure of ThCBM·1.25CS_2, in which a nearly-isosteric thienyl five-membered ring has replaced the phenyl group in PCBM, there are two unique ThCBM molecules.[67] One has seven nearest neighbors with a mean ⊙···⊙ distance of 10.03 Å (the range is 9.98–10.19 Å) and the other has *ten* nearest neighbors with a mean ⊙···⊙ distance of 9.99 Å (the range is 9.84–10.19 Å).[67] Finally, in the 90 K structure of PCBM·*o*-$C_6H_4Cl_2$, the one exception that proves the rule, there are only six, not seven, ⊙···⊙ distances, although the mean distance is still small, only 10.01 (the range is 10.00–10.22 Å). (All of the individual ⊙···⊙ distances as well as the mean distances for all of the structures just discussed are listed in Table 1.5.) Whatever space is taken

up by solvent molecules in structures of PCBM and related molecules, the fullerene–fullerene interactions can be as strong and as extensive as in solvent-free structures. It remains to be seen whether the presence of *all* types of solvent molecules, not just the ones examined so far, and/or the presence of other so-called "impurities" in fullerene domains *always* have a deleterious effect on electron mobility in blended donor-acceptor thin films and/or on power conversion efficiencies of OPV devices made with such films.

As stated above, and as previously suggested by others,[20,62,63,65-70] whether or not the nearest-neighbor ⊙···⊙ vectors in a fullerene domain point in three dimensions, and not just in two-dimensional layers, should affect electron mobility in a three-dimensional domain as much as the number of and the distances to the nearest neighbor fullerene molecules. The three-dimensional nature of the packing patterns in the X-ray structures of **2** and solvent-free PCBM are shown in Figures 1.16 and 1.17. The corresponding figures for the X-ray structures of PCBM·0.5CS_2, PCBM·0.5C_6H_5Cl, PCBM·*o*-$C_6H_4Cl_2$, and ThCBM·1.25CS_2 are shown in Figure 1.19. In all cases but one, the packing is three dimensional. In the case of PCBM·*o*-$C_6H_4Cl_2$, the packing is essentially two dimensional and, as pointed out by the authors of the paper reporting the structure, this should hamper three-dimensional-hopping electron transport.[70]

1.2.7. Understanding the transformation 1 → 2 + "HF". According to O3LYP//OLYP DFT calculations, the transformation **1** → **2** + HF is exothermic by 42 kJ mol^{-1} in the gas phase and 60 kJ mol^{-1} in a PhCN-like dielectric continuum. However, **1** was unchanged after heating an *o*-DCB solution at 160(5) °C for 2 h. Therefore, this reaction does not occur rapidly by a thermally-activated intramolecular pathway in a non-basic solvent. Nevertheless, the synthesis of **1** resulted in the formation of significant amounts of **2** depending on the reaction conditions. To

test the idea that **2** can be produced from **1** as an intermediate (although not necessarily as an obligate intermediate), the following series of reactions were performed.

The reagent SnH(*n*-Bu)$_3$ and byproduct Sn$_2$(*n*-Bu)$_6$ that are present during the synthesis of **1** and **2** can form Sn(*n*-Bu)$_3$• radicals. In a separate experiment, we heated **1** in *o*-DCB at 160 °C with added Sn$_2$(*n*-Bu)$_6$. Unlike the 160 °C experiment described in the previous paragraph, complete conversion of **1** to **2** occurred within 2 h in the presence of Sn$_2$(*n*-Bu)$_6$. Since the reagents SnH(*n*-Bu)$_3$ and Sn$_2$(*n*-Bu)$_6$ are not "simple" one-electron reducing agents, the reaction of **1** with 1 equiv. of CoCp$_2$ in PhCN at 23(1) °C was studied. This also caused the conversion of **1** to **2**, as shown by ^{19}F NMR spectroscopy.

If the one-electron reduced species **1**$^-$ loses an H atom, as do other one-electron reduced hydrofullerenes, the intermediate would be CoCp$_2^+$C$_{60}$(CF$_2$C$_6$F$_5$)$^-$ (i.e., CoCp$_2^+$[**1** − H]$^-$), which would react further to form **2** and CoCp$_2^+$F$^-$. A simpler way to generate [**1** − H]$^-$ is by deprotonation. When 1.0 equiv. of the strong base PS was added to a 90/10 (v/v) PhCN/C$_6$D$_6$ solution of **1** at 23(1) °C, the formation of **2** was complete within 5 min, as shown in Figure 1.7. At longer times, a new ^{19}F peak appeared at δ −139.6. Based on the chemical shift, the magnitude of the coupling constant (145 Hz), and the abundance of the I = 1/2 species to which the F atoms are coupled (ca. 5%), the new peak is assigned to an "SiF$_n$" species,[73-78] indicating that HF, or species with HF-like reactivity towards glass, such as ion-paired [H(PS)]$^+$F$^-$ and/or HF$_2^-$, were byproducts of the reaction. Rapid exchange between HF, F$^-$, and HF$_2^-$ is probably the reason why ^{19}F peaks due to one or more of these species were not observed during or after the reaction, only an SiF$_n$ species due to reaction of the HF-like species with the walls of the NMR tube. When **1** was treated with excess PS in CDCl$_3$ for 24 h, the reaction mixture contained 24% **1**, 76% **2**, and a precipitate (the amounts of **1** and **2** were determined by integrating the ^{19}F NMR

spectrum of the reaction mixture). The precipitate was soluble in CD_3CN and exhibited a δ −155.8 ^{19}F NMR singlet and a broad δ 19.0 ^{1}H NMR singlet, both of which are commensurate with $H(PS)^+F^-$.[79]

On the basis of the experiments just described, the treatment of **1** with PS resulted in deprotonation to give $H(PS)^+$ and $C_{60}(CF_2C_6F_5)^-$ as first-formed intermediates and that $C_{60}(CF_2C_6F_5)^-$ formed **2** and "F^-" within minutes. At longer times, $[H(PS)]^+F^-$ or an equivalent fluoride-like species present reacted with the glass NMR tube to form the SiF_n species. Even though the putative intermediate $C_{60}(CF_2C_6F_5)^-$ disappeared too rapidly to observe before an ^{19}F NMR spectrum could be recorded, its presence can be proposed because simple deprotonation of hydrofullerenes to give anionic fullerene species is well documented (i.e., hydrofullerenes are known to be Brønsted acids: the pK_a values for $C_{60}(CN)H$,[80] $C_{60}H_2$,[81] and $C_{60}(t\text{-Bu})H$[82] were found to be 2.5, 4.7, and 5.7, respectively). Interestingly, when **1** was treated with only 0.25 equiv. of PS in 90/10 (v/v) $PhCN/C_6D_6$ solution, the complete conversion to **2** also occurred, but only after 48 h, as shown in Figure 1.20. This autocatalytic transformation of **1** into **2** presumably results from the first-formed 0.25 equiv. byproduct F^- (or $[H(PS)]^+F^-$ or HF_2^-), which formed rapidly, acting as a base and continuing to deprotonate, albeit more slowly, additional molecules of **1** until it is completely converted to **2**. In a control experiment to inhibit the proposed catalytic effect of F^- as a general base, a few drops of saturated aqueous $Ca(NO_3)_2$ were added to a similar NMR-scale reaction containing ca. 0.3 equiv. of PS (based on **1**). In this case, the conversion of **1** to **2** was only 30–40% complete after 48 h, a white gelatinous precipitate formed in the aqueous layer (presumably CaF_2), and the ^{19}F NMR peak assigned to the SiF_n species was absent even after 48 h.

The rapid conversion of deprotonated **1** (i.e., [**1** − H]$^-$) to **2** most likely occurs by an intramolecular S_NAr mechanism whereby the [**1** − H]$^-$ fullerene carbanion attacks one of the *ortho*-C–F bonds of the $CF_2C_6F_5$ substituent. Fullerenes aside, intermolecular S_NAr reactions involving aromatic C–halogen bonds have been extensively studied.[83-87] In contrast, the scope of intramolecular S_NAr reactions that result in breaking an aromatic C–F bond and concomitant loss of F$^-$ is limited.[88-90] In the examples most relevant to this work, Hughes and co-workers showed that perfluorobenzyl ligands on either Co[89] or Rh[90] can undergo intramolecular S_NAr substitution of an *ortho*-F atom to form either six- or five-membered chelate rings, respectively. There is general agreement that, all other things being equal, aromatic C–F bonds undergo S_NAr substitution much faster than aromatic C–Cl, C–Br, or C–I bonds.[83-87] However, there is still controversy about whether a true Meisenheimer[91] intermediate is formed (even if it cannot be detected spectroscopically)[92-98] or whether the reaction involves a single Meisenheimer-like transition state.[99-102]

Reactions of $C_{60}R^-$ carbanions with electrophilic substrates EX to form new C_{60}(E)R species and X$^-$ are well known,[26,103,104] but to our knowledge there is no previous example of an S_NAr reaction involving a fullerene *cage* carbanion (i.e., not including examples such as the negatively-charged N atom of a deprotonated *cyclo*-pyrrolidinofullerene undergoing an intermolecular S_NAr reaction with an aryl chloride[105]), let alone an *intra*molecular S_NAr reaction of a fullerene cage carbanion attacking an Ar–F bond. Therefore, the intramolecular S_NAr hypothesis for the observed transformation [**1** − H]$^-$ → **2** + F$^-$ was determined by DFT-optimized structures and relative energies for **1** and **2** as well as for three different states of [**1** − H]$^-$. Figure 1.21 shows the OLYP DFT-optimized structures and the O3LYP//OLYP relative energies of these five species. Both gas-phase and PhCN-like dielectric continuum relative

energies were calculated. Drawings of the upper fragments of the gas-phase optimized structures are shown in Figure 1.22 and relevant interatomic distances and angles are listed in Table 1.6.[106] Larger drawings of the optimized species are shown in Figures 1.23 to 1.28. The calculated solvation energies for the ground-state (GS), transition-state (TS), and Meisenheimer-like intermediate-state (IS) structures of the deprotonated [**1** − H]$^-$ anion are listed in Table 1.7. This table also lists the gas-phase relative energies using other DFT functionals for the three [**1** − H]$^-$ states along the proposed S_NAr reaction coordinate.

The DFT results show that an S_NAr mechanism is energetically viable for the unimolecular intramolecular annulation reaction [**1** − H]$^-$ → **2** + F$^-$, even without the probable stabilizing effect of hydrogen bonding of either H(PS)$^+$ or HF to the three [**1** − H]$^-$ structures. The transition state structure of [**1** − H]$^-$ is only ca. 70 kJ mol^{-1} above the ground-state structure; transition states of 45–130 kJ mol^{-1} have been calculated for non-fullerene S_NAr transition states involving nitrogen or sulfur nucleophiles and aromatic C–F bonds.[96-98] This is consistent with the observed reaction time of only minutes when **1** was mixed with 1 equiv. of PS in 90/10 (v/v) PhCN/C_6D_6 at 23(1) °C. Apparently, there is sufficient conformational flexibility in the $CF_2C_6F_5$ substituent in [**1** − H]$^-$ to accommodate the nascent five-membered ring in the transition state.

The structural changes in the C1–C9 moiety of five fullerene species along the proposed S_NAr reaction coordinate can be appreciated using Figure 1.22 and the results listed in Table 1.6. There is a significant change in the degree of pyramidalization (θ_p; see Table 1.6) of C1 and in the set of three C1–C distances for the first step in the reaction sequence, the deprotonation of **1**. The former changes from 18.2° for **1** to 9.6° for GS [**1** − H]$^-$ and the latter from (1.59, 1.53, 1.53 Å) for **1** to (1.52, 1.42, 1.43) for GS [**1** − H]$^-$, signaling a change in hybridization of C1 from sp^3 in **1** to a blend of sp^3 and sp^2 in GS [**1** − H]$^-$. The ground-state anion is a carbanion, but the

negative charge and the putative "lone pair" are delocalized throughout the C_{60} cage. Significantly, the 9.6° θ_p degree of pyramidalization for C1 in GS [**1** − H]$^-$ is smaller, than the 11.6° θ_p value for the cage C atoms in C_{60}.[106] (The delocalization of the negative charge in $C_{60}R^-$ carbanions was previously proposed by Van Lier, Geerlings, and coworkers based on computational results.[107-109]) As expected, the C_6F_5 rings in **1** and GS [**1** − H]$^-$ are virtually congruent. Even the C8–C9 bond distance is unaffected by the deprotonation.

In the second step, GS [**1** − H]$^-$ is transformed into TS [**1** − H]$^-$. Even though the C1···C2 distance, at 1.981 Å, is very long, the C1 θ_p value increases from 9.6° to 16.2°, which is 90% of its original value in **1**. Accordingly, the three C1–C_{cage} distances increase from (1.52, 1.42, 1.43) in GS [**1** − H]$^-$ to (1.56, 1.47, 1.48) in TS [**1** − H]$^-$. At the same time, C2 is developing sp^3 character: the C2–C3 and C2–C7 distances increase from 1.40 and 1.41 Å in GS [**1** − H]$^-$ to 1.43 and 1.44 Å in TS [**1** − H]$^-$, and the sum of the three angles at C2 involving C3, C7, and F is 344° in TS [**1** − H]$^-$ whereas this sum is 360° in GS [**1** − H]$^-$. Another way to depict the distortion in the C_6F_5 group in TS [**1** − H]$^-$ is as follows. The 10 atoms C2–C7 and F3–F6 are coplanar to within ±0.02 Å in both GS [**1** − H]$^-$ and TS [**1** − H]$^-$. However, in GS [**1** − H]$^-$ atom F (i.e., the F atom bonded to C2) is also in that plane whereas in TS [**1** − H]$^-$ it is displaced 0.86 Å from that plane. As expected, the C2–F bond in TS [**1** − H]$^-$, at 1.42 Å, is significantly longer than the 1.34 Å distance in both hydrofullerene precursor **1** and the GS [**1** − H]$^-$ anion.

The Meisenheimer-like intermediate, denoted IS [**1** − H]$^-$, exhibits further repyramidalization of C1 and further pyramidalization of C2. Both of these atoms are essentially tetrahedral in the intermediate, with four single bonds. In fact, the C1 θ_p value, 19.6°, is only 0.1° different than the ideal θ_p tetrahedral angle (19.5°), and the sum of the three angles at C2 involving C3, C7, and F is 328.6°, within 0.1° of the expected sum for a tetrahedral C atom (i.e., 3 × 109.5° = 328.5°).

Furthermore, the C2–F bond, at 1.567 Å, is exceptionally long and is clearly developing a significant amount of F^- character. Note that all C–F bond distances measured by X-ray crystallography (as of 1987) are shorter than 1.4 Å.[110]

Finally, in the last step of the reaction sequence shown in Figures 1.21 and 1.22, F^- dissociates from the intermediate and the C_6F_4 ring undergoes rearomatization (i.e., the C2–C3 and C2–C7 bond distances shorten from 1.46 Å in IS $[\mathbf{1} - H]^-$ to 1.40 Å in **2**.

1.2.8. Time resolved microwave conductivity measurements. The denser packing of **2** relative to PCBM and the nearly-equal $E_{1/2}(0/-)$ values for **2** and C_{60} suggested that **2** might be an efficacious electron acceptor in OPV bulk heterojunction thin films. The charge generation and decay dynamics of **2** when blended with regioregular poly-3-hexylthiophene (rr-P3HT) using time-resolved microwave conductivity (TRMC) was investigated.[111] There are two advantages to measuring photoconductance with TRMC: (i) it is a contactless method and is therefore specific to processes occurring in an OPV active-layer film under illumination; and (ii) the ns–μs timescale of TRMC measurements is the same as the timescale of charge-carrier dynamics in an OPV device.[20] Figure 1.29 shows the $\varphi\Sigma\mu$ TRMC figure of merit for three thin-film samples (φ is the quantum yield of mobile-charge-carrier generation (i.e., electrons and holes) and $\Sigma\mu$ is the sum of charge-carrier mobilities at the limit of low excitation intensity).[112]

The $\varphi\Sigma\mu$ value for a blend of rr-P3HT and **2** is nearly two orders of magnitude higher than for a neat rr-P3HT thin film and is comparable to the $\varphi\Sigma\mu$ value for an rr-P3HT/PCBM blend, as shown in Figure 1.29. The latter observation is indicative of efficient free-charge-carrier generation in the rr-P3HT/**2** blend, a combination of a high φ value as well as a large $\Sigma\mu$ contribution due to electron mobility in domains of **2** within the bulk heterojunction thin film, as previously observed for rr-P3HT blends with other high-performance OPV acceptors.[20,112,113]

The decay profiles of the transients for the rr-P3HT/**2** and rr-P3HT/PCBM blends are nearly identical, as also shown in Figure 1.29. The signals are longer lived than for the neat donor polymer, which is normally attributed to high electron mobility in the fullerene phase.[112] Taken together, the TRMC results indicate that **2** is a promising acceptor for OPV. Its higher electron affinity relative to PCBM suggests that it may be better to blend **2** with "push-pull" low-bandgap donor polymers with HOMO and LUMO energies deeper than P3HT in order to offset open-circuit-voltage losses,[114] and the perfluorinated nature of its substituent suggests and it may be better to blend **2** with fluorinated donor polymers.

Two new low band gap high performance donor polymers, PTB7 and PBDT-TPD, were explored. When these polymers were blended with $PC_{70}BM$, reported and confirmed power conversion efficiencies are 9.2%[78] and 5.5%,[77] respectively. Our goal was to measure the $\varphi\Sigma\mu$ of the highest reported PCEs with our thermal treatment. A total of 24 active layer blends (12 per polymer) were deposited (drop cast) onto quartz substrates. Within each polymer, four fullerenes were used in triplicate. Within each fullerene subset, one sample will be thermally treated. As can be seen in Figure 1.34, the $\varphi\Sigma\mu$ of the three fullerenes ($PC_{70}BM$, $PC_{60}BM$, and **2** ($MC_{60}MA$)) all show comparable figure of merits suggesting that **2** should be investigated with other low band gap or fluorinated high performance polymers.

1.2.9. Bulk heterojunction solar cells. The promising TRMC results of compound **2** prompted the interest in device performance. As part of his graduate work, Dr. Bryon W. Larson fabricated a set of devices containing the active layer blend ratios of 70:30, 50:50, and 30:70 (polymer:fullerene) with the device architecture ITO/PEDOT:PSS/P3HT:**2**/Ca/Al. Each device was fabricated in duplicate for reproducibility. Also, a set (and duplicates) of P3HT:PCBM devices were fabricated for comparison purposes. All 12 device active layers were deposited

using the same technique resulting in the same active layer thickness within each P3HT:**2**/PCBM loading. However, between each P3HT:**2**/PCBM loadings, the active layer thicknesses differ and increases with more P3HT content. The film thicknesses are important because it determines the amount of absorbed light in the film and contributes to the length the charge carriers must travel to reach the electrodes.

Figure 1.30 summarizes the data for the 12 fabricated devices for each loading. Each substrate contains 6 cells and each substrate was duplicated totaling the 12 devices. All of the data measurements were averaged and plotted as horizontal data points. The error bars shown are the range of values that were used to calculate the average values with the highest being the max data point and the lowest being the minimum data point. Although these devices were not optimized for performance, the same preparation procedures used allow for direct comparisons.

The P3HT:**2** devices perform much more consistently (smaller error bars) than P3HT:PCBM devices. It is especially evident when comparing the V_{oc} figure of merit. Interestingly, the $E_{1/2}$ of **2** was identical to C_{60} and was 90 mV easier to reduce in solution than PCBM. This translates to a higher V_{oc} for PCBM devices (higher E(LUMO) level); however, the average V_{oc} for P3HT:**2** and P3HT:PCBM devices at 30% fullerene loading were 0.491 mV and 0.422 mV, respectively. The average PCE values across all fabricated devices with 30%, 50%, and 70% fullerene loading for P3HT:**2** and P3HT:PCBM devices were 1.58%, 0.77%, 0.10% and 0.94%, 0.69%, 0.18%, respectively. We attribute that devices with 30% fullerene loading was better for 2 in comparison to PCBM to the fact that, as discussed in Section 1.2.6, the crystal packing density is ca. 15% higher than PCBM. This larger crystal packing density suggests that less material can be used to obtain similar PCBM device performance. In all cases, but at 70% fullerene loading, devices made with **2** perform better than devices made with PCBM. The decrease in device performance

with higher fullerene loading was a result of poorer film uniformity and bulk morphology. Fully optimized devices will be fully investigated in the near future.

1.2.10. Assessment of OPV active layers for use in space. The use of fullerenes as electron acceptors in OPVs has been widely incorporated; however, they have yet to be fully realized for space applications. Most solar cells in space consist of rigid panels made of inorganic semiconductors. Launching these cells come at a cost from both the production of inorganic solar cells and relatively large mass. OPVs offer an alternative for lower cost, lightweight, and flexible solar cells. As part of a collaboration research project with engineers from VectorSum, three fullerene compounds and their efficacy towards space applications under thermal, radiative, and photo stress.

The first set of experiments was to determine if vacuum treatment (six mTorr atmosphere) would affect the TRMC performance of thin films made with an active layer blend. Nine active layer blends containing three fullerene samples C_{60}, PCBM, and **2** were prepared by drop casting from a *o*-DCB solution in triplicate with a 30:70 (wt:wt) fullerene:P3HT loading. Within each set of P3HT:fullerene blends, one sample was not treated under vacuum while the other two were. Not only did the mass of active layer blends not change post-vacuum treatment, but their $\varphi\Sigma\mu$ TRMC figure of merit showed no change concluding that these samples will survive vacuum treatment without any detrimental effects.

The next set of experiments was to heat and cool active layer blends from −78 °C to 100 °C rapidly 16 times and measure their pre- and post- treatment TRMC performance. Relative $\varphi\Sigma\mu$ figure of merits are shown in Table 1.8 for compounds C_{60} and **2**. Samples were prepared similarly to those above regarding the vacuum treatment. The samples that were thermally cycled showed an improvement in the $\varphi\Sigma\mu$ in comparison to the control samples. It is well documented

that thermally annealing thin films improves device performance of polymer:fullerene active layers.[115,116] The annealing process has been contributed to the slight increase in absorption and an increase in interfacial area between the cathode and active layer.[117]

Finally, three different radiation tests (UV radiation, electron-beam exposure, and proton-beam exposure) were performed on the active layer materials. UV-vis spectroscopy was used as the method of analysis for these experiments. It has been shown that there is a correlation between the changes in absorption spectra of thin films of OPV fullerene-polymer-blend active layers and the $\varphi\Sigma\mu$ figure of merit derived from TRMC experiments.

The samples were exposed to UV radiation at CSU by placing them ca. 5" from a 450 W high-pressure mercury-arc lamp, a 30 keV electron-beam at CSU using SEM JEOL-JSM 6500F instrumentation, and exposed to a 3 MeV proton beam using the 9SDH-2 NEC Pelletron in Dr. Vaithiyalingam Shutthanandan's lab at PNNL.

For UV irradiation, samples M30C and P30C were used for UV irradiation experiments (M = **2**; P = PCBM). Each film was prepared by drop casting a solution containing a P3HT:fullerene blend in a 30:70 wt:wt ratio and allowed to dry by simple evaporation in air. Both samples were previously thermally cycled continuously at 100 °C for 45 minutes and at −78 °C for 45 minutes for a duration of 24 h. UV-vis spectra were recorded with the samples oriented differently in the UV-vis sample compartment. UV-vis spectra were taken after various exposure times are shown in Figure 1.31.

The M30C sample had clearly deteriorated after radiation experiments (i.e., it was substantially different in appearance), and a concomitant decrease in absorption band intensities was observed. However, the P30C sample maintained a similar UV-Vis spectrum throughout most of the experiment. This could be attributed to the oxidation of PCBM. It has been regarded

that oxidized PCBM may form a protective layer preventing further oxidation of PCBM which, in turn, helps stabilize the P3HT polymer, whereas the possible oxidation of **2** did not occur.[34] These experiments were not optimized. The films were not deposited as evenly as possible as evidence by the UV-vis spectra varying over different parts of the samples. More importantly, the UV exposure was performed in air, and the "UV damage" observed will almost certainly be mitigated when the samples are exposed to UV radiation in an inert atmosphere. An inert atmosphere will be a more relevant environment for solar cell materials that will be hermetically sealed in an inert atmosphere in solar cells and deployed in space.

For proton beam exposures, four samples (M30A, M30B, P30A, and P30B) were used for these experiments (A = no thermal treatment; B = thermally treated). Each film was fabricated by drop casting as described above. The thermally treated samples were taken through the aforementioned hot/cold cycles during a 24 h period.

UV-vis spectra (Figure 1.32) were recorded before and after proton-beam exposure. The parameters of proton-beam exposure are as follows: 3 MeV proton (H^+) beam was obtained by irradiating the sample at a dose of 4.17×10^{17} ions cm^{-2} at a current of 0.3 nA for 100 ms. The radiation dose was calculated by converting the recommended dose of 14 krad to ions cm^{-2}. Total dose per film was delivered after 0.107 s.

Samples M30A, M30B, and P30B showed UV-vis spectroscopic evidence for degradation. In contrast, the UV-vis peak intensities increased significantly for sample P30A. At this time, no compelling argument explains this difference in behavior. Each film was subjected to a second round of annealing at 100 °C for 24 h under an inert atmosphere. It appears that each active layer absorption characteristics are enhanced slightly. This may be the result of radiation recovery; however, further characterization of the polymer:fullerene blends needs to be investigated.

For electron beam exposure, two samples, M30-1 and P30-1, were used for the electron-beam exposure experiment. Each film was fabricated by drop casting as described above. The samples were then annealed at 100 °C for 24 h under an inert atmosphere. The UV-vis spectra (Figure 1.33) were recorded prior to annealing and electron bombardment. Negligible mass loss was observed after annealing (as expected from previous experiments). The dose was calculated by converting the 14 krad dose to ions cm^{-2} and adjusting for the much lower incident energy of 30 kV.

Note that only a slight change in the UV-vis spectrum of **2** was observed (Figure 1.33). A more dramatic change in the spectra was observed for PCBM. Based on these results, annealing is more important for PCBM-containing active layers than for in comparison to **2** containing active layer films. Preliminary results suggests that no significant changes to the UV-vis spectra occur after a total dwell time per pixel (*ca*. 12 mm^2) for 60 seconds. The only sample radiated with electrons is **2**. The red spectrum is the average between the two UV-vis spectra, while the green spectrum is of only the side of the thin film where radiation occurred. This could result in two hypotheses: 1) the active layer material withstands the 30 kV electron bombardments, or 2) the damage from 30 kV electron bombardments is subtle due to only radiating a small area before experiment was interrupted.

1.3. Summary and Conclusions.

A new family of C_{60} and C_{70} fullerene faux hawk compounds bearing perfluorinated substituents were synthesized and characterized. The transformation from **1** into **2** was discussed and supported by DFT calculations. A similar transformation between **3** and **4** is expected to follow similar transitions. The TRMC figure of merit, $\varphi\Sigma\mu$, of **2** rivals that of $PC_{60}BM$ and $PC_{70}BM$ when blended with P3HT and other high performance polymers such as PTB7 and

PBDT-TPD. The X-ray crystallography analysis revealed that **2** packs more densely than PCBM and contains more nearest neighbors suggesting that **2** may be efficacious for use in OPVs.

1.4. Experimental.

General methods, reagents, and solvents. An inert-atmosphere glovebox and/or standard benchtop inert-atmosphere techniques[118] (dioxygen and water vapor levels ≤ 1 ppm) were used to perform reactions and, in general, to prepare samples for spectroscopic, electrochemical, and microwave conductivity analysis. Following filtration through silica gel, reaction mixtures were exposed to air, in most cases with minimal exposure to light. HPLC purifications were also performed in the presence of air.

The following reagents and solvents were obtained from the indicated sources and were used as received or were purified/treated/stored as indicated: C_{60} (MTR Ltd., 99.5+%); phenyl-C_{61}-butyric acid methyl ester (PCBM, Nano-C, 99+%); regioregular (rr) poly-3-hexylthiophene (rr-P3HT, Sigma-Aldrich, 90+% rr); heptafluorobenzyl iodide ($C_6F_5CF_2I$, SynQuest, 90%); tri-*n*-butyltin hydride ($SnH(n\text{-}Bu)_3$, Strem Chemicals, 95+%), hexabutylditin(Sn–Sn) ($Sn_2(n\text{-}Bu)_6$, Alfa Aesar, 98%); 1,2-dichlorobenzene (*o*-DCB, Acros Organics, 99%, dried over and distilled from CaH_2); dichloromethane (DCM, Fisher Scientific, ACS grade); benzonitrile (PhCN, Aldrich, 99+%, dried over 3 Å molecular sieves); chloroform-d ($CDCl_3$, Cambridge Isotope Labs, 99.8%); benzene-d_6 (C_6D_6, Cambridge Isotope Labs, dried over 3 Å molecular sieves), hexafluorobenzene (Oakwood Products); 1,4-bis(trifluoromethyl)benzene ($C_8H_4F_6$, Central Glass Co., 99%); ferrocene ($FeCp_2$, Acros Organics, 98%); cobaltocene ($CoCp_2$, Strem Chemical, purified by sublimation and stored in the glovebox); silica gel (Sigma-Aldrich, 70−230 mesh, 60 Å); 1,8-bis(dimethylamino)naphthalene (Proton Sponge (PS), $C_{14}H_{18}N_2$, Sigma-Aldrich, purified by sublimation and stored in the glovebox); toluene (Fisher Scientific, ACS grade); heptane

(Mallinckrodt, ACS grade); acetonitrile (Mallinckrodt Chemicals, ACS grade); and tetra-*n*-butylammonium tetrafluoroborate ($N(n\text{-}Bu)_4BF_4$, $TBABF_4$, Fluka, puriss grade, dried under vacuum at 70 °C for 24 h and stored in the glovebox).

Synthesis of compounds. 1,9-$C_{60}(CF_2C_6F_5)H$. The compounds C_{60} (120 mg, 0.167 mmol), $C_6F_5CF_2I$ (0.263 mL, 1.67 mmol), and $SnH(n\text{-}Bu)_3$ (0.225 mL, 0.835 mmol) were dissolved in *o*-DCB, heated at 160(5) °C for 2 h, and cooled to 23(1) °C. All volatiles, including the byproduct I_2, were removed from the purple reaction mixture under vacuum. The solid residue was dissolved in toluene, added to a preparative-scale COSMOSIL Buckyprep HPLC column by injection, and eluted with 80/20 (v/v) toluene/heptane at 16 mL min^{-1}. The fraction that eluted from 8.0 to 8.3 min was collected and evaporated to dryness under vacuum, yielding 55 mg of **1** (35% yield based on C_{60}). The ^{19}F NMR spectrum of the isolated product demonstrates that compound **1** prepared in this way is at least 97 mol% pure.

Synthesis of compounds. 1,9-C_{60}(cyclo-CF_2(2-C_6F_4)). The fraction of the HPLC purification described above that eluted between 9.9 and 10.6 minutes was collected and evaporated to dryness, yielding 11 mg of **2** (7% yield based on C_{60}). The ^{19}F NMR spectrum of the isolated product demonstrates that compound **2** prepared in this way is at least 95 mol% pure.

Alternatively, **1** (5.0 mg) was treated with excess Proton Sponge (PS) in CH_2Cl_2 at 23(1) C for 24 h. The brown reaction mixture was filtered through silica gel to remove $[H(PS)]^+F^-$ and unreacted PS. The filtrate was evaporated to dryness under vacuum. The solid residue was redissolved in toluene, added to the semi-preparative-scale Buckyprep HPLC column by injection (see below), and eluted with toluene at 5 mL min^{-1}. The fraction that eluted from 6.8 to 7.9 min was collected and evaporated to dryness under vacuum, yielding 3.9 mg of **2** (76% yield based on **1**).

A. High-performance liquid chromatography. HPLC separation and analysis was carried out on samples exposed to air using a Shimadzu LC-6AD system with a SPD-20A UV/vis detector, a SPD-M20A diode array detector, and a CBM-20A communication bus module. The columns used were preparative- and semi-preparative-scale COSMOSIL Buckyprep columns (20 × 250 mm or 10 × 250 mm, respectively; Nacalai Tesque) and a COSMOSIL Buckyprep-M semi-preparative-scale column (10 × 250 mm, Nacalai Tesque) at a flow rate of 5 mL min^{-1} and observed at 370 nm unless otherwise indicated.

B. NMR and UV-vis spectroscopy and mass spectrometry. Fluorine-19 (376 MHz) and ^{1}H (400 MHz) NMR spectra were recorded using a Varian INOVA 400 instrument using a 1 s relaxation time, 60° pulse angle, and 90/10 (v/v) PhCN/C_6D_6 or $CDCl_3$ as the solvent with a trace amount of C_6F_6 ($\delta(^{19}F)$ −164.90) added as the internal standard. Samples for spectra of **1** or **2** recorded at 23(1) °C were prepared without the exclusion of air; samples for spectra recorded at elevated temperatures and/or with added PS, $CoCp_2$, or $Sn_2(n\text{-Bu})_6$ were prepared anaerobically. The program MestReNova 8.1.1 was used to simulate the ^{19}F NMR spectra of **1** and **2**. The uncertainties in the fitted *J*(FF) values are probably ±1 Hz. Mass spectra were recorded using a 2000 Finnigan LCQ-DUO mass-spectrometer with CH_3CN used as the carrier solvent. UV-vis spectra of samples dissolved in toluene were recorded using a Cary 500 UV-vis-NIR spectrometer.

C. Electrochemistry. Cyclic and square-wave voltammograms were recorded in an inert-atmosphere glovebox using ca. 2 mM *o*-DCB solutions containing 0.1 M $N(n\text{-Bu})_4BF_4$ as the electrolyte, $FeCp_2$ as the internal standard, and a PAR 263 potentiostat/galvanostat. The electrochemical cell was equipped with 0.125 mm diameter platinum working and counter

electrodes and a 0.5 mm diameter silver wire quasi-reference electrode. The scan rate was 100 mV s^{-1}.

D. Electron affinity measurement by low-temperature photoelectron spectroscopy (LT-PES). The spectroscopy and procedures used were described previously.[4,45] Anions $\mathbf{2}^-$ were generated by electrospraying a 0.1 mM solution of **2** dissolved in toluene/acetonitrile to which a dilute acetonitrile solution of TDAE had been added dropwise until a color change from light brown to brown was observed. The anions were guided by quadrupole ion guides into a cryogenic ion trap, then transferred into the time-of-flight mass spectrometer. Mass-selected anions $\mathbf{2}^-$ were intersected by a Nd:YAG laser (266 nm; 4.661 eV) in the photodetachment zone of the magnetic-bottle photoelectron analyzer. Photoelectrons were collected at nearly 100% efficiency, and the energy resolution (delE/E) obtained was ca. 2%. The gas-phase electron affinity (EA) of **2** was determined from the 0–0 transition in the 12 K LT-PES spectrum of the $\mathbf{2}^-$ radical anion.

E. Time-resolved microwave conductivity (TRMC). Samples for TRMC were 200–250 nm thick 1/1 (wt/wt) blended films of rr-P3HT and either PCBM or **2** prepared by spin coating 30 mg mL^{-1} *o*-DCB solutions onto 1 × 2 cm quartz substrates in an inert-atmosphere glovebox. Neat P3HT films with similar thicknesses were prepared by spin coating 20 mg mL^{-1} *o*-DCB solutions in the same way. The samples were placed in the resonance cavity at one end of a ca. 9 GHz X-band microwave waveguide. The films were exposed through the quartz substrate to 5 ns pulses of 500 nm photons using a Continuum Panther optical parametric oscillator pumped by the 355 nm harmonic of a Continuum Powerlite Q-switched Nd:YAG laser. The transient change in photoconductance ($\Delta G(t)$) was measured by monitoring changes in the microwave power in the cavity ($\Delta P(t)$) due to absorption of microwave photons by photogenerated electrons and holes in the thin film according to the equation:

$$\Delta G(t) = -(K\,(\Delta P(t) / P)^{-1}$$

where K is a experimentally-determined calibration factor that depends on the microwave cavity resonance characteristics and the dielectric properties of the sample.[111] The peak photoconductance, ΔG_{peak}, is used to determine the yield of free carriers (i.e., electron and holes), φ, times the sum of the free carrier mobilities, $\Sigma\mu$, according to the equation:

$$\Delta G_{peak} = \beta\ q_e\ I_0\, F_A\, \varphi\, \Sigma\mu$$

where β is the ratio of the dimensions of the cross-section of the waveguide (2.2 in our instrumentation), q_e is the charge on an electron, I_0 is the incident photon flux, and F_A is the fraction of laser pump photons absorbed by the sample.

F. X-ray structure of 1,9-C_{60}(cyclo-CF_2(2-C_6F_4)). Crystals of **2** were grown by slow evaporation of a carbon disulfide solution. Data were collected on the Advanced Photon Source synchrotron instrument on beamline 15ID-B at Argonne National Laboratory, using a wavelength of 0.41328 Å, a diamond 111 monochromator, and a Bruker D8 goniometer. Unit cell parameters were obtained from a least-squares fit to the angular coordinates of all reflections. Intensities were integrated from a series of frames from ω and ϕ rotation scans. Absorption and other corrections were applied using TWINABS.[119] The structure was solved as a non-merohedral twin using direct methods and refined on F^2 against one major and two minor twin components. Standard Bruker control and integration software (APEX II) was employed,[120,121] and Bruker SHELXTL software was used with Olex 2 for the structure solution, refinement, and molecular graphics.[122,123] For $C_{67}F_6$: M = 918.67, orthorhombic, a = 9.9998(6), b = 20.6538(12), c = 31.3512(18) Å, V = 6475.1(7) Å^3, T = 15(2) K, space group *Pbca* (no. 61), Z = 8, 9670 reflections measured, 8340 unique which were used in all calculations. The final R and wR values are 0.073 (observed reflections) and 0.163 (all reflections), respectively. Further details

about the crystal structure investigation may be obtained from the Fachinformations-zentrum Karlsruhe, 76344 Eggenstein-Leopoldshafen, Germany (fax: +49-7247-808-666; e-mail: crysdata@fizkarlsruhe.de), by quoting the depository number CSD-428507.

G. Computational methods. Optimization of molecular structures, transition states, and intrinsic reaction coordinate (IRC) calculations were performed *in vacuo* using the Priroda code[124,125] at the OLYP level[126,127] with the original TZ2P-quality basis set implemented in the code. Point energy calculations at the O3LYP/6-311G** level were performed using Firefly suite.[128] We used the OLYP and O3LYP functionals because they have been shown to give good results for transition state energies for S_N2 reactions.[129-131] Solvation energies in benzonitrile (as a model for the experimental solvent mixture 90/10 (v/v) PhCN/C_6D_6) was computed using the C-PCM approach[132] implemented in Firefly.

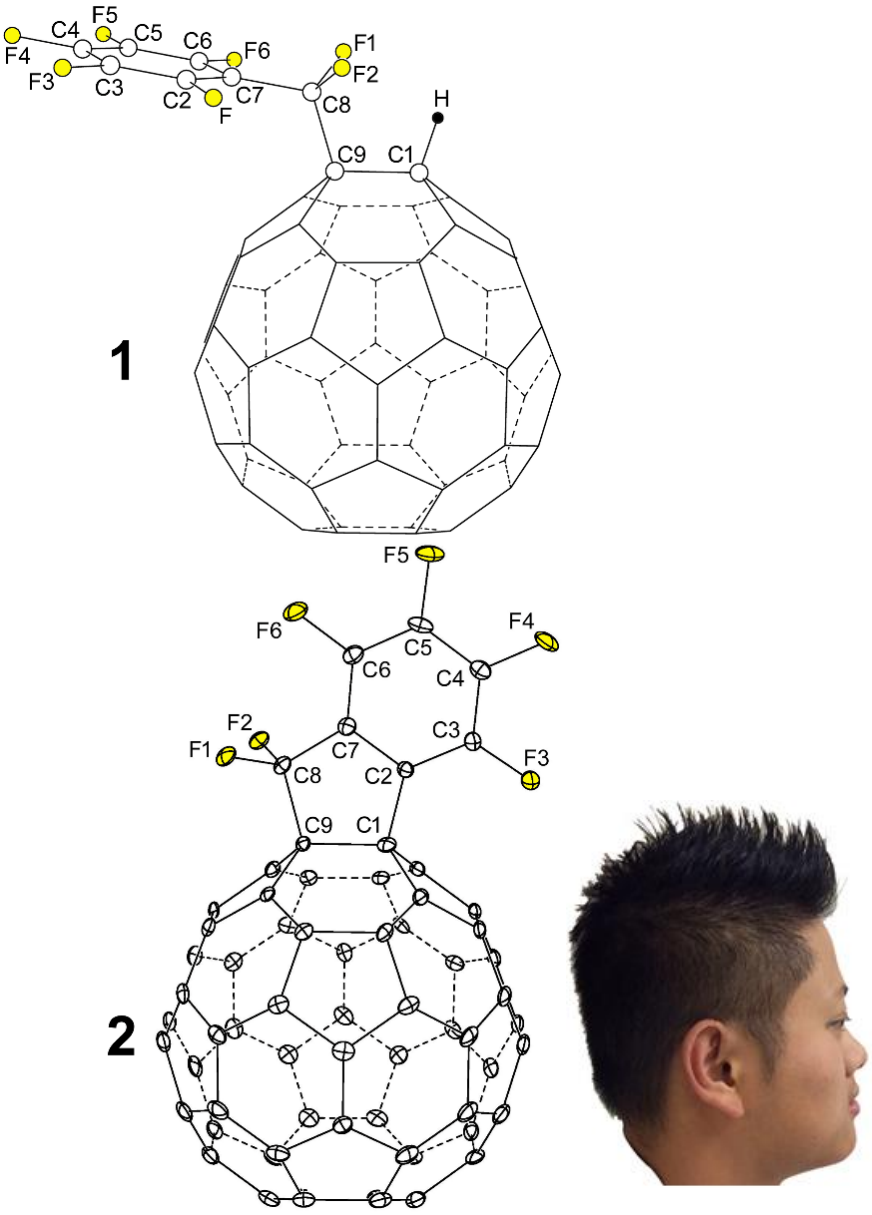

Figure 1.1. OLYP DFT-optimized structure of 1,9-$C_{60}(CF_2C_6F_5)H$ (**1**) and the X-ray structure of 1,9-C_{60}(*cyclo*-CF_2(2-C_6F_4)) (**2**; 50% probability ellipsoids). Only the major twin portion of the X-ray structure is shown. The shape of compound **2** is reminiscent of a hairstyle known as the faux hawk is also shown.

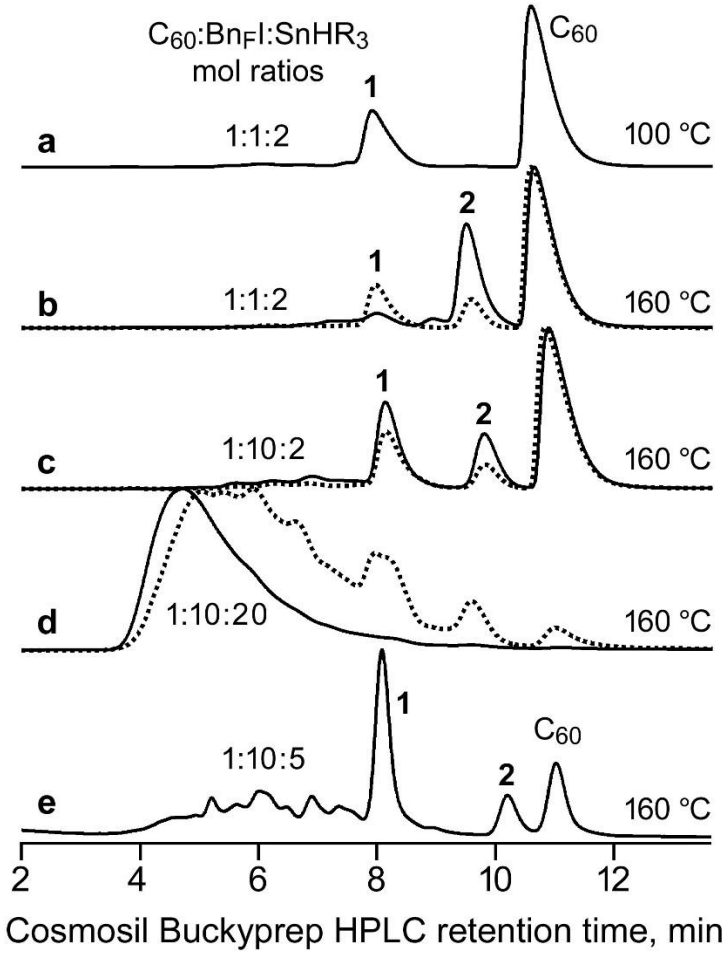

Figure 1.2. HPLC traces of C_{60} + Bn_FI + $(n\text{-Bu})_3SnH$ reaction mixtures (Bn_FI = $C_6F_5CF_2I$; R = *n*-Bu). The dotted-line traces are for 1 h reactions; the solid-line traces are for 2 h reactions. Compounds **1** and **2** are 1,9-$C_{60}(CF_2C_6F_5)H$ and 1,9-C_{60}(*cyclo*-$CF_2(2\text{-}C_6F_4)$), respectively.

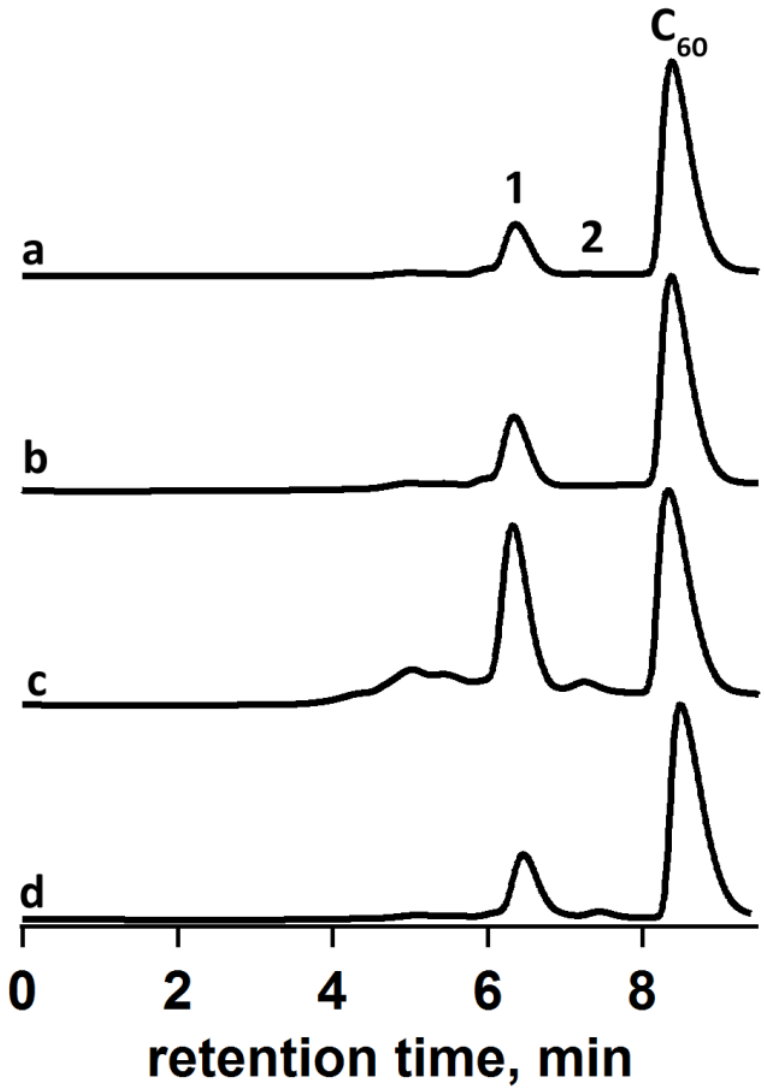

Figure 1.3. HPLC chromatograms of photolysis reactions. Reactions were performed at room temperature. HPLC chromatograms were obtained with a 100% toluene mobile phase and a COSMOSIL Buckyprep semi-preparative column at a 5 mL min^{-1} flow rate.

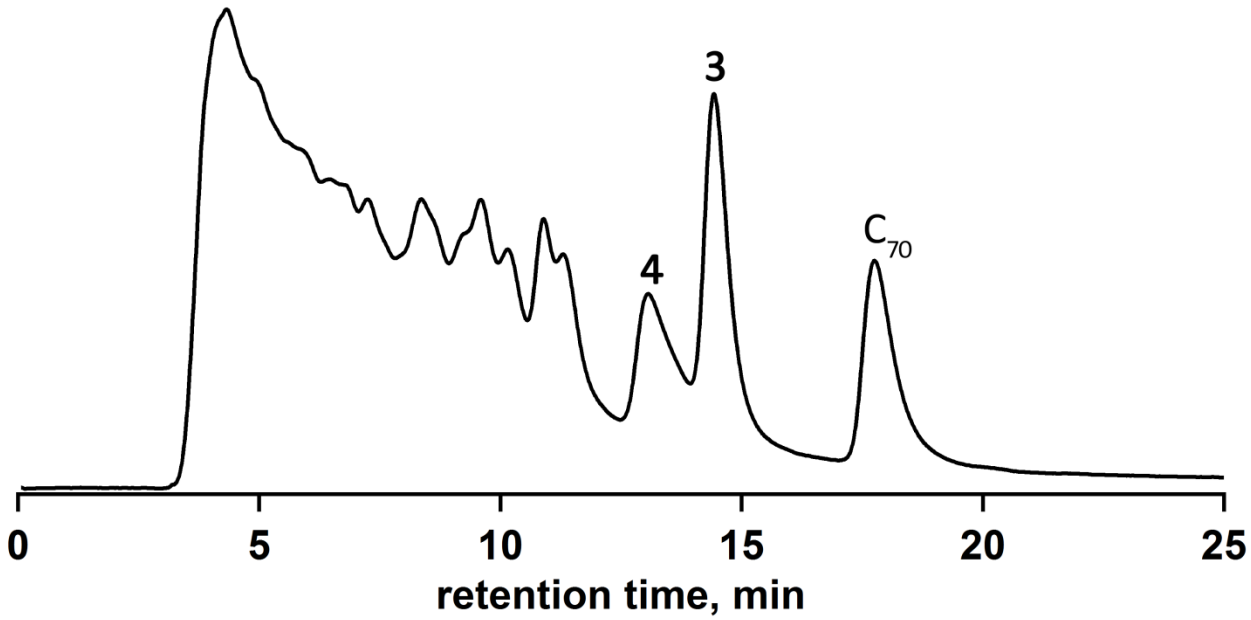

Figure 1.4. HPLC trace of C_{70} + Bn_FI + $(n\text{-}Bu)_3SnH$ reaction mixture. Compounds **3** and **4** are $C_{70}(CF_2C_6F_5)H$ and $C_{70}(cyclo\text{-}CF_2(2\text{-}C_6F_4))$, respectively. HPLC chromatograms were obtained with a 80/20 (v/v) toluene/heptane mobile phase and a COSMOSIL Buckyprep semi-preparative column at a 5 mL min^{-1} flow rate.

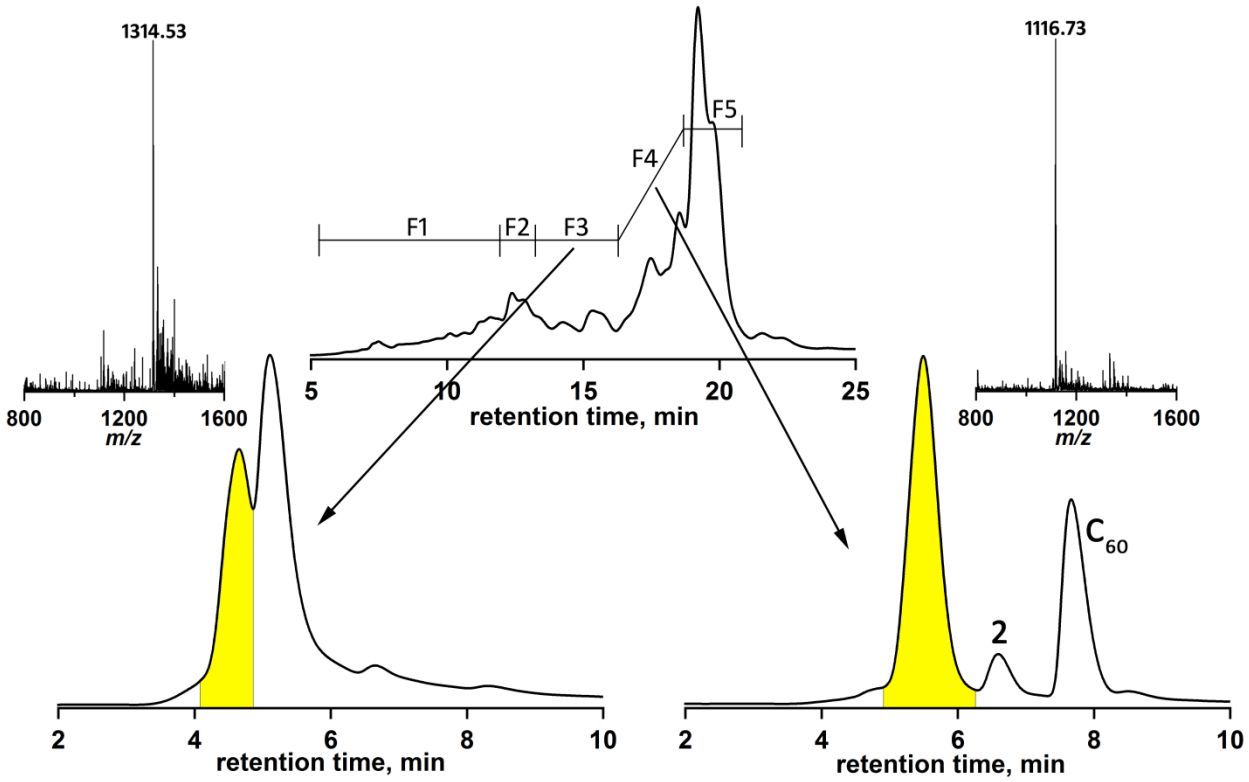

Figure 1.5. HPLC separation scheme for bis/tris-faux hawk compounds. From F3 (top trace), the peak highlighted in yellow (bottom left trace) contains a mixture of tris-faux hawks. From F4 (top trace), the peak highlight in yellow (bottom right trace) contains a mixture of bis-faux hawks. NI-APCI MS spectra are also shown. Top trace was obtained with a 50/50 (v/v) toluene/heptane mobile phase and a COSMOSIL Buckyprep preparative column at a 16 mL min^{-1} flow rate. Bottom traces were obtained with a 100% toluene mobile phase and a COSMOSIL Buckyprep semi-preparative column at a 5 mL min^{-1} flow rate

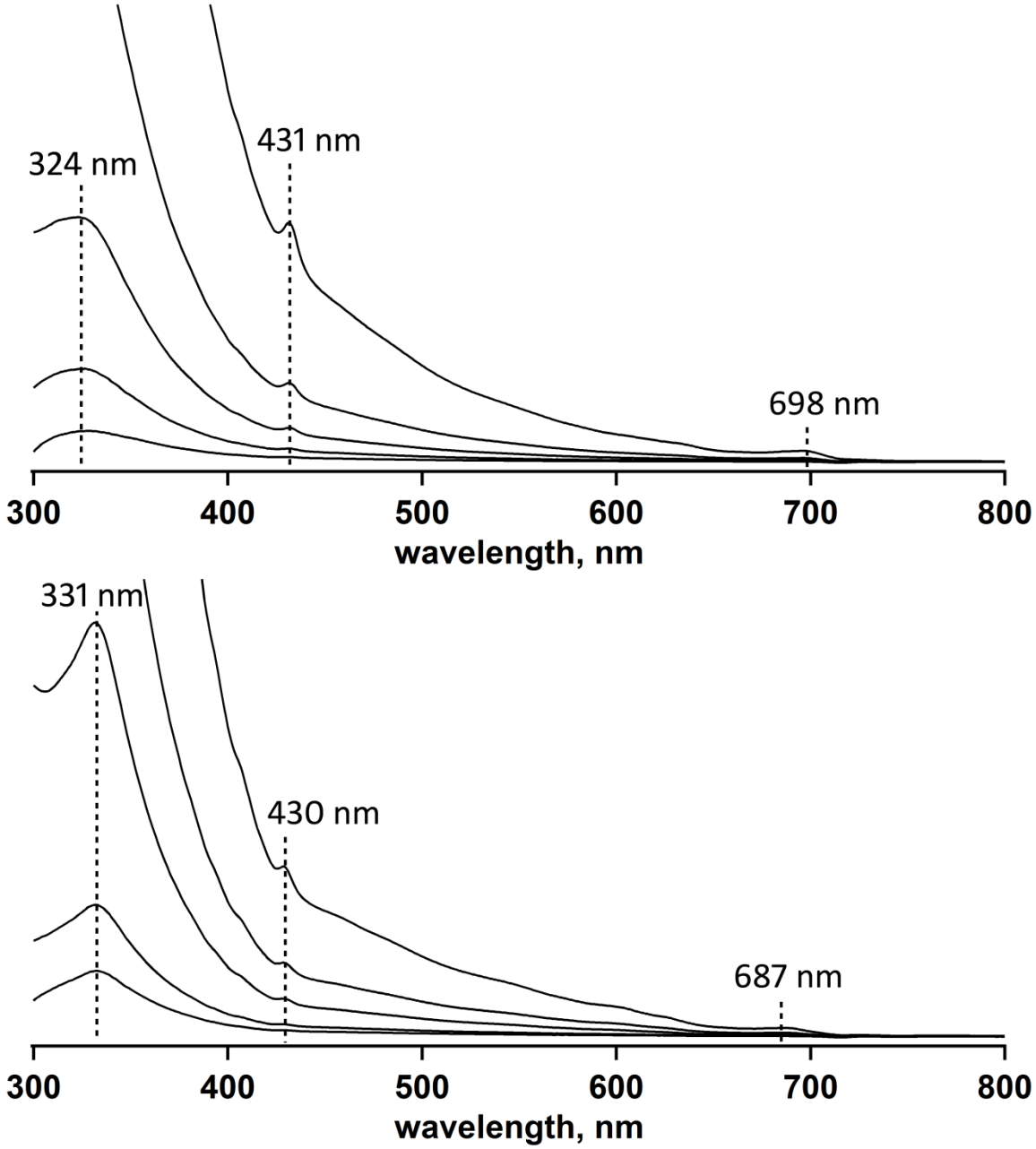

Figure 1.6. UV-vis spectra of **1** (top) and **2** (bottom) dissolved in toluene. Successive dilutions allow key absorption features to be seen.

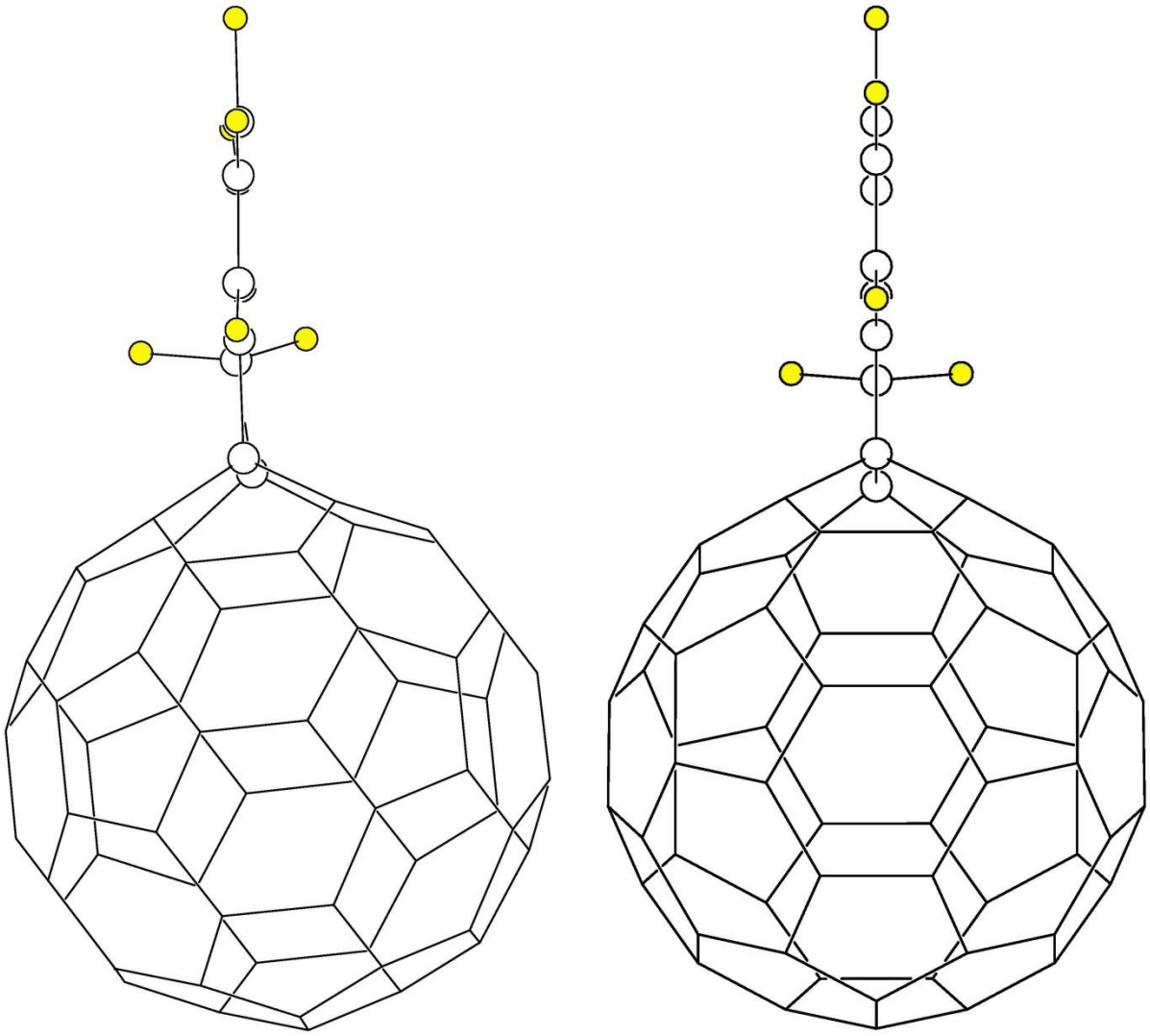

Figure 1.7. Visual comparison of the X-ray structure (left) and OLYP DFT-optimized structure (right) of **2** with respect to the planarity of the faux hawk substituent and its placement perpendicular to the surface of the C_{60} cage. The faux hawk C and F atoms are shown as spheres of arbitrary size; the F atoms are highlighted in yellow.

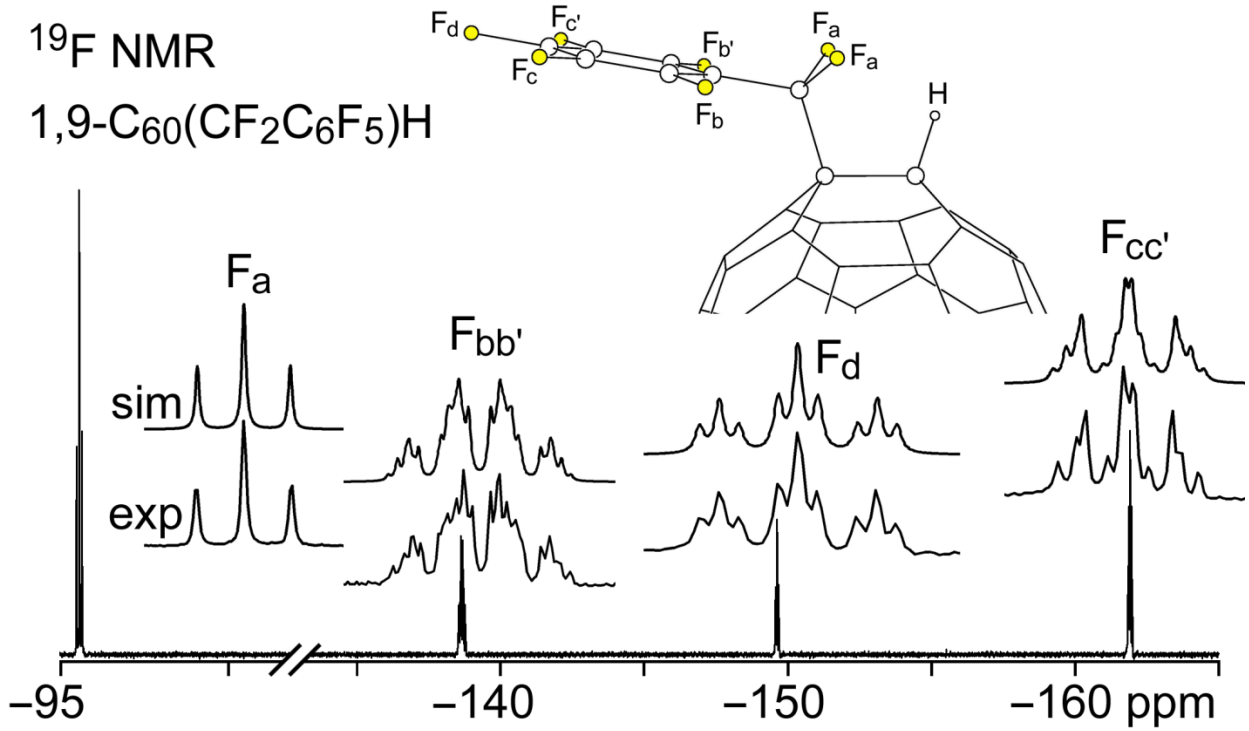

Figure 1.8. Experimental and simulated 376.5 MHz ^{19}F NMR spectra of HPLC-purified 1,9-$C_{60}(CF_2C_6F_5)H$ (**1**) in $CDCl_3$. Chemical shifts and coupling constants are listed in Table 1.3.

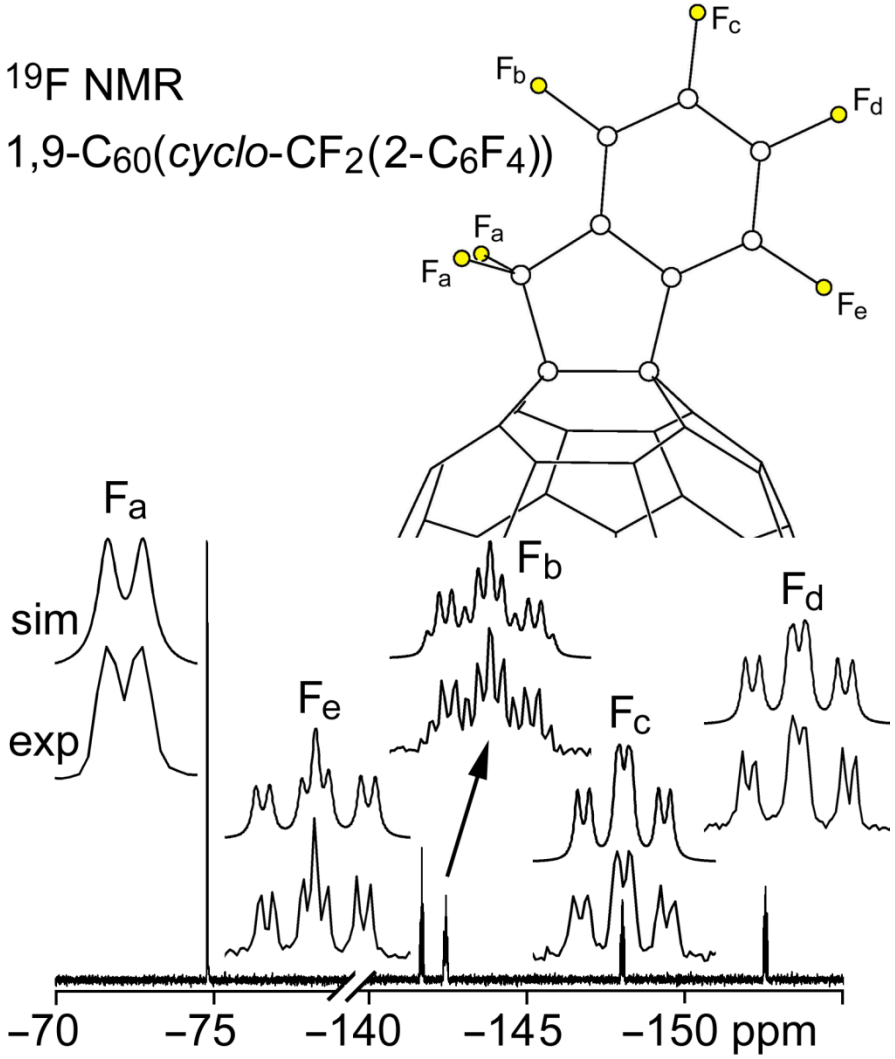

Figure 1.9. Experimental and simulated 376.5 MHz ^{19}F NMR spectra of HPLC-purified 1,9-C_{60}(*cyclo*-CF_2(2-C_6F_4)) (**2**) in $CDCl_3$. Chemical shifts and coupling constants are listed in Table 1.3.

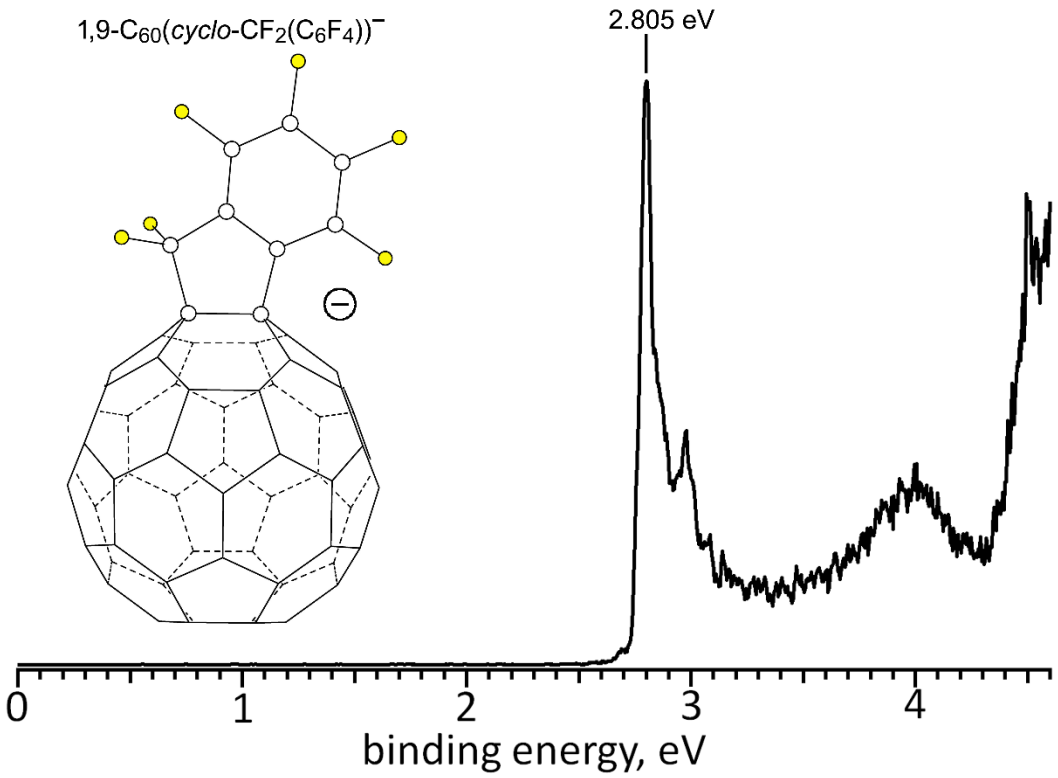

Figure 1.10. Low-temperature 266 nm photoelectron spectrum of the faux hawk fullerene radical anion 1,9-C_{60}(*cyclo*-CF_2(2-C_6F_4))$^-$ (**2**$^-$), from which the 2.805(10) eV gas-phase electron affinity of faux hawk fullerene **2** was determined.

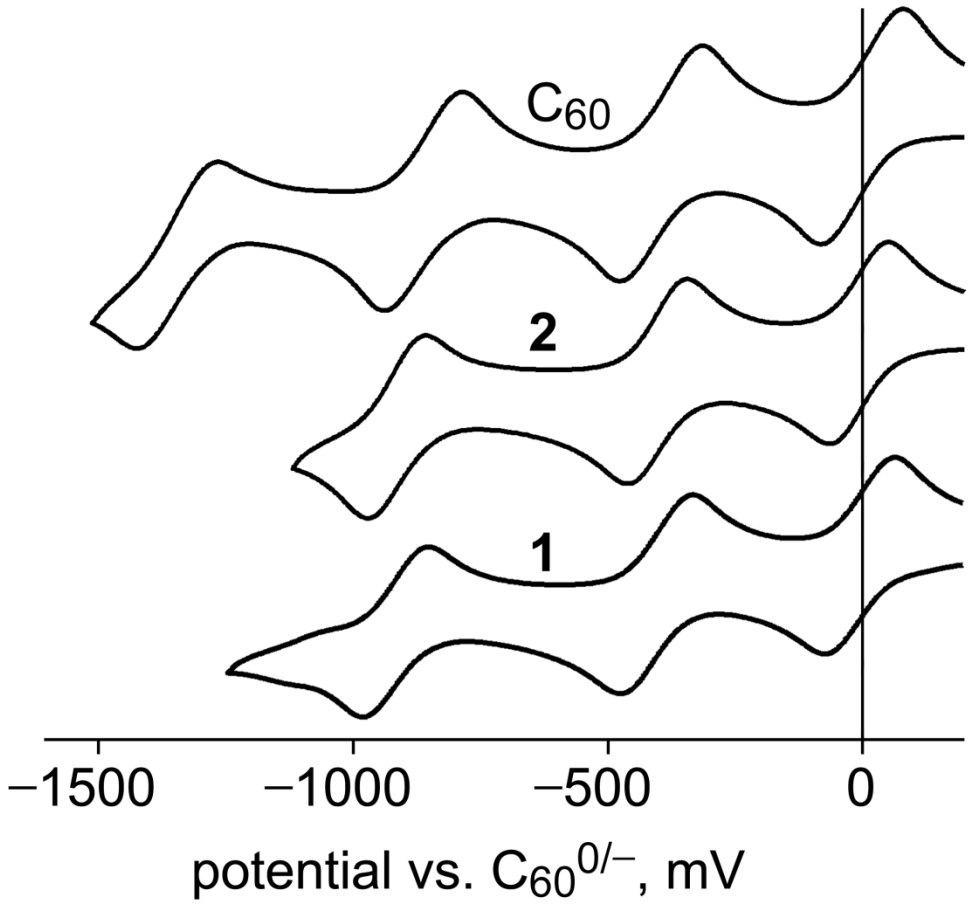

Figure 1.11. Cyclic voltammograms of C_{60}, 1,9-$C_{60}(CF_2C_6F_5)H$ (**1**), and 1,9-C_{60}(*cyclo*-CF_2(2-C_6F_4)) (**2**) in *o*-DCB containing 0.1 M N(*n*-Bu)$_4BF_4$ and $FeCp_2$ as an internal standard. The $FeCp_2^{+/0}$ redox waves are not shown.

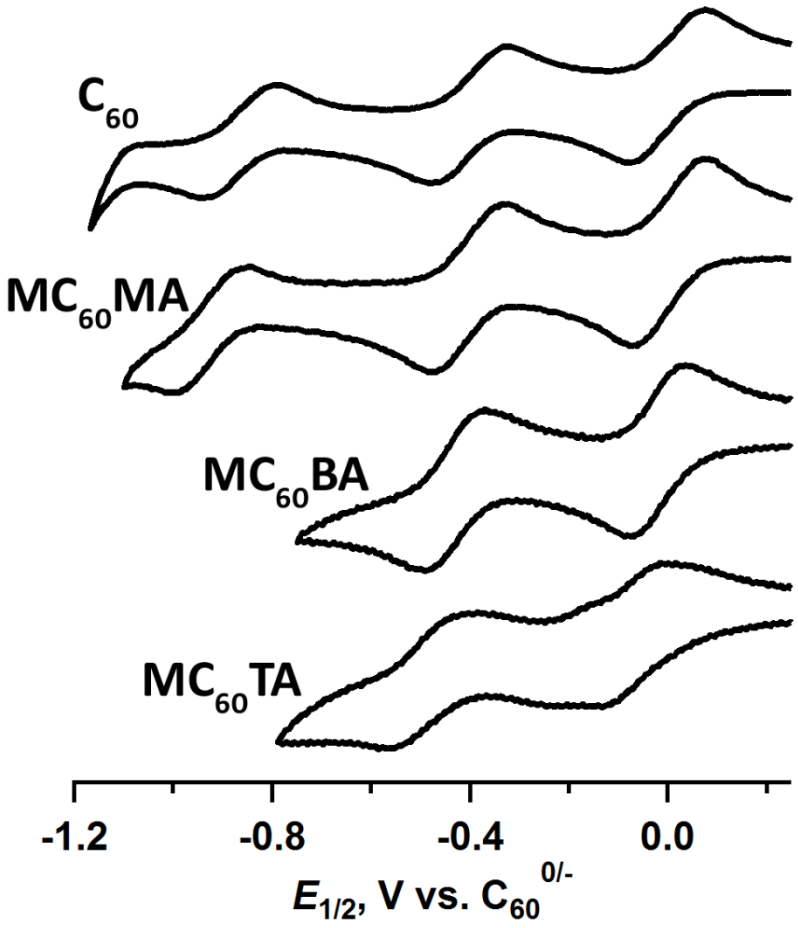

Figure 1.12. Cyclic voltammograms of C_{60}, **1** (FCMA), bis-adduct (FCBA), and tris-adduct (FCTA) in *o*-DCB containing 0.1 M N(*n*-Bu)$_4$BF$_4$ and $FeCp_2$ as an internal standard. The $FeCp_2^{+/0}$ redox waves are not shown.

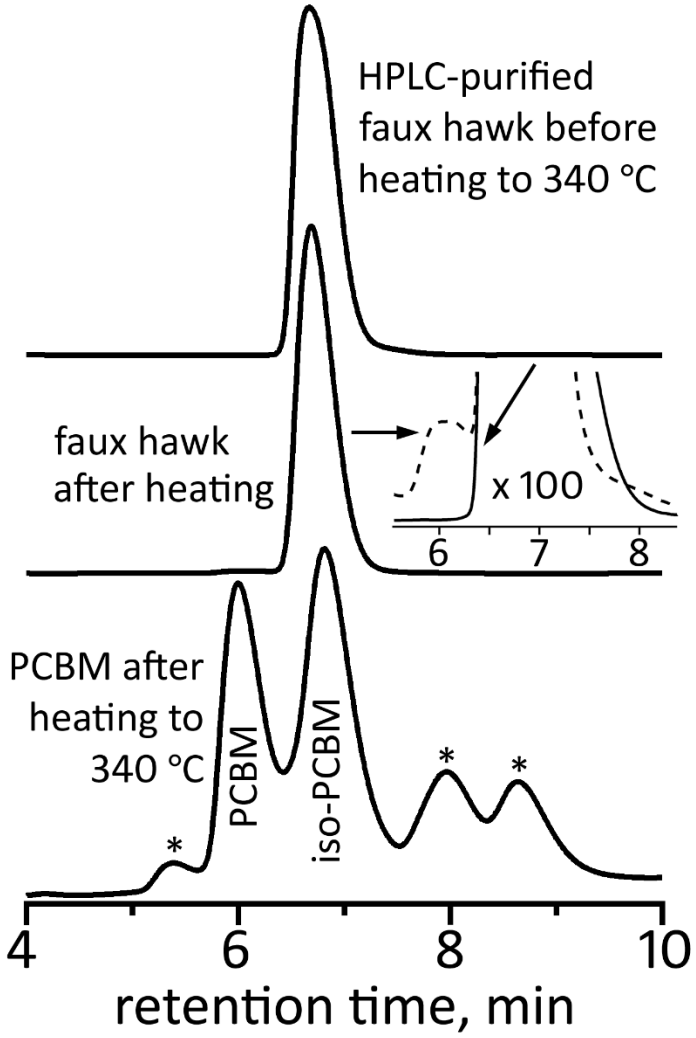

Figure 1.13. HPLC traces of faux hawk fullerene 1,9-C_{60}(*cyclo*-CF_2(2-C_6F_4)) (**2**) before and after heating to 340 °C for 20 min and HPLC trace of PCBM after heating to 340 °C for 20 min. The PCBM HPLC data were reported in reference 55. The inset for the middle HPLC trace has been expanded 100 times on the vertical axis (the after-heating trace in the inset is the dashed line). The asterisks in the PCBM after-heating trace are unidentified thermal decomposition products. For all three HPLC traces, a COSMOSIL Buckyprep column was used with a toluene eluent rate of 5 mL min^{-1} and 300 nm detection.

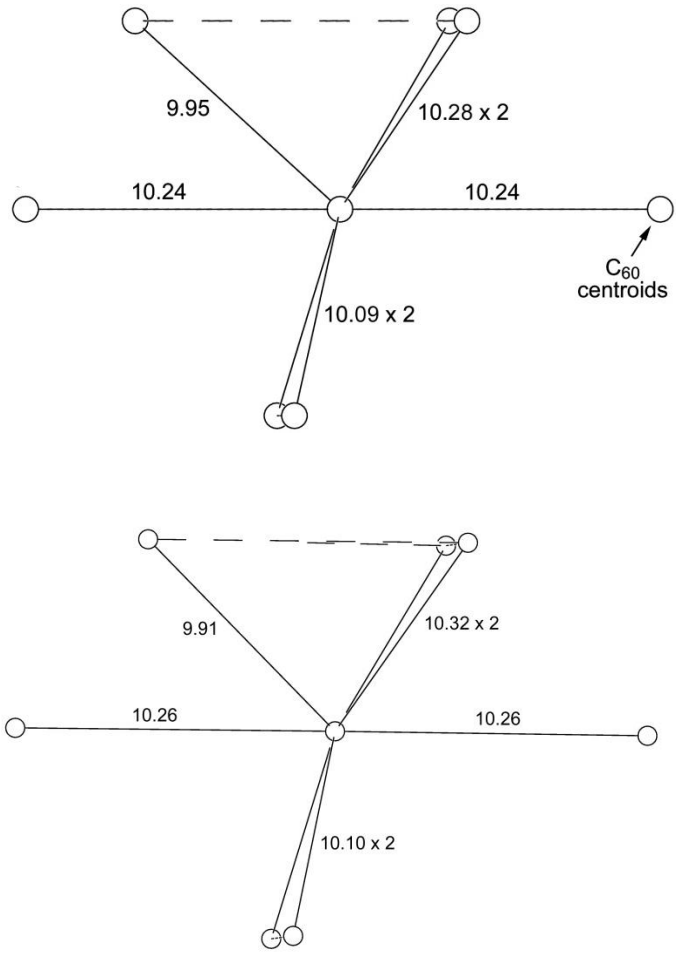

Figure 1.14. Comparison of the nearest-neighbor centroid packing patterns in the single-crystal X-ray structure (top; Paternò, G.; Warren, A. J.; Spencer, J.; Evans, G.; García Sakai, V.; Blumberger, J.; Cacialli, F. *J. Mater. Chem.* **2013**, *1*, 5619; data collected at 100 K) and the powder X-ray diffraction structure (bottom; Casalegno, M.; Zanardi, S.; Frigerio, F.; Po, R.; Carbonera, C.; Marra, G.; Nicolini, T.; Raos, G.; Meille, S. V. *Chem. Commun.* **2013**, *49*, 4525; data collected at 300 K) of solvent-free PCBM (PCBM = phenyl-C_{61}-butyric acid methyl ester). The averages of the seven nearest-neighbor distances are 10.17 (top) and 10.18 Å (bottom).

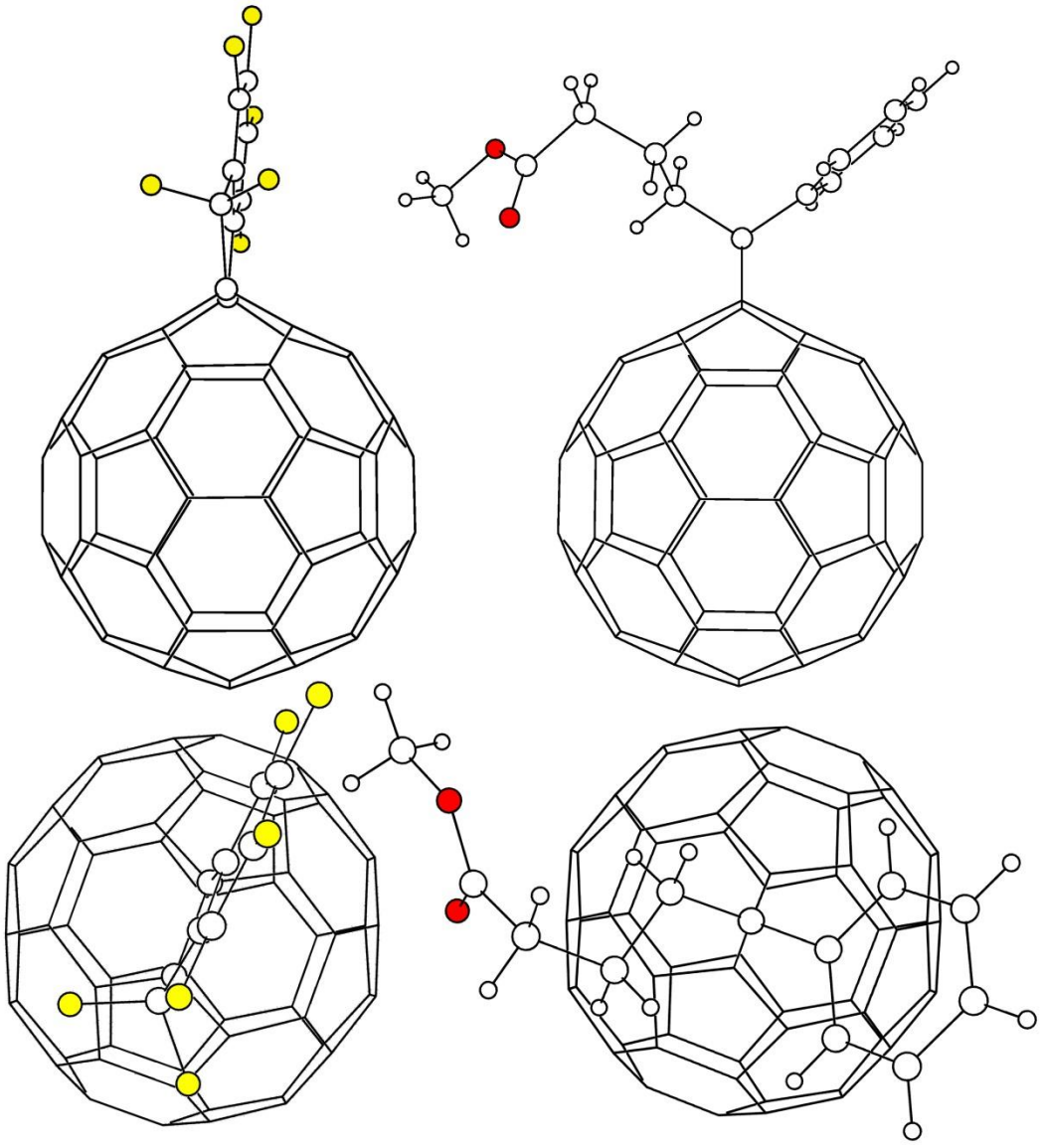

Figure 1.15. Comparison of the molecular structures of faux hawk fullerene **2** (left, this work) and PCBM (right, ref 133). The large and small white spheres represent C and H atoms, respectively; the red and yellow spheres represent O and F atoms, respectively. The fullerene cages and the substituent atoms in the two structures are scaled equally.

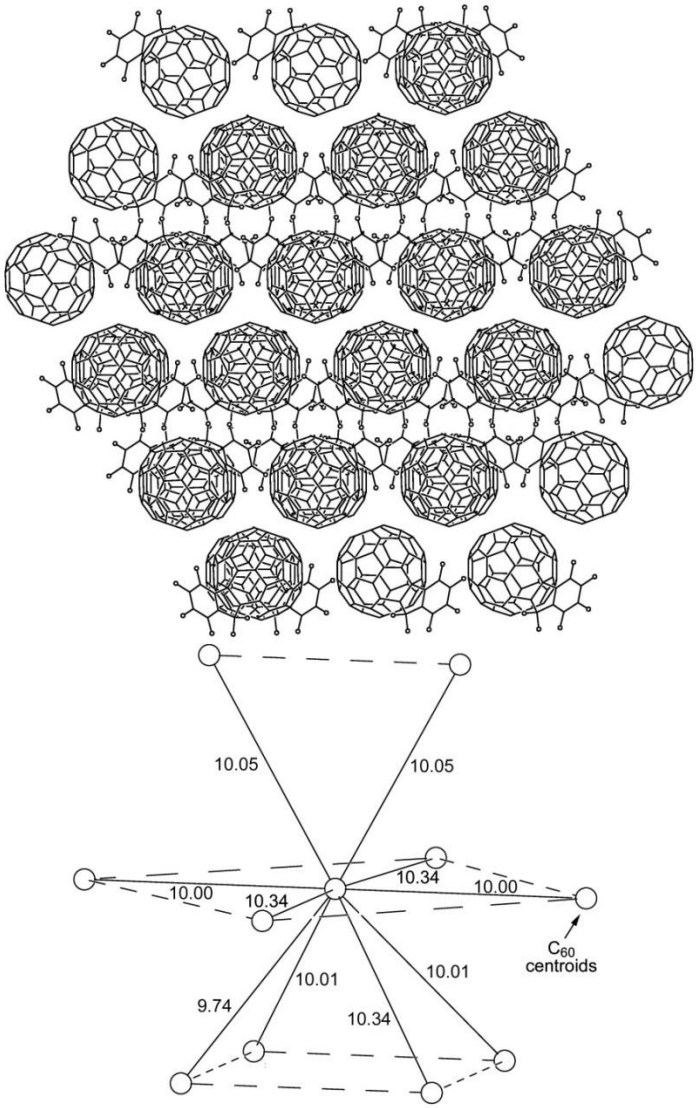

Figure 1.16. The packing of molecules of the faux hawk fullerene (**2**) determined by single-crystal X-ray diffraction. The molecules are arranged in layers with rigorously co-planar C_{60} cage centroids. The layers are stacked in the direction parallel to the long axis of the page, which in this case is parallel to the crystallographic *c* axis. Each faux hawk fullerene molecule is surrounded by 10 nearest neighbor molecules with C_{60} centroid···centroid distances that range from 9.74 to 10.34 Å (ave. 10.09 Å). The lower centroid diagram is only slightly turned and tilted from the orientation of molecules in the upper packing diagram for clarity.

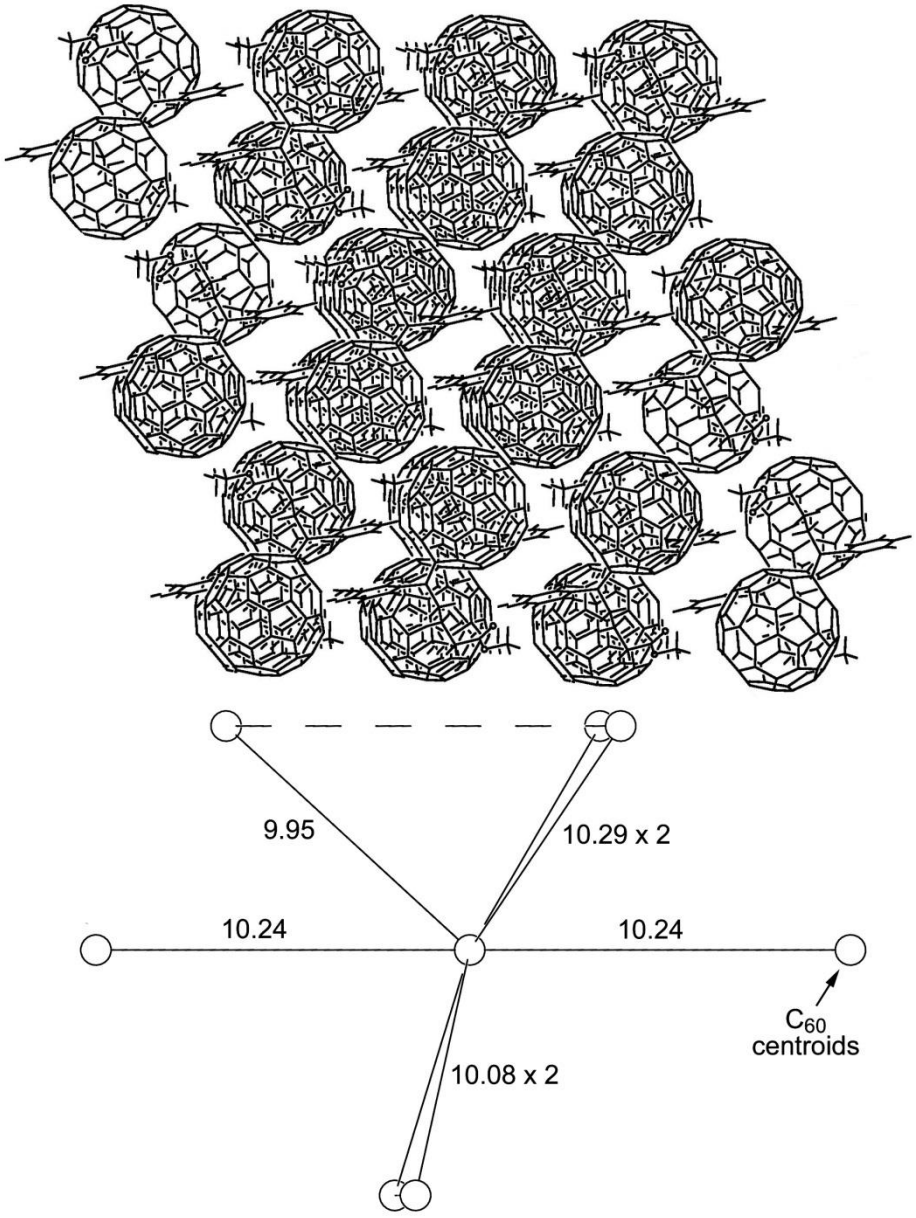

Figure 1.17. The packing of molecules of PCBM in the solvent-free structure determined by single-crystal X-ray diffraction (ref 133). The molecules are arranged in layers with rigorously co-planar C_{60} cage centroids. The layers are stacked in the direction parallel to the long axis of the page. Each PCBM molecule is surrounded by 7 nearest neighbor molecules with centroid···centroid distances that range from 9.95 to 10.28 Å (ave. 10.17 Å). The orientations of the centroids in the lower diagram and the molecules in the upper packing diagram are the same.

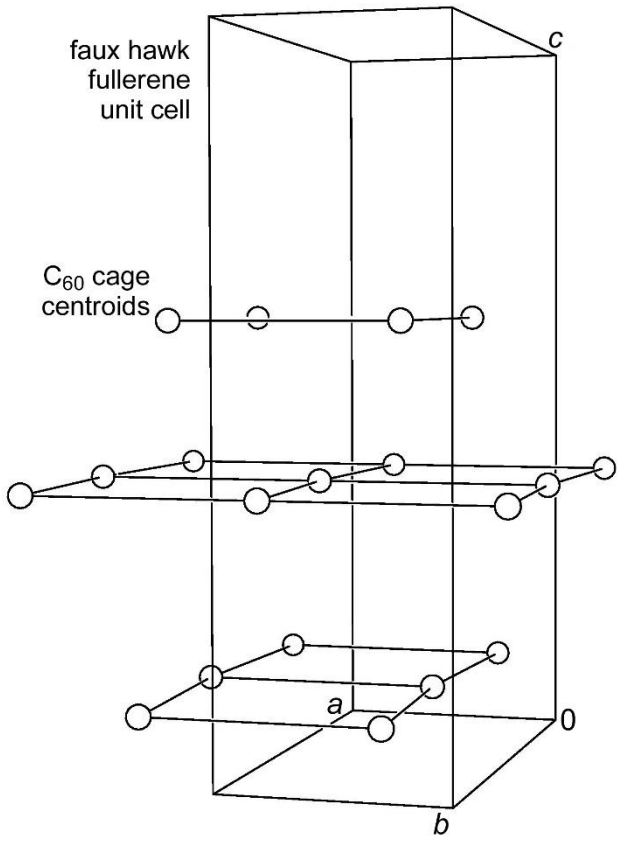

Figure 1.18. Unit cell and packing pattern of the C_{60} cage centroids in the crystal structure of faux hawk fullerene **2**. The rigorously planar, approximately square arrays of centroids are stacked along the crystallographic *c* axis.

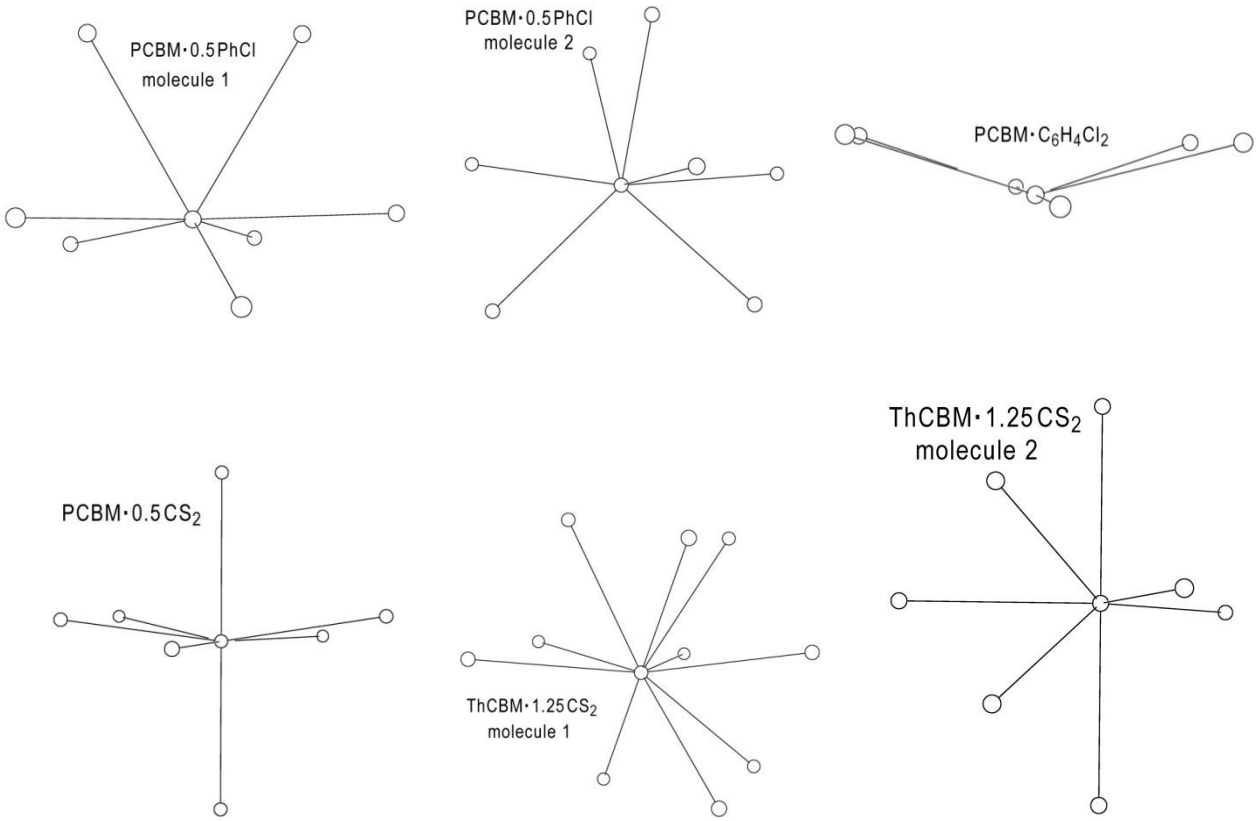

Figure 1.19. Packing patterns of the C_{60} cage centroids in the X-ray structures of PCBM·0.5C_6H_5Cl (two unique molecules in the asymmetric unit), PCBM·*o*-$C_6H_4Cl_2$, PCBM·0.5CS_2, and ThCBM·1.25CS_2 (two unique molecules in the asymmetric unit). In all cases except for PCBM·*o*-$C_6H_4Cl_2$, the packing of the centroids and hence the packing of the fullerene molecules is three dimensional. The literature references for these structures are given in the main text.

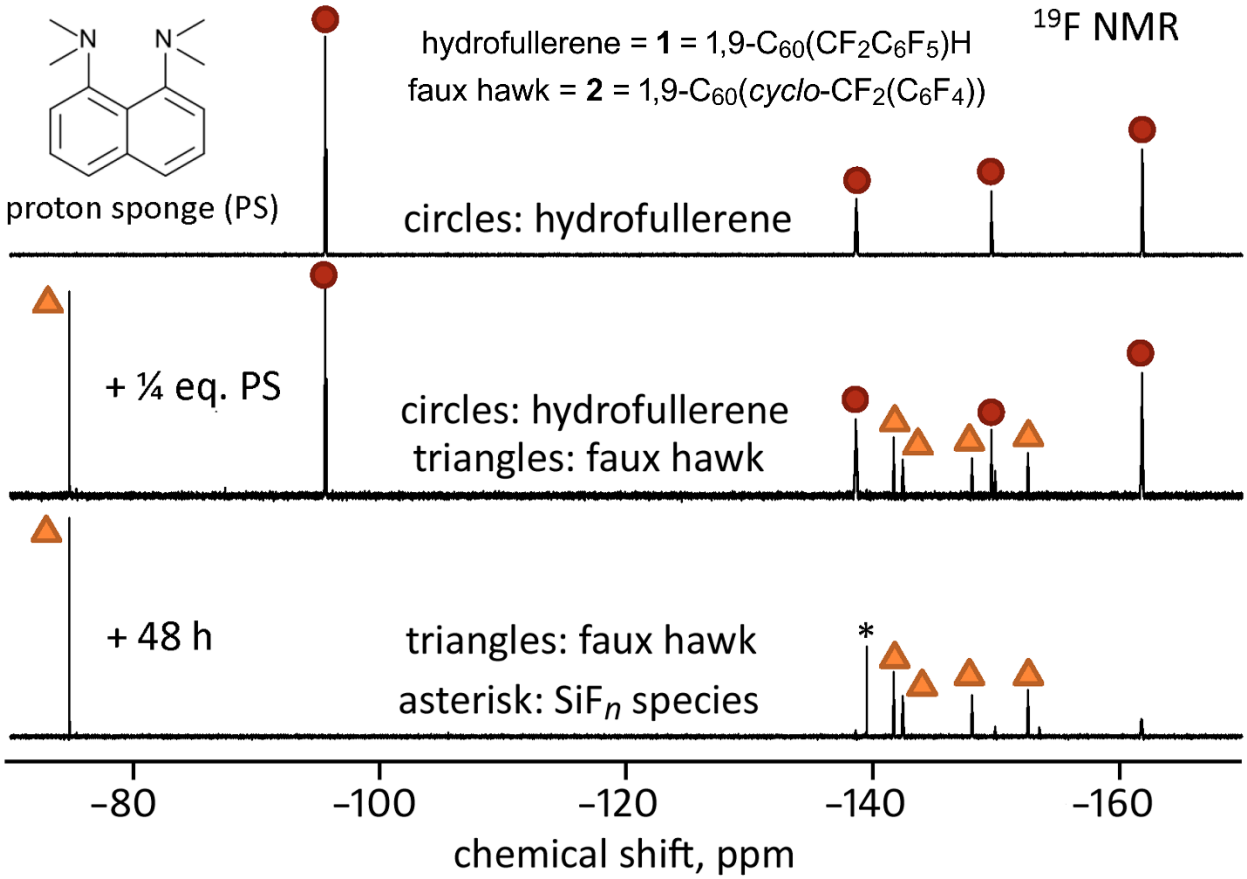

Figure 1.20. Fluorine-19 NMR spectra (90/10 (v/v) PhCN/C_6D_6; 23(1) °C) of the reaction of hydrofullerene **1** with 0.25 equiv. of PS monitored over time. Note that the formation of faux hawk fullerene **2** was not complete within minutes (the middle spectrum) or after 48 h, and that the slow growth of an SiF_n species (labeled with an asterisk) over 48 h indicates that HF or an HF-like species had been present in solution. Note also that a trace amount of **1** is present in the bottom spectrum.

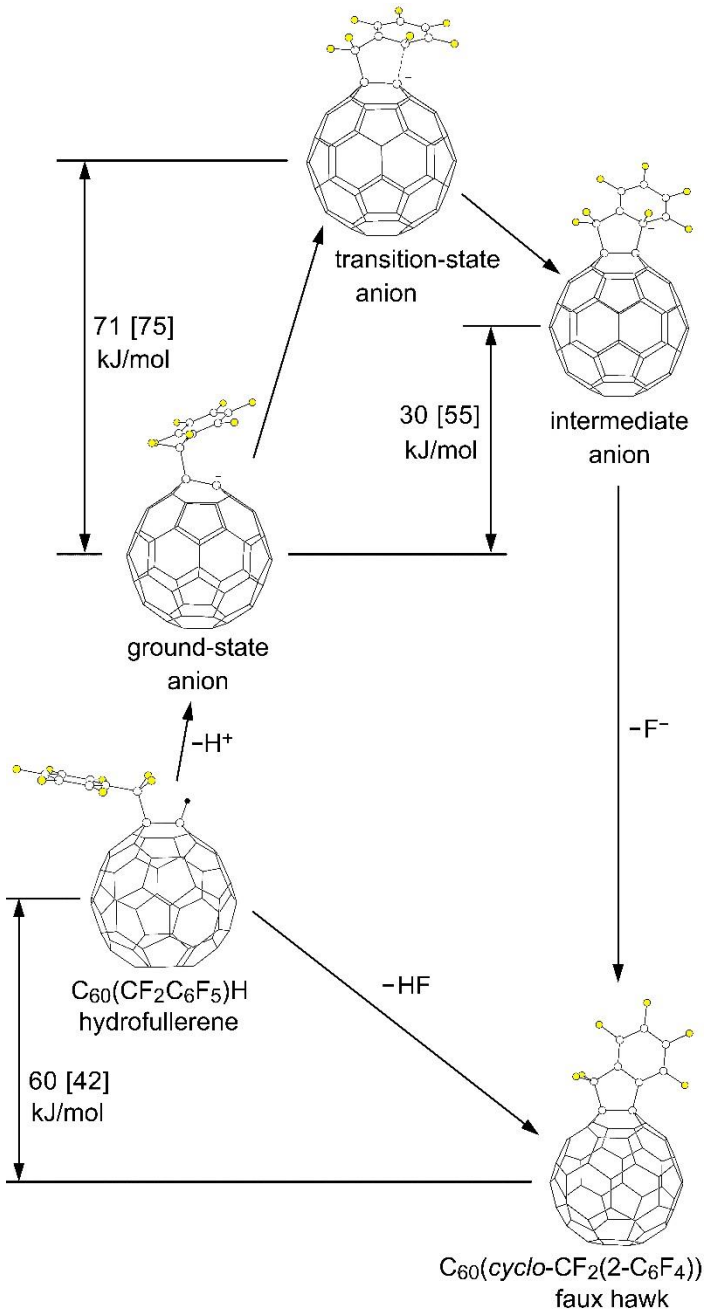

Figure 1.21. OLYP DFT-optimized structures and O3LYP//OLYP relative energies of 1,9-$C_{60}(CF_2C_6F_5)H$ (**1**; hydrofullerene), 1,9-C_{60}(*cyclo*-CF_2(2-C_6F_4)) (**2**; faux hawk), and the three [**1** − H]$^-$ anions proposed for the S_NAr transformation [**1** − H]$^-$ → **2** + F^- (the ground-state, transition-state, and intermediate $C_{60}(CF_2C_6F_5)^-$ anions). The energy changes shown, which are not to scale on the vertical axis, are for (i) a dielectric continuum equivalent to benzonitrile (no brackets) and (ii) the gas phase (square brackets).

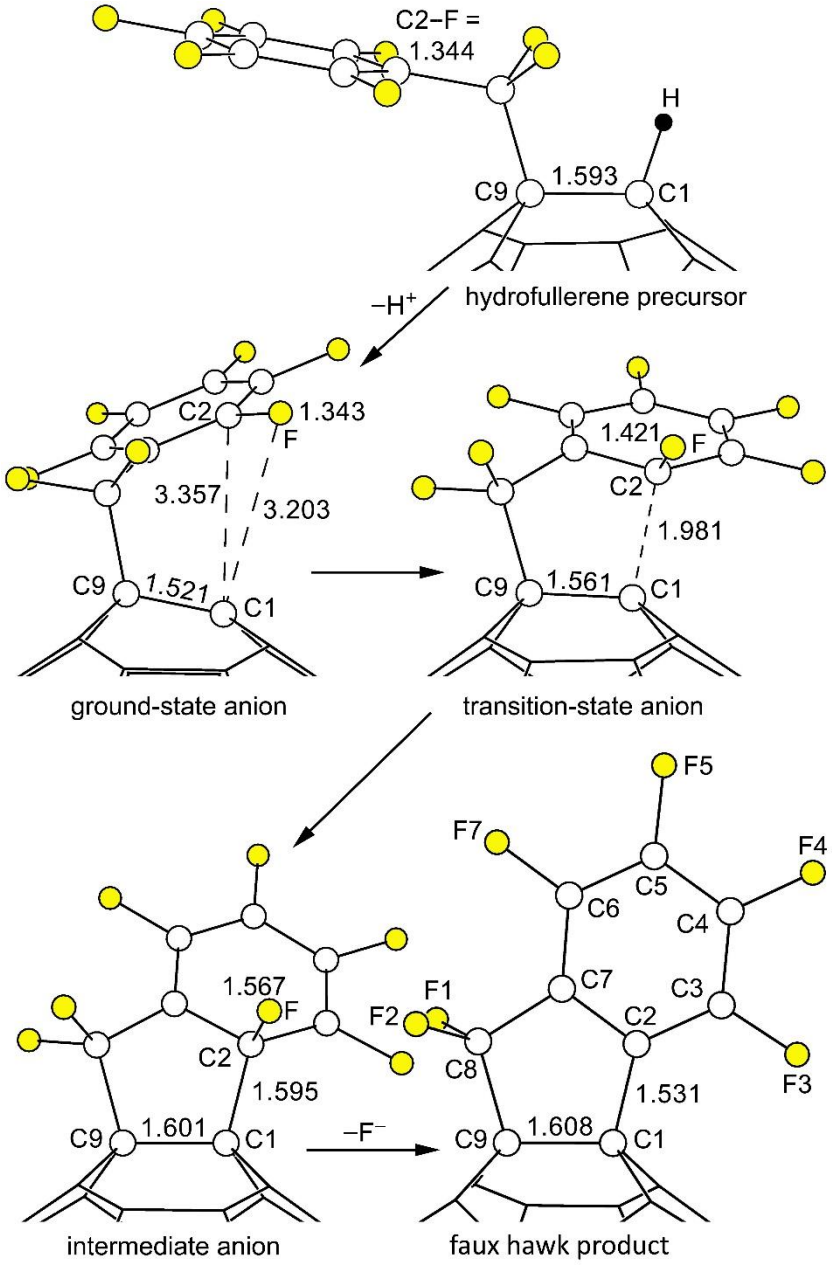

Figure 1.22. Parts of the OLYP DFT-optimized structures and O3LYP//OLYP relative energies of 1,9-$C_{60}(CF_2C_6F_5)H$ (**1**; hydrofullerene), 1,9-C_{60}(*cyclo*-CF_2(2-C_6F_4)) (**2**; faux hawk), and the three $[\mathbf{1} - H]^-$ anions proposed for the S_NAr transformation $[\mathbf{1} - H]^- \rightarrow \mathbf{2} + F^-$ (i.e., the ground-state, transition-state, and intermediate $C_{60}(CF_2C_6F_5)^-$ anions).

OLYP DFT-optimized gas-phase structure of 1,9-$C_{60}(CF_2C_6F_5)H$ (**1**)

This hydrofullerene derivative is the precursor to the faux hawk fullerene.
This drawing represents the lowest energy conformation

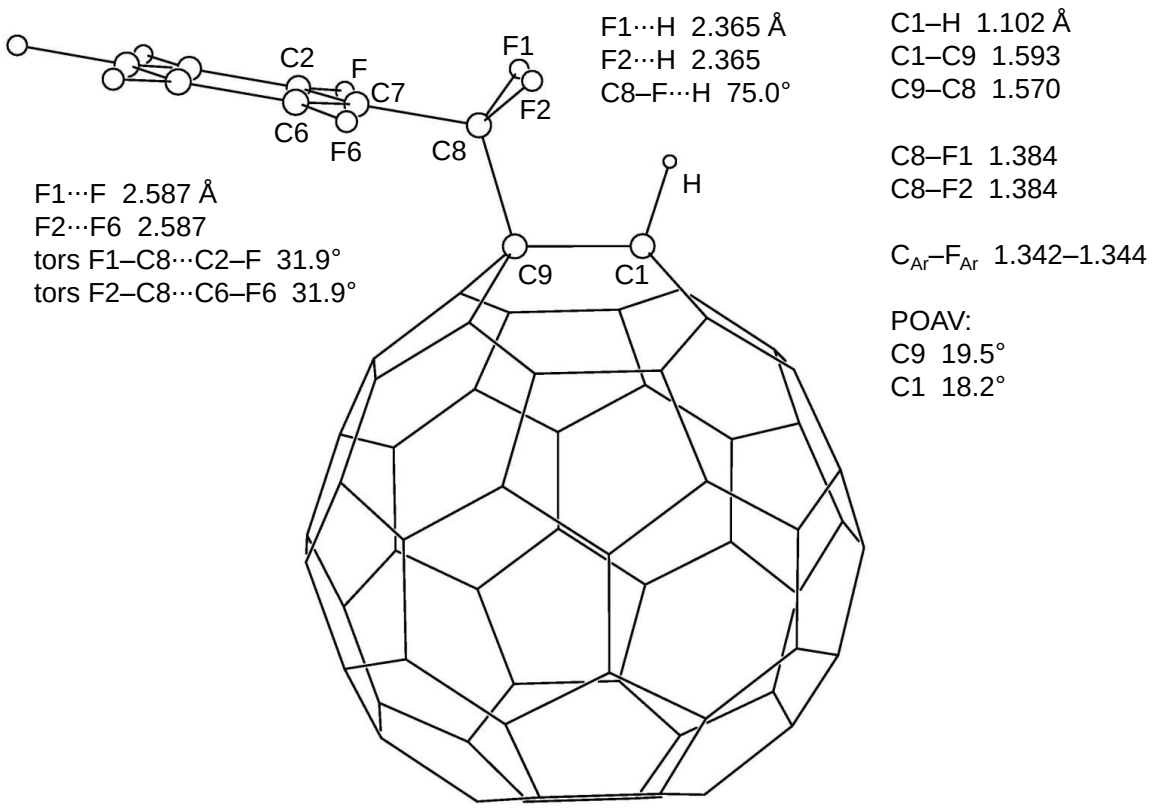

Figure 1.23. Distances and angles for the gas-phase OLYP DFT-optimized lowest-energy conformer of **1**.

Alternate OLYP DFT-optimized gas-phase structure of 1,9-$C_{60}(CF_2C_6F_5)H$ (**1**)

This conformer is a false minimum and was found to be 6.1 kJ/mol less stable than the conformer the one on the previous page

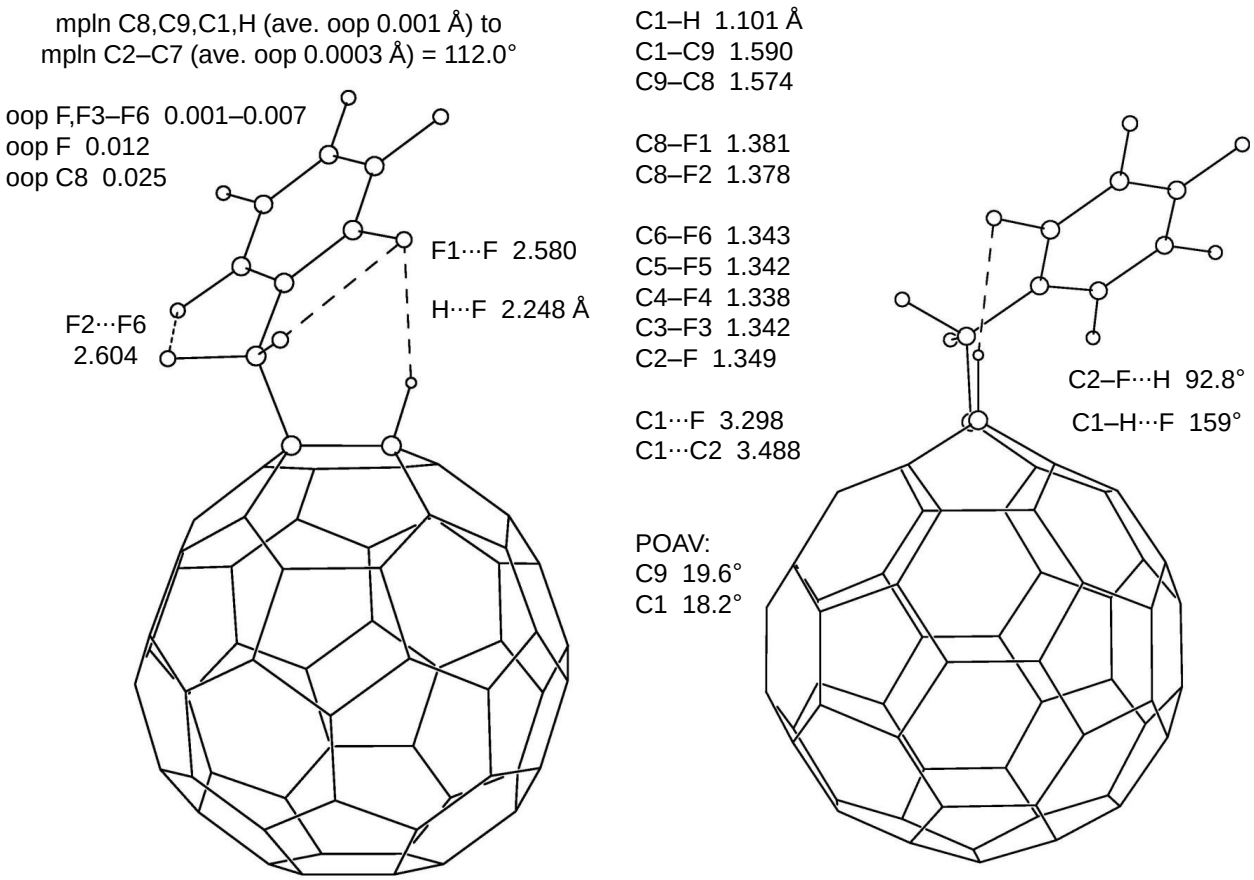

Figure 1.24. Distances and angles for a gas-phase OLYP DFT-optimized conformer of **1** that is 6.1 kJ/mol less stable than the structure shown in Figure 1.23.

OLYP DFT-optimized gas-phase structure of the ground state [**1** − H]$^-$ anion

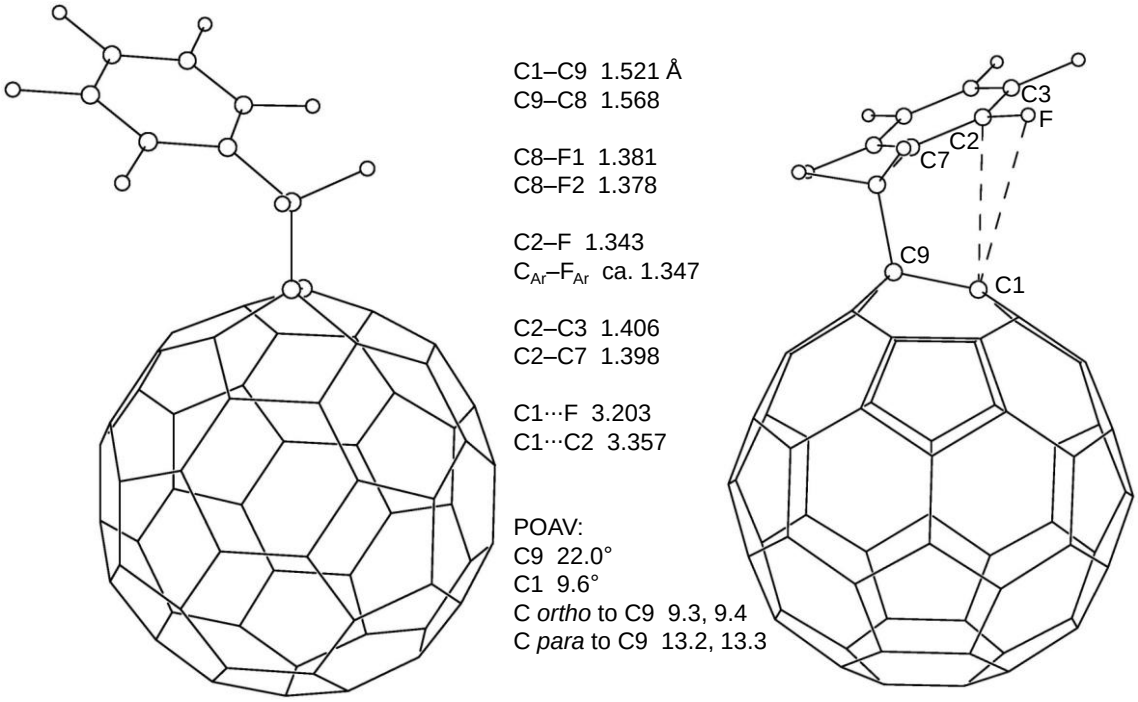

Figure 1.25. Distances and angles for the gas-phase OLYP DFT-optimized structure of the ground state
[**1** − H]$^-$ anion.

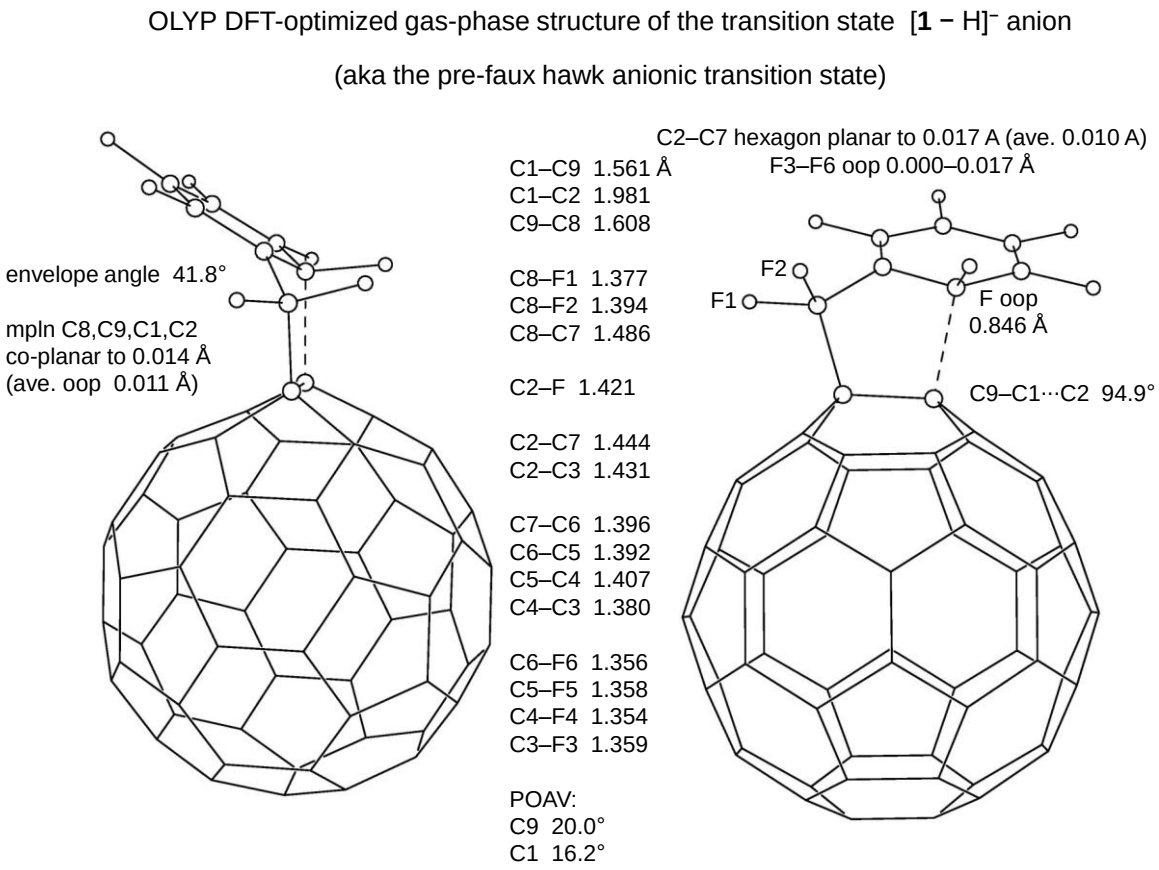

Figure 1.26. Distances and angles for the gas-phase OLYP DFT-optimized structure of the transition state [**1** − H]⁻ anion.

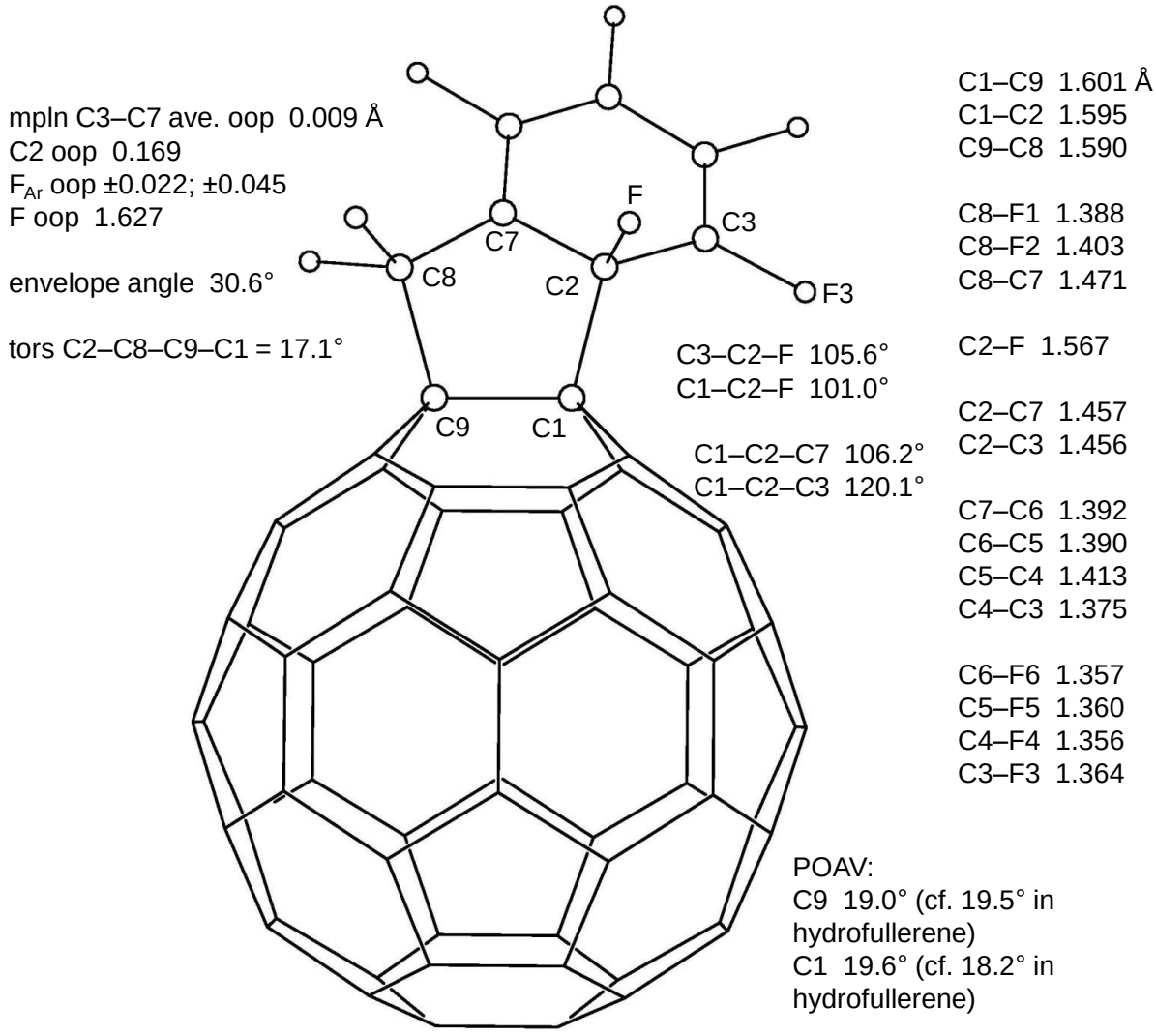

Figure 1.27. Distances and angles for the gas-phase OLYP DFT-optimized structure of the intermediate state [**1** − H]⁻ anion.

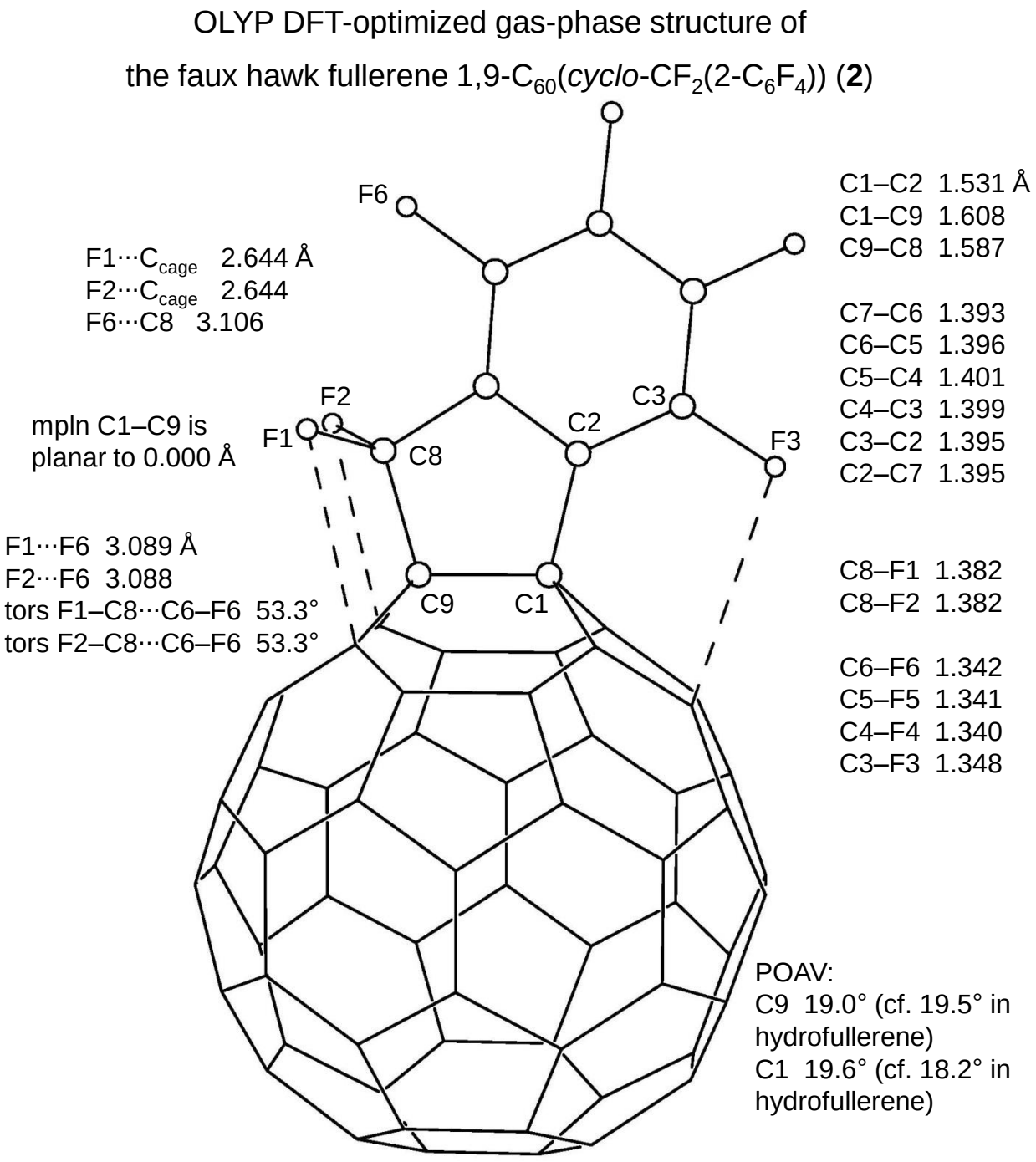

Figure 1.28. Distances and angles for the gas-phase OLYP DFT-optimized structure of **2**.

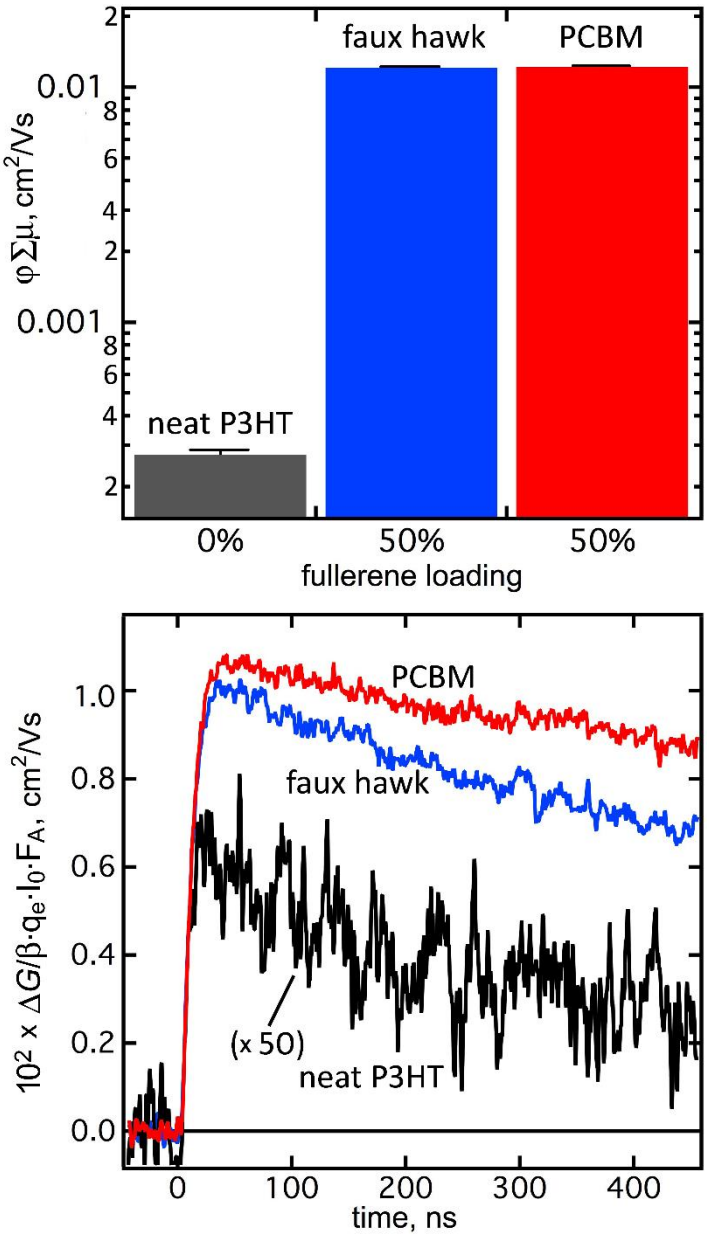

Figure 1.29. (Top) Peak $\varphi\Sigma\mu$ values for thin films of neat P3HT and 50/50 (wt/wt) blends of P3HT and either faux hawk fullerene 1,9-C_{60}(*cyclo*-CF_2(2-C_6F_4)) (**2**) or PCBM. The uncertainty for each measurement is shown on each bar. (Bottom) Transient profile decay curves over 450 ns at incident 500-nm photon fluxes of ca. 1×10^{13} cm^{-2} for neat P3HT and ca. 2×10^{11} cm^{-2} for the blends (ΔG is the change in photoconductance, β is the ratio of the waveguide cross-section dimensions (2.2 in the instrument used), q_e is the electron charge, I_0 is the incident photon flux, and F_A is the fraction of photons absorbed by the sample).

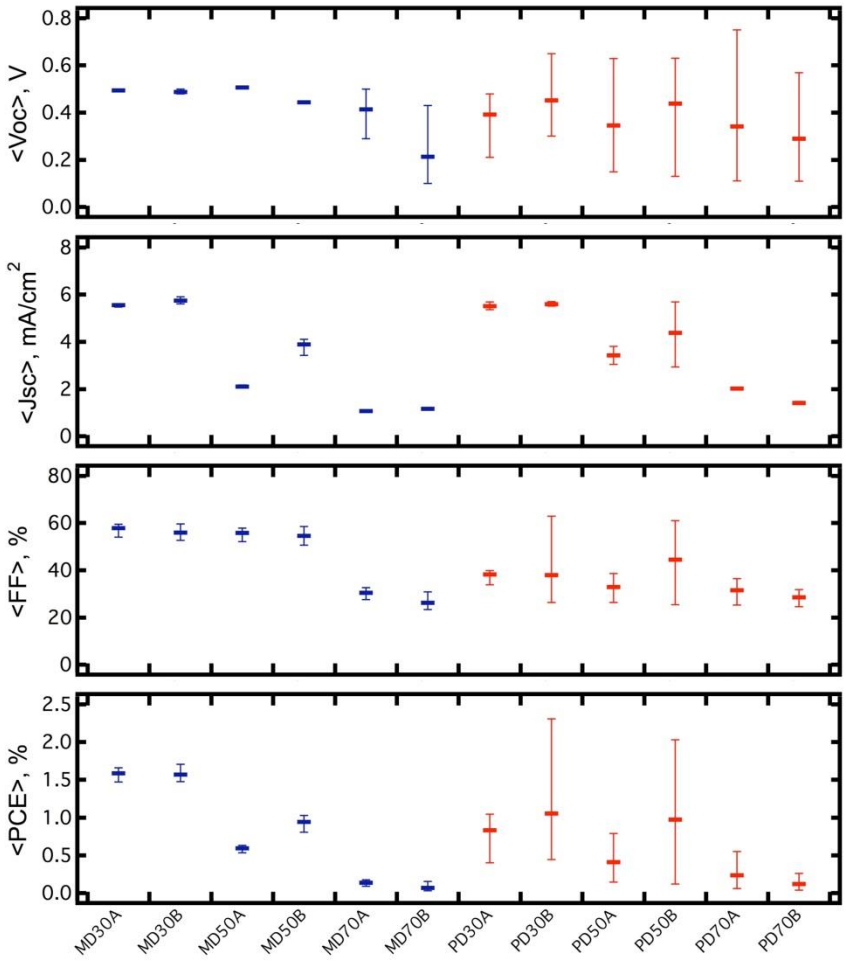

Figure 1.30. Shown top to bottom are averages of V_{oc}, J_{sc}, *FF*, and PCE for **2** (blue data) and PCBM devices (red data). An M in the x-axis tick marks corresponds to **2**, a P corresponds to PCBM, and the number corresponds to the loading of that fullerene in the active layer. The error bars represent the range of data collected for each device and the thick horizontal data point is the average of all data points.

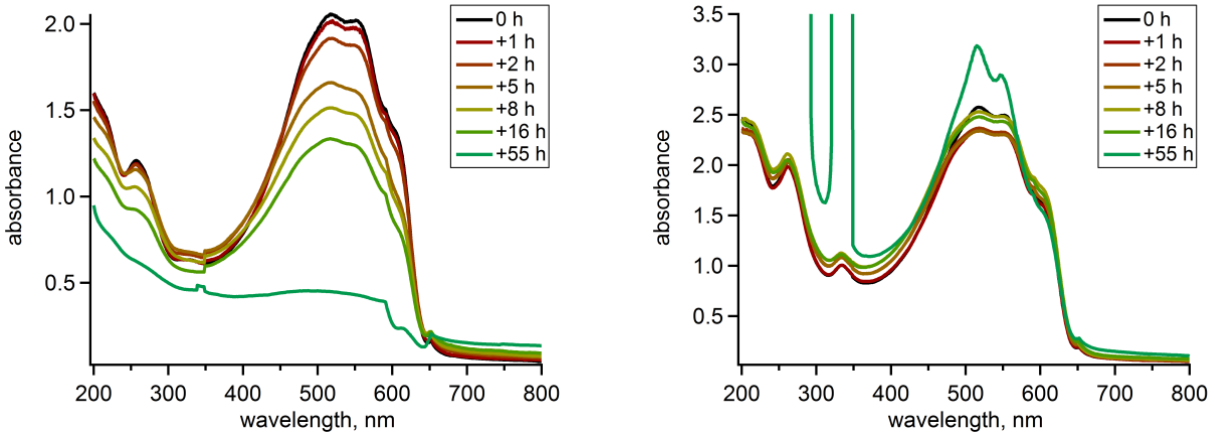

Figure 1.31. UV-vis spectra taken after UV exposure for various amounts of time. The left set of spectra corresponds to the sample M30C sample. The right set of spectra corresponds to the P30C sample.

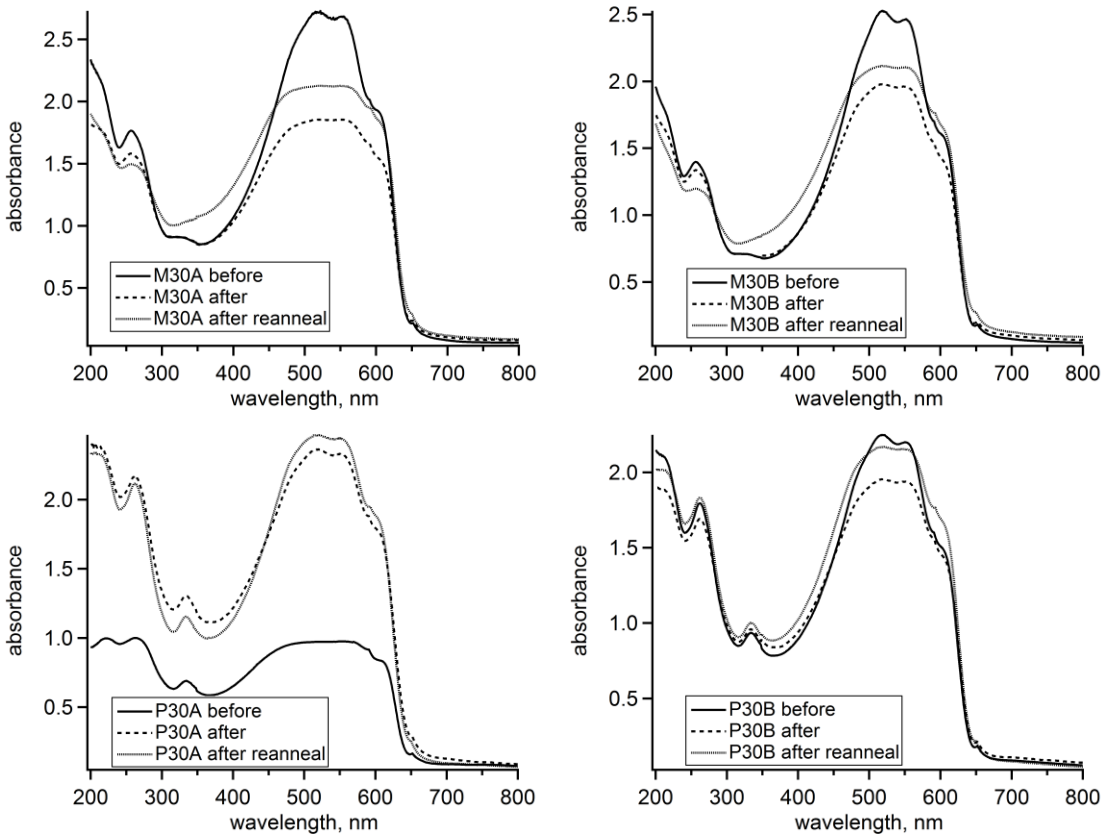

Figure 1.32. The top two sets of UV-vis spectra correspond to **2** and the bottom two sets of UV-vis spectra correspond to PCBM of proton beam exposed films. Samples labeled A were not thermally cycled; samples labeled B were thermally cycled.

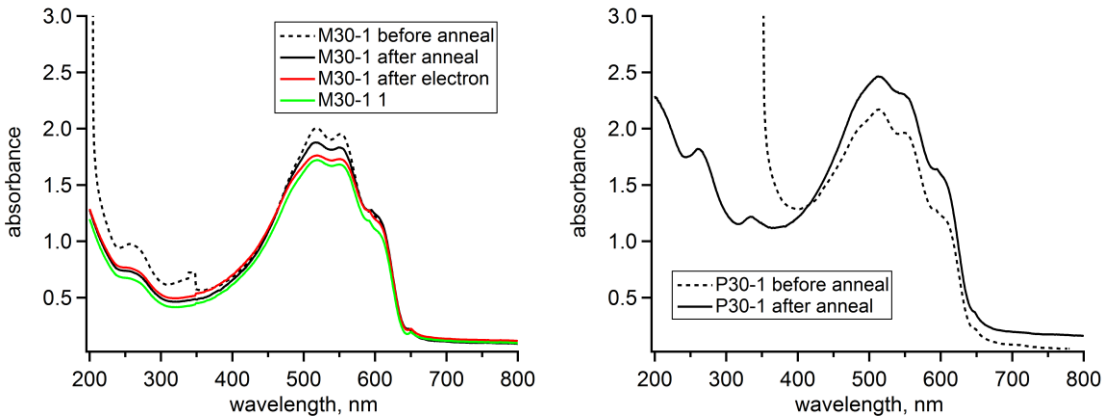

Figure 1.33. UV-vis spectra of **2** (left) and PCBM (right) of electron beam exposure.

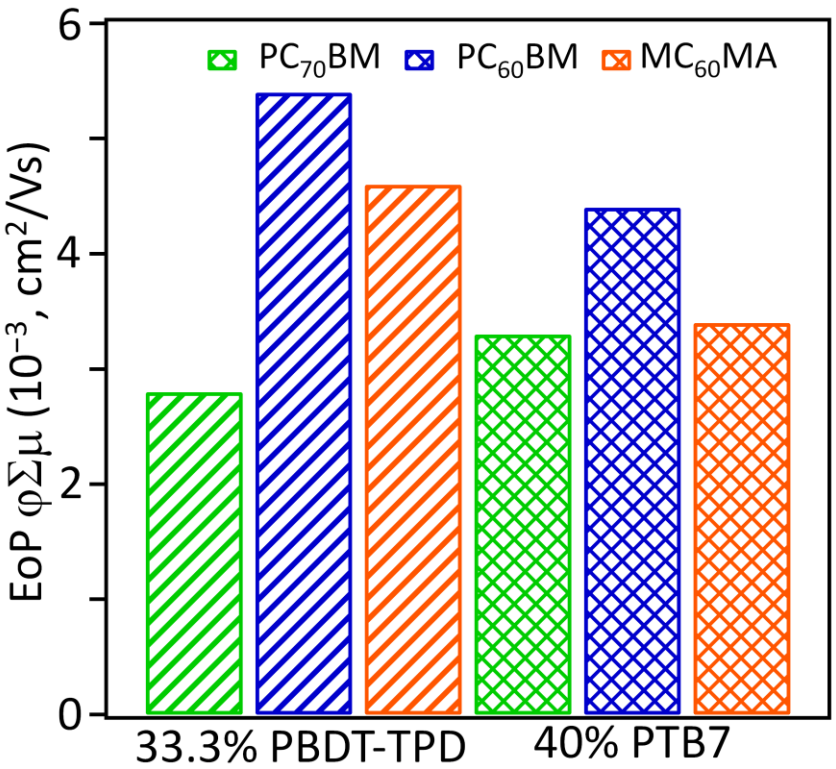

Figure 1.34. $\varphi\Sigma\mu$ of the active layer blends containing the indicated high performance polymers. Data shown for post thermal cycling as there was little to no change in $\varphi\Sigma\mu$ in comparison to the control sample. $MC_{60}MA$ = compound **2**.

Table 1.1. Reactions producing 1,9-$C_{60}(CF_2C_6F_5)H$ (**1**) and 1,9-C_{60}(*cyclo*-$CF_2(2\text{-}C_6F_4)$) (**2**)[a]

Figure 2 HPLC trace	temp., °C	equiv. Bn_FI[b]	equiv. R_3SnH[c]	product mixture mol% by HPLC integration[d]		
				1	**2**	unreacted C_{60}
a	100(2)	1	2	24	ca. 0	70
b	160(5)	1	2	(15) 6	(8) 30	(70) 55
c	160(5)	10	2	(18) 22	(7) 13	(64) 51
d	160(5)	10	20	(14) 3	(5) 1	(31) ca. 0
e	160(5)	10	5	29	7	13

[a] All reactions in *o*-DCB. All volatiles (*o*-DCB, I_2) were removed under vacuum. The solid residue was redissolved in toluene, injected into a COSMOSIL Buckyprep HPLC column, and eluted with 80/20 (v/v) toluene/heptane. The HPLC traces are shown in Figure 2. [b] Per equiv. C_{60}; $Bn_FI = C_6F_5CF_2I$. [c] Per equiv. C_{60}; R = *n*-Bu. [d] The mol% values in parentheses are for 1 h reactions; all other mol% values are for 2 h reactions. The mol% values do not add up to 100% because other, unidentified fullerene byproducts were also present.

Table 1.2. Interatomic distances (Å) and angles (deg) for the X-ray structure of **2** and the OLYP DFT-optimized structures of 1,9- and 1,2-C_{60}(*cyclo*-CF_2(2-C_6F_4))[a]

parameter	X-ray	DFT	DFT
	2	1,9-C_{60}(*cyclo*-CF_2(2-C_6F_4))	1,2-C_{60}(*cyclo*-CF_2(2-C_6F_4))
C1–C9	1.610(5)	1.608	1.636
C1–C2	1.538(6)	1.531	1.531
C2–C7	1.374(6)	1.395	1.395
C7–C8	1.482(5)	1.496	1.503
C8–C9	1.572(5)	1.587	1.589
F1···F6	2.997(6)	3.088	3.049
F2···F6	3.151(6)	3.088	3.141
C2–C1–C9	102.6(3)	103.6	103.2
C2–C1–C	109.5(3); 115.8(3)	114.3 × 2	112.7; 114.9
C8–C9–C1	105.2(3)	105.5	105.1
C8–C9–C	109.2(3); 113.6(3)	114.5 × 2	112.0; 113.4
C1–C2–C7	113.0(3)	112.9	113.2
C2–C7–C6	121.4(4)	121.8	121.5
C2–C7–C8	111.7(4)	111.6	111.9
C7–C8–C9	106.4(3)	106.4	106.3

[a] The X-ray structure of **2** and the DFT 1,9- isomer which has the faux hawk substituent attached to a C_{60} cage bond shared by two hexagons. The hypothetical DFT 1,2- isomer (not observed) has the substituent attached to a C_{60} cage bond shared by a hexagon and a pentagon.

Table 1.3. 376 MHz ^{19}F NMR δ and *J*(FF) values for **1** and **2** (δ(C_6F_6) = −164.9)

	1,9-C_{60}($CF_2C_6F_5$)H (**1**)	1,9-C_{60}(*cyclo*-CF_2(2-C_6F_4)) (**2**)
δ(F_a)	−95.5 (t)	−74.8 (d)
J($F_aF_{bb'}$)/*J*(F_aF_b)	30	5.5
δ($F_{bb'}$)/δ(F_b)	−138.7 (qt)	−142.4 (m)
J($F_bF_{b'}$)	5	
J($F_{bb'}F_d$)/*J*(F_bF_d)	5.5	6
J(F_bF_c)	26	18
J($F_bF_{c'}$)	7	
J(F_bF_e)		23
δ($F_{cc'}$)/δ(F_c)	−161.9 (m)	−148.0 (td)
J($F_{cc'}F_d$)/*J*(F_cF_d)	22	20
J(F_cF_e)		5
δ(F_d)	−149.6 (tt)	−152.6 (td)
J(F_dF_e)		18
δ(F_e)		−141.7 (tt)

[a] Coupling constants (Hz) are estimated (±1 Hz) from simulated spectra. [b] d = doublet; t = triplet; q = quartet; m = multiplet. The solvent was $CDCl_3$.

Table 1.4. Electrochemical reduction potentials[a,b]

compd	0/− potential, V vs. $C_{60}^{0/-}$	−/2− potential, V vs. $C_{60}^{0/-}$	2−/3− potential, V vs. $C_{60}^{0/-}$	3−/4− potential, V vs. $C_{60}^{0/-}$
1,9-$C_{60}(CF_2C_6F_5)H$[b]	−0.02	−0.45	−0.98	—
1,9-C_{60}(*cyclo*-CF_2(2-C_6F_4))[b]	−0.01	−0.40	−0.92	−1.36[c]
C_{60}	0.00	−0.39	−0.85	−1.31
PCBM	−0.09	−0.48	−0.99	
iso-PCBM[d]	−0.08			
1,9-$C_{60}(CH_2C_6H_5)H$[e]	−0.08	−0.48		
1,9-$C_{60}H_2$[f]	−0.13			
1,9-$C_{60}(CH_3)_2$[g]	−0.13			
1,9-C_{60}(*cyclo*-C_2F_4)[h]	0.03			

[a] All potentials from cyclic voltammograms unless otherwise indicated. Conditions (unless otherwise noted): purified dinitrogen atmosphere glovebox; 1,2-$C_6H_4Cl_2$ (*o*-DCB) solutions at 23(1) °C; 0.1 M N(*n*-Bu)$_4BF_4$ electrolyte; $Fe(Cp)_2$ internal standard; scan rate 100 mV s^{-1}; Pt working and counter electrodes; Ag wire quasi-reference electrode. The uncertainty for each measurement is ±0.01 V. [b] 1,9-$C_{60}(CF_2C_6F_5)H$ = **1**; 1,9-C_{60}(*cyclo*-CF_2(2-C_6F_4)) = **2**. [c] Potential from square-wave voltammetry. [d] Ref 61. [e] At 25 °C in benzonitrile; ref 24. [f] At −50 °C in 90/10 (v/v) toluene/dimethylformamide; ref 50. [g] At 25 °C in benzonitrile; ref 51. [h] Ref 52.

Table 1.5. Centroid···centroid distances in solvent-free and solvent-included fullerene X-ray structures[a,b]

9.739	9.952	9.910	9.843	9.945	10.000	9.840	9.982
10.000	10.092	10.096	9.945	9.948	10.000	9.903	9.982
10.000	10.092	10.096	9.994	9.948	10.104	9.930	9.998
10.010	10.278	10.262	10.046	9.994	10.183	9.982	10.018
10.010	10.278	10.262	10.054	10.046	10.183	9.982	10.021
10.046	10.236	10.322	10.101	10.064	10.217	9.997	10.026
10.046	10.236	10.322	10.138	10.101		9.998	10.189
10.331						10.018	
10.342						10.026	
10.342						10.189	
10.087	10.166	10.181	10.017	10.007	10.115	9.987	10.031
faux hawk	Paterno	Casalegno	Rispens et al.	Rispens et al.	Rispens et al.	Choi et al.	Choi et al.
(this work)	et al.	et al.	PCBM.0.5PhCl	PCBM.0.5PhCl	PCBM.*o*-$C_6H_4Cl_2$	ThCBM.1.25CS_2	ThCBM.1.25CS_2
	single-	PXRD	molecule 1	molecule 2			
	crystal	solvent-					
	solvent-	free PCBM					
	free PCBM						

[a] The mean values are given in the line just above the text. [b] The literature references are given below.

Paternò et al. = Paternò, G.; Warren, A. J.; Spencer, J.; Evans, G.; García Sakai, V.; Blumberger, J.; Cacialli, F. *J. Mater. Chem.* **2013**, *1*, 5619.

Casalegno et al. = Casalegno, M.; Zanardi, S.; Frigerio, F.; Po, R.; Carbonera, C.; Marra, G.; Nicolini, T.; Raos, G.; Meille, S. V. *Chem. Commun.* **2013**, *49*, 4525.

Rispens et al. = Rispens; M. T.; Meetsma, A.; Rittberger, R.; Brabec, C. J.; Sariciftci, N. S.; Hummelen, J. C. *Chem. Commun.* **2003**, 2116.

Choi et al. = Choi, J. H.; Honda, R.; Seki, S.; Fukuzumi, S. *Chem. Commun.* **2011**, *47*, 11213.

Table 1.6. DFT-Predicted Interatomic Distances (Å) and Angles (deg) for Species Along the Proposed S_NAr Reaction Coordinate Leading from **1** to **2** + HF[a]

distance or angle	**1**	ground-state [**1** − H]$^-$ anion	transition state [**1** − H]$^-$ anion	intermediate [**1** − H]$^-$ anion	**2**[b]
C1–C2	—	3.357	1.981	1.595	1.531
C1–C9	1.593	1.521	1.561	1.601	1.608
other C1–C_{cage}	1.527, 1.527	1.424, 1.425	1.474, 1.484	1.528, 1.533	1.541, 1.541
C2–F	1.344	1.343	1.421	1.567	—
other C_{Ar}–F	1.342 × 2, 1.339, 1.344	1.345 × 2, 1.347 × 2	1.354, 1.356, 1,358, 1.359	1.356, 1.357, 1.360, 1.364	1.340, 1.341, 1.342, 1.348
C2–C3	1.397	1.398	1.431	1.456	1.395
C2–C7	1.406	1.406	1.444	1.457	1.395
other C_{Ar}–C_{Ar}[c]	1.395 × 2, 1.397, 1.406	1.393 × 2, 1.397, 1.405	1.380, 1.407, 1.392, 1.396	1.375, 1.390, 1.392, 1.413	1.395, 1.396, 1.399, 1.401
C1–C2–C3	—	136.3	117.1	120.1	128.1
C1–C2–C7	—	67.6	98.2	106.2	112.9
C3–C2–C7	121.8	121.7	116.5	113.3	119.0
F–C2–C1	—	71.9	94.9	101.0	—
F–C2–C3	116.5	116.1	111.6	105.6	—
F–C2–C7	121.7	122.2	116.1	109.7	—
C1 POAV θ_p[d]	18.2	9.6	16.2	19.6	19.3
C9 POAV θ_p[d]	19.5	22.0	20.0	19.0	19.1

[a] OLYP DFT-optimized structures. **1** = 1,9-$C_{60}(CF_2C_6F_5)H$; **2** = 1,9-C_{60}(*cyclo*-CF_2(2-C_6F_4)). [b] A comparison of the DFT-predicted and experimental X-ray diffraction distances and angles for **2**. [c] These four distances are listed in the order C3–C4, C4–C5, C5–C6, and C6–C7. [d] The π-orbital axis vector (POAV) for a fullerene C atom is defined as the vector that makes equal angles to the three C_{cage} atoms to which it is attached (see ref 106). The common angle is denoted $\theta_{\sigma\pi}$ and $\theta_p = \theta_{\sigma\pi} - 90°$. The angle θ_p denotes the degree of pyramidalization of a fullerene cage C atom. For an idealized trigonal-planar C(sp^2) atom, $\theta_p = 0°$; for an idealized tetrahedral C(sp^3) atom, $\theta_p = 19.5°$.

Table 1.7. DFT relative energies (kJ/mol) for other functionals and O3LYP//OLYP solvation energies[a]

functional	ground state **1**$^-$ anion	transition state **1**$^-$ anion	intermediate **1**$^-$ anion
PBE	0.0	72.4	49.8
OLYP	0.0	85.3	67.3
O3LYP//OLYP solvation energy	123.2	128.1	148.7

[a] The designations "ground state," "transition state," and "intermediate" are the same as those used in Figure 21. (The O3LYP//OLYP relative energies, in the gas-phase and in a PhCN-like dielectric continuum, are shown in Figure 1.21.

Table 1.8. TRMC $\varphi\Sigma\mu$ figure of merits for pre- and post- thermal cycle. The % difference is relative to the control samples. The first letters C = C_{60} and **2** = faux hawk, while the second letter A = control sample (no thermal treatment) and B and C = thermally treated samples.

$\varphi\Sigma\mu$ (cm^2/Vs)	% difference	sample name
0.0086879	–	CA
0.010649	+22.6	CB
0.049065	+464.8	CC
0.0054669	–	**2**A
0.0072567	+32.7	**2**B
0.020309	+271.5	**2**C

Chapter 1 References

(1) Boltalina, O. V.; Kuvychko, I. V.; Shustova, N. B.; Strauss, S. H. In *Handbook of Carbon Materials, Volume 1, Syntheses and Supramolecular Systems*; Desouza, F., Kadish, K. M., Eds.; World Scientific: Singapore, 2010, p pp 101.

(2) Isanbor, C.; O'Hagan, D. *J. Fluorine Chem.* **2006**, *127*, 303.

(3) Goryunkov, A. A.; Kuvychko, I. V.; Ioffe, I. N.; Dick, D. L.; Sidorov, L. N.; Strauss, S. H.; Boltalina, O. V. *J. Fluorine Chem.* **2003**, *124*, 61.

(4) Kuvychko, I. V.; Whitaker, J. B.; Larson, B. W.; Folsom, T. C.; Shustova, N. B.; Avdoshenko, S. M.; Chen, Y.; Wen, H.; Wang, X.; Dunsch, L.; Popov, A. A.; Boltalina, O. V.; Strauss, S. H. *Chem. Sci.* **2012**, *3*, 1399.

(5) Shustova, N. B.; Popov, A. A.; Newell, B. S.; Miller, S. M.; Anderson, O. P.; Seppelt, K.; Bolskar, R. D.; Boltalina, O. V.; Strauss, S. H. *Angew. Chem. Int. Ed.* **2007**, *46*, 4111.

(6) Kareev, I. E.; Kuvychko, I. V.; Shustova, N. B.; Lebedkin, S. F.; Bubnov, V. P.; Anderson, O. P.; Popov, A. A.; Strauss, S. H.; Boltalina, O. V. *Angew. Chem. Int. Ed.* **2008**, *47*, 6204.

(7) Kareev, I. E.; Popov, A. A.; Kuvychko, I. V.; Shustova, N. B.; Lebedkin, S. F.; Bubnov, V. P.; Anderson, O. P.; Seppelt, K.; Strauss, S. H.; Boltalina, O. V. *J. Am. Chem. Soc.* **2008**, *130*, 13471.

(8) Popov, A. A.; Shustova, N. B.; Boltalina, O. V.; Strauss, S. H.; Dunsch, L. *ChemPhysChem* **2008**, *9*, 431.

(9) Shustova, N. B.; Kuvychko, I. V.; Boltalina, O. V.; Strauss, S. H. *Acta Cryst.* **2007**, *E63*, o4575.

(10) Popov, A. A.; Kareev, I. E.; Shustova, N. B.; Lebedkin, S. F.; Strauss, S. H.; Boltalina, O. V.; Dunsch, L. *Chem. Eur. J.* **2008**, *14*, 107.

(11) Popov, A. A.; Kareev, I. E.; Shustova, N. B.; Stukalin, E. B.; Lebedkin, S. F.; Seppelt, K.; Strauss, S. H.; Boltalina, O. V.; Dunsch, L. *J. Am. Chem. Soc.* **2007**, *129*, 11551.

(12) Coffey, D. C.; Larson, B. W.; Hains, A. W.; Whitaker, J. B.; Kopidakis, N.; Boltalina, O. V.; Strauss, S. H.; Rumbles, G. *J. Phys. Chem. C* **2012**, *116*, 8916.

(13) Bunce, R. A.; Nago, T.; Sonobe, N.; Slaughter, L. M. *J. Heterocyclic Chem.* **2009**, *45*, 551.

(14) Janjetovic, M.; Träff, A. M.; Ankner, T.; Wettergren, J.; Hilmersson, G. *Chem. Commun.* **2013**, *49*, 1826.

(15) Kuvychko, I. V.; Shustova, N. B.; Avdoshenko, S. M.; Popov, A. A.; Strauss, S. H.; Boltalina, O. V. *Chem. Eur. J.* **2011**, *17*, 8799.

(16) Yoshida, M.; Suzuki, D.; Iyoda, M. *Chem. Lett.* **1996**, 1097.

(17) Wienk, M. M.; Kroon, J. M.; Verhees, W. J. H.; Knol, J.; Hummelen, J. C.; van Hal, P. A.; Janssen, R. A. J. *Angew. Chem. Int. Ed.* **2003**, *42*, 3371.

(18) Huang, Y.-C.; Tsao, C.-S.; Chuang, C.-M.; Lee, C.-H.; Hsu, F.-H.; Cha, H.-C.; Chen, C.-Y.; Lin, T.-H.; Su, C.-J.; Jeng, U.-S.; Su, W.-F. *J. Phys. Chem. C* **2012**, *116*, 10238.

(19) Bouwer, R. K. M.; Wetzelaer, G.-J. A. H.; Blom, P. W. M.; Hummelen, J. C. *J. Mater. Chem.* **2012**, *22*, 15412.

(20) Nardes, A. M.; Ferguson, A. J.; Whitaker, J. B.; Larson, B. W.; Larsen, R. E.; Maturová, K.; Graf, P. A.; Boltalina, O. V.; Strauss, S. H.; Kopidakis, N. *Adv. Funct. Mater.* **2012**, *22*, 4115.

(21) Kadish, K. M.; Gao, X.; Van Caemelbecke, E.; Suenobu, T.; Fukuzumi, S. *J. Phys. Chem. A* **2000**, *104*, 3878.

(22) Yoshida, M.; Morishima, A.; Morinaga, Y.; Iyoda, M. *Tetrahedron Lett.* **1994**, *35*, 9045.

(23) Jousselme, B.; Sonmez, G.; Wudl, F. *J. Mater. Chem.* **2006**, *16*, 3478.

(24) Yang, W.-W.; Li, Z.-J.; Gao, X. *J. Org. Chem.* **2010**, *75*, 4086.

(25) Neretin, I. S.; Slovokhotov, Y. L. *Russ. Chem. Rev.* **2004**, *73*, 455.

(26) Hirsch, A.; Brettreich, M. *Fullerenes - Chemistry and Reactions*; Wiley-VCH: Weinheim, 2005.

(27) Hu, Y. L.; Lu, M.; Ge, Q.; Wang, P. C.; Zhang, S. B.; Lu, T. T. *J. Chin. Chem. Soc.* **2010**, *55*, 97.

(28) van der Made, A. W.; van der Made, R. H. *J. Org. Chem.* **1993**, *58*, 1262.

(29) Goesten, M. G.; Gupta, K. B. S. S.; Ramos-Fernandez, E. V.; Khajavi, H.; Gascon, J.; Kapteijn, F. *CrystEngComm* **2012**, *14*, 4109.

(30) Clikeman, T. T.; Bukovsky, E. V.; Kuvychko, I. V.; San, L. K.; Deng, S. H. M.; Wang, X.-B.; Chen, Y.-S.; Strauss, S. H.; Boltalina, O. V. *Chem. Commun.* **2014**, *50*, 6263.

(31) Larson, B. W.; Whitaker, J. B.; Wang, X.-B.; Popov, A. A.; Rumbles, G.; Kopidakis, N.; Strauss, S. H.; Boltalina, O. V. *J. Phys. Chem. C* **2013**, *117*, 14958.

(32) San, L. K.; Bukovsky, E. V.; Kuvychko, I. V.; Popov, A. A.; Strauss, S. H.; Boltalina, O. V. *Chem. Eur. J.* **2014**, *20*, 4373.

(33) Mack, J.; Vogel, P.; Jones, D.; Kaval, N.; Sutton, A. *Org. Biomol. Chem* **2007**, *5*, 2448.

(34) Reese, M. O.; Nardes, A. M.; Rupert, B. L.; Larsen, R. E.; Olson, D. C.; Lloyd, M. T.; Shaheen, S. E.; Ginley, D. S.; Rumbles, G.; Kopidakis, N. *Adv. Funct. Mater.* **2010**, *20*, 3476.

(35) Petrakis, L.; Sederholm, C. H. *J. Chem. Phys.* **1961**, *35*, 1243.

(36) Wang, X.-B.; Wang, L.-S. *Rev. Sci. Instrum.* **2008**, *79*, 073108.

(37) Kuvychko, I. V.; Dubceac, C.; Deng, S. H. M.; Wang, X.-B.; Granovsky, A. A.; Popov, A. A.; Petrukhina, M. A.; Strauss, S. H.; Boltalina, O. V. *Angew. Chem. Int. Ed.* **2013**, *52*, 7505.

(38) Peralta, J. E.; Contreras, R. H.; Snyder, J. P. *Chem. Commun.* **2000**, 2025.

(39) Arnold, W. D.; Mao, J.; Sun, H.; Oldfield, E. *J. Am. Chem. Soc.* **2000**, *122*, 12164.

(40) Tuttle, T.; Grafenstein, J.; Cremer, D. *Chem. Phys. Lett.* **2004**, *394*, 5.

(41) Li, Y.; Li, C.; Yue, W.; Jiang, W.; Kopecek, R.; Qu, J.; Wang, Z. *Org. Lett.* **2010**, *12*, 2374.

(42) Kareev, I. E.; Kuvychko, I. V.; Lebedkin, S. F.; Miller, S. M.; Anderson, O. P.; Seppelt, K.; Strauss, S. H.; Boltalina, O. V. *J. Am. Chem. Soc.* **2005**, *127*, 8362.

(43) Kareev, I. E.; Santiso-Quinones, G.; Kuvychko, I. V.; Ioffe, I. N.; Goldt, I. V.; Lebedkin, S. F.; Seppelt, K.; Strauss, S. H.; Boltalina, O. V. *J. Am. Chem. Soc.* **2005**, *127*, 11497.

(44) Shustova, N. B.; Kuvychko, I. V.; Bolskar, R. D.; Seppelt, K.; Strauss, S. H.; Popov, A. A.; Boltalina, O. V. *J. Am. Chem. Soc.* **2006**, *128*, 15793.

(45) Wang, X. B.; Wang, L. S. *Rev. Sci. Instrum.* **2008**, *79*, 073108/1.
(46) Schaub, T.; Fischer, P.; Meins, T.; Radius, U. *Eur. J. Inorg. Chem* **2011**, *2011*, 3122.
(47) Yoshida, M.; Morinaga, Y.; Ueda, M.; Kamigata, N.; Iyoda, M. *Chem. Lett.* **1992**, 227.
(48) Puplovskis, A.; Kacens, J.; Neilands, O. *Tetrahedron Lett.* **1997**, *38*, 285.
(49) Guarr, T. F.; Meier, M. S.; Vance, V. K.; Clayton, M. *J. Am. Chem. Soc.* **1993**, *115*, 9862.
(50) Boulas, P.; D'Souza, F.; Henderson, C. C.; Cahill, P. A.; Jones, M. T.; Kadish, K. *J. Phys. Chem.* **1993**, *97*, 13435.
(51) Caron, C.; Subramanian, R.; D'Souza, F.; Kim, J.; Kutner, W.; Jones, M. T.; Kadish, K. *J. Am. Chem. Soc* **1993**, *115*, 8505.
(52) Turkmen, G.; Sarica, H.; Erten-Ela, S. *Solid-State Electron.* **2014**, *100*, 61.
(53) Yang, W.-W.; Li, Z.-J.; Gao, X. *J. Org. Chem.* **2011**, *76*, 6067.
(54) Ni, L.; Chang, W.; Hou, H.-L.; Li, Z.-J.; Gao, X. *Org. Biomol. Chem.* **2011**, *9*, 6646.
(55) Larson, B. W.; Whitaker, J. B.; Popov, A. A.; Kopidakis, N.; Rumbles, G.; Boltalina, O. V.; Strauss, S. H. *Chem. Mater.* **2014**, *26*, 2361.
(56) Brabec, C. J.; Cravino, A.; Meissner, D.; Sariciftci, N. S.; Fromherz, T.; Rispens, M. T.; Sanchez, L.; Hummelen, J. C. *Adv. Funct. Mater.* **2001**, *11*, 374.
(57) Sevryugina, Y.; Rogachev, A. Y.; Jackson, E. A.; Scott, L. T.; Petrukhina, M. A. *J. Org. Chem.* **2006**, *71*, 6615.
(58) Scharber, M. C.; Mühlbacher, D.; Koppe, M.; Denk, P.; Waldauf, C.; Heeger, A. J.; Brabec, C. J. *Adv. Funct. Mater.* **2006**, *18*, 789.
(59) Chiechi, R. C.; Havenith, R. W. A.; Hummelen, J. C.; Koster, L. J. A.; Loi, M. A. *Mater. Today* **2013**, *16*, 281.
(60) Brabec, C. J.; Hauch, J. A.; Schilinsky, P.; Waldauf, C. *MRS Bull.* **2005**, *30*, 50.
(61) Brabec, C. J.; Durrant, J. R. *MRS Bull.* **2008**, *33*, 670.
(62) Nyakatura, E. K.; Reimann, O.; Vagt, T.; Salwiczek, M.; Koksch, B. *RSC Adv.* **2013**, *3*, 6319.
(63) Hughes, R. P.; Lindner, D. C.; Liable-Sands, L. M.; Rheingold, A. L. *Organometallics* **2001**, *20*, 363.
(64) Filatov, A. S.; Ferguson, M. V.; Spisak, S. N.; Li, B.; Campana, C. F.; Petrukhina, M. A. *Cryst. Growth Des.* **2014**, *14*, 756.
(65) Sawada, T.; Okeya, Y.; Hashizume, M.; Serizawa, T. *Chem. Commun.* **2013**, *49*, 5088.
(66) Wilson, A. J. *Chem. Soc. Rev.* **2009**, *38*, 3289.
(67) Xiao, W.; Passerone, D.; Ruffieux, P.; Aït-Mansour, K.; Gröning, O.; Tosatti, E.; Siegel, J. S.; Fasel, R. *J. Am. Chem. Soc.* **2008**, *130*, 4767.
(68) Schmidt-Mende, L.; Fechtenkötter, A.; Müllen, K.; Moons, E.; Friend, R. H.; MacKenzie, J. D. *Science* **2001**, *293*, 1119.
(69) Hasegawa, T.; Takeya, J. *Sci. Technol. Adv. Mater.* **2009**, *10*, 024314.
(70) Yu, C.-C.; Jiang, K.-J.; Huang, J.-H.; Zhang, F.; Bao, X.; Wang, F.-W.; Yang, L.-M.; Song, Y. *Org. Electron.* **2013**, *14*, 445.
(71) Serbenta, A.; Pavelyev, V. G.; Hummelen, J. C.; van Loosdrecht, P. H. M.; Pshenichnikov, M. S. *EPJ Web of Conferences* **2013**, *41*, 04012.

(72) Wells, A. F. *Structural inorganic chemistry*; 5th ed. ed.; Clarendon Press Oxford University Press: Oxford: New York, 1984.

(73) Nuzzo, D. D.; Wetzelaer, G.-J. A. H.; Bouwer, R. K. M.; Gevaerts, V. S.; Meskers, S. C. J.; Hummelen, J. C.; Blom, P. W. M.; Janssen, R. A. J. *Adv. Energy Mater.* **2013**, *3*, 85.

(74) Lu, S.; Jin, T.; Yasuda, T.; Islam, A.; Akhtaruzzaman, M.; Han, L.; Alamry, K. A.; Kosa, S. A.; Asiri, A. M.; Yamamoto, Y. *Tetrahedron* **2013**, *69*, 1302.

(75) Matsuo, Y. *Chem. Lett.* **2012**, *41*, 754.

(76) Lenes, M.; Shelton, S. W.; Sieval, A. B.; Kronholm, D. F.; Hummelen, J. C.; Blom, P. W. M. *Adv. Funct. Mater.* **2009**, *19*, 3002.

(77) Zou, Y.; Najari, A.; Berrouard, P.; Beaupré, S.; Aïch, B. R.; Tao, Y.; Leclerc, M. *J. Am. Chem. Soc.* **2010**, *132*, 5330.

(78) Lu, L.; Yu, L. *Adv. Mater.* **2014**, *26*, 4413.

(79) Chambers, R. D.; Korn, S. R.; Sandford, G. *J. Fluorine Chem.* **1994**, *69*, 103.

(80) Keshavzarz-K, M.; Knight, B.; Srdanov, G.; Wudl, F. *J. Am. Chem. Soc.* **1995**, *117*, 11371.

(81) Champeil, E.; Crean, C.; Larraya, C.; Pescitelli, G.; Proni, G.; Ghosez, L. *Tetrahedron* **2008**, *64*, 10319.

(82) Fagan, P. J.; Krusic, P. J.; Evans, D. H.; Lerke, S. A.; Johnston, E. *J. Am. Chem. Soc* **1992**, *114*, 9697.

(83) Roy, S.; Gregg, B. T.; Gribble, G. W.; Le, V.-D.; Roy, S. *Tetrahedron* **2011**, *67*, 2161.

(84) Bailly, F.; Cottet, F.; Schlosser, M. *Synthesis* **2005**, 791.

(85) Blay, G.; Cardona, L.; Fernández, I.; Michelena, R.; Pedro, J. R.; Ramírez, T. *Synlett* **2003**, *15*, 2325.

(86) Breyer, D.; Berger, J.; Braun, T.; Mebs, S. *J. Fluorine Chem.* **2012**, *143*, 263.

(87) Filler, R.; Saha, R. *Future Med. Chem.* **2009**, *1*, 777.

(88) Bonnet-Delpon, D.; Charpentier-Morize, M.; Jacquot, R. *J. Org. Chem.* **1988**, *53*, 759.

(89) Hughes, R. P.; Lindner, D. C. *Organometallics* **1996**, *15*, 5678.

(90) Le, V. P.; Wells, P. R. *Aust. J. Chem.* **1992**, *45*, 1057.

(91) Kuvychko, I. V.; Castro, K. P.; Deng, S. H. M.; Wang, X.-B.; Strauss, S. H.; Boltalina, O. V. *Angew. Chem. Int. Ed.* **2013**, *52*, 4871.

(92) Klebach, T. C.; Turkenburg, L. A. M.; Bickelhaupt, F. *Tetrahedron Lett.* **1978**, *19*, 1099.

(93) Hosokawa, K.; Inukai, K. *Nippon Kagaku Kaishi* **1977**, 1163.

(94) Brown, H. C.; Genwanter, H. L.; White, D. M.; Woods, W. G. *J. Org. Chem.* **1960**, *25*, 634.

(95) Chan, L. C.; Cox, B. G.; Jones, I. C.; Tomasi, S. *J. Phys. Org. Chem.* **2011**, *24*, 751.

(96) Urata, H.; Fuchikami, T. *Tetrahedron Lett.* **1991**, *32*, 91.

(97) Kuvychko, I. V.; Spisak, S. N.; Chen, Y.-S.; Popov, A. A.; Petrukhina, M. A.; Strauss, S. H.; Boltalina, O. V. *Angew. Chem. Int. Ed.* **2012**, *51*, 4939.

(98) Meier, M. S.; Bergosh, R. G.; Gallagher, M. E.; Spielmann, H. P.; Wang, Z. *J. Org. Chem.* **2002**, *67*, 5946.

(99) Sun, H.; Putta, A.; Billion, M. *J. Phys. Chem. A.* **2012**, *116*, 8015.

(100) Hosokawa, K.; Inukai, K. *Nippon Kagaku Kaishi* **1972**, 383.
(101) Hosokawa, K.; Inukai, K. *Nippon Kagaku Kaishi* **1976**, 1791.
(102) Hosokawa, K.; Fujii, S.; Inukai, K. *Nippon Kagaku Kaishi* **1979**, 294.
(103) Hirsch, A. *Fullerenes and Related Structures* **1999**, *199*, 1.
(104) Kitagawa, T.; Takeuchi, K. *Bulletin of the Chemical Society of Japan* **2001**, *74*, 785.
(105) Dawe, L. N.; AlHujran, T. A.; Tran, H.-A.; Mercer, J. I.; Jackson, E. A.; Scott, L. T.; Georghiou, P. E. *Chem. Commun.* **2012**, *48*, 5563.
(106) Haddon, R. C. *Science* **1993**, *261*, 1545.
(107) Seiders, T. J.; Baldridge, K. K.; Grube, G. H.; Siegel, J. S. *J. Am. Chem. Soc.* **2001**, *123*, 517.
(108) Wu, D.; Shao, T.; Men, J.; Chen, X.; Gao, G. *Dalton Trans.* **2014**, *43*, 1753.
(109) Baldridge, K. K.; Hardcastle, K. I.; Seiders, T. J.; Siegel, J. S. *Org. Biomol. Chem* **2010**, *8*, 53.
(110) Dey, J.; Will, A. Y.; Agbaria, R. A.; Rabideau, P. W.; Abdourazak, A. H.; Sygula, R.; Warner, I. M. *J. Fluoresc.* **1997**, *7*, 231.
(111) He, Y.; H.-Y., C.; Hou, J.; Li, Y. *J. Am. Chem. Soc.* **2010**, *132*, 1377.
(112) Troshin, P. A.; Hoppe, H.; Renz, J.; Egginger, M.; Mayorova, J. Y.; Goryachev, A. E.; Peregudov, A. S.; Lyubovskaya, R. N.; Gobsch, G.; Sariciftci, N. S.; Razumov, V. F. *Adv. Funct. Mater.* **2009**, *19*, 779.
(113) Sheppard, W. A. *J. Am. Chem. Soc.* **1962**, *84*, 3072.
(114) Nixon, P. G.; Winter, R.; Castner, D. G.; Holcomb, N. R.; Grainger, D. W.; Gard, G. L. *Chem. Mater.* **2000**, *12*, 3108.
(115) Reyes-Reyes, M.; Kim, K.; Carroll, D. L. *Appl. Phys. Lett.* **2005**, *87*, 083506.
(116) Yang, X.; Uddin, A. *Renew. Sust. Energy Rev.* **2014**, *30*, 324.
(117) Kim, H.; So, W.-W.; Moon, S.-J. *Sol. Energy Mater. Sol. Cells* **2007**, *91*, 581.
(118) Shriver, D. F.; Drezdzon, M. A. *The Manipulation of Air-Sensitive Compounds, 2nd Ed.*; Wiley-Interscience: New York, 1986.
(119) Lyapustina, S. A.; Xu, S.; Nilles, J. M.; Bowen Jr., K. H. *J. Chem. Phys.* **2000**, *112*, 6643.
(120) Schiedt, J.; Knott, W. J.; Le Barbu, K.; Schlag, E. W. *J. Chem. Phys.* **2000**, *113*, 9470.
(121) Sheldrick, G. M. *Acta Cryst.* **2008**, *A64*, 112.
(122) Chen, G.; Cooks, R. G.; Corpuz, E.; Scott, L. T. *J. Am. Soc. Mass Spectrom.* **1996**, *7*, 619.
(123) Valenti, G.; Bruno, C.; Rapino, S.; Fiorani, A.; Jackson, E. A.; Scott, L. T.; Paolucci, F.; Marcaccio, M. *J. Phys. Chem. C* **2010**, *114*, 19467.
(124) Laikov, D. N. *Chem. Phys. Lett.* **1997**, *281*, 151.
(125) Laikov, D. N.; Ustynuk, Y. A. *Russ. Chem. Bull.* **2005**, *54*, 820.
(126) Parisi, M. T. *Pediatr. Radiol.* **2011**, *41*, 803.
(127) Le Bars, D. *J. Fluorine Chem.* **2006**, *127*, 1488.
(128) Kirk, K. L. *J. Fluorine Chem.* **2006**, *127*, 1013.
(129) Cataldo, F.; Iglesias-Groth, S.; Manchado, A. *Fullerenes, Nanotubes, Carbon Nanostruct.* **2009**, *17*, 428.
(130) Withers, J. C.; Loutfy, R. O.; Lowe, T. P. *Fullerene Sci. Technol.* **2007**, *5*, 1.
(131) McKillop, A.; Madjdabadi, F. A.; Long, D. A. *Tetrahedron Lett.* **1983**, *24*, 1933.

(132) Cossi, M.; Rega, N.; Scalmani, G.; Barone, V. *J. Comp. Chem.* **2003**, *24*, 669.
(133) Paternò, G.; Warren, A. J.; Spencer, J.; Evans, G.; Sakai, V. G.; Blumberger, J.; Cacialli, F. *J. Mater. Chem. C* **2013**, *1*, 5619.

Chapter 2.

Designing Polycyclic Aromatic Hydrocarbons with Fluorinated Electron Withdrawing Moieties

Section 2.2 describes the study of polyperfluoroalkylation of naphthalene (NAPH) that was published in *Chem. Eur. J.* 2014, DOI: 10.1002/chem.201304554. The research involved a high-temperature gas-phase, solvent- and catalyst-free reaction of NAPH with an excess of R_FI reagent (R_F = CF_3, C_2F_5, *n*-C_3F_7, and *n*-C_4F_9) that was performed for the first time. It produced a series of highly perfluoroalkylated NAPH products NAPH$(R_F)_n$ with n = 2 – 5. These new compounds were fully characterized by ^{19}F and ^{1}H NMR spectroscopy, X-ray crystallography (for R_F = CF_3 and C_2F_5), atmospheric-pressure chemical ionization mass spectrometry, and cyclic and square-wave voltammetry. DFT calculations confirmed that the employed synthesis yielded the most stable isomers that have not been accessed by alternative preparation techniques. The author of this dissertation performed all of the synthetic reactions, chromatography, spectroscopy, mass spectrometry, cyclic voltammetry, and grew single crystals suitable for X-ray diffraction studies. Eric V. Bukovsky and Dr. Igor V. Kuvychko solved the X-ray structures and analyzed the solid-state packing. Dr. Alexey A. Popov performed the DFT calculations. Unpublished low temperature photoelectron spectroscopy measurements were performed by Dr. Xue-bin Wang.

Section 2.3 describes the perfluorobenzylation of corannulene (CORA). The work was submitted and accepted for publication in *Chem. Eur. J.*, DOI: 10.1002/chem.201500465. This section reports on two members of a new class of organic-acceptor perfluorobenzyl CORAs

prepared via gas-phase and highly-selective solution-phase reactions at elevated temperatures. The peculiar single-crystal X-ray structure of C_5-$C_{20}H_5(CF_2C_6F_5)_5$ revealed two high-energy conformers with drastically different bowl depths and orientations of perfluorobenzyl blades. The author of this dissertation performed all of the synthetic reactions, chromatography, spectroscopy, mass spectrometry, cyclic voltammetry (preliminary results were obtained by Dr. Igor V. Kuvychko), and grew single crystals suitable for X-ray diffraction studies. Tyler T. Clikeman performed the X-ray crystallography structural analysis from the data collected by Dr. Yu-Sheng Chen. Cristina Dubceac and Prof. Marina A. Petrukhina provided the CORA samples. Dr. Alexey A. Popov performed the DFT calculations.

Section 2.4 describes the perfluorobenzylation of anthracene (ANTH). It reports on the new compound 9,10-ANTH$(Bn_F)_2$, among other ANTH$(Bn_F)_n$ derivatives, which were prepared in solution at elevated temperatures. 9,10-ANTH$(Bn_F)_2$ exhibited deep blue fluorescence and greater air and photo stability than the parent ANTH molecule. The fluorescence quantum yield was measured and was also shown to be one of the highest among the reported fluorinated ANTH derivatives. The solid-state packing shows no π-π interactions between ANTH cores. The author of this dissertation performed all of the synthetic reactions, chromatography, spectroscopy, quantum yield measurements, and photostability experiments. Tyler T. Clikeman performed the X-ray crystallography structural analysis with collaborator Dr. Yu-Sheng Chen.

Project supervision by Prof. Steven H. Strauss and Dr. Olga V. Boltalina.

2.1. Introduction

Carbon-rich chemistry has evolved dramatically over the past 50 years. From larger compounds such as fullerenes[1] (a carbon allotrope which contains fused hexagons and pentagons) and endometallofullerenes[2] (a fullerene with an encapsulated metal) to small

molecules such as polycyclic aromatic hydrocarbons (PAHs),[3] research efforts to functionalize these compounds have afforded numerous new compounds for various applications. Organic semiconductors have potential applications in various organic electronics such as organic photovoltaics (OPVs),[4-6] organic light emitting diodes (OLEDs),[7,8] and organic field-effect transistors (OFETs).[9] Although current organic electronics may be inferior in efficiency to its inorganic counterparts, the reduced cost of production,[10] its roll-to-roll industrial solution process ability,[11] and its scalability outweigh this disadvantage making its commercialization viable today.

Functionalized PAHs are emerging as alternative substrates towards efficient organic semiconductors for use in organic electronics.[12-14] High charge carrier mobility *p*-type semiconductors, such as rubrene, have been well established and studied.[15] The need for *n*-type semiconductors with high charge carrier mobility is also crucial for the charge separation and collection in these devices. PAHs can delocalize electrons in their conjugated pi-systems making them useful electron acceptors. One methodology for making better *n*-type semiconductors is by the introduction of electron withdrawing groups.

In fact, it has been shown that the introduction of electron withdrawing groups to PAHs 1) makes them stronger electron acceptors by increasing the electron affinity and 2) the increase in electron affinity improves the stability against O_2 and H_2O. Compounds with electron affinities above 2.8 eV are predicted to make air-stable compounds in organic field effect transistors.[9] The trifluoromethyl[16,17] and perfluoroalkyl[18,19] functionalization of PAHs have been widely explored and been shown as an excellent method for tuning the electronic properties and improving stability towards heat, air, and moisture. The first section of this chapter deals with the results of (poly)perfluoroalkylation of naphthalene (NAPH), the simplest PAH, using original synthetic

techniques developed in this work. Furthermore, sections 2.2 and 2.3 describe the derivatization of PAHs with perfluorobenzyl (Bn_F, $CF_2C_6F_5$) electron withdrawing groups that have never been investigated in reactions with PAHs. To explore the perfluorobenzyl properties, reactions with corannulene (CORA) and anthracene (ANTH) were investigated in this work.

2.2. Polyperfluoroalkylation of naphthalene (NAPH).

Fluorine or perfluoroalkyl substituents strongly augment physicochemical and biological properties of organic molecular substrates. Organofluorine compounds have been designed for medicinal applications[20-22] such as drug discovery[23,24] and diagnostic imaging.[25,26] One example of the importance of perfluoroalkyl modification to drug discovery is the CF_3-bearing fluoxetine, ((*RS*)-*N*-methyl-3-phenyl-3-[4-(trifluoromethyl)-phenoxy]propan-1-amine) known as Prozac, one of the most common antidepressants.[27] Another recently emerged field for applications of organofluorine compounds is molecular electronics.

Several methodologies for introducing CF_3 groups into aromatics and heterocyclics have been described in the literature.[28,29] These reactions typically result in one or, more rarely, two CF_3 substituents attached to the aromatic substrate. A known exception is hexakis(trifluoromethyl)benzene prepared via a cyclization of three bis(trifluoromethyl)acetylene molecules[30,31] or a reaction of hexaiodobenzene with trifluoromethylcopper.[32] For naphthalene (NAPH), several mono- and bis- substituted CF_3 derivatives have been reported[33-39] while only one highly substituted derivative (2,3,6,7-tetrakis-(trifluoromethyl)naphthalene) has been reported.[40] Syntheses of mono- and bis-(trifluoromethyl)naphthalenes have been typically accomplished via multi-step reactions: i) assembly of the NAPH core from CF_3-bearing organic precursor molecules (using Friedel-Crafts intramolecular cyclization[41,42] or Diels-Alder cyclization with CF_3-carrying benzyne intermediate[34]); ii) fluorination of NAPH derivatives

bearing suitable CF_3-precursor groups (fluorination of naphthoic acids by SF_4[43] or fluorination of (naphthalene) methyldithiocarboxylates by $H_2F_3^-$ fluorine source and 1,3-dibromo-5,5-dimethylhydantoin (DBDMH) oxidizer[43]); and iii) direct substitution of iodine in various iodonaphthalenes with CF_3 group(s) using (trifluoromethyl)copper generated in situ.[44,45]

To circumvent the laborious and multi-step synthetic procedures, a simple and highly efficient alternative approach was proposed in this work: substitution of multiple aromatic hydrogen atoms in naphthalene with R_F• radicals generated by thermolysis of R_FI precursors (R_F = CF_3, C_2F_5, *n*-C_3F_7, and *n*-C_4F_9) in the gas-phase.[17,46,47] For the first time, a systematic study of the electronic effects of perfluoroalkyl groups on the NAPH core were ascertained using experimental and theoretical methods. Additionally, molecular structures and physical properties of NAPH$(R_F)_n$ were determined.

2.2.1. Synthesis and non-chromatographic separation of NAPH$(R_F)_n$. The perfluoroalkylation reactions were accomplished by reacting eight equivalents of R_FI (R_F = CF_3, C_2F_5, *n*-C_3F_7, and *n*-C_4F_9) with one equivalent of NAPH at 300 °C for 3 hours in sealed Pyrex glass ampoules as shown in Scheme 2.2.1. Complete vaporization of NAPH was observed at *ca*. 150 °C *before* any visible formation of iodine due to R_FI dissociation; therefore, perfluoroalkylation took place fully in the gas phase (possible effects of ampoule walls are unlikely but cannot be ruled out).

After the removal of iodine (with an aqueous $Na_2S_2O_3$ wash), the crude off-white solid products were weighed, dissolved in 3.0 mL of 5.3 mM solution of (*n*-Bu)$_4$NBF$_4$ in $CDCl_3$, and analyzed by quantitative ^{1}H and ^{19}F NMR spectroscopy. Due to the presence of (*n*-Bu)$_4$NBF$_4$ internal standard, the relative molar concentrations of aromatic H atoms and R_F groups could be determined via integration of the NMR spectra. This information was used to determine the average number of R_F groups per NAPH core, which was used to calculate the total molar yield

of crude products, see Table 2.2.1. No unreacted NAPH was detected in any of the four crude products by ^{1}H NMR spectroscopy, which demonstrates the completeness of the NAPH conversion (Figure 2.2.1).

2.2.2. Characterization of NAPH(R_F)$_n$ compounds.

Mass spectrometry. Negative ion atmospheric pressure chemical ionization (NI-APCI) mass spectrometry has been applied to determine the maximal substitution degree in samples A–D (Table 2.2.1). Earlier, NI-APCI mass spectrometry was found to be highly effective for the direct analysis of perfluoroalkylation products of larger PAHs,[17,29,46] but the analogous mass spectrometry analysis of products A–D (Table 2.2.1) required use of a reducing agent (tetrakis(dimethylamino)ethylene (TDAE) to generate NAPH$(R_F)_n^-$ anions. Treatment with TDAE, which has an ultra-low ionization potential of 5.3 eV,[32] led to the color change from a very pale-yellow color to a pale-green color (for $R_F = CF_3$) or to a dark-yellow color (for $R_F = C_2F_5$, *n*-C_3F_7, and *n*-C_4F_9) color suggesting the formation of NAPH$(R_F)_n^-$• radical anions.[17] Indeed, these chemically reduced NAPH$(R_F)_n$ samples produced mass spectra shown on Figure 2.2.2, in which the maximum number of R_F substituents was five for $R_F = CF_3$ and four for $R_F = C_2F_5$, *n*-C_3F_7, and *n*-C_4F_9. Lower mass peaks due to loss of HF have been observed more prominently for $R_F = C_2F_5$. Their fragmentation origin was established upon analysis of the purified compounds (see Figure 2.2.3). The lower degree of perfluoroalkylation observed for the longer-chain R_F groups is consistent with their larger steric requirements in comparison to CF_3 groups.

Physical properties. Perfluoroalkylation resulted in significant changes in physical properties compared to the parent NAPH compound. For example, solubility of tetra-substituted derivatives NAPH$(R_F)_4$ in polar solvents was strongly reduced compared to bis- and tris- derivatives. The

findings allowed the development of a simple and efficient method of isolation of 95+%-pure NAPH(R_F)$_4$ compounds from the crude materials using fast and simple precipitation/wash protocols with *ca*. 5–10 mol% yield (calculated relative to the starting naphthalene). The compositional purity was confirmed by NI-APCI mass spectrometry: as mentioned above, isolated low-solubility samples readily formed molecular anions NAPH(R_F)$_4^-$ when chemically reduced by TDAE in solution, see Figure 2.2.3. Notably, partial fragmentation due to loss of one and two HF molecules was observed for NAPH(C_2F_5)$_4$, NAPH(*n*-C_3F_7)$_4$, and for NAPH(*n*-C_4F_9)$_4$. Proton and ^{19}F NMR spectroscopy revealed the isomeric purity of the isolated compounds, which possess the idealized C_{2h} symmetry; thus, allowing for unambiguous structural assignment for the 1,3,5,7-pattern of R_F groups for all four isolated compounds, see Figure 2.2.4 through Figure 2.2.8 for NMR data, and Figure 2.2.9 for NAPH core numbering scheme.

Preliminary studies of the remaining soluble fractions after the extraction of NAPH(R_F)$_4$ compounds were carried out, which determined the presence of several isomers of NAPH(R_F)$_n$ where n = 2,3, in agreement with the NMR data on the average molecular compositions (see Table 2.2.1). While the use of the HPLC method[17] for separation of NAPH(CF_3)$_{2,3}$ and NAPH(*n*-C_3F_7)$_{2,3}$ has not yet been successful, one isomer of NAPH(C_2F_5)$_2$ and one isomer of NAPH(C_2F_5)$_3$ were isolated with high purity, and tentative structural assignments were proposed for them and for the second identified abundant isomer of NAPH(C_2F_5)$_3$ based on NMR (Figure 2.2.10 and Figure 2.2.11) and DFT data (Tables 2.2.1 and 2.2.2).

The melting points and the sublimation rates of NAPH, 1,3,5,7-NAPH(CF_3)$_4$, and 1,3,5,7-NAPH(C_2F_5)$_4$ were measured, see Table 2.2.5. The highest melting point was observed for 1,3,5,7-NAPH(CF_3)$_4$, followed by 1,3,5,7-NAPH(C_2F_5)$_4$, and then NAPH. The sublimation rates

were measured in the TGA instrument at 25.0 °C under the constant stream of nitrogen, and were found to decrease from NAPH to 1,3,5,7-NAPH$(CF_3)_4$ to 1,3,5,7-NAPH$(C_2F_5)_4$, in accord with their molecular weights. High volatility of pentafluoroethyl naphthalene derivatives contributed to the lower isolated yields.[48]

HPLC Chromatography. The HPLC analysis of NAPH$(R_F)_n$ compounds provide a unique insight in the types of molecular interactions with the stationary phase. In this case, the stationary phase of the FluoroFlash column contains a modified silica backbone with perfluorooctyl chains. Compounds bearing a larger number of fluorine atoms were observed to have a higher affinity for the C_8F_{17}-functionalized stationary phase (due to their high "fluorophilicity") and therefore displayed longer retention times. When using 100% MeCN as the mobile phase, the crude product mixture of NAPH$(R_F)_n$ have progressively longer retention times with increasing R_F chain length (Figure 2.2.12). The addition of 10% water to the mobile phase not only provides better separation of compounds, but significantly increases the retention times as seen in Figure 2.2.13. For example, the retention time of NAPH$(n\text{-}C_3F_7)_4$ is ca. 70 minutes (Figure 2.2.12) in 100% MeCN, but was nowhere to be found beyond 70 minutes (Figure 2.2.13) in 90/10 (v/v) MeCN/H_2O, which makes HPLC separation inefficient. (See Figure 2.2.14 for the HPLC chromatogram of the crude product mixture of NAPH$(C_2F_5)_n$.) Hence, the non-chromatographic separation method was used to separate and purify the main four 1,3,5,7-NAPH$(R_F)_4$ compounds.

Cyclic voltammetry. Electrochemical properties of 1,3,5,7-NAPH$(R_F)_4$ (R_F = CF_3, C_2F_5, n-C_3F_7, and n-C_4F_9) were studied by cyclic voltammetry and square-wave voltammetry in 0.1 M solution of $(n\text{-}Bu)_4NClO_4$ in dry deoxygenated dimethoxyethane under an inert atmosphere, see Figure 2.2.15. The compounds displayed a quasi-reversible first reduction except for 1,3,5,7-NAPH(n-

$C_4F_9)_4$ which was difficult to assess due to its lower solubility in dimethoxyethane. The first reduction potentials of 1,3,5,7-NAPH$(R_F)_4$ were anodically shifted by 1.46, 1.45, 1.53, and 1.52 V from NAPH for R_F = CF_3, C_2F_5, *n*-C_3F_7, and *n*-C_4F_9, respectively. It should be noted that the electron-withdrawing effects of different R_F groups cannot be compared directly using only the data on the first reduction potentials due to differences in the solvation energies. For example, our earlier study of 1,7-$C_{60}(R_F)_2$ compounds showed how solvation energy differences can compensate the higher electron affinity of the molecules bearing longer R_F groups, leading to equalization of the observed solution-phase first reduction potentials across the series of different R_F substituents.[49] It is notable that earlier studies of R_F-substituted perylene diimides[50] and R_F-substituted nitrobenzenes[51] showed negligible differences in the first reduction potentials between molecules bearing different R_F groups, which may also be due to the similar "equalizing" effect of solvation energy.

The overall shift in $E_{1/2}$ of 1,3,5,7-NAPH$(R_F)_4$ relative to NAPH (*ca*. 1.5 V) is surprisingly large, especially when compared to the 0.95 V shift of $E_{1/2}$ observed for the penta(trifluoromethyl)corannulene C_5-$C_{20}H_5(CF_3)_5$, relative to corannulene, or 0.2 V shift in tetrakis(trifluoromethyl)fullerene $C_{60}(CF_3)_4$,[49,52] relative to C_{60}. This suggests that the electron-withdrawing effect of the R_F groups may vary greatly for organic substrates of different sizes and structures.[17] Earlier DFT calculations performed on the series of fluorinated and trifluoromethylated acenes agree with these findings: the largest incremental shift in reduction potential and electron affinity was found for benzene, followed by naphthalene, and then larger acenes.[16,46,53]

The observed large enhancement in electron accepting properties of NAPH$(R_F)_n$ in solution helps explain the fact that peaks due to NAPH$(R_F)_{2,3}$ were not observed mass spectrometrically

in samples A–D (Figure 2.2.2), despite the "fluorophilicity"[54,55] based HPLC analysis (Figure 2.2.13) and NMR evidence (Table 2.2.1) that they represent the bulk of the crude products. This is likely due to i) their low electron affinity (*EA*) (or reduction potentials in solution) and ii) presence of the species with significantly higher *EA*s in these crude samples (i.e., NAPH$(R_F)_4$). A strong correlation between the *EA* of an analyte and its ionization efficiency under NI-APCI conditions as well as the suppression of the signals from less electronegative molecules is well documented in the literature.[56-58] The results of earlier theoretical and experimental data showed that EAs of poly(trifluoromethyl)PAHs increase roughly proportionately to the number of CF_3 substituents.[16,17,46] Using the calculated *EA* values of NAPH (−0.511 eV) and hypothetical NAPH$(CF_3)_8$ (3.262 eV),[16] the mean *EA* increase of 0.47 eV/*n*(CF_3) in NAPH$(CF_3)_n$ can be calculated. Therefore the estimated *EA*(NAPH$(R_F)_n$) values for *n* = 2 (0.432 eV) and *n* = 3 (0.904 eV) are apparently too low for these species to be observed in NI-APCI mass spectrometry, even with TDAE-assisted chemical reduction. At the same time, the peak due to NAPH$(CF_3)_5^-$ (with the estimated *EA*(NAPH$(CF_3)_5$) of *ca*. 1.84 eV) is likely to be overrepresented in the mass spectrum compared to its real content in the crude mixture (Figure 2.2.2, top left).

As mentioned above, literature experimental data on the synthesis of polysubstituted perfluoroalkylnaphthalenes are very scarce, even less is known about their electronic properties. A thorough literature search resulted in only one relevant publication, which, as we found, has never been cited outside Russian-language journals. Thirty years ago, Yagupolsky and coworkers showed that consecutive two, three, or four hydrogen substitutions (into 1, 4, 5 and/or 8 positions) with R_F = CF_3 and/or –O-CF_2 groups in naphthalene lead to positive shifts in reduction potentials of 0.77, 1.16, and 1.44 V vs. naphthalene, respectively.[47] This leads to an

incremental shift of $E_{1/2}/n(R_F') = 0.36$ V for 1,4,5,8-NAPH$(R_F')_n$, whereas a larger increment $E_{1/2}/n(R_F) = 0.37 – 0.38$ V was determined in our study for 1,3,5,7-NAPH$(R_F)_4$ isomers.

Low-temperature photoelectron spectroscopy. The experimental gas phase electron affinity values of 1,3,5,7-NAPH$(R_F)_4$ (R_F = CF_3, C_2F_5, *n*-C_3F_7, and *n*-C_4F_9) were measured by low temperature photoelectron spectroscopy (LT-PES)[59] in collaboration with Dr. Xue-bin Wang from Pacific Northwest National Laboratory. Similarly to the LT-PES experiments described in Chapter 1, molecular anions were generated by electrospraying a solution containing NAPH$(R_F)_4$ compound after a dilute acetonitrile solution of TDAE has been added dropwise until a color change. The anions were then guided by quadrupole ion guides into a cryogenic ion trap, and then transferred into a time-of-flight mass spectrometer. Mass selected anions of NAPH$(R_F)_4$ were intersected by a Nd:YAG laser in the photodetachment zone of the magnetic bottle photoelectron analyzer. The gas phase electron affinity of NAPH$(R_F)_4$ was determined from the 0–0 transition in the 12 K LT-PES spectrum. Table 2.2.5 shows the DFT predicted and experimental gas phase electron affinities for NAPH$(R_F)_4$ compounds. The electron affinity changes by 0.32 eV from 1.795 eV for NAPH$(CF_3)_4$ to 2.115 eV for NAPH$(C_4F_9)_4$ due to the different electron-withdrawing abilities of the perfluoroalkyl functional groups. These results demonstrated that the size of the R_F groups has a profound effect on electron affinity values of NAPH$(R_F)_n$. In contrast, this effect in $C_{60}(R_F)_2$ was found to be much smaller.[49]

2.2.3. DFT calculations of relative energies for NAPH$(CF_3)_n$ isomers. To determine possible substitution patterns of R_F groups for NAPH, we have performed DFT computations for all isomers of NAPH$(CF_3)_n$ (n = 1-4) at the DFT level of theory. Complete list of isomers and their relative energies are available in Table 2.2.1, but here, we will briefly summarize the main trends. Unsubstituted NAPH has two types of C(H) atoms, C1 and symmetry related C4, C5, and

C8 (we will designate them as *a*-type position) and position C2 and related C3, C6, and C7 (denoted as *b*) as shown on Figure 2.2.9. An increase of the number of attached CF_3 groups results in the rich variety of their relative positions and hence possible isomers.

From ten possible isomers of NAPH$(CF_3)_2$, the most stable ones are those which combine two CF_3 groups in distant *b*-type positions (isomers 2,6 and 2,7 are isoenergetic within 0.3 kJ/mol). They are followed by three isomers combining *a* and *b*-type groups (1,3, 1,6, and 1,7 with relative energies of 8, 6 and 7 kJ/mol, respectively) and then by two isomers with only *a*-type distant positions (1,4 and 1, 5 with ΔE of 16 and 13 kJ/mol). It can be seen that when CF_3 groups are at distant positions (i.e., do not interact), relative energies can be roughly rationalized as a number of groups in position *a* times an increment of *ca*. 7 kJ/mol. However, when two CF_3 groups are close enough to interact, such interaction significantly destabilized the structures. The isomer 2,3 with two neighboring CF_3 groups in adjacent *b*-type positions has an energy of 25 kJ/mol, two CF_3 groups in adjacent *a* and *b* positions 50 kJ/mol, whereas the least stable isomer has two CF_3 groups in close *a*-type position (1,8). In the latter, naphthalene framework is non-planar to avoid close $CF_3 \cdots CF_3$ contacts.

Three CF_3 groups can be arranged in NAPH$(CF_3)_3$ in 13 different ways, and the relative energies of these isomer span the range of 106 kJ/mol. Since it is impossible to arrange all three groups in *b*-type position and avoid close $CF_3 \cdots CF_3$ contacts, the lowest energy isomers are those combining one *a*-type and two *b*-type groups (1,3,6 and 1,3,7). These isomers are followed by two isomers with two *a*-sites and one *b*-site (1,3,5 and 1,4,6; ΔE = 8 kJ/mol for both isomers). All other isomers have at least one pair of neighboring CF_3 groups and are less stable. From them, the most stable is isomer 2,3,6 with relative energy of 18 kJ/mol followed by the isomer

1,2,6 whose relative energy is already 42 kJ/mol. The least stable isomers have three groups in neighboring positions (1,2,3 and 1,2,8).

The largest number of isomers in the whole NAPH$(CF_3)_n$ series, 21, is possible for n = 4. However, four CF_3 groups are already too crowded, and 1,3,5,7-NAPH$(CF_3)_4$ is the only isomer without adjacent CF_3 groups. The second most stable isomer with ΔE of 16 kJ/mol has CF_3 groups in 1,3,6,7 position, whereas the earlier reported 2,3,6,7-NAPH$(CF_3)_4$ is the third most stable isomer with the relative energy of 33 kJ/mol. The energies of other isomers span the range of 41–142 kJ/mol. It is clear that the 2,3,6,7-isomer was a kinetic product whose structure was directed by the synthetic pathway.[40] Contrariwise, the high temperature synthetic method used in this work tends to give thermodynamic products.

2.2.4. X-ray crystallography of NAPH$(CF_3)_4$ and NAPH$(C_2F_5)_4$. The structures of 1,3,5,7-NAPH$(CF_3)_4$ (Figure 2.2.16) and 1,3,5,7-NAPH$(C_2F_5)_4$ (Figure 2.2.17) were unambiguously confirmed by the single-crystal X-ray diffraction study. The molecular structure of 1,3,5,7-NAPH$(CF_3)_4$ is more planar and less distorted than expected, and with an interesting packing motif. The distances between the closest overlapping parallel planes of the naphthalene cores of 1,3,5,7-NAPH$(CF_3)_4$ are decreased to 3.75 Å or 4.23 Å from 6.77 Å in the parent naphthalene.[60] The addition of the CF_3 groups increases the intermolecular interactions through a F–H close contact of 2.631 Å and a F-to-naphthalene centroid distance of 3.089 Å which pulls the molecules within a layer of parallel oriented naphthalene molecules closer together.

The overall packing structure of the CF_3 groups in one layer of molecules point towards each other creating a channel between layers of 1,3,5,7-NAPH$(CF_3)_4$, the rings between layers are rotated 83.6° (increased from 50.7° in naphthalene) from planes of adjacent layers, but the naphthalene cores are rigorously parallel within their respective layers. When rotated 90° about

the central horizontal, it exhibits the common herringbone pattern. The addition of the CF_3 groups to naphthalene increases intermolecular interactions between CF_3 groups and naphthalene cores. The increase in R_F moiety length to the NAPH$(C_2F_5)_4$ compound creates packing with distinct naphthalene regions and perfluoroethyl regions (see Figure 2.2.17). The closest distance between overlapping parallel planes of NAPH$(C_2F_5)_4$ is 10.575 Å. There are three different orientations of the naphthalene cores in NAPH$(C_2F_5)_4$, and it is evident that the structure is dominated by the ridged C_2F_5 moiety rather than by any other interactions. See Table 2.2.8 for additional X-ray diffraction data.

2.2.5. Summary and conclusions. To conclude, an efficient synthetic approach for the preparation of highly perfluoroalkylated naphthalenes that possess pronounced electron acceptor properties compared to underivatized naphthalene (which has a negative EA of −0.5 eV) is developed. A non-chromatographic isolation of the new four symmetric tetrakis- derivatives provides easy access to these new molecules for further studies. Additionally, applicability of the HPLC method developed earlier by us for separation of perfluoroalkyfullerenes was demonstrated for the isolation of high-purity single isomers of NAPH$(C_2F_5)_{2,3}$. This "tour-de force" approach to perfluoroalkylation of naphthalene organically complements existing elaborate and elegant solution chemistry, which is mostly focused on (and capable of) regioselective preparations of mono- and/or di- substituted perfluoroalkyl derivatives.

2.2.6. Experimental.

Methods, reagents and solvents. Naphthalene (Sigma Aldrich, 99%), iodotrifluoromethane, iodopentafluoroethane, 1-iodoheptafluoropropane, 1-iodononafluorobutane (SynQuest Labs), sodium thiosulfate ($Na_2S_2O_3$, Fisher Scientific, ACS grade), tetrakis(dimethylamino)ethylene (TDAE, Sigma-Aldrich), chloroform-d ($CDCl_3$, Cambridge Isotopes), 1,4-bis-

(trifluoromethyl)benzene (Sigma Aldrich), tetrabutylammonium tetrafluoroborate ($(n\text{-Bu})_4NBF_4$, Sigma-Aldrich), dichloromethane (Fisher Scientific, ACS grade), carbon disulfide (Alfa Aesar, HPLC grade), acetonitrile (Fisher Scientific, ACS grade), acetone (technical grade) were used as received. Deionized distilled water was purified by a Barnstead NANOpure Ultrapure Water system (final resistance 18 MΩ). Dimethoxyethane (Sigma-Aldrich, distilled from CaH_2 under nitrogen atmosphere), ferrocene (Acros Organics, 98%), and tetrabutylammonium perchlorate (Sigma-Aldrich, dried at 80 °C under dynamic vacuum for 24 h) were used for electrochemical measurements.

Instrumentation. HPLC analysis and separation were carried on a Shimadzu instrument (composed of Shimadzu LC-6AD pump, a Shimadzu UV detector SPD-20A set for 300 nm detection wavelength and a communication bus module Shimadzu CBM-20A). The instrument was equipped with a FluoroFlash column (Fluorous Technologies, Inc., PF-C8, 5 μm); 90/10 v/v mixture of acetonitrile/water was used as the eluent at a flow rate of 2 $mL \cdot min^{-1}$. Proton (400 MHz) and ^{19}F (376 MHz) NMR spectra were recorded on a Varian INOVA instrument in $CDCl_3$ solution using 1,4-bis-(trifluoromethyl)benzene ($\delta(^{19}F) = -66.35$; $\delta(^{1}H) = 7.77$) as the internal standard. Negative-mode atmospheric pressure chemical ionization mass spectrometry analysis was performed on a 2000 Finnigan LCQ-DUO mass-spectrometer using CH_3CN carrier solvent at 0.3 $mL \cdot min^{-1}$ flow rate. The samples were dissolved in dry deoxygenated acetonitrile in a nitrogen-atmosphere glovebox and treated with a small amount (1-2 drops) of tetrakis(dimethylamino)ethylene solution in acetonitrile in order to generate negative ions (a few drops of TDAE solution were added to the samples which changed color from colorless to pale-yellow). Cyclic voltammetry measurements were carried out on a PAR 263 potentiostat/galvanostat using an electrochemical cell equipped with platinum counter and

working electrodes (0.125 mm diameter) and a silver reference electrode (0.5 mm diameter). The samples were dissolved in a 0.1 M $TBAClO_4$ solution in dimethoxyethane; the cyclic voltammetry was performed at 500 $mV \cdot s^{-1}$ scan rate, unless otherwise indicated, and referenced versus ferrocene internal standard. Melting points were determined using a Laboratory Devices Mel-Temp instrument with a mercury thermometer (−10 °C – 260 °C ± 0.1 °C) and a heating rate of *ca*. 1 – 2 °C/min; all samples were sealed in 1.0 × 90 mm melt point capillary tubes. Sublimation rate studies were performed using TA Instruments Series-2950 instrumentation. Prior to each TGA experiment, the platinum pan was rinsed with ethyl alcohol and flamed three times (until dull red glow). Upon sample loading, care was taken to distribute the sample evenly over the aluminum pan surface. During the sublimation rate experiments, TGA temperatures were set at 25.00 °C and held isothermally throughout the experiment. The X-ray crystallography data were collected using a Bruker Kappa APEX II CCD diffractometer employing Mo Kα radiation and a graphite monochromator. Unit cell parameters were obtained from least-squares fits to the angular coordinates of all reflections, and intensities were integrated from a series of frames (ω and ϕ rotation) covering more than a hemisphere of reciprocal space. Absorption and other corrections were applied using SCALE (G.M. Sheldrick, SADABS, v. 2.10 - a program for area detector absorption corrections, Bruker AXS, Madison, WI, 2003). The structures were solved using direct methods and refined (on F^2, using all data) by a full-matrix, weighted least-squares process. Standard Bruker control and integration software (APEX II) was employed (G.M. Sheldrick, Crystallography Program APEX2, v. 2.0-2, Bruker AXS, Madison,WI, 2006), and Bruker SHELXTL software was used for structure solution, refinement, and molecular graphics (G.M. Sheldrick, Crystallography Software Package SHELXTL, v. 6.12 UNIX, Bruker AXS, Madison, WI, 2001.).

NMR determination of mol% yield of NAPH(R_F)$_n$ and the average number of R_F groups per naphthalene core (n(R_F)). The ampoules containing products A–D were cooled in acetone/dry ice bath, cut open under air, and quickly evacuated to remove the highly volatile R_FI, R_FH, and $(R_F)_2$ components. Then the ampoules were allowed to warm up, the crude products were dissolved in 3–5 mL of $CDCl_3$, and the resulting solutions were washed with aqueous a 1M $Na_2S_2O_3$ solution to remove I_2 (only trace amounts of insoluble black carbonaceous materials were present in each product). The organic layer (bottom layer) was extracted and the solvent was quickly evaporated under a stream of dry air. Despite the great care taken to limit the losses of the NAPH$(R_F)_n$ products due to evaporation at this step, it is virtually certain that some losses were incurred. The resulting dry products were dissolved in 3.0 mL of 5.3 mM solution of (*n*-Bu)$_4$NBF$_4$ in $CDCl_3$. 750 µL aliquots of these solutions were analyzed by ^{1}H and ^{19}F NMR spectroscopy using the following acquisition parameters:

^{19}F NMR: 25 s relaxation delay, 45° flip angle, acquisition time = 2.000 s, 32 scans

^{1}H NMR: 25 s relaxation delay, 45° flip angle, acquisition time = 2.556 s, 32 scans

Using the integrated intensity of ^{1}H and ^{19}F NMR peaks due to (*n*-Bu)$_4$NBF$_4$ standard and NAPH$(R_F)_n$ products, the molar concentration of aromatic protons and the molar concentration of R_F groups of NAPH$(R_F)_n$ were calculated. The total number of R_F groups and aromatic protons in any NAPH$(R_F)_n$ product is equal to eight; therefore, the combined molar concentration of all NAPH$(R_F)_n$ products is equal to the sum of the molar concentration of aromatic protons and the molar concentration of R_F groups divided by eight, which allows to calculate the total number of moles of NAPH$(R_F)_n$ products. It is notable that no traces of unreacted naphthalene were observed in the products A–D by ^{1}H NMR spectroscopy (see Figure 2.2.1).

Isolation of NAPH(R_F)$_4$ products. Separate batches of crude materials prepared under conditions A–D (see Table 2.2.6) were used to isolate isomerically pure NAPH(R_F)$_4$ materials. In all cases the ampoules were open under air, the products were dissolved in 3–5 mL of dichloromethane, and the resulting solutions were washed with 1 M aqueous solution of $Na_2S_2O_3$ to remove I_2. The resulting solution was rapidly concentrated to dryness under a flow of dry air.

NAPH(CF_3)$_4$. The concentrated crude material resulting from experiment A (see Table 2.2.6) was dissolved in *ca*. 2 mL of 90/10 (v/v) acetonitrile/water mixture; NAPH(CF_3)$_4$ precipitated out and was filtered through a pipette with a plug made of a glass microfiber filter. The filter was washed with *ca*. 1 mL of 90/10 (v/v) acetonitrile/water mixture; then the purified NAPH(CF_3)$_4$ was dissolved in $CDCl_3$ and analyzed by ^{1}H and ^{19}F NMR spectroscopy, and NI-APCI mass spectroscopy which demonstrated 95+% molar purity.

NAPH(C_2F_5)$_4$. The concentrated crude material resulting from experiment B (see Table 2.2.6) was washed several times with 50-100 μL of dichloromethane. The remaining white CH_2Cl_2-insoluble material was dissolved in $CDCl_3$ and analyzed by ^{19}F and ^{1}H NMR spectroscopy, HPLC analysis, and APCI mass spectrometry which showed it to be 95+% pure NAPH(C_2F_5)$_4$.

NAPH(*n*-C_3F_7)$_4$. The concentrated crude material resulting from experiment C (see Table 2.2.6) was mixed with 500–1000 μL of absolute ethanol. A system with two immiscible liquid layers was formed; the yellow oil blob was separated and concentrated to dryness under the flow of dry air. The resulting yellow solid was washed three times with 250-500 μL of dichloromethane leaving behind a white insoluble material. This material was dissolved in $CDCl_3$ and analyzed by ^{19}F and ^{1}H NMR spectroscopy, and APCI mass spectrometry which showed it to be 95+% pure NAPH(*n*-C_3F_7)$_4$.

NAPH(n-C_4F_9)$_4$. The concentrated crude material resulting from experiment D (see Table 2.2.6) was diluted with 1–2 mL of dichloromethane and filtered through a pipette with a plug made of a glass microfiber filter. The insoluble material was washed twice with a minimum amount of dichloromethane; then it was dissolved in *ca*. 4 mL of $CDCl_3$. The solution was analyzed with ^{19}F and ^{1}H NMR spectroscopy, and NI-APCI mass spectrometry which showed that it contained 95+% pure NAPH(*n*-C_4F_9)$_4$.

A. Perfluoroalkylation of naphthalene. A flame-dried reactor ampoule made out of Pyrex glass (40 mL internal volume) and equipped with a sealing neck and a 90-degree Teflon vacuum valve was charged with naphthalene (20 mg, 0.16 mmol). Eight equivalents of a perfluoroalkyl iodide reagent R_FI was either measured using a PVT method and condensed into the liquid nitrogen-cooled reactor ampoule (R_F = CF_3, *n*-C_2F_5, gaseous reagents at room temperature), or measured using a 500 µL gas-tight syringe (R_F = *n*-C_3F_7, *n*-C_4F_9; liquid reagents at room temperature). The ampoule was cooled in liquid nitrogen and all non-condensable gases were evacuated, then the ampoule was flame-sealed and heated in a tube furnace at 300 °C for 3 hours, see Table 2.2.6. **(CAUTION!!! All operations with the gas transfer and the reactor ampoule must be performed by qualified personnel. Ampoule explosion due to over pressurization or inadequate quality of the flame seal may occur!)** After heating, the ampoule was cooled to room temperature. Each of the experiments A–D (Table 2.2.6) was repeated at least twice, yielding practically identical product compositions (as determined by ^{1}H and ^{19}F NMR spectroscopy). Two batches of products underwent different work-up procedures.

B. Crystallography. The X-ray quality single crystals of 1,3,5,7-NAPH(CF_3)$_4$ and 1,3,5,7-NAPH(C_2F_5)$_4$ were grown by slow evaporation of their CS_2 and $CDCl_3$ solutions, respectively (at room temperature). Both compounds formed clear colorless crystals.

***C. DFT calculations*.** Atomic coordinates of all studied molecules were first optimized at the PBE/TZ2P level using Priroda code[61] then followed by B3LYP-D3/def2-TZVP computations performed using ORCA suite.[62]

2.3. Perfluorobenzylation of corannulene (CORA).

Since the discovery of corannulene (CORA) in 1966,[63] collective research efforts towards improving its synthesis led to current industrial-scale production.[64-66] The first synthesis of CORA involved a 17 step reaction resulting in a 1% overall yield.[67] Further improvements to the synthesis were investigated, ultimately reducing it to a 3 step reaction and yield gram quantities.[64,65] Potential applications of CORA and its derivatives span from lithium ion batteries,[68] optoelectronics,[69-73] precursor materials for assembling fullerenes and other nanocarbons,[74,75] and as single-molecule polycyclic aromatic hydrocarbon molecular rotors.[76,77]

The substitution with electron withdrawing groups such as chlorine,[78,79] bromine,[80] fluorine,[81] and trifluoromethyl[81-83] to CORA have been useful for facile further substitution or manipulating the electronic properties. Other syntheses of CORA bearing electron withdrawing groups have been discussed elsewhere.[84] Investigation of the perfluorobenzyl electron withdrawing group has never been investigated; hence, the application of a recently developed direct synthetic method for introducing perfluoroalkyl groups[17,83,85-87] was adapted for the perfluorobenzylation of highly substituted perfluorobenzylation of CORA. This afforded the preparation and characterization of two members of a new class of perfluorobenzylated CORA derivatives, $C_{20}H_{10-x}(CF_2C_6F_5)_x$, that not only possess significantly enhanced acceptor properties compared to parent corannulene, but also exhibit unusual behavior in the crystalline phase due to unprecedented conformational flexibility of perfluorobenzyl substituents. This provided insight

into the reactivity between CORA and perfluorobenzyl groups, the feasibility for the use in organic electronics, and the electron withdrawing nature of perfluorobenzyl groups.

2.3.1. Perfluorobenzylation of CORA in solution- and gas-phase. Two different synthetic procedures were developed for mono- and multi- substituted derivatives (Figure 2.3.1 scheme). A highly selective synthesis of a monosubstituted compound, $C_{20}H_9(CF_2C_6F_5)$ (**CORA(Bn$_F$)**), was carried out in DMSO solution with Cu promoter at 160 °C (method a, Figure 2.3.1 scheme).[88] Separation of the products from unreacted CORA and small unidentified impurities was performed by using HPLC. The yield of **CORA(Bn$_F$)** based on HPLC peak integration was 29% (Figure 2.3.1, bottom panel). Spectroscopic characterization with ^{19}F and ^{1}H NMR will be discussed below. The soft-ionization APCI mass spectrometry did not work for the purified sample of **CORA(Bn$_F$)** when analyzed either in neat acetonitrile or when mixed with donor molecules, the approach used successfully for naphthalene$(R_F)_n$ mass analysis.[86] Apparently, electron withdrawing effect of one perfluorobenzyl group is relatively weak, and **CORA(Bn$_F$)** possesses sufficiently high ionization potential and low electron affinity to prevent ionization (similarly, ionization of CORA[83,89] could not be achieved under identical conditions).[83]

The second synthetic method involved heating a mixture of CORA and $C_6F_5CF_2I$ in a sealed glass ampoule at 200 °C (method b, Figure 2.3.1 scheme). Under these conditions, sublimation of CORA takes place and the reaction proceeds in the gas phase.[17,83,86] The HPLC and mass spectrometry analysis of the crude product showed nearly quantitative conversion (mostly into pentasubstituted perfluorobenzyl derivatives) and albeit low selectivity (Figure 2.3.1). When the reaction was performed with fewer equivalents of $C_6F_5CF_2I$ or at shorter reaction times, products with fewer substitutions prevailed in the mixture. The crude material was then separated by HPLC (Figure 2.3.1). One of the main products, $C_{20}H_5(CF_2C_6F_5)_5$ (**CORA(Bn$_F$)$_5$**), was isolated

with 20% yield. Its composition was determined by negative-ion APCI mass spectrometry in acetonitrile, which showed the peaks with *m*/*z* 1372 and 1330, the former corresponding to an adduct of the molecular anion $C_{20}H_5(CF_2C_6F_5)_5^-$ (*m*/*z* 1330) with acetonitrile (Figure 2.3.1). Surprisingly, several minor products with the general formula $C_{20}H_{9-n}$ $(CF_2C_6F_5)_n(C_6F_5)$ (n = 3,4) were also detected among the isolated compounds. Presumably C_6F_5 radicals form via the heat-facilitated cleavage of the $C(CF_2)$–$C(C_6F_5)$ bond; no such products were observed in solution-phase reaction that were carried out at lower temperatures. Previously, a CORA derivative with two pentafluorophenyl moieties was only made via a multistep bottom-up synthetic procedure.[81]

2.3.2. HPLC separation of CORA(Bn$_F$)$_n$. Each fraction was HPLC-processed further until the main component appeared as a single peak and spectroscopic characterization followed. In all, but one, fractions the most abundant single-compound was isolated and tentative compositions are suggested based on the combined NMR spectroscopy and mass spectrometry data. In one case, fraction F1 contained an inseparable mixture of two isomers. The details of isolation and characterization are given in Figure 2.3.3 to Figure 2.3.8. Only in one case, C_5-$C_{20}H_5(CF_2C_6F_5)_5$, the structure was confirmed with X-ray crystallography. For other isolated compounds from this gas-phase reaction, the current assignments of molecular compositions are to be considered preliminary.

2.3.3. Characterization of CORA(Bn$_F$)$_n$.

NMR spectroscopy. The ^{19}F NMR spectra of the purified **CORA(Bn$_F$)$_5$** and **CORA(Bn$_F$)** shown in Figure 2.3.9 are very similar; presence of only four resonances for **CORA(Bn$_F$)$_5$** compound is indicative of its high symmetry. We used the internal standard (1,4-$(CF_3)_2$-C_6H_4) while recording NMR spectra to help us ascertain molecular compositions for the isolated compounds, especially when they were not amenable to mass spectrometry analysis (Table 2.3.1). The $F(CF_2)$ and the

F(C_6F_5) resonances appear in the expected regions at −δ 82 – 86 and 140 – 170, respectively. The F(CF_2) resonances in each CORA(Bn_F)$_n$ compound appear as triplets.

In the ^{1}H NMR spectra of the **CORA(Bn_F)** and **CORA(Bn_F)$_5$** (Figures 2.3.10 and 2.3.11), the following trend is observed. The proton resonances of **CORA(Bn_F)** span the range δ 7.8 – 8.1 (cf. a unique proton signal in parent CORA is δ 7.82). Noteworthy, the single proton resonance of the C_5-**CORA(Bn_F)$_5$** (δ 8.40) is shifted 0.3 ppm downfield (deshielded) compared to the monosubstituted derivative, but it is 0.13 ppm upfield shifted when compared to the stronger acceptor C_5-CORA(CF_3)$_5$ (δ 8.53) under the same conditions.[83] NMR spectroscopy analysis of other CORA(Bn_F)$_n$ compounds are shown in Figures 2.3.12, Figure 2.3.13, and Figure 2.3.14.

Absorption and emission spectroscopy. The absorption spectra of CORA(Bn_F)$_5$, the putative CORA(Bn_F)$_4$, and CORA(Bn_F) are shown in Figures 2.3.15, 2.3.16, and 2.3.17, respectively, were collected in CH_2Cl_2. In the absorption spectra, two prominent features are observed at 254 nm and 289 nm for CORA.[71] Interestingly, these spectral features are red shifted for all CORA(Bn_F)$_n$ compounds except for **CORA(Bn_F)** (see Figure 2.3.2 for concentrations and absorption maxima), a phenomenon observed when the conjugated π-system is extended.[71,90] The red shift could be explained by the rigidity of the acetylene bridge promoting more π-delocalization; however, it is not necessary to molecularly engineer CORA derivatives with extended π-systems to absorb more of the visible spectrum as evidence by these CORA(Bn_F)$_n$ compounds. This is in agreement with calculated[70] and experimental[91] absorption spectra that suggest the red shift depends on the number and size of the substituent.

In the emission spectra (Figure 2.3.2.) of **CORA(Bn_F)$_5$** and **CORA(Bn_F)**, the λ_{max} is red shifted 8 nm, 6 nm, and 1 nm, 0 nm, respectively, from the parent CORA compound for the two

most prominent absorption features. It appears that multiple substitutions of CORA hydrogen atoms promote red shifts in the absorption features. Indeed, decakis(phenylthio)corannulene appears red in color.[91]

Cyclic voltammetry. Electrochemical properties of the new CORA derivatives were studied by cyclic and square-wave voltammetry. The $E_{1/2}$ of **CORA(Bn$_F$)** was not possible to measure in *o*-dichlorobenzene (*o*DCB) due to the cathodic potential limit of the solvent and the insufficient electron accepting abilities of **CORA(Bn$_F$)**. On the other hand, **CORA(Bn$_F$)$_5$** displayed irreversible electrochemical behavior (see Figure 2.3.18). The first reduction peak potential deduced from square-wave voltammetry of C_5-**CORA(Bn$_F$)$_5$** (−1.66 V) is cathodically shifted by 0.06 V than C_5-CORA(CF$_3$)$_5$ (−1.60 V)[83] under the same electrochemical conditions (see Table 2.3.2 for additional electrochemical experiments conducted). To gain further insights on the electronic properties of CORA(Bn$_F$)$_n$ and compare with the observed electrochemical behavior, DFT-computed redox potentials were calculated for selected molecules.

Table 2.3.3 compiles the DFT-computed relative energies, electron affinity (EAs), $E_{1/2}$ (versus CORA) and solvation energies of several $C_{20}H_{10-x}(R_F)_x$ compounds. For R_F = $CF_2C_6F_5$, the values for three (x = 4) or four (x = 5) conformers were computed; however, only the values for the lowest energy conformers are shown in Table 2.3.3 (see Table 2.3.4 for complete list). There are only three possible CORA(Bn$_F$)$_4$ isomers without close contacts of Bn$_F$ groups (two DFT-optimized asymmetric isomers are shown on Figure 2.3.19). Mulliken analysis showed that the net contribution of perfluorobenzyl groups to the LUMO remains near 8–9% through the whole CORA(Bn$_F$)$_n$ series (to avoid unphysical results often resulting from the use of large basis set in Mulliken analysis, the LUMO composition was studied at the B3LYP/6-311G* level).

CORA(R_F)$_n$ derivatives with R_F = $CF_2C_6F_5$ have higher gas-phase EAs than the analogous derivatives with R_F = CF_3 groups (e.g., 0.06 eV for x = 5 or 0.09 eV for x = 4) (Figure 2.3.19). At the same time, in *o*DCB solution, CORA(CF_3)$_n$ derivatives have more positive first reduction potentials because of more favorable ΔE_{solv} values. The latter is mostly because of the higher solvation energies of CORA(Bn_F)$_n$ derivatives in the neutral state.

2.3.4. X-ray crystallography of C_5-CORA(Bn_F)$_5$. Slow evaporation of an acetonitrile solution of **CORA(Bn_F)$_5$** afforded thin, pale yellow needles suitable for X-ray diffraction study that confirmed the C_5-symmetry. It crystallizes with $P2_1/c$ symmetry and contains one toluene molecule per **CORA(Bn_F)$_5$** (most likely solvent trapped after HPLC separation).[92] One disordered toluene molecule and **CORA(Bn_F)$_5$** pack in columns along the *c* axis exhibiting the same bowl direction within each column and the other toluene molecule lies in a void between the columns having no π-π or hydrogen bonding interactions with **CORA(Bn_F)$_5$** (Figure 2.3.20 and Figure 2.3.21). The disordered toluene centroid between two **CORA(Bn_F)$_5$** molecules lies 3.65 Å from the centroid of one **CORA(Bn_F)$_5$** pentagon hub. The shortest distance between hub centroids is 3.72 Å. Two different conformers of **CORA(Bn_F)$_5$** are present in the crystal structure which is likely influenced by the inclusion of toluene within the crystal. In one conformer, **A**, four Bn_F blades point perpendicularly "down" and one blade points "parallel" to the hub plane; and in the other conformer, **B**, all five blades point "parallel". The **A** and **B** conformers also exhibit two significantly different bowl depths, 0.65 and 0.82 Å, respectively, compared to 0.870(8) Å for CORA.[93] Such a significant difference in bowl depth of 0.17 Å for two CORA conformers within the same crystal structure has not been observed before to our knowledge. For comparison, "down" and "up" conformers within the crystal structure of an imide-fused CORA derivative exhibit only a slight difference of 0.04 Å in bowl depths (0.67 and

0.63 Å, respectively).[94] It is, however, not uncommon that significant variations in bowl depth may occur upon exhaustive hydrogen substitution of CORA with various organic functional groups,[95-97] or by varying composition of alkali metal ion CORA complexes; in the latter case bowl depths vary by as much as 0.62 Å.[98] Such effective chemical control of CORA bowl depth may be utilized in material designs for energy storage.[99]

To test the hypothesis that the observed considerable conformational variations in **CORA(Bn_F)$_5$** are the result of the solid-state interactions, and not intrinsic molecular properties in the gas-phase, we calculated relative energies of **CORA(Bn_F)$_5$** conformers by DFT (B3LYP-D3/def2-TZVPP//PBE/TZ2P). Whereas for freely rotating CF_3 groups, the problem of the CF_3 conformations with respect to the CORA backbone does not exist,[83] it is not the case for $CF_2C_6F_5$ substituents: different orientations of $CF_2C_6F_5$ result in substantially different energies. Figure 2.3.22 shows three different C_5-symmetic conformers with all Bn_F blades "down", "parallel" or "up" (i.e., all perfluorobenzyl groups in the **CORA(Bn_F)$_5$** conformers have the same orientation) have relative energies of 0.0, 33.9, and 20.4 kJ/mol, respectively. Note that the "parallel" conformer corresponds to conformer **B** in the X-ray structure (relative energy of conformer **A** is 17.8 kJ/mol). Thus, the conformers observed in the solid state are not the lowest energy conformers in the gas state. This reveals an unexpected and significant effect of intermolecular interactions on the conformation of the perfluorobenzyl groups in the crystalline state.

Furthermore, these interactions also influence the CORA bowl depth. The computed bowl depths for conformers **A** and **B** optimized at the PBE/TZ2P level were 0.81 and 0.84 Å, respectively. This difference of only 0.03 Å, compared to 0.17 Å from the X-ray structure, suggests that the observed large difference in bowl depth is more influenced by the crystal packing rather than the direction of the Bn_F blades. Additional supporting evidence is provided

by the calculated bowl depths for the “up” and “down” conformers (shown on Figure 2.3.22) of 0.78 and 0.80 Å, respectively. For additional crystallographic data, see Table 2.3.5.

2.3.5. Summary and conclusions. In summary, a new class of corannulene derivatives with perfluorobenzyl groups was prepared and characterized. The pentasubstituted derivative exhibits excellent acceptor properties and peculiar conformational behavior in the solid phase due to the exceptional substituent flexibility. This ability to change molecular geometry in different environments can be utilized in supramolecular designs, donor-acceptor assemblies and applied material studies.

2.3.6. Experimental

Reagents and Solvents. The reagents and solvents perfluorobenzyl iodide ($C_6F_5CF_2I$, SynQuest), chloroform-d ($CDCl_3$, Cambridge Isotope Laboratories, Inc., 99.8%), 1,4-bis-(trifluoromethyl)benzene ($C_8H_4F_6$, Central Glass Co., LTD., 99%), dimethyl sulfoxide (C_2H_6OS, Fisher Scientific, ACS grade), magnesium sulfate anhydrous ($MgSO_4$, Fisher Scientific), Cu powder (Strem Chemicals, 99%), tetrakis(dimethylamino)ethylene (TDAE, Sigma-Aldrich), and cobaltocene ($CoCp_2$, purified by sublimation and stored under N_2) were used as received. Corannulene ($C_{20}H_{10}$) was prepared as previously reported and sublimed prior to use ((a) G. Mehta, G. Panda, *Tetrahedron Lett.* **1997**, *38*, 2145–2148; (b) L. T. Scott, P.-C. Cheng, M. M. Hashemi, M. S. Bratcher, D. T. Meyer, H. B. Warren, *J. Am. Chem. Soc.* **1997**, *119*, 10963–10968; (c) A. Sygula, G. Xu, Z. Marcinow, P. W. Rabideau, *Tetrahedron* **2001**, *57*, 3637–3644). Toluene (Fisher Scientific, ACS grade), heptane (Mallinckrodt Chemicals, ACS grade), acetonitrile (Mallinckrodt Chemicals, ACS grade), dichloromethane (EMD, ACS grade), diethyl ether anhydrous (EMD, ACS grade), and deionized distilled water (purified by a Barnstead NANOpure Ultrapure Water system producing water with a final resistance of at least 18 MΩ)

for HPLC separation and purification were used as received. 1,2-dichlorobenzene (Acros Organics, 99%, dried over 3 Å molecular sieves), ferrocene (Acros Organics, 98%), and tetrabutylammonium tetrafluoroborate ($N(n\text{-}Bu)_4BF_4$, $TBABF_4$, Strem Chemicals, 99%) were used for electrochemical measurements.

Instrumentation. High-Performance Liquid Chromatography (HPLC) separation and analysis was carried on a Shimadzu LC-6AD equipped with a UV/vis detector (Shimadzu, SPD-20A), a diode array detector (Shimadzu, SPD-M20A) observed at 300 nm, and a communication bus module (Shimadzu, CBM-20A). The columns used were a COSMOSIL Buckyprep semi-preparative column (10 × 250 mm, Nacalai Tesque, Inc.), a COSMOSIL Buckyprep-M semi-preparative column (10 × 250 mm, Nacalai Tesque, Inc.) at a flow rate of 5 mL min^{-1} or FluoroFlash column (Fluorous Technologies, Inc., PF-C8, 5 μm) at a flow rate of 2 mL min^{-1} unless otherwise indicated. Fluorine-19 (376 MHz) and ^1H (399 MHz) NMR spectra were recorded on a Varian INOVA 400 MHz instrument using 1 second relaxation time, 45 ° pulse angle, $CDCl_3$, and 1,4-bis-(trifluoromethyl)benzene ($\delta(^{19}F) = -66.35$; $\delta(^1H) = 7.77$) as an internal standard. Mass spectrometry analysis was performed on a 2000 Finnigan LCQ-DUO mass-spectrometer (CH_3CN carrier solvent at 0.3 mL min^{-1}). UV-vis spectroscopy analysis was performed on Cary 500 UV-VIS-NIR in dichloromethane. Fluorescence spectroscopy analysis was performed on AVIV ATF-105 Auto-Titrating Differential/Ratio Spectrofluorimeter with a 90° measurement geometry in dichloromethane. Cyclic voltammetry and square wave voltammetry measurements were carried out on a PAR 263 potentiostat/galvanostat using a three electrode electrochemical cell equipped with platinum counter and working electrodes (0.125 mm diameter) and a silver reference electrode. Cyclic voltammetry and square wave

voltammetry were performed at 100 mV s^{-1} scan rate (referenced to $Fe(Cp_2)^{+/0}$ internal standard) in *o*DCB.

Gas-phase reactions. The reaction consists of charging a glass ampoule (l = 165 mm, o.d. = 19 mm, i.d. = 16 mm) with CORA (10.0 mg, 0.040 mmol) and 20 eq. $C_6F_5CF_2I$ (135 μL, 0.80 mmol) and allowed to condense under liquid N_2. The ampoule was evacuated three times using a freeze-pump-thaw technique, flamed sealed, and heated at 200±5 °C for 1 h. Upon the completion of the reaction, the ampoule was cooled to room temperature and opened. The reaction contents were extracted with dichloromethane and concentrated to dryness.

Solution-phase reactions. The reaction consists of charging a glass ampoule with the CORA (10.0 mg, 0.040 mmol), Cu powder (7.6 mg, 0.12 mmol), and $C_6F_5CF_2I$ (13.4 μL, 0.08 mmol) in dimethyl sulfoxide. The ampoule was evacuated three times using a freeze-pump-thaw technique and placed into an oil bath set at 160±5 °C for 24 h. Upon completion of the reaction, the ampoule is cooled to room temperature and the contents are extracted with diethyl ether. The organic layer is washed with deionized distilled water at least four times removing the aqueous layer between each rinse. Anhydrous $MgSO_4$ is added to the organic layer and purified by silica gel chromatography.

2.4. Perfluorobenzylation of anthracene (ANTH).

Small organic molecules have begun to revolutionize the organic semiconductor (OSC) industry in attempt to replace the need for silicon and metal-based electronic components. Several advantages that OSCs offer over its inorganic counterparts are that optoelectronics can be made flexible, be processed from solutions which can reduce the cost of manufacturing, be light weight, and still be robust. Acenes such as anthracene, tetracene and higher homologues represent materials that have promising applications in optoelectronics especially organic light

emitting diodes (OLEDs). For instance, investigation of anthracene and its electronic properties began in the 1960s[100,101] and since then, many new anthracene derivatives have been synthesized and characterized with distinct absorption and emission properties including 9,10-di(2-naphthyl)anthracene and 2-methyl-9,10-di(2-naphthyl)anthracene.[19,102-104] In fact, 9,10-bis(phenyl)anthracene has been considered as a fluorescence reference material due to its near unity quantum yield.[105,106]

OLEDs have attracted considerable research because they have potential use for flat panel displays and solid state lighting applications. For full color displays, the colors red, green and blue emitters are required; however, red and green emitters are far more superior in lifetime and stability. The development of efficient blue emitters is crucial towards realizing commercial applications.[7,8] One criterion hypothesized for the development of efficient blue emitter calls for limited π–π interactions resulting in decreased fluorescence quenching. Not only will bulky substituents disrupt this intermolecular interaction, they may provide chemical stability and prevent photo-oxidation. It was shown that the applied voltage of at least 100 V was required to obtain significant light intensity from anthracene (ANTH).[101] Attempts to reduce the drive voltage below 100 V were successful, but at the cost of a decrease in quantum efficiencies.[107] Such a decrease in operating voltage was predicted to reduce power consumption and to extend the lifetime of blue emitters.

Fluorinated substituents have been predicted by DFT to improve device air stability simply by increasing electron affinities of organic semiconductors.[16] For example, our group reported ANTH$(CF_3)_5$ and ANTH$(CF_3)_6$ with gas-phase electron affinity values of 2.4 and 2.8 eV, respectively, a significant increase in comparison to the electron affinity value for ANTH of 0.5 eV.[17] The perfluorobenzylation of PAHs have not been studied prior to this work as mentioned in

previous sections. The bulkiness of the perfluorobenzyl groups and the flexibility of $–CF_2$ linker between the PAH core and C_6F_5 moiety may not only provide enhancement in acceptor properties, but also the necessary π-π disruption for enhanced fluorescence. Thus, we decided to explore reactions between ANTH and $C_6F_5CF_2I$ in the gas- and solution-phase. Our recent example of C_5-pentakis(perfluorobenzyl)corannulene showed excellent electron accepting abilities and unusual structural flexibility, indication towards air stability and disrupting π–π interactions.[108] For example, $CORA(CF_3)_5$ forms stacks with bowl distances of 3.8 Å[83] whereas $CORA(Bn_F)_5$ forms columns with bowl distances of 3.7 Å.[108]

We set out to selectively add one or two perfluorobenzyl groups to ANTH and to understand functionalization effects on the properties of linear PAHs. Typical syntheses of 9,10-disubstituted anthracenes can be achieved by the use of 9,10-dibromoanthracene[18,19,109,110] or anthraquinone[111] precursors followed by the introduction of the desired functional group, but the direct substitution of hydrogen atoms is far more limited.

2.4.1. Gas-phase and solution-phase reactions. Our group has explored the gas-phase perfluoroalkylation of polycyclic aromatic hydrocarbons (PAHs) which afforded several new perfluoroalkylated PAHs possessing strong electron accepting abilities.[17,83,85-87] When ANTH reacted with 20 equiv. of Bn_FI ($Bn_F = C_6F_5CF_2$) in the gas-phase at 200 °C for 3 h, multiple products were formed requiring time-consuming and extensive multi-stage HPLC separations. On the other hand, derivitization of organic substrates is commonly carried out in solution. For example, Li *et al*. demonstrated that selective perfluoroalkylation of PAHs was observed in high yields using 3 equiv. of copper promotor and 2 equiv. of perfluoroalkyliodides in DMSO at a reaction temperature of 120 °C for 24 h.[88] We recently investigated solution-phase reactions of corannulene using DMSO as the reaction solvent.[108] When ANTH dissolved in DMSO was

heated at temperatures between 120 °C to 140 °C in the presence of 2 equiv. of Bn_FI and 3 equiv. of copper promotor for 24 h, compounds 9,10-ANTH$(Bn_F)_2$ and 9-ANTH(Bn_F) among other ANTH$(Bn_F)_n$ compounds were formed. No unreacted ANTH was found in the crude product mixture resulting in complete conversion of ANTH into ANTH$(Bn_F)_n$ compounds. From the HPLC separation scheme (Figure 2.4.1), two compounds were separated with sufficient purity: 9,10-ANTH$(Bn_F)_2$ and 9-ANTH(Bn_F). The two large uncolored peaks from the separation scheme comprise of a complex mixture of ANTH$(Bn_F)_n$ compounds with similar retention times; therefore, this solution-phase reaction produced two major products and several minor products.

2.4.2. Characterization of 9-ANTH(Bn_F) and 9,10-ANTH(Bn_F)$_2$.

NMR spectroscopy. Among other ANTH$(Bn_F)_n$ compounds, 9-ANTH(Bn_F) and 9,10-ANTH$(Bn_F)_2$ were separated by HPLC (see Figure 2.4.1 for full separation scheme) with 14 mol% yield and 7 mol% yield, respectively, and characterized by ^{19}F (Figure 2.4.2) and ^{1}H NMR (see Figure 2.4.3) spectroscopy. Under a different set of reaction conditions (i.e., instead of 2 equiv. of Bn_FI, 10 equiv. of Bn_FI was used), a higher yield of 9,10-ANTH$(Bn_F)_2$ was achieved. In the ^{19}F NMR spectra (Figure 2.4.2), only four resonances in a 2:2:1:2 ratio were observed, commensurate with the previously reported compounds bearing Bn_F groups,[108,112] for both HPLC purified 9-ANTH(Bn_F) and 9,10-ANTH$(Bn_F)_2$. The F(CF_2) and F(C_6F_5) resonances appear in the expected regions of δ −71 to −74 and δ −140 to −165, respectively. Through-space F–F coupling was observed between the CF_2 groups and the *meta*-Ar_F resulting in a triplet and multiplet, respectively. Using the internal standard 1,4-$C_6H_4(CF_3)_2$ to determine the molar F/H ratio, an experimental value of 1.74 (theoretical = 1.75) confirmed the composition of ANTH$(Bn_F)_2$.

Absorption and emission spectroscopy. Absorption and emission spectra of ANTH, 9,10-ANTH$(Bn_F)_2$, and quinine sulfate (QS) in cyclohexane are shown in Figure 2.4.4. The λ_{abs} and

λ_{em} for ANTH, 9,10-ANTH(Bn_F)$_2$, and QS are (376 nm, 381 nm), (402 nm, 416 nm), and (348 nm, 452 nm), respectively. The 36 nm blue shift in λ_{em} of 9,10-ANTH(Bn_F)$_2$ in comparison to QS results in a deeper blue fluorescence color. Only ANTH obeys the mirror image rule whereas 9,10-ANTH(Bn_F)$_2$ and QS lose vibronic structure in the emission spectra. This may be the result of different conformations upon relaxation.[113] The Stokes' shift was larger for 9,10-ANTH(Bn_F)$_2$ (837 cm^{-1}) than for ANTH (381 cm^{-1}) in which larger Stokes' shifts are attributed to the attenuation of fluorescence self-quenching processes. The band gap energy (E_g) decreases from ANTH (3.28 eV) to 9,10-ANTH(Bn_F)$_2$ (3.05 eV). This decrease in E_g has been regarded as one method for improving the efficiencies in OLEDs performance as lower applied voltage will be required for operation in OLED applications.

The photophysical data of ANTH and 9,10-ANTH(Bn_F)$_2$ are summarized in Table 2.4.1. The fluorescence quantum yield (Φ_f) significantly increases from ANTH (0.40) to 9,10-ANTH(Bn_F)$_2$ (0.85) by over 200%. The measured Φ_f of ANTH in cyclohexane is in agreement with literature reported values ranging from 0.28 to 0.36.[19,114-116] The increase in Φ_f was previously observed for 9,10-X-ANTH derivatives bearing fluorine-containing electron withdrawing groups. For example, the Φ_f increases from 0.28 for ANTH to 0.54 (X = F) to 0.68 (X = CF_3) in cyclohexane.[19] To our knowledge, 9,10-ANTH(Bn_F)$_2$ has one of the highest Φ_f among fluorinated ANTH and rival that reported for ANTH(Ph)$_2$ of 0.84 to 1.00.[105] Interestingly, the opposite trend was observed for (poly)trifluoromethylated perlyene compounds. The Φ_f for (poly)trifluoromethylated perlyene decreases over 50% in comparison to the parent perlyene.[17]

2.4.3. Photostability experiments. Several photostability experiments using UV-vis spectroscopy were reported in the literature to compare ANTH and ANTH derivatives to understand if photostability enhancements were observed due to chemical modification of ANTH.[18,19] Changes

to the UV-vis spectra have been used as an indication of compound decomposition. It is well established that ANTH can be oxidized to form anthraquinone rapidly upon exposure to light. In addition, endoperoxides were shown to form from some perfluoroalkylated ANTH derivatives in the presence of oxygen at room temperature within minutes when irradiated with a high pressure mercury lamp.[19] At longer irradiation times, complete decomposition can occur as observed for 9,10-bis(perfluorooctyl)anthracene.[18]

To investigate the photostability of 9,10-ANTH(Bn_F)$_2$ in comparison to ANTH, using a UV-vis spectrometer, the absorbance was measured over 53 days in the presence of oxygen and plotted (Figure 2.4.8). Both samples were dissolved in CH_2Cl_2 and irradiated with a 34 W incandescent light source. The UV-vis spectra measured for ANTH (Figure 2.4.8) monitored over time showed that new absorbance features begin to appear suggesting the presence of a different compound. Interestingly, the UV-vis spectra measured for 9,10-ANTH(Bn_F)$_2$ showed no new absorbance features over time which might imply that no new compound was formed. To gain insight on the rate of decomposition, the UV-vis spectral band of ANTH (359 nm) and 9,10-ANTH(Bn_F)$_2$ (380 nm) from Figure 2.4.8 were normalized and plotted against time (Figure 2.4.5). It appears that the rate of decomposition from the photo irradiation of ANTH (−0.0004) is slower than 9,10-ANTH(Bn_F)$_2$ (−0.007). These rates may be misleading due to contribution of UV-vis spectral bands from other new compounds.

To observe the effects of photo irradiation of ANTH and 9,10-ANTH(Bn_F)$_2$, complementary NMR spectroscopic analyses have been carried out for both photo irradiated samples (see Figure 2.4.6 and Figure 2.4.7). In accordance with the NMR spectrum of the photo irradiated ANTH sample, ANTH was no longer present, small amount of anthraquinone, and other unidentified products (presumably oxidized species) were observed in the ^{1}H NMR spectra. At the same time,

despite the absence in changes in the UV-vis spectra of 9,10-ANTH(Bn_F)$_2$ during irradiation, a new symmetric compound was clearly present as observed in the ^{1}H NMR spectra besides 9,10-ANTH(Bn_F)$_2$ in a 4:1 ratio. The results discussed here show that even if spectral features in the UV-vis spectra are not changing, which can be misinterpreted as the photostability of a compound, degradation still occurs as revealed by NMR spectroscopy of the photo irradiated 9,10-ANTH(Bn_F)$_2$ sample. Surprisingly, UV-vis spectroscopy monitoring is a common methodology in the literature for determining photostability, often without subsequent complementary analyses.[18,19,113]

The HPLC analysis of both irradiated ANTH and 9,10-ANTH(Bn_F)$_2$ samples revealed that at least three compounds are present from the photo irradiated ANTH sample, in accordance with the earlier report.[19] From the photo irradiated 9,10-ANTH(Bn_F)$_2$ sample, one major product with t_R = 6 minutes besides 9,10-ANTH(Bn_F)$_2$ (t_R = 4.5 minutes) was observed in the HPLC chromatogram (see Figure 2.4.9). These results confirmed the fact that decomposition of the starting materials occurs and support the NMR spectroscopy post photo irradiation analysis.

To further investigate the origin of the new symmetric product that was formed from irradiating 9,10-ANTH(Bn_F)$_2$ in the presence of oxygen (Figure 2.4.6), another photostability experiment was carried out with a mercury arc lamp, a stronger irradiation source. To examine the possible effects of oxygen, the experiment was carried out under air-free conditions. In that experiment, a sample of 9,10-ANTH(Bn_F)$_2$ dissolved in $CDCl_3$, placed in an NMR tube, degassed with three freeze-pump-thaw cycles and irradiated with a high-pressure mercury arc lamp. The CF_2 resonance peak intensity with internal reference C_6F_6 (δ_F = −164.9 ppm) was recorded as a function of total irradiated time (Figure 2.4.10).

A gradual decrease in the % remaining of 9,10-ANTH(Bn_F)$_2$ can be seen in Figure 2.4.10. Even after 200 minutes of irradiation, ca. 65% of the compound was still present and only after ca. 1500 minutes of irradiation, the intensity of the CF_2 signal reaches 30%. Then, this same sample was exposed to air and irradiated for an additional 120 minutes, after which 9,10-ANTH(Bn_F)$_2$ was quantitatively converted to the same symmetric compound discussed above (see Figure 2.4.11 for ^{19}F NMR spectra). The composition of this oxidized compound was determined to be the endoperoxide decomposition product of 9,10-ANTH(Bn_F)$_2$ by mass spectrometry analysis.

The details of these photostability experiments suggest that caution should be exercised by researchers when interpreting UV spectra upon photo irradiation. Uses of subsequent complementary spectroscopic and chromatographic analyses of the photo irradiated products are imperative in fully appreciating and understanding the photostability of these organic semiconductors.

2.4.4. X-ray crystallography of 9,10-ANTH(Bn_F)$_2$. Slow evaporation of a dichloromethane solution of 9,10-ANTH(Bn_F)$_2$ at 2 °C afforded off-white plates suitable for X-ray diffraction studies which confirmed the structural assignment. Figure 2.4.12, 2.4.13, and 2.4.14 show different orientations of the solid-state packing of 9,10-ANTH(Bn_F)$_2$. From the top view (Figure 2.4.12), two distinct columns are shown in orange and black. It appears to have significant π-π overlap from the tail of one column and the head of the next column from the top view, but there is virtually no π-π overlap as shown in Figure 2.4.13. In fact, the two hexagons that appear to overlap are separated by 4.154 Å and are not in the same plane. Viewing along the major axis of the ANTH core, the columns of molecules are insulated by the Bn_F group (shown in yellow), which further inhibits any electronic coupling between columns as shown in Figure 2.4.14. The

zero π-π overlap results in reduced electronic communication between molecules and can be seen as beneficial for OLED applications due to the increased chances of an excited molecule to relax via fluorescence.

2.4.5. Summary and conclusions. In summary, the perfluorobenzylation of ANTH was performed for the first time. The reaction produced a di-substituted ANTH derivative bearing perfluorobenzyl groups. The emission spectroscopy of 9,10-ANTH(Bn_F)$_2$ revealed its deep blue fluorescence, and the bulkiness of the perfluorobenzyl functional groups disrupts any π-π intermolecular interactions between the ANTH cores as revealed by solid-state packing. These results in conjunction with its high fluorescence quantum yield and increased photostability indicate that 9,10-ANTH(Bn_F)$_2$ may be useful in OLED applications. It is also important to use a multitude of analytical instrumentation to fully understand the photostability of new organic semiconductors.

2.4.6. Experimental.

Solvents and reagents. The following reagents and solvents were used as received unless otherwise indicated: anthracene (TCI America, 94%); heptafluorobenzyl iodide ($C_6F_5CF_2I$, SynQuest, 90%); cyclohexane (Mallinckrodt); 1,4-bis-(trifluoromethyl)benzene ($C_8H_4F_6$, Central Glass Co., LTD., 99%); dimethyl sulfoxide (C_2H_6OS, Fisher Scientific, ACS grade); magnesium sulfate anhydrous ($MgSO_4$, Fisher Scientific); Cu powder (Strem Chemicals, 99%); dichloromethane (EMD, ACS grade); quinine hemisulfate salt monohydrate (Fluka); sulfuric acid (EMD chemicals); diethyl ether anhydrous (EMD, ACS grade); chloroform-d ($CDCl_3$, Cambridge Isotope Labs, 99.8%); hexafluorobenzene (C_6F_6, Oakwood Products); deionized distilled water (purified by a Barnstead NANOpure Ultrapure Water system producing water with a final resistance of at least 18 MΩ); and silica gel (Sigma-Aldrich, 70–230 mesh, 60 Å).

For HPLC separations: acetonitrile (Fisher Scientific ACS grade); toluene (Fisher Scientific, ACS grade); heptane (Mallinckrodt Chemicals, ACS grade) were used as received.

Instrumentation. Fluorine-19 (376 MHz) and ^{1}H (400 MHz) NMR spectra were recorded using a Varian INOVA 400 instrument with trace amount of $C_8H_4F_6$ ($\delta(^{19}F)$ −66.35) added as the internal standard. UV-vis spectroscopy analysis was performed on Cary 500 UV-VIS-NIR. Fluorescence spectroscopy analysis was performed on AVIV ATF-105 Auto-Titrating Differential/Ratio Spectrofluorimeter with 90° measurement geometry.

Gas-phase reactions. $CF_2C_6F_5I$ (565 μL, 3.4 mmol) was syringed into a flame-dried reactor ampoule made out of Pyrex glass containing anthracene (30 mg, 0.17 mmol), cooled in liquid nitrogen, and all non-condensable gases were evacuated. The ampoule was then flame-sealed and heated in a tube furnace at 200 °C for 3 h. The reaction contents were extracted with toluene and concentrated under vacuum.

Solution-phase reactions. $CF_2C_6F_5I$ (19 μL, 0.11 mmol) was syringed into a glass ampoule containing anthracene (10 mg, 0.056 mmol) and copper powder (11 mg, 0.17 mmol) dissolved in DMSO, and degassed three times by a freeze-pump-thaw technique. The ampoule was then heated in an oil bath at 160 °C for 24 h. The reaction contents were extracted with Et_2O and washed four to six times with doubly distilled water removing the aqueous later each time. Anhydrous $MgSO_4$ was added to the organic layer and passed through silica gel with DCM as the eluent. The organic layer was then concentrated to dryness.

Absorption and Emission Spectroscopy. Absorption spectra were collected under aerobic conditions in cyclohexane. Measurements were repeated three times and averaged. Emission spectra were collected between 300 and 800 nm with an emission step of 2.000 nm at 1.0 seconds per step, emission bandwidth of 2.000 nm. The samples were degassed using a freeze-

pump-thaw technique. A blank of pure cyclohexane was also measured and used to correct the fluorescence spectra. The absorbance of the standard and sample were matched at the excitation wavelength and the absorbance at and above the excitation wavelength was kept below 0.1. The temperature was held constant at 25.0 ± 0.2 °C. The excitation wavelength used was 333 nm. The concentrations used for ANTH, 9,10-ANTH(Bn_F)$_2$, and quinine sulfate were 1.89, 1.14, and 1.94 (10^{-5} M), respectively. Relative quantum yields were calculated using:

$$\Phi_x = \Phi_{std}\left(\frac{\int F_x}{\int F_{std}}\right)\left(\frac{1\text{-}10^{-A_{std}}}{1\text{-}10^{-A_x}}\right)\left(\frac{n_x^{\,2}}{n_{std}^{\,2}}\right)$$

Φ_x = quantum yield of analyte
Φ_{std} = quantum yield of standard in 0.1 M H_2SO_4 (quinine sulfate Φ_f = 0.55 in 0.1 M H_2SO_4)
$\int F_x$ = integrated area of analyte from fluorescence spectrum
$\int F_{std}$ = integrated area of standard from fluorescence spectrum
A_{std} = absorbance of standard at excitation wavelength
A_x = absorbance of analyte at excitation wavelength
n_x = refractive index of analyte solvent (cyclohexane = 1.4262 @ 20 °C)
n_{std} = refractive index of standard solvent (H_2O = 1.333 @ 20 °C)

2.5. Chapter Summary and Conclusions.

In Chapter 2, three projects aimed at the synthesis and characterization of the new perfluorobenzyl(aryl) PAHS were described. First, the polyperfluoroalkylation of NAPH revealed that the gas-phase reaction produced the most thermodynamically stable NAPH isomers containing four R_F (R_F = CF_3, C_2F_5, *n*-C_3F_7, and *n*-C_4F_9) groups. These NAPH(R_F)$_4$ compounds were isolated based on solvent solubility differences and were determined to have the same substitution pattern. The electron withdrawing abilities of these perfluoroalkyl groups increases from CF_3 to *n*-C_4F_9 and should continue this trend with longer perfluoroalkyl chain lengths; however, the electron withdrawing effect should diminish and longer perfluoroalkyl chains will not increase the electron withdrawing abilities as shown for the experimental and DFT-predicted electron affinities for the same R_F series in 1,7-C_{60}(R_F)$_2$.[49] Secondly, the perfluorobenzylation of

CORA showed that five substitutions produced one isomer with the same substitution pattern as C_5-CORA$(CF_3)_5$. The flexibility of the perfluorobenzyl rotors allowed for the different conformers to be observed in the solid-state packing of CORA$(Bn_F)_5$. The effect on electron affinity of the perfluorobenzyl groups slightly increases in comparison to the trifluoromethyl groups making CORA$(Bn_F)_5$ a better electron acceptor than CORA$(CF_3)_5$. The perfluorobenzyl group is a unique fluoro functional group which can be used to design a molecular rotor to introduce conformational flexibility. Finally, the perfluorobenzylation of ANTH interrupts the π-π interactions in the solid-state which are regarded as detrimental for OLED emitter applications as they may increase the non-radiative decay processes. The quantum yield of 9,10-ANTH$(Bn_F)_2$ was measured to be over 200% greater than the parent ANTH molecule along with greater air and photo stability.

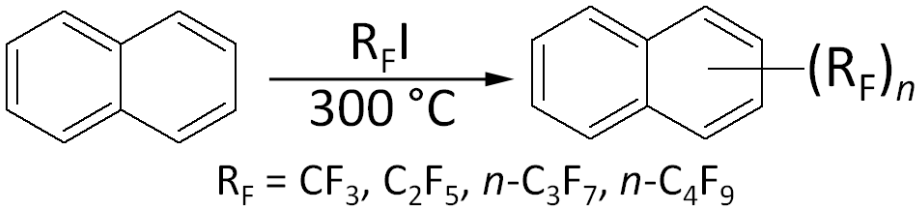

Scheme 2.2.1. Gas phase perfluoroalkylation of NAPH.

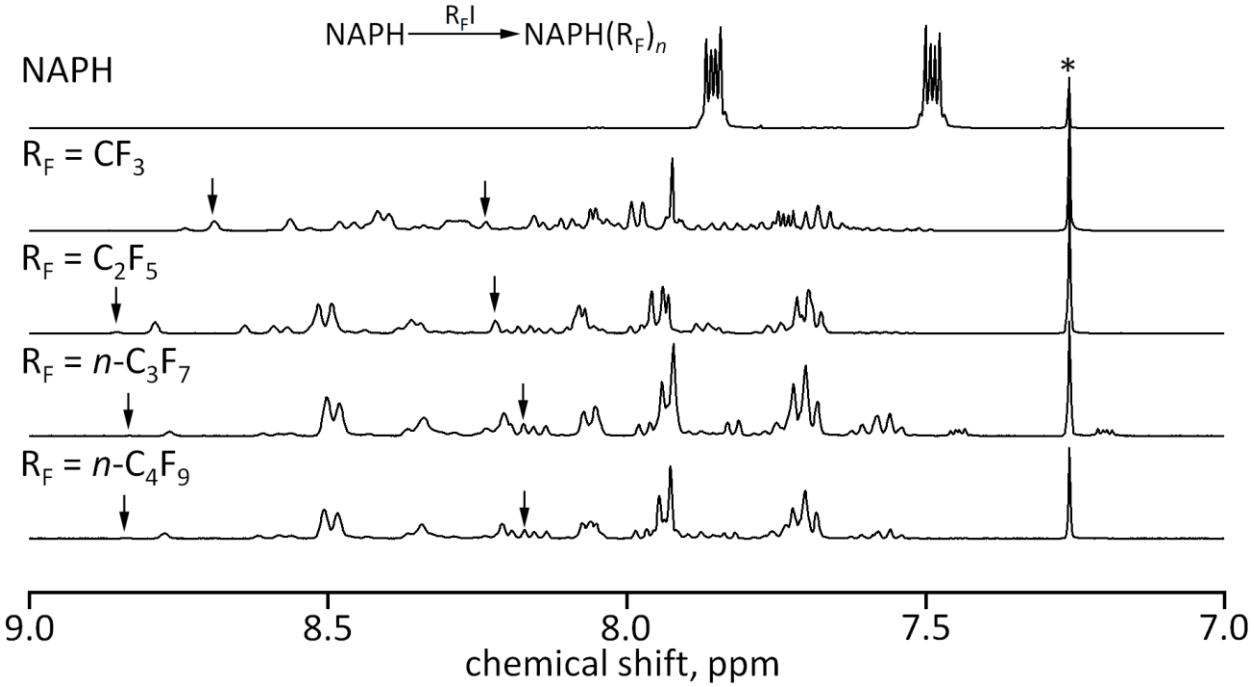

Figure 2.2.1. Proton NMR spectra of pure naphthalene and crude product mixture A-D (from top to bottom). The peak marked with an asterisk is due to the residual solvent $CHCl_3$ (δ 7.26). The arrows signify the proton peaks corresponding to 1,3,5,7-NAPH(R_F)$_4$. Complete conversion of NAPH is observed in each case.

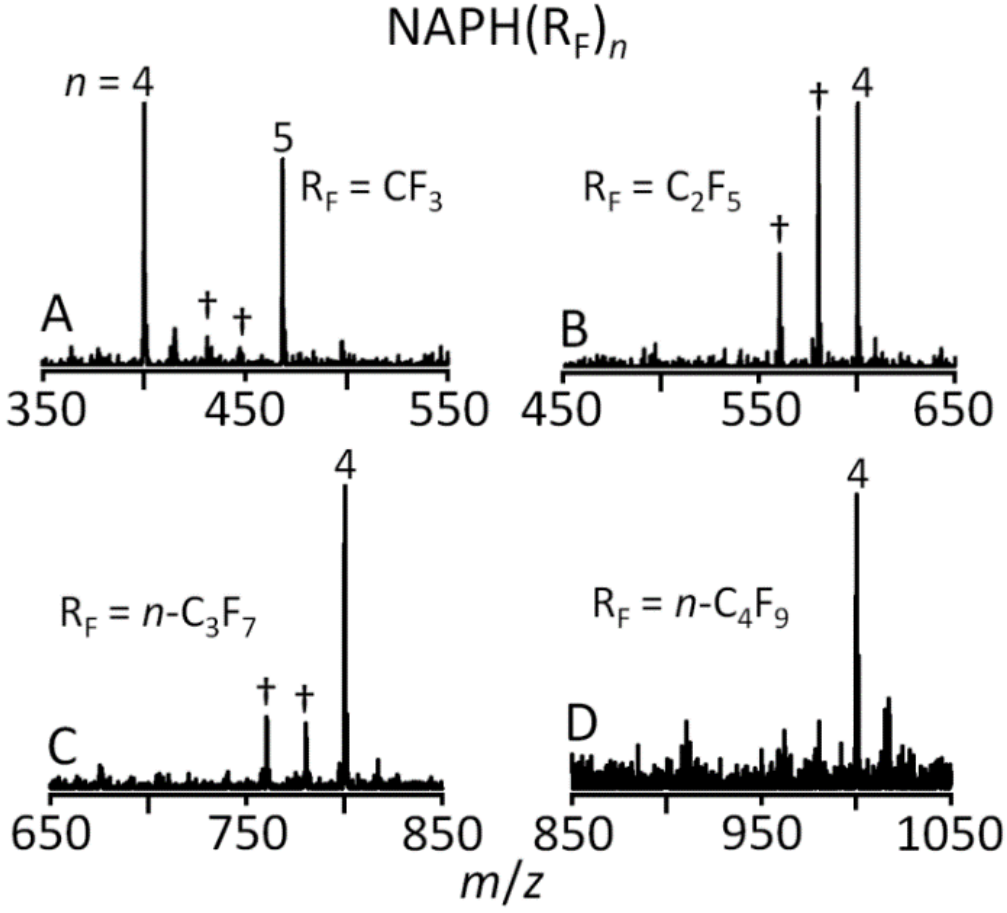

Figure 2.2.2. Negative-ion APCI mass spectra of the TDAE-reduced crude products of naphthalene perfluoroalkylation: A) NAPH$(CF_3)_n$; B) NAPH$(C_2F_5)_n$; C) NAPH$(n\text{-}C_3F_7)_n$; and D) NAPH$(n\text{-}C_4F_9)_n$. Peaks marked with daggers are due to fragments resulting from loss of HF from parent ions.

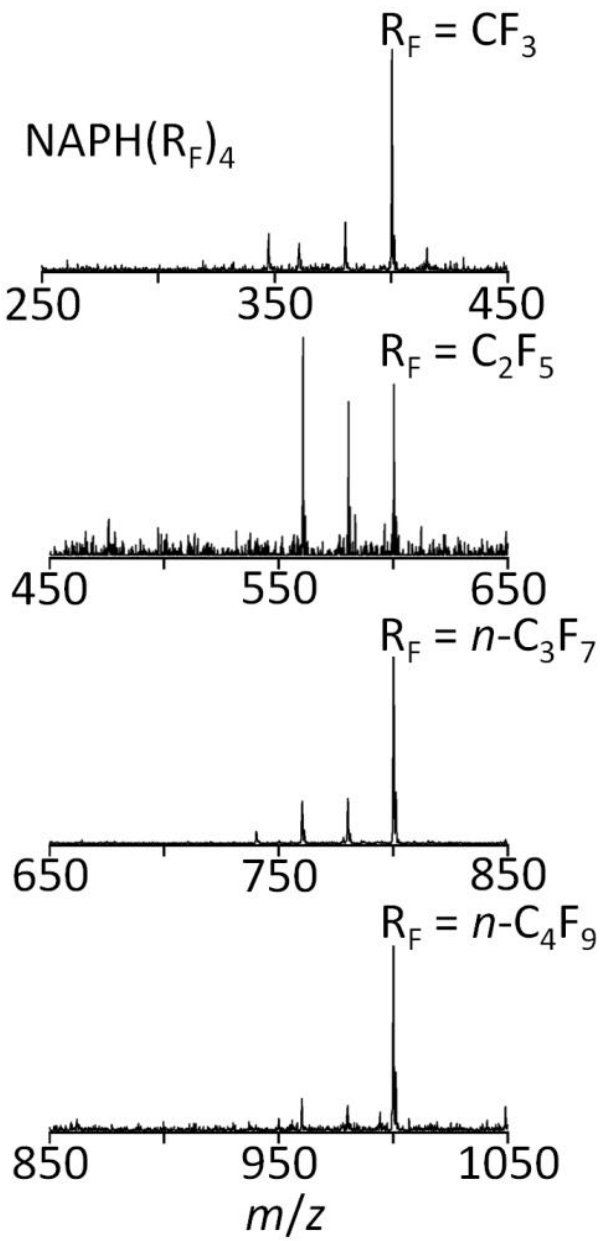

Figure 2.2.3. Negative ion APCI mass spectra of isolated 1,3,5,7-NAPH(R_F)$_4$ compounds (R_F = CF_3, C_2F_5, *n*-C_3F_7, and *n*-C_4F_9). Chemical reduction by TDAE was necessary to enable the MS observation. Losses of HF fragmentations are observed in each mass spectra.

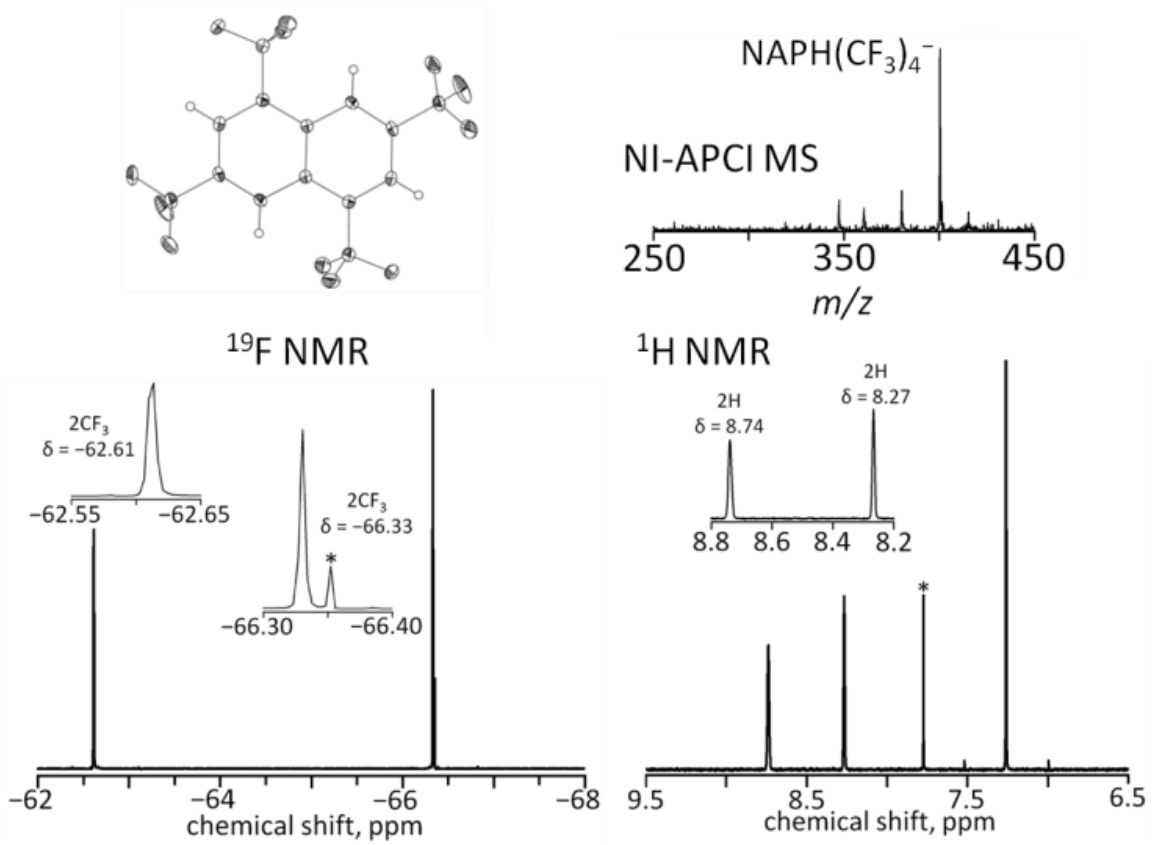

Figure 2.2.4. Single-crystal X-ray diffraction structure of 1,3,5,7-NAPH$(CF_3)_4$, 50% probability ellipsoids used for all non-hydrogen atoms of the ORTEP drawing (top left), NI-APCI mass spectrum (TDAE-reduced; top right), ^{19}F NMR (bottom left), and ^{1}H NMR spectra (bottom right) with expansions of the 95%+ pure 1,3,5,7-NAPH$(CF_3)_4$. Peaks marked with asterisks are due to internal standard, and peak at δ 7.26 due to residual solvent ($CHCl_3$).

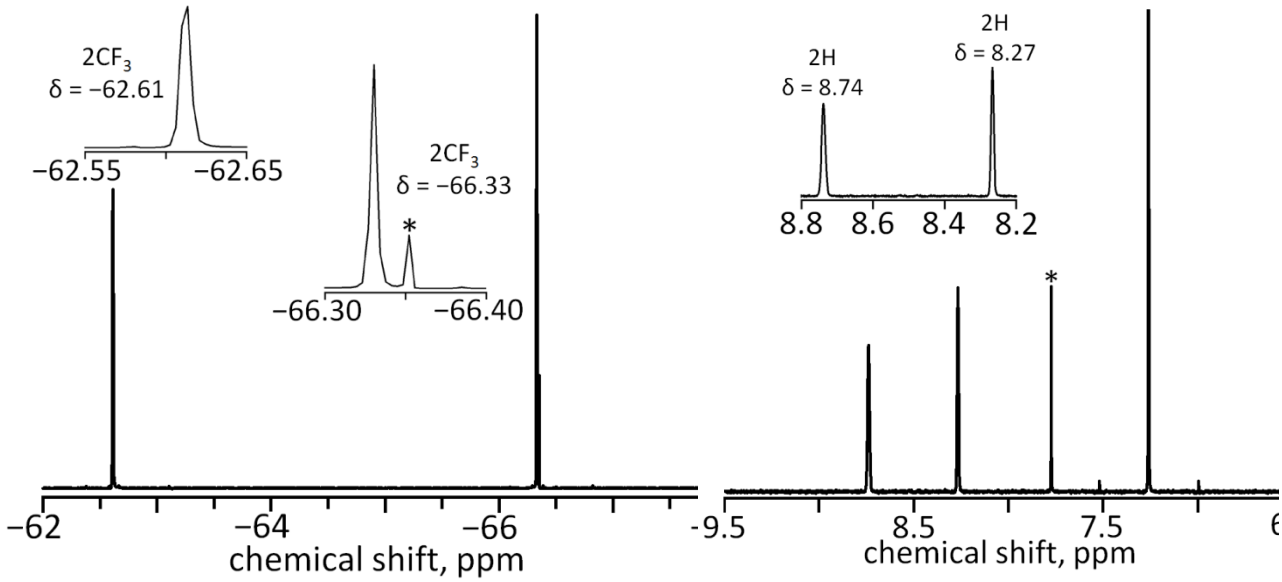

^{19}F NMR: δ −62.61 (s, 2CF_3), −66.33 (s, 2CF_3).

^{1}H NMR: δ 8.74 (s, 2H); 8.27 (s, 2H).

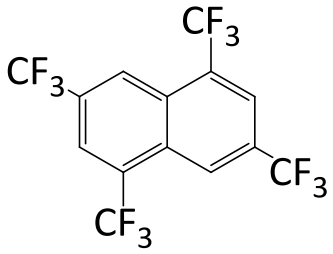

Figure 2.2.5. Fluorine-19 (top left) and ^{1}H (top right) NMR spectra and molecular drawing (bottom) of NAPH(CF_3)$_4$. The peaks marked with an asterisks are due to the internal integration standard 1,4-C_6H_4(CF_3)$_2$; the experimental mol F/mol H ratio based on the peak integration was found to be 2.9 (theoretical value is 3.0).

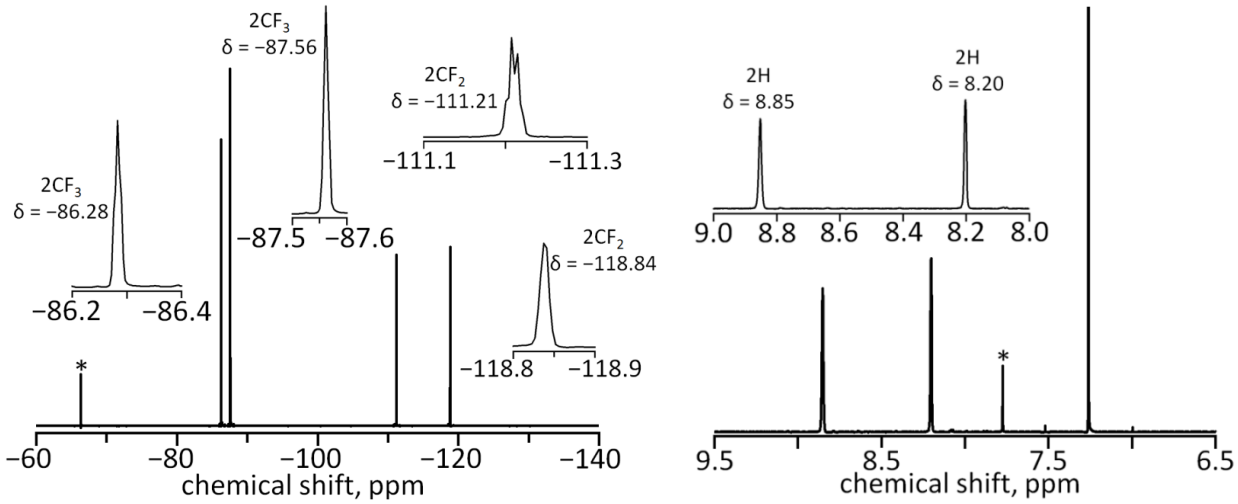

^{19}F NMR: δ −86.28 (m, 2CF_3), −87.56 (m, 2CF_3), −111.21 (m, 2CF_2), and −118.84 (m, 2CF_2).

^{1}H NMR: δ 8.85 (singlet, 2H); 8.20 (singlet, 2H).

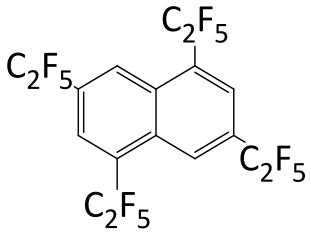

Figure 2.2.6. Fluorine-19 (top left) and ^{1}H (top right) NMR spectra and molecular drawing (bottom) of NAPH(C_2F_5)$_4$. The peaks marked with an asterisks are due to the internal integration standard 1,4-$C_6H_4(CF_3)_2$; the experimental mol F/mol H ratio based on the NMR peak integration was found to be 5.0 (theoretical value is 5.0).

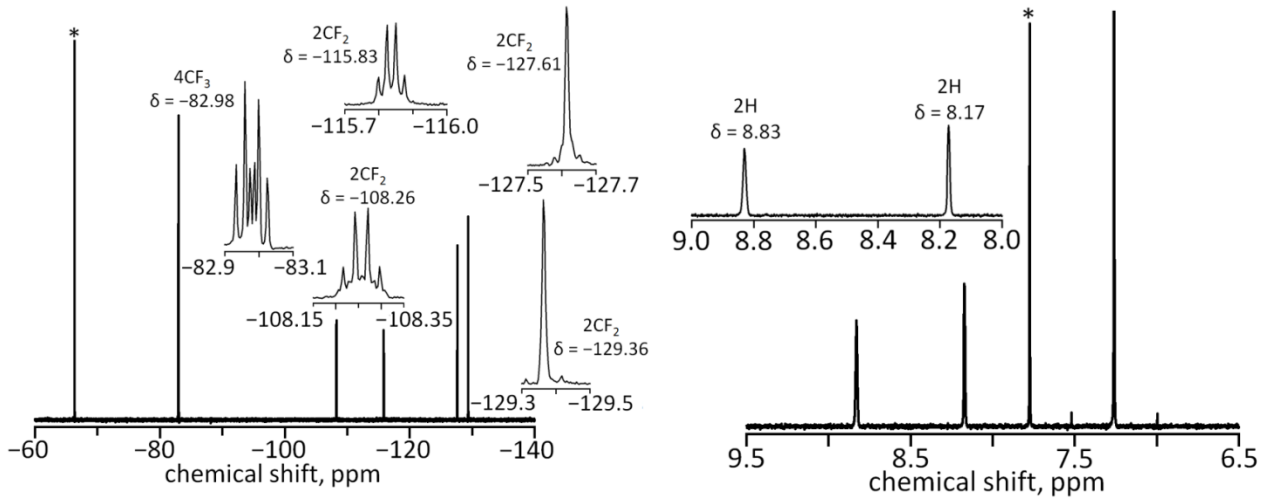

^{19}F NMR: δ −82.98 (dt, 4CF_3), −108.26 (m, 2CF_2), −115.83 (q, 2CF_2), −127.61 (s, 2CF_2), and −129.36 (s, 2CF_2).

^{1}H NMR: δ 8.83 (singlet, 2H); 8.17 (singlet, 2H).

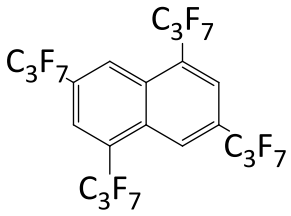

Figure 2.2.7. Fluorine-19 (top left) and ^{1}H (top right) NMR spectra and molecular drawing (bottom) of NAPH(*n*-C_3F_7)$_4$. The peaks marked with an asterisks are due to the internal integration standard 1,4-$C_6H_4(CF_3)_2$; the experimental mol F/mol H ratio based on the NMR peak integration was found to be 6.7 (theoretical value is 7.0).

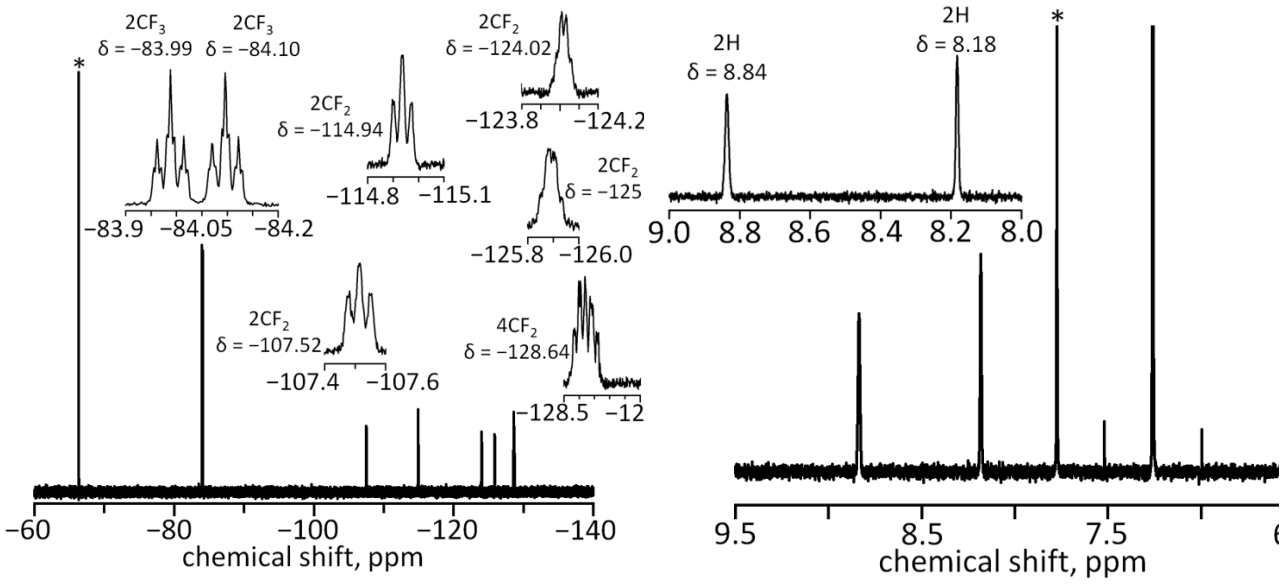

^{19}F NMR: δ −83.99 (tt, $2CF_3$), −84.10 (tt, $2CF_3$), −107.52 (m, $2CF_2$), −114.94 (m, $2CF_2$), −124.02 (m, $2CF_2$), −125.89 (m, $2CF_2$), and −128.64 (m, $4CF_2$).

^{1}H NMR: δ 8.84 (singlet, 2H); 8.18 (singlet, 2H).

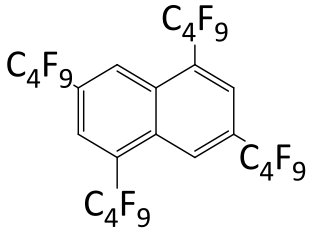

Figure 2.2.8. Fluorine-19 (top left) and ^{1}H (top right) NMR spectra and molecular drawing (bottom) of NAPH(*n*-C_4F_9)$_4$. The peaks marked with an asterisks are due to the internal integration standard 1,4-$C_6H_4(CF_3)_2$; the experimental mol F/mol H ratio based on the NMR peak integration was found to be 8.5 (theoretical value is 9.0).

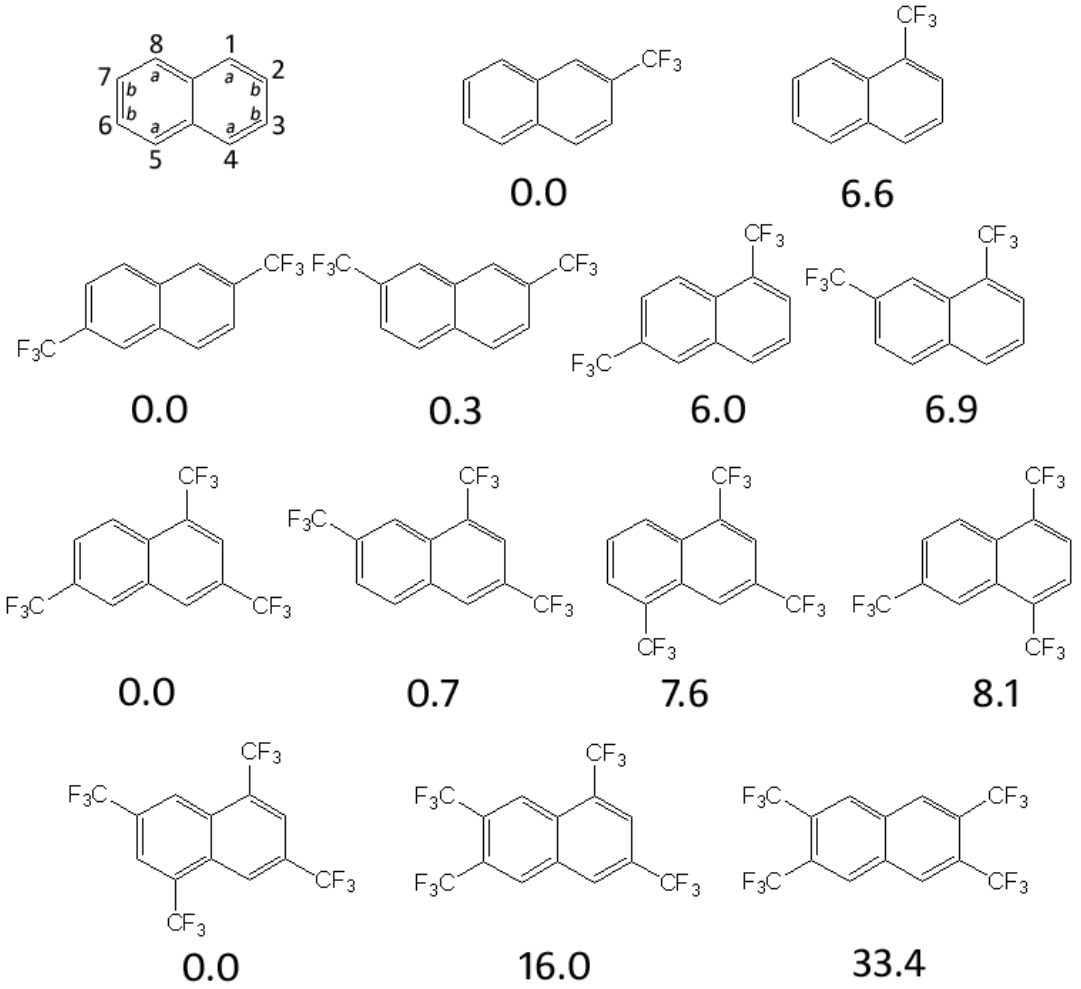

Figure 2.2.9. Numbering scheme (1 through 8) and symmetry related positions (*a* and *b*) for substitutions in NAPH and drawings of the most stable isomers of NAPH$(CF_3)_{1\text{-}4}$, DFT-calculated relative energies (in kJ/mol) are given under each structure.

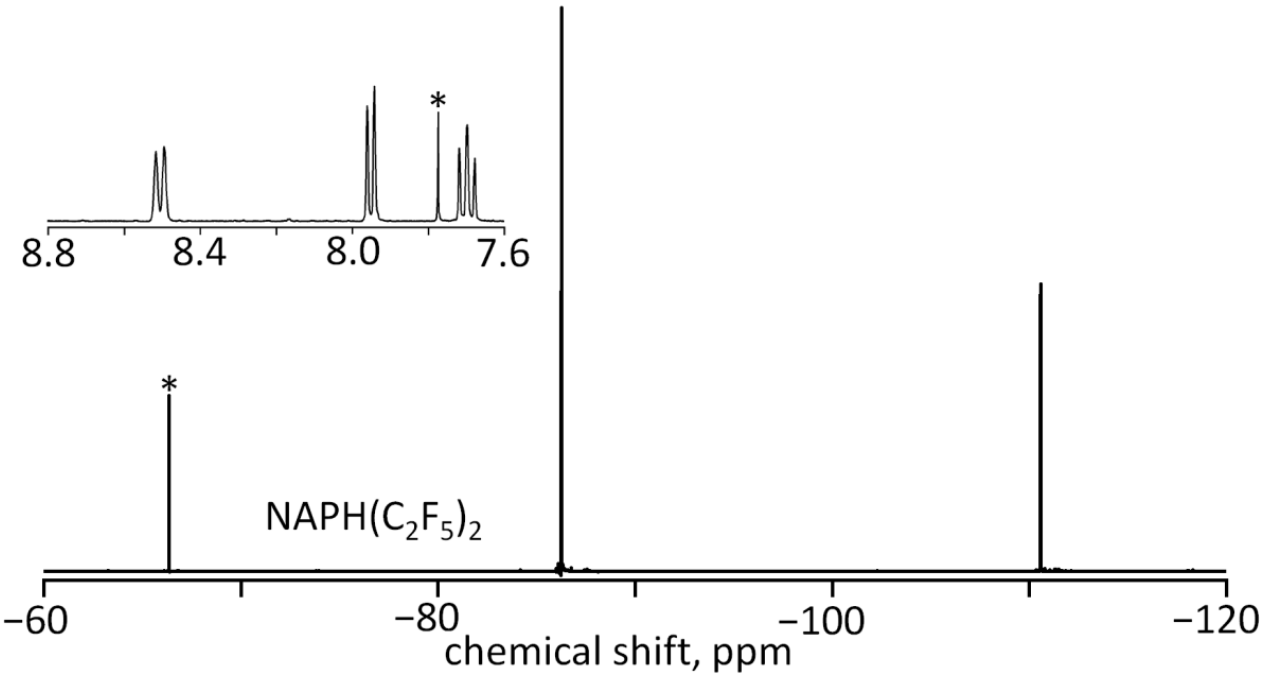

^{19}F NMR: δ −86.25 (s, 2CF_3), −110.56 (s, 2CF_2).

^{1}H NMR: δ 8.50 (d, 2H); 7.95 (d, 2H); 7.70 (t, 2H).

Figure 2.2.10. Fluorine-19 and ^{1}H NMR (inset) spectra for NAPH(C_2F_5)$_2$. The peaks marked with an asterisks are due to the internal integration standard 1,4-C_6H_4-(CF_3)$_2$. The experimental mol F/mol H ratio based on the NMR peak integration was found to be 1.5 (theoretical value is 1.7).

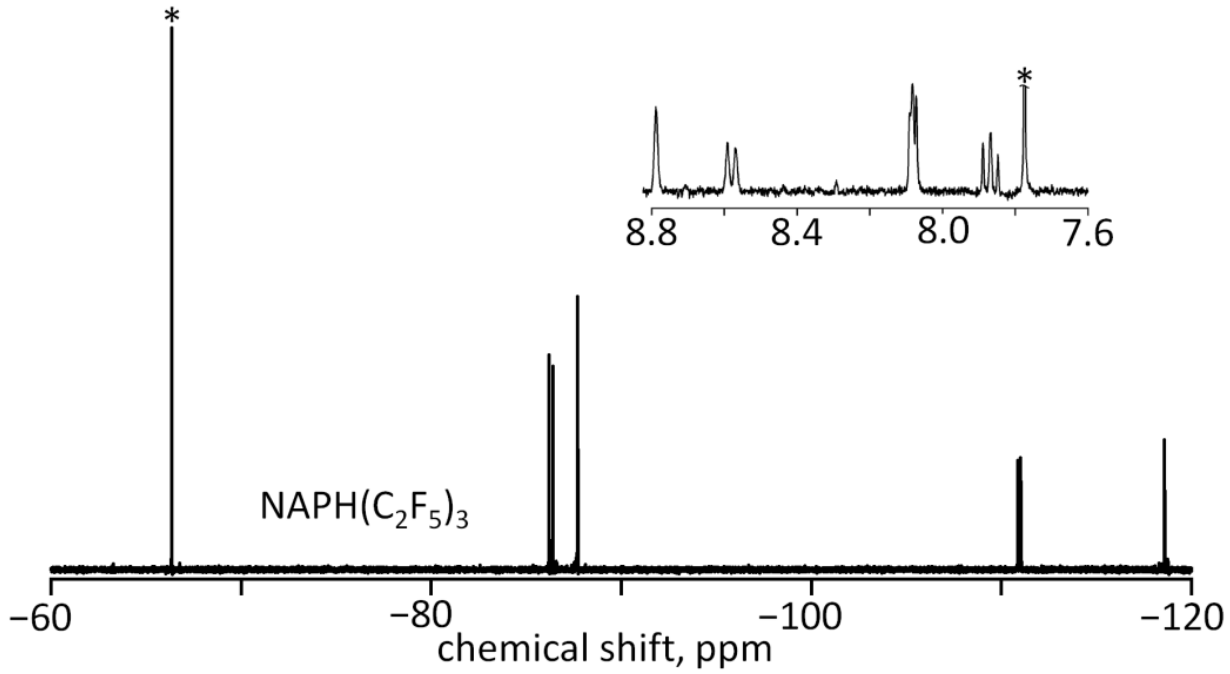

^{19}F NMR: δ −86.20 (s, 1CF_3), −86.40 (s, 1CF_3); −87.71 (s, 1CF_3); −110.87 (q, 1CF_2); −111.01 (s, 1CF_2); −118.58 (s, 1CF_2).

^{1}H NMR: δ 8.79 (s, 1H); 8.58 (d, 1H); 8.08 (m, 2H); 7.87 (t, 1H).

Figure 2.2.11. Fluorine-19 and ^{1}H NMR (inset) spectra for NAPH(C_2F_5)$_3$ (the isolated fraction with t_R. = 13 min as shown on Figure 3.2.14). The peaks marked with an asterisks are due to the internal integration standard 1,4-C_6H_4-(CF_3)$_2$. The experimental mol F/mol H ratio based on the NMR peak integration was found to be 4.0 (theoretical value is 3.0).

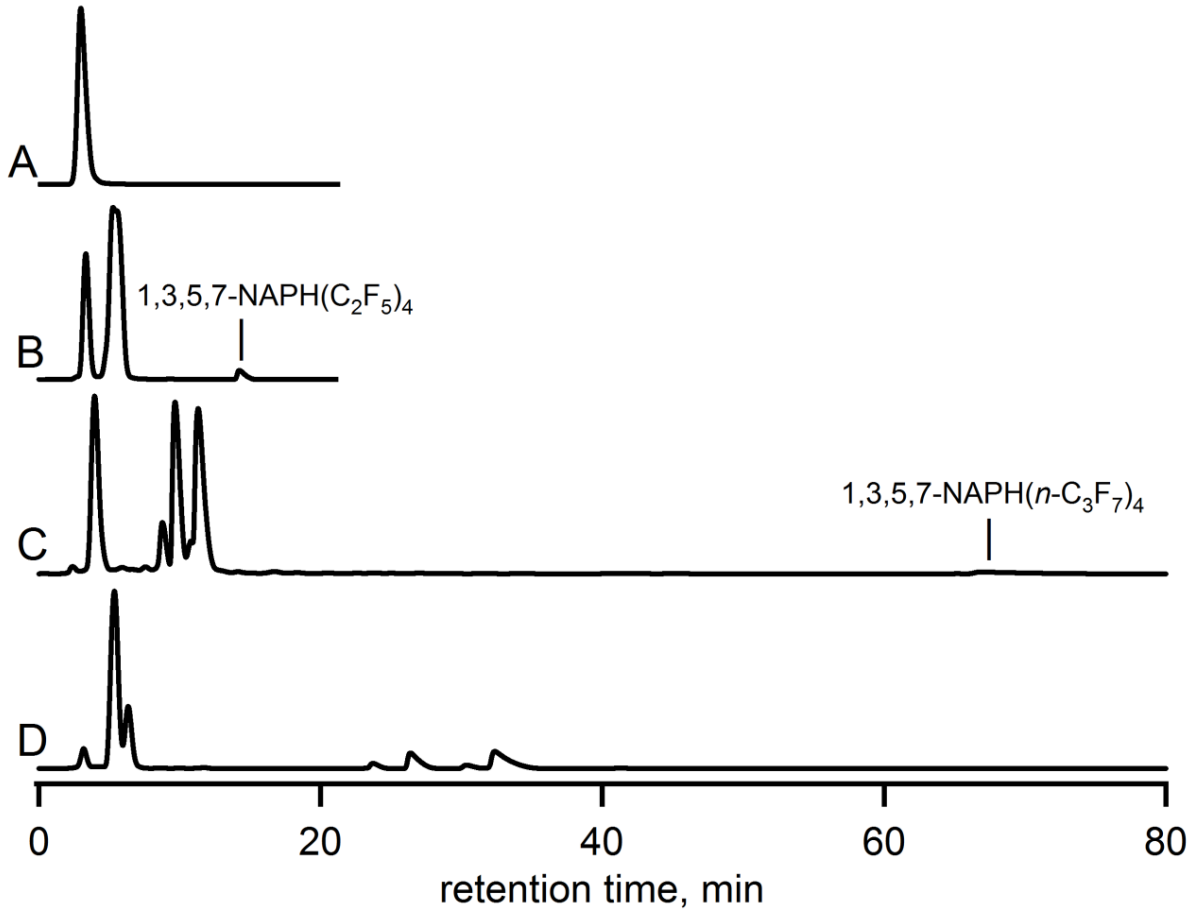

Figure 2.2.12. HPLC analysis of crude products of naphthalene perfluoroalkylation using 100% acetonitrile eluent: A) NAPH$(CF_3)_n$; B) NAPH$(C_2F_5)_n$; C) NAPH$(n\text{-}C_3F_7)_n$; and D) NAPH$(n\text{-}C_4F_9)_n$.

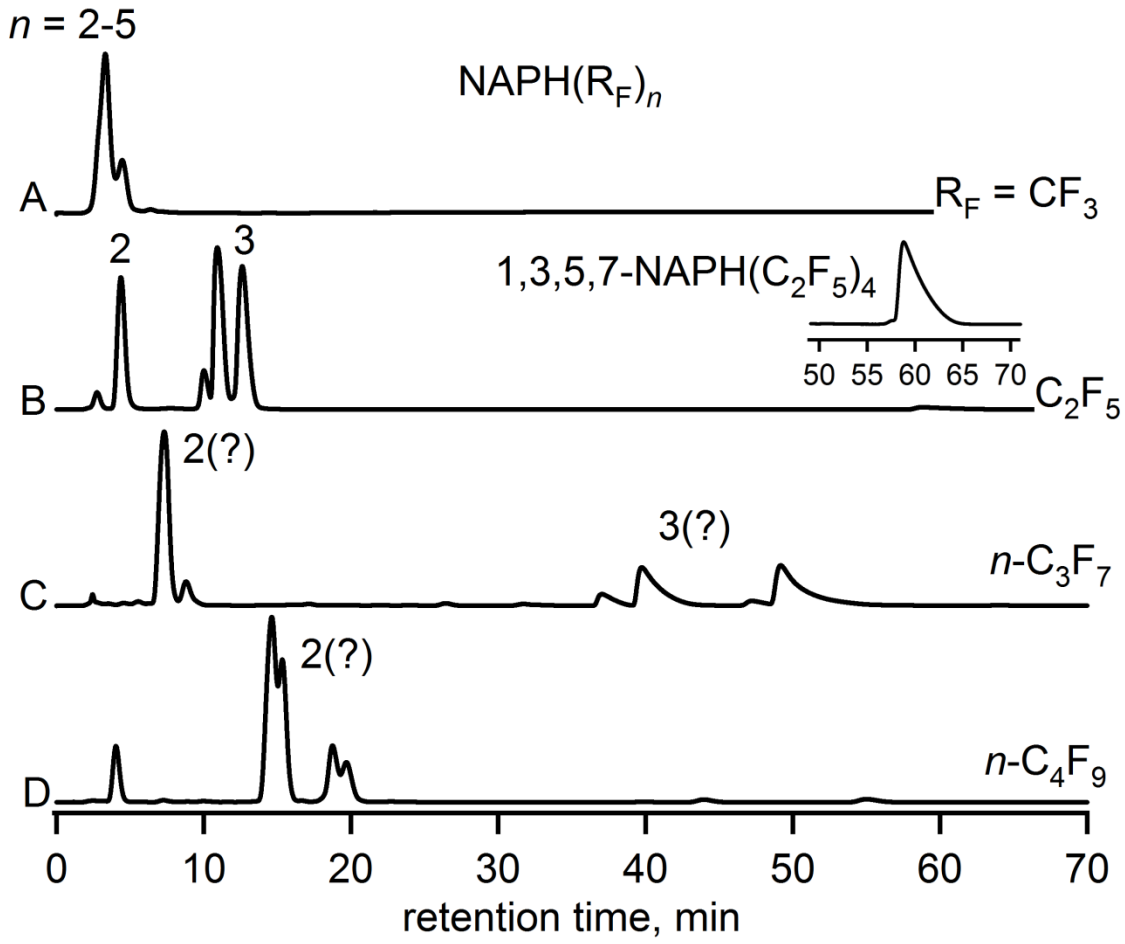

Figure 2.2.13. HPLC analysis of the crude products A–D using a 90/10 v/v acetonitrile/water mobile phase and a specialized reverse-phase FluoroFlash column packed with silica particles functionalized with C_8F_{17} perfluoroalkyl chains: A) NAPH$(CF_3)_n$; B) NAPH$(C_2F_5)_n$; C) NAPH$(n\text{-}C_3F_7)_n$; and D) NAPH$(n\text{-}C_4F_9)_n$. The numbers with question marks represent a tentative composition assignment based on fluorophilicity.

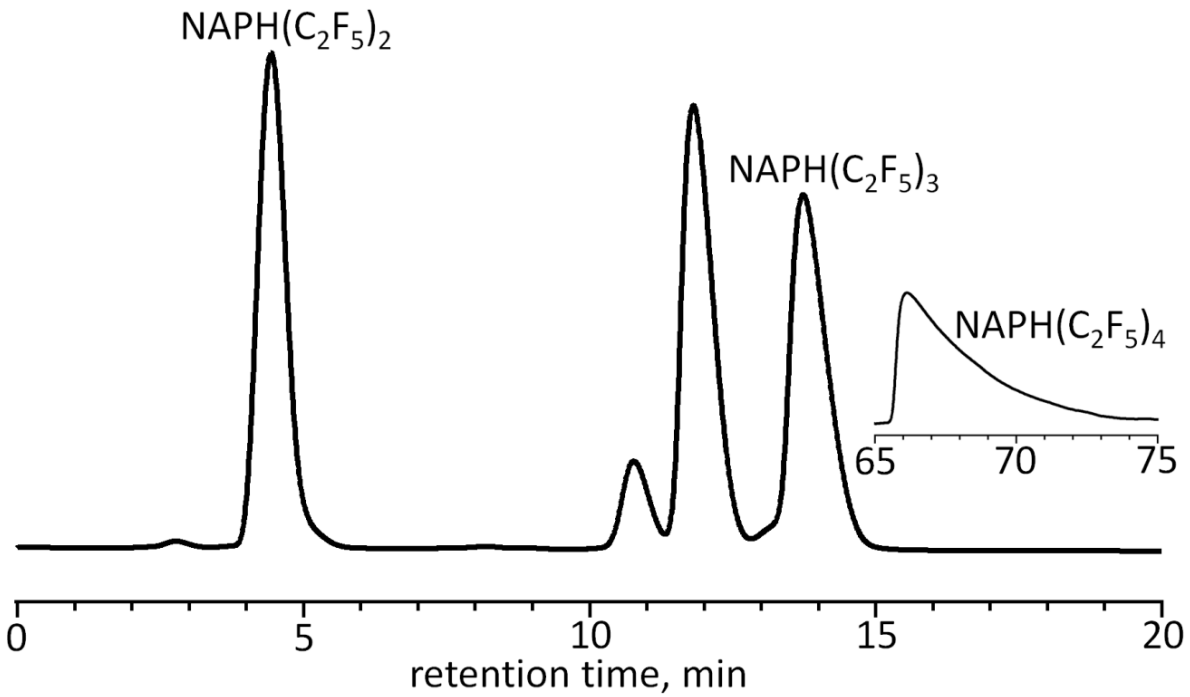

Figure 2.2.14. HPLC trace of the crude product mixture from the reaction between naphthalene and C_2F_5I. We have assigned the peak at t_R = 4 minutes to correspond $NAPH(C_2F_5)_2$ and the peak at t_R = 13 minutes to correspond to $NAPH(C_2F_5)_3$.

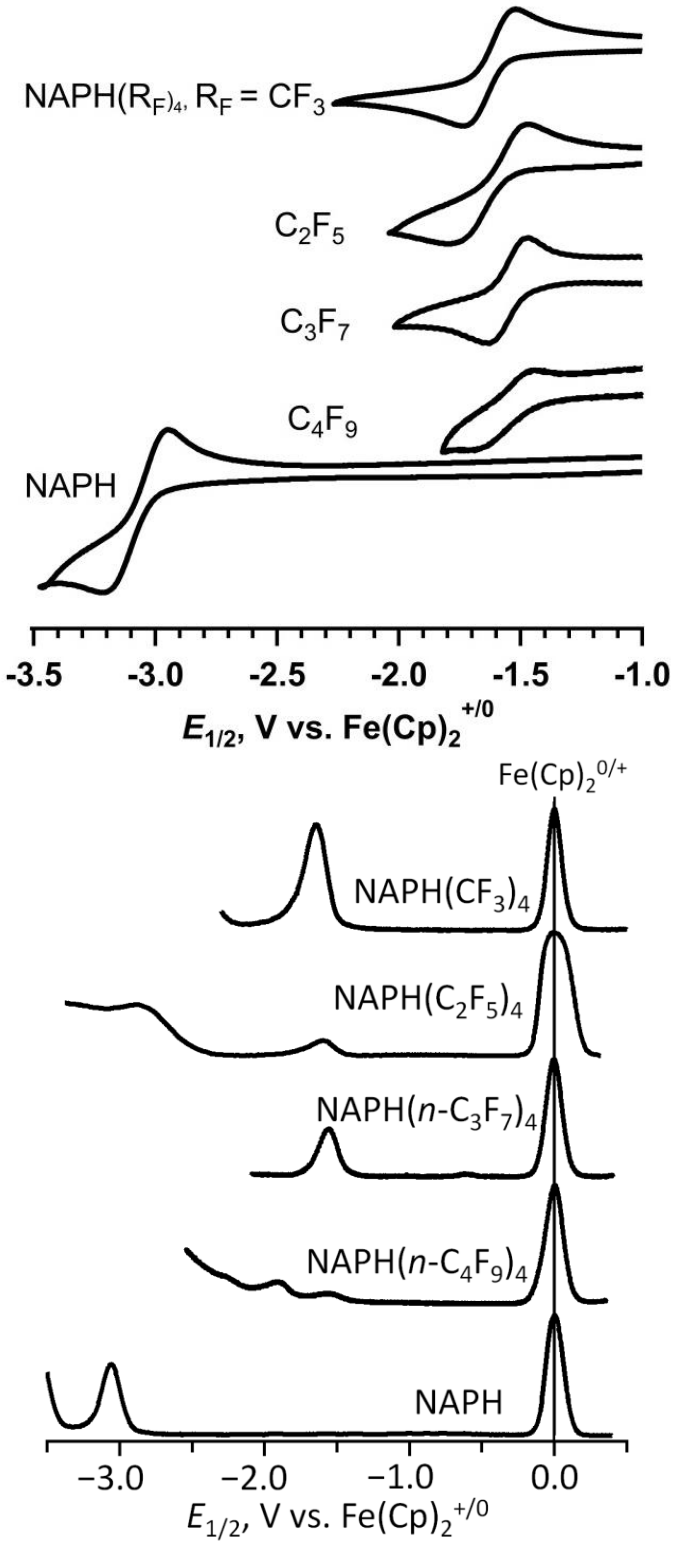

Figure 2.2.15. Cyclic (top) and square-wave (bottom) voltammograms at scan rate 100 $mV \cdot s^{-1}$ of NAPH and pure 1,3,5,7-NAPH$(R_F)_4$ compounds in dimethoxyethane (0.1 M (n-Bu)$_4$NClO$_4$). All measurements are shown relative to $Fe(Cp_2)^{+/0}$ defined as 0.0 V.

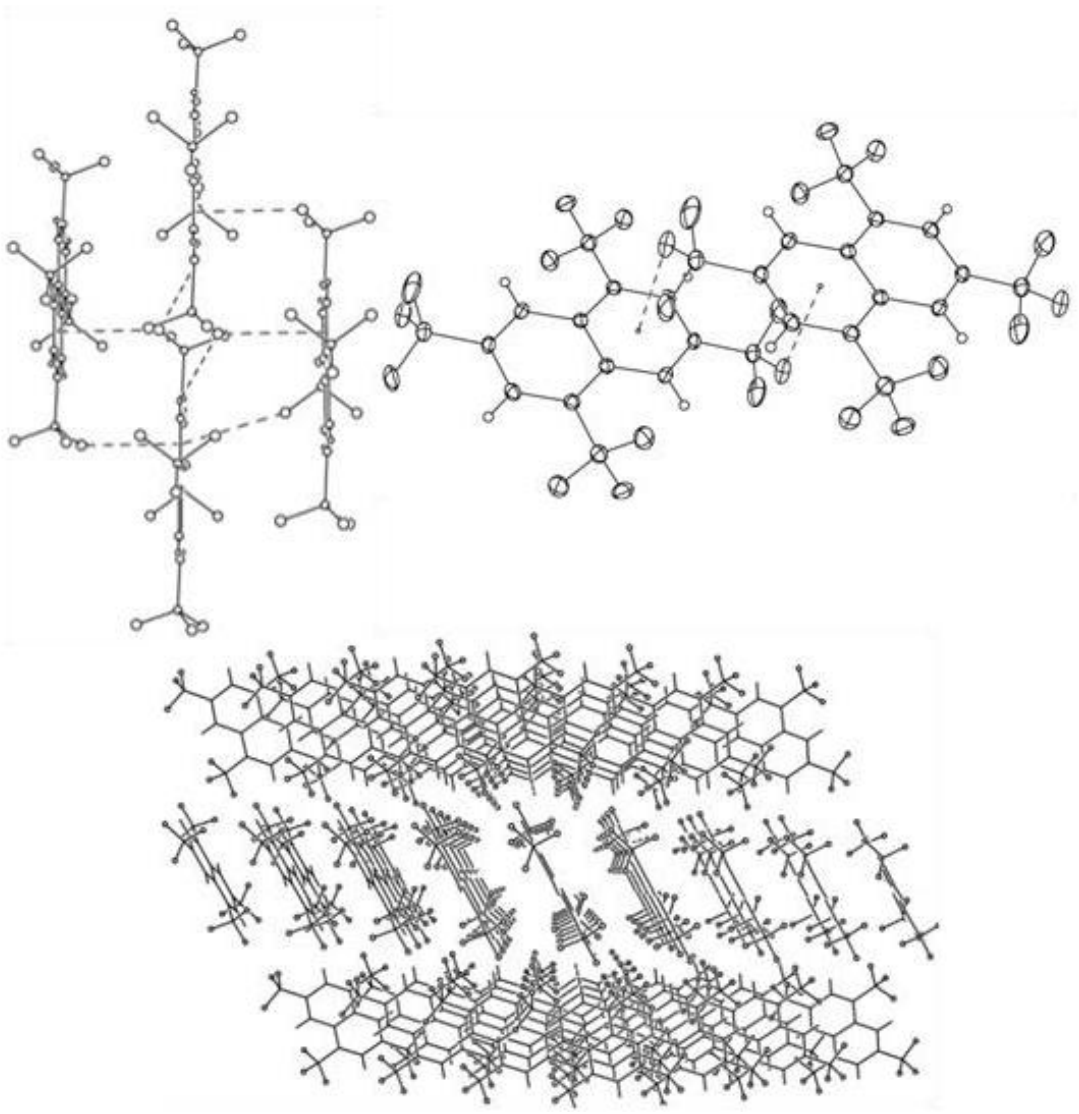

Figure 2.2.16. Crystal packing in 1,3,5,7-NAPH(CF_3)$_4$.

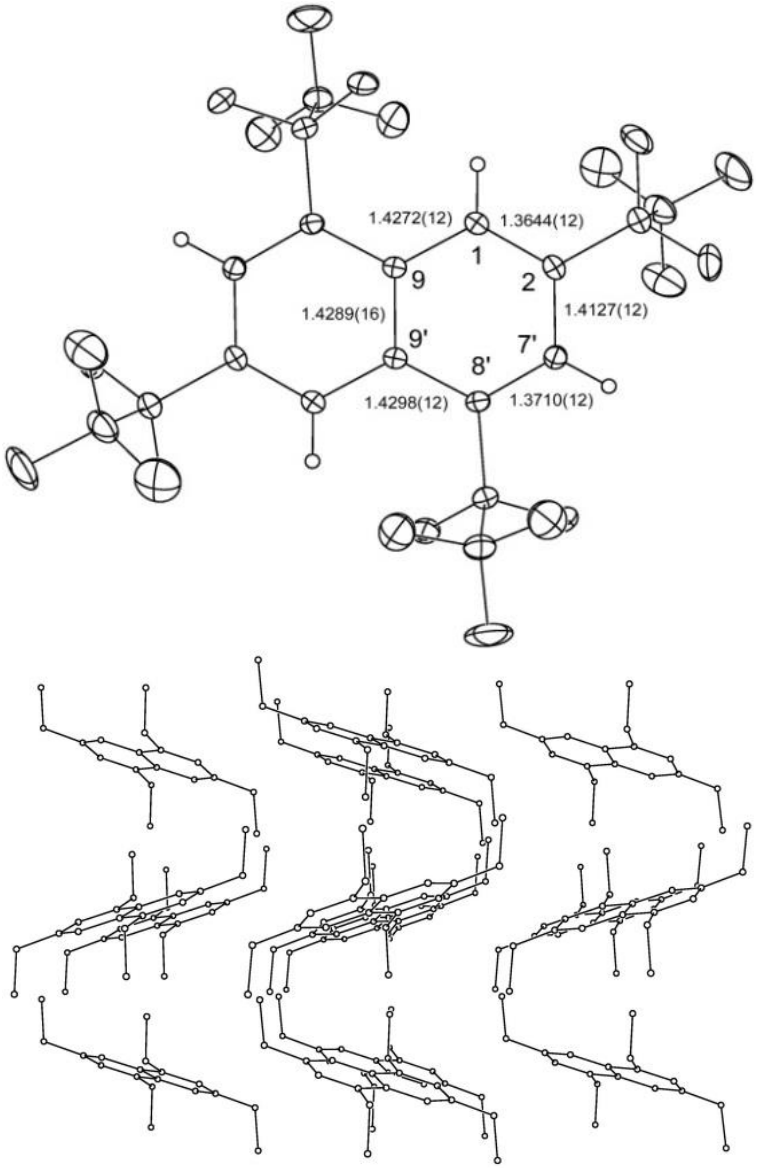

Figure 2.2.17. Top: Single-crystal X-ray diffraction structure of 1,3,5,7-NAPH$(C_2F_5)_4$, 50% probability ellipsoids used for all non-hydrogen atoms of the ORTEP drawing. Bottom: Crystal packing in 1,3,5,7-NAPH$(C_2F_5)_4$. Fluorine and hydrogen atoms are removed for clarity.

Table 2.2.1. Molar yields of crude NAPH(R_F)$_n$ products and the average number of R_F groups per NAPH core.

product	R_F	molar yield of crude NAPH(R_F)$_n$, %	average n(R_F) per NAPH core
A	CF_3	80±15	2.4±0.1
B	C_2F_5	70±15	2.3±0.1
C	n-C_3F_7	95±10	1.9±0.1
D	n-C_4F_9	95±10	1.9±0.1

Table 2.2.2. DFT relative energies (kJ/mol) of NAPH$(CF_3)_n$.

compound	PBE/TZ2P	B3LYP-D3/def-TZVP
2-NAPH(CF_3)	0.0	0.0
1-NAPH(CF_3)	8.3	6.6
2,6-NAPH$(CF_3)_2$	0.0	0.0
2,7-NAPH$(CF_3)_2$	0.0	0.3
1,6-NAPH$(CF_3)_2$	7.8	6.0
1,7-NAPH$(CF_3)_2$	9.1	6.9
1,3-NAPH$(CF_3)_2$	9.9	7.7
1,5-NAPH$(CF_3)_2$	17.0	13.4
1,4-NAPH$(CF_3)_2$	19.1	15.8
2,3-NAPH$(CF_3)_2$	25.5	25.0
1,2-NAPH$(CF_3)_2$	51.1	50.0
1,8-NAPH$(CF_3)_2$	76.5	75.6
1,3,6-NAPH$(CF_3)_3$	0.0	0.0
1,3,7-NAPH$(CF_3)_3$	1.2	0.7
1,3,5-NAPH$(CF_3)_3$	9.9	7.6
1,4,6-NAPH$(CF_3)_3$	9.8	8.1
2,3,6-NAPH$(CF_3)_3$	16.0	17.7
1,2,6-NAPH$(CF_3)_3$	40.7	41.6
1,2,7-NAPH$(CF_3)_3$	41.8	42.3
1,2,5-NAPH$(CF_3)_3$	49.9	49.6
1,2,4-NAPH$(CF_3)_3$	53.4	53.1
1,3,8-NAPH$(CF_3)_3$	68.5	68.6
1,4,5-NAPH$(CF_3)_3$	79.8	79.3
1,2,3-NAPH$(CF_3)_3$	83.5	83.7
1,2,8-NAPH$(CF_3)_3$	105.8	106.0
1,3,5,7-NAPH$(CF_3)_4$	0.0	0.0
1,3,6,7-NAPH$(CF_3)_4$	13.8	16.0
2,3,6,7-NAPH$(CF_3)_4$	29.0	33.4
1,2,5,7-NAPH$(CF_3)_4$	39.5	40.9
1,2,4,6-NAPH$(CF_3)_4$	40.9	43.2
1,2,4,7-NAPH$(CF_3)_4$	40.8	43.3
1,2,6,7-NAPH$(CF_3)_4$	53.9	57.0
1,3,6,8-NAPH$(CF_3)_4$	57.7	60.6
1,3,5,8-NAPH$(CF_3)_4$	69.7	71.1
1,2,3,6-NAPH$(CF_3)_4$	70.1	73.5
1,2,3,7-NAPH$(CF_3)_4$	71.1	74.2
1,2,3,5-NAPH$(CF_3)_4$	80.0	81.5
1,2,5,6-NAPH$(CF_3)_4$	78.7	82.0
1,2,6,8-NAPH$(CF_3)_4$	94.6	97.3
1,2,5,8-NAPH$(CF_3)_4$	104.8	106.6
1,2,4,8-NAPH$(CF_3)_4$	106.5	108.0
1,2,4,5-NAPH$(CF_3)_4$	109.8	112.8
1,2,7,8-NAPH$(CF_3)_4$	129.6	132.0
1,2,3,8-NAPH$(CF_3)_4$	132.1	134.9
1,4,5,8-NAPH$(CF_3)_4$	137.9	141.1
1,2,3,4-NAPH$(CF_3)_4$	139.4	142.0

Table 2.2.3. Comparison of DFT relative energies (kJ/mol) for the selected NAPH$(C_2F_5)_{3,4}$ and NAPH$(CF_3)_{3,4}$ isomers calculated using B3LYP-D3/def-TZVP.

compound	$R_F = CF_3$	$R_F = C_2F_5$
1,3,6-NAPH$(R_F)_3$	0.0	0.0
1,3,7-NAPH$(R_F)_3$	0.7	0.3
1,3,5-NAPH$(R_F)_3$	7.6	15.8
1,4,6-NAPH$(R_F)_3$	8.1	17.2
1,3,5,7-NAPH$(R_F)_4$	0.0	0.0
1,3,6,7-NAPH$(R_F)_4$	16.0	22.0
2,3,6,7-NAPH$(R_F)_4$	33.4	48.1

Table 2.2.4. First reduction potentials $E_{1/2}$ and peak potentials for The $E_{1/2}^{0/-}$ of naphthalene and 1,3,5,7-NAPH$(R_F)_4$ compounds relative to $Fe(Cp_2)^{+/0}$ defined as 0.0 V.

compound	$E_{1/2}$, V	1st peak potential, V
NAPH	−3.08	−3.05
NAPH$(CF_3)_4$	−1.62	−1.64
NAPH$(C_2F_5)_4$	−1.63	−1.59
NAPH$(C_3F_7)_4$	−1.55	−1.56
NAPH$(C_4F_9)_4$	−1.56	−1.56

Table 2.2.5. DFT calculated and experimental gas phase electron affinities (eV) for NAPH(R_F)$_4$ derivatives.

R_F =	standard	augmented	experimental
CF_3	1.685	1.744	1.795
C_2F_5	1.839	1.902	1.930
n-C_3F_7	1.925	1.985	2.055
n-C_4F_9	1.988	2.045	2.115

Values calculated with "standard" were performed using B3LYP-D3/def2-TZVP, augmented contain additional diffuse functions, and experimental were determined by LT-PES. The uncertainty in the experimental measurement is ±0.020 eV.

Table 2.2.6. Melting points and sublimation rates of NAPH, 1,3,5,7-NAPH(CF_3)$_4$, and 1,3,5,7-NAPH(C_2F_5)$_4$ at 25.0 °C.

compound	melting point, °C	sublimation rate, μmol min^{-1}
NAPH	75.0 – 78.0	3.6×10^{-2}
1,3,5,7-NAPH(CF_3)$_4$	99.0 – 99.8	3.7×10^{-3}
1,3,5,7-NAPH(C_2F_5)$_4$	88.5 – 89.0	7.3×10^{-4}

Table 2.2.7. Reaction conditions used for naphthalene perfluoroalkylation and mass of crude NAPH(R_F)$_n$ products.

exp.	R_FI reagent	reaction temperature, °C	reaction time, min	*n*(NAPH), mmol	*n*(R_FI), mmol	m(crude product),[a] mg
A	CF_3I	300	180	0.157	1.36	70
B	C_2F_5I	300	180	0.157	1.34	45
C	1-C_3F_7I	300	180	0.163	1.30	69
D	1-C_4F_9I	300	180	0.165	1.31	91

[a] The mass was determined upon concentrating the crude product mixture to dryness under a stream of air.

Table 2.2.8. Concentrations of R_F and hydrogen substituents for NAPH$(R_F)_n$ solutions and molar yields of NAPH$(R_F)_n$ products.

exp.	R_F	[R_F], mM	[H], mM	*n*(NAPH$(R_F)_n$), µmol	yield of NAPH$(R_F)_n$,[a] mol%
A	CF_3	98	230	123	79 ± 15
B	C_2F_5	87	210	111	70 ± 15
C	*n*-C_3F_7	95	310	152	95 ± 10
D	*n*-C_4F_9	100	310	154	96 ± 10

[a] 160 µmol of naphthalene starting material was used for each perfluoroalkylation experiment.

Table 2.2.9. Selected crystallographic and data-collection parameters for NAPH$(CF_3)_4$ and NAPH$(C_2F_5)_4$.

compound	1,3,5,7-NAPH$(CF_3)_4$	1,3,5,7-NAPH$(C_2F_5)_4$
empirical formula	$C_{14}H_4F_{12}$	$C_{18}H_4F_{20}$
formula weight	400.17	600.21
habit, color	plate, colorless	plate, colorless
crystal size (mm)	0.26 × 0.15 × 0.05	0.52 × 0.29 × 0.15
space group	P2(1)/C	Pbca
a (Å)	6.6592(7)	11.2782(3)
b (Å)	6.3490(6)	10.4581(3)
c (Å)	15.7170(17)	16.6261(5)
α (°)	90.00	90.00
β (°)	91.099(5)	90.00
γ (°)	90.00	90.00
V (Å^3)	664.38(12)	1961.02(10)
Z	2	4
T (K)	120(2)	120(2)
ρ_{calc} (g cm^{-3})	2.000	2.033
R(F) ($I>2\sigma(I)$)[a]	0.0339	0.0359
wR(F^2) [all data][a]	0.0787	0.1032

[a] $R(F) = \Sigma \left| |F_o| - |F_c| \right| / \Sigma |F_o|$; $wR(F^2) = (\Sigma[w(F_o^2 - F_c^2)^2] / \Sigma[w(F_o^2)^2])^{1/2}$.

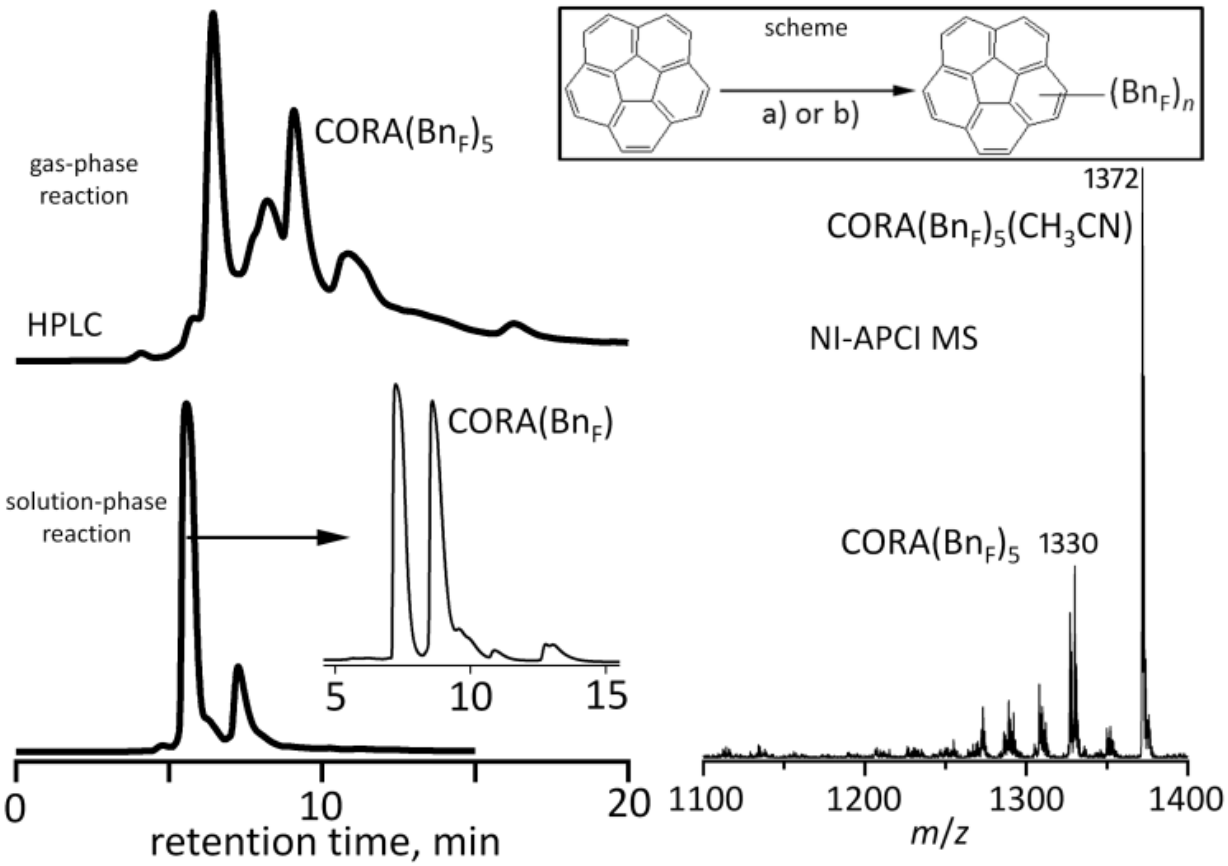

Figure 2.3.1. Left: HPLC chromatograms of the crude products of: gas-phase (top panel) and solution-phase (bottom panel) reactions (250 × 10 mm i.d. COSMOSIL Buckyprep column, 25/75 (v/v) toluene/heptane eluent, 5 mL min^{-1} flow rate, 300 nm UV detection). Inset shows second separation step (100% MeCN eluent, 5 mL min^{-1} flow rate) for **CORA(Bn_F)**. Right: Reaction scheme between $C_{20}H_{10}$ and $C_6F_5CF_2I$: a) solution-phase, 1 eq. CORA, 2 eq. $C_6F_5CF_2I$, 3 eq. Cu, DMSO, 160 °C, 24 h; b) gas-phase, sealed ampoule, 1 eq. CORA, 20 eq. $C_6F_5CF_2I$, 200 °C, 1 h (top panel); Negative-ion APCI mass spectrum of **CORA(Bn_F)$_5$** (bottom panel).

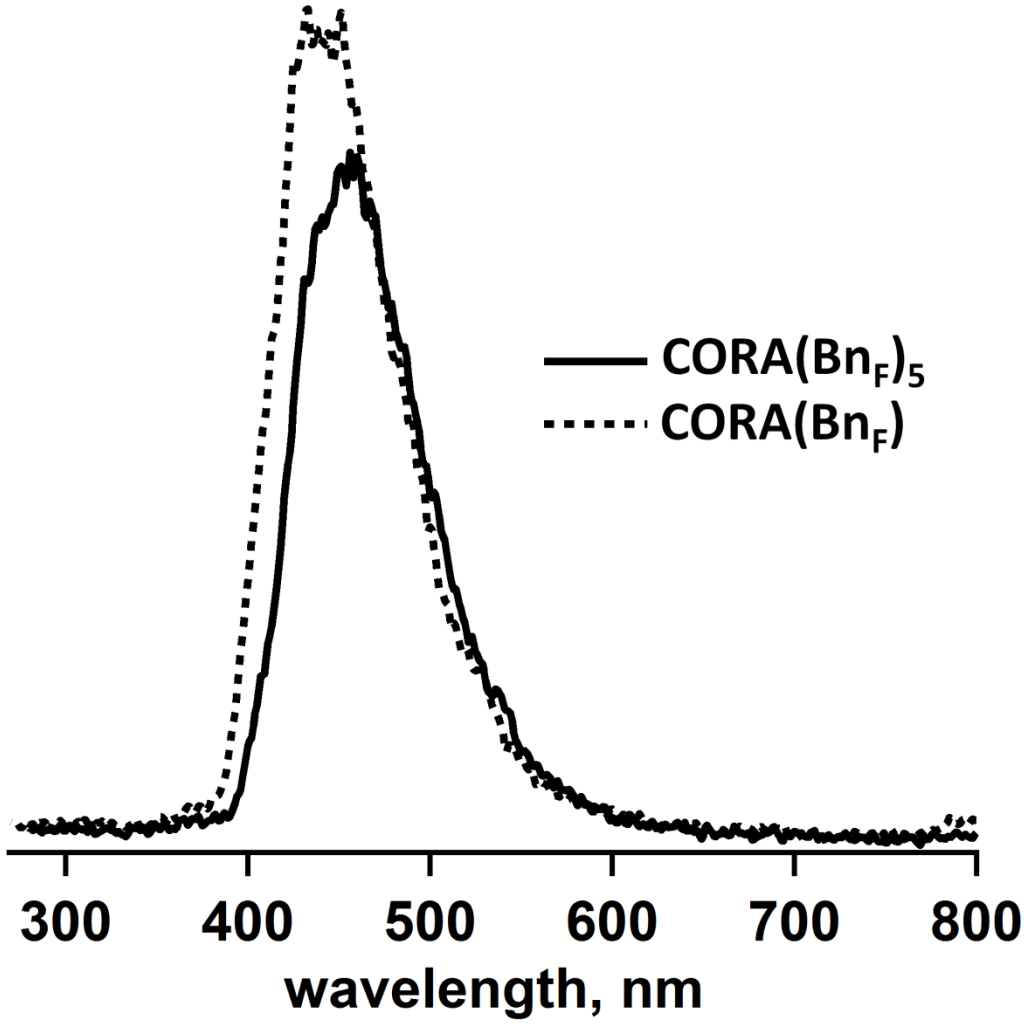

compound	concentration (M)	λmax (nm)	Δλmax (nm)	λmax (nm)	Δλmax (nm)
CORA*	3.9×10^{-6}	254	–	289	–
CORA(Bn$_F$)$_5$	8.1×10^{-5}	262	+8	295	+6
CORA(Bn$_F$)	1.5×10^{-4}	255	+1	289	0

Figure 2.3.2. Emission spectra of **CORA(Bn$_F$)$_5$** and **CORA(Bn$_F$)** in CH_2Cl_2. * Values taken from J. Mack, P. Vogel, D. Jones, N. Kaval, A. Sutton, *Org. Biomol. Chem.* **2007**, *5*, 2448-2452.

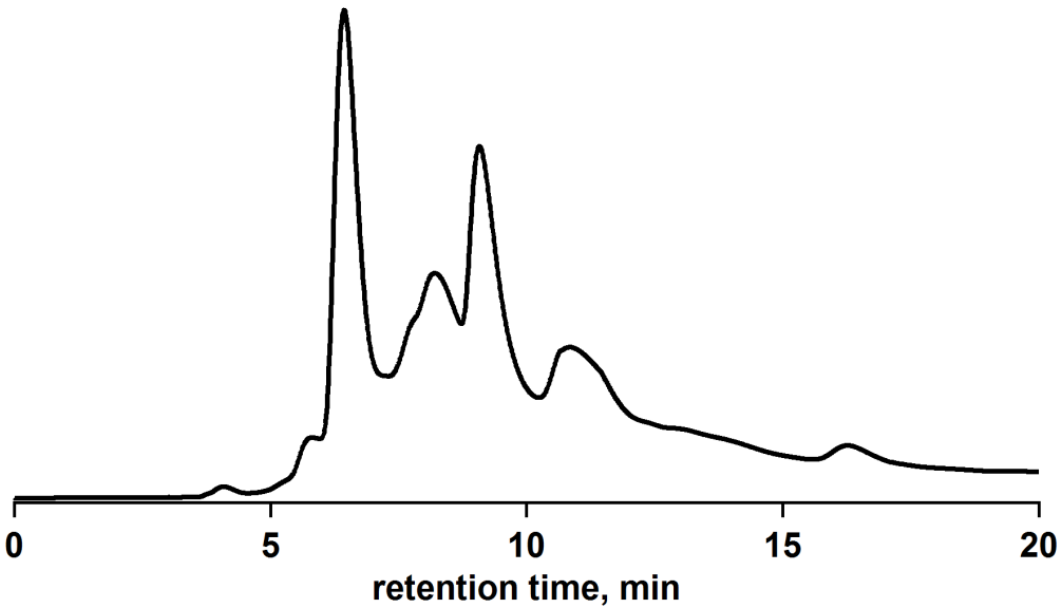

The first separation stage resulted in four fractions:

F1 fraction between t_R = 6.1–7.2 min $C_{20}H_6(CF_2C_6F_5)_4$ isomers

F2 fraction between t_R = 7.0–8.8 min $C_{20}H_6(CF_2C_6F_5)_3(C_6F_5)$

F3 fraction between t_R = 8.5–10.0 min C_5-$C_{20}H_5(CF_2C_6F_5)_5$ [**CORA(Bn$_F$)$_5$**]

F4 fraction between t_R = 10.1–11.7 min $C_{20}H_6(CF_2C_6F_5)_4(C_6F_5)$

Figure 2.3.3. 1st stage HPLC chromatogram of the crude product mixture from the gas-phase reactions using the Buckyprep semi-preparative column using a 25/75 (v/v) toluene/heptane mobile phase at a flow rate of 5 mL min^{-1}.

Separation of fraction F1

From **Figure 2.3.3**, the fraction between t_R = 6.1–7.2 min. was collected and further purified by collecting the fraction between t_R = 14.6–17.2 min. (**Figure 2.3.4** top) using 100% acetonitrile mobile phase and Buckyprep semi-preparative column. This fraction was then further purified by collecting the fraction between t_R = 7.7–9.5 min. (**Figure 2.3.4** bottom) using 100% heptane mobile phase and Buckyprep-M semi-preparative column. A total of three stages of separation were used.

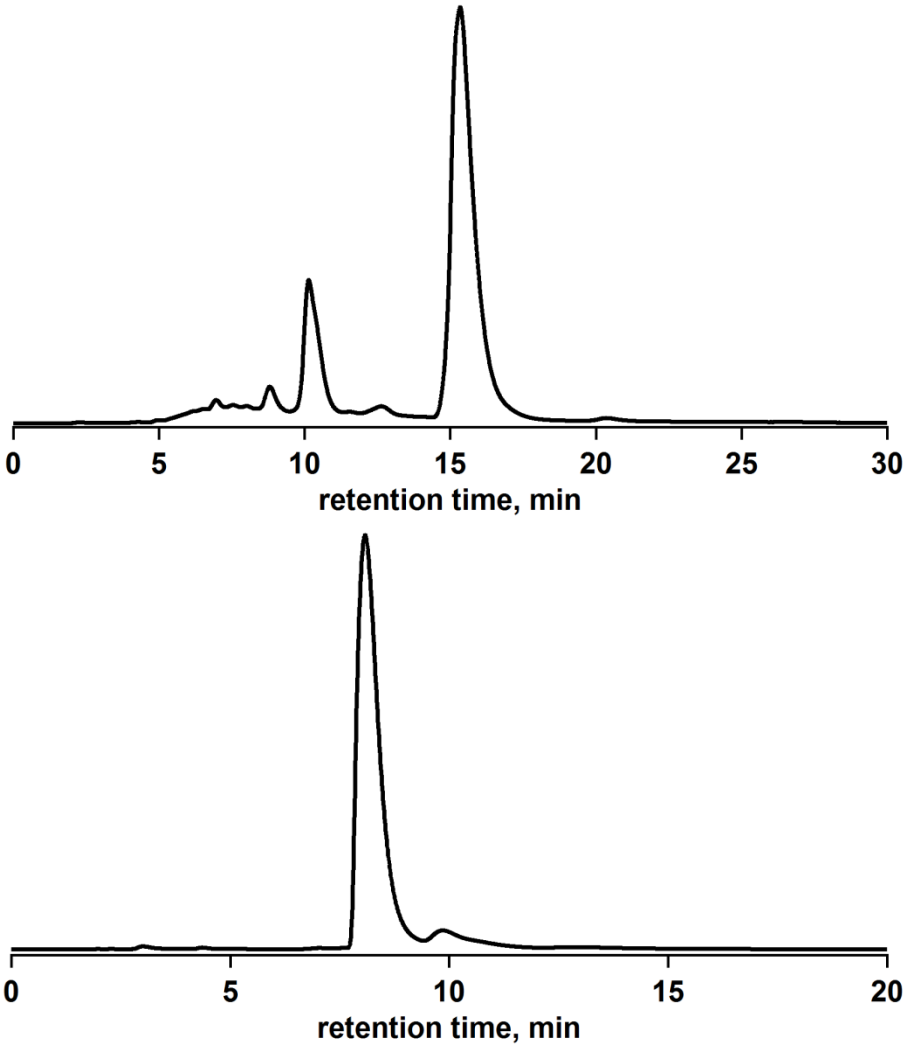

Figure 2.3.4. HPLC chromatogram of the 2nd (top) and 3rd (bottom) stage of separation for Fraction F1.

Separation of fraction F2

From **Figure 2.3.3**, the fraction F2 between t_R = 8.5–10.0 min. was collected and further purified by collecting the fraction between t_R = 16.8–19.5 min. (**Figure 2.3.5**) using 10/90 (v/v) toluene/heptane and Buckyprep semi-preparative column at a flow rate of 7 mL min^{-1}. A total of two stages of separation were used.

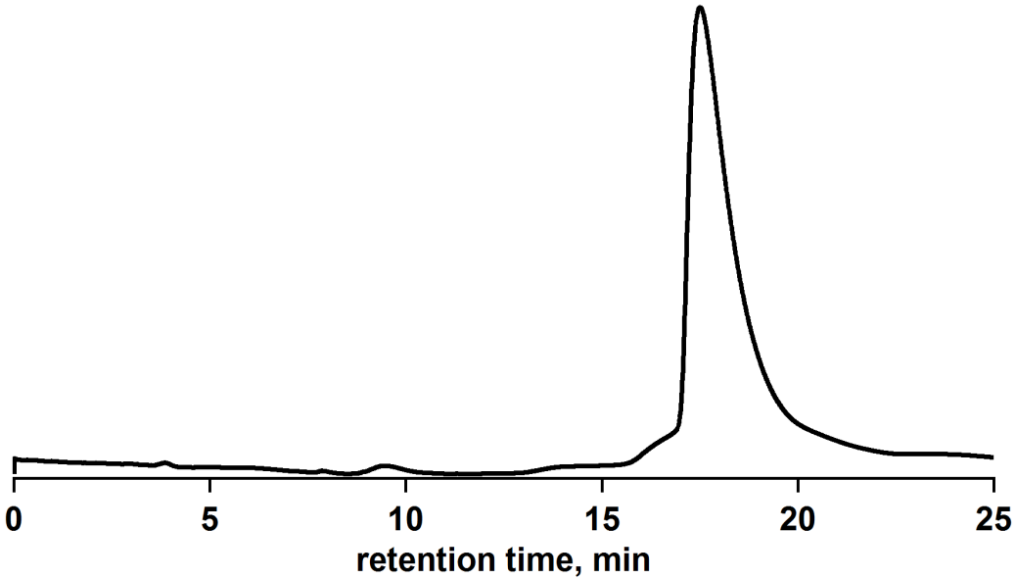

Figure 2.3.5. HPLC chromatogram of the 2nd stage of separation for **CORA(Bn_F)$_5$**.

Separation of fraction F3

From **Figure 2.3.3**, the fraction between t_R = 10.1–11.7 min. was collected and further purified by collecting the fraction between t_R = 18.5–22.4 min. (**Figure 2.3.6** top) using 100% acetonitrile and Buckyprep semi-preparative column at a flow rate of 8 mL min^{-1}. This fraction was then further purified by collecting the fraction between t_R = 9.5-11.2 min. (**Figure 2.3.6** bottom) using 100% heptane mobile phase and Buckyprep-M semi-preparative column. A total of three stages of separation were used.

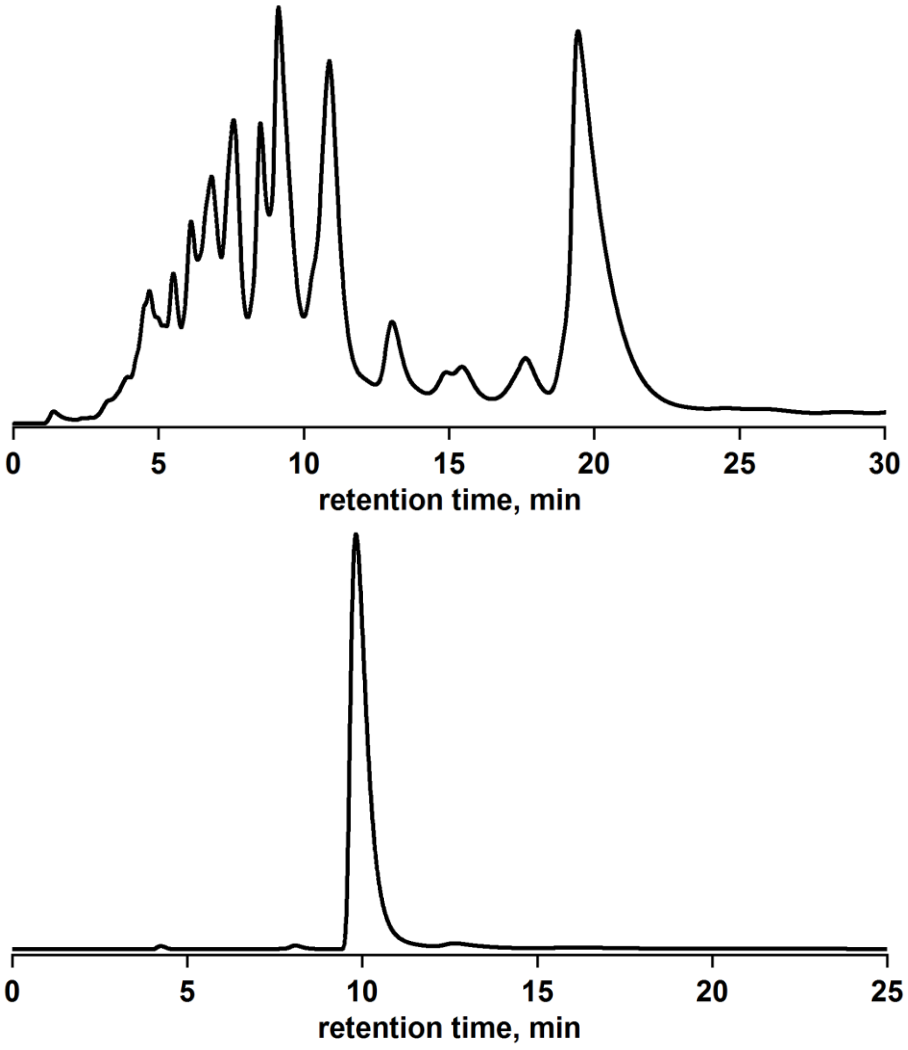

Figure 2.3.6. HPLC chromatogram of the 2nd (top) and 3rd (bottom) stage of separation for Fraction F4.

Separation of fraction F4

From **Figure 2.3.3**, the fraction between t_R = 7.0–8.8 min. was collected and further purified by collecting the fraction between t_R = 18.9–21.5 min. (trace a) using 100% acetonitrile and Buckyprep semi-preparative column. This fraction was further purified by collecting the fraction between t_R = 3.4–4.6 min. (trace b) using 100% acetonitrile and FluoroFlash column. This fraction was further purified by collecting the fraction between t_R = 18.2–23.0 min. (trace c) using 10/90 (v/v) toluene/heptane and Buckyprep semi-preparative column. This fraction was further purified by collecting the fraction between t_R = 25.0–29.2 min. (trace d) using 60/40 (v/v) acetonitrile/methanol and Buckyprep semi-preparative column. This fraction was further purified by collecting the fraction between t_R = 10.1–11.5 min. (trace e) using 90/10 (v/v) acetonitrile/water and FluoroFlash column.

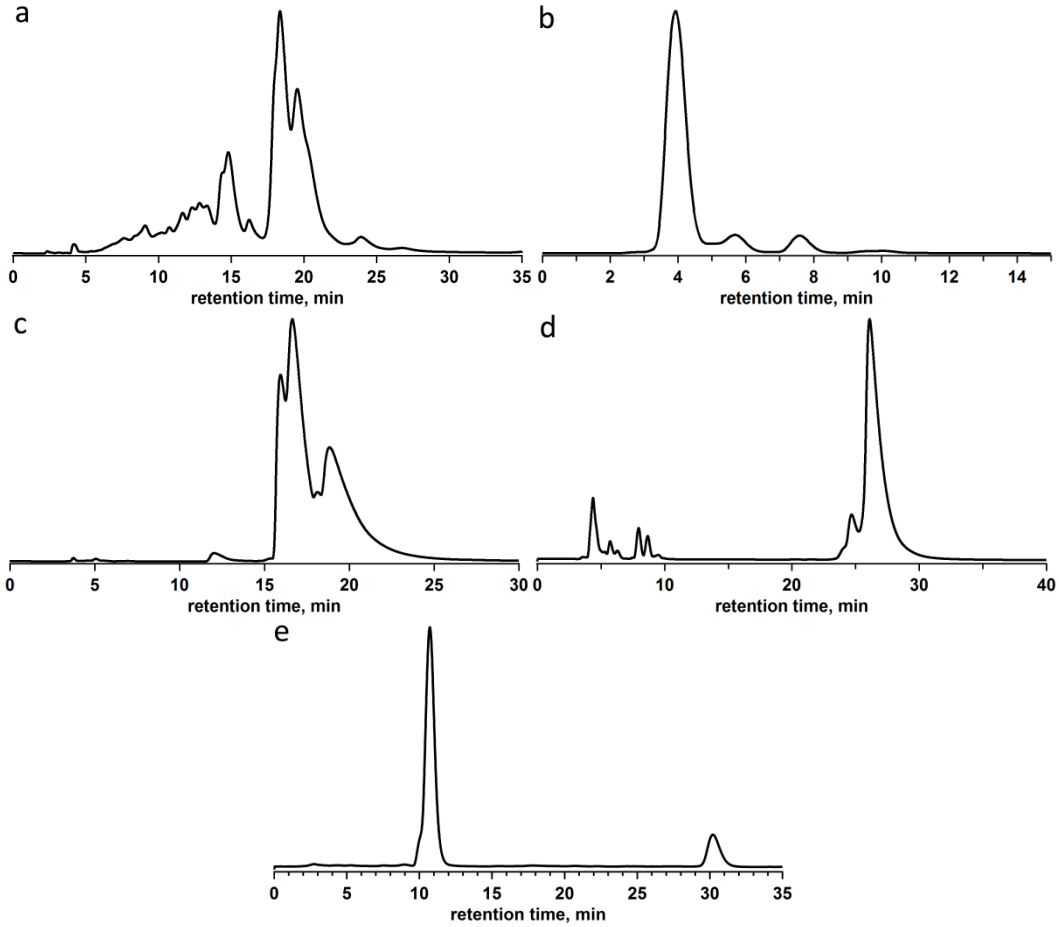

Figure 2.3.7. HPLC chromatograms for separation of Fraction F2.

Isolation of CORA(Bn$_F$), $C_{20}H_9(CF_2C_6F_5)$:

From the solution-phase reaction, the fraction between t_R = 5.5–6.2 min. was collected in the 1st stage of separation (**Figure 2.3.8** top) using 25/75 (v/v) toluene/heptane and Buckyprep semi-preparative column. This fraction was then further purified collecting t_R = 8.2–8.9 min. (**Figure 2.3.8** bottom) using 100% acetonitrile and Buckyprep semi-preparative column.

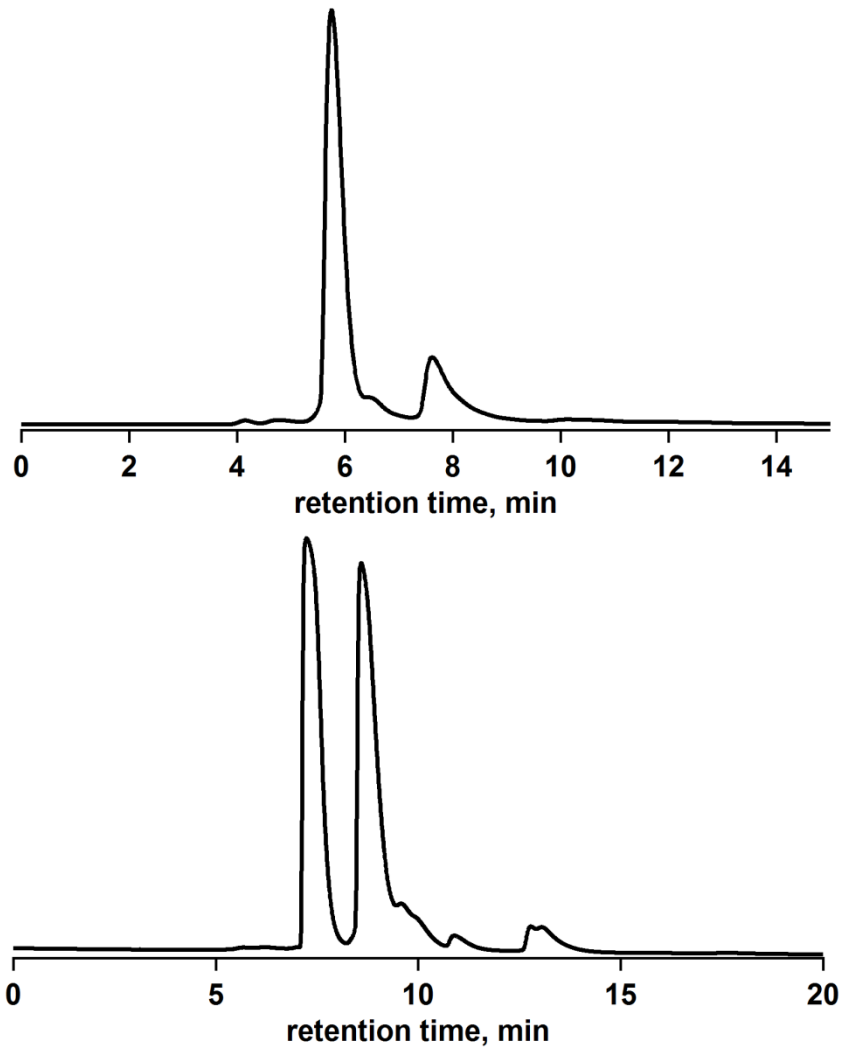

Figure 2.3.8. HPLC chromatogram of the 1st stage of separation (top) and the 2nd stage of separation (bottom) for **CORA(Bn$_F$)**.

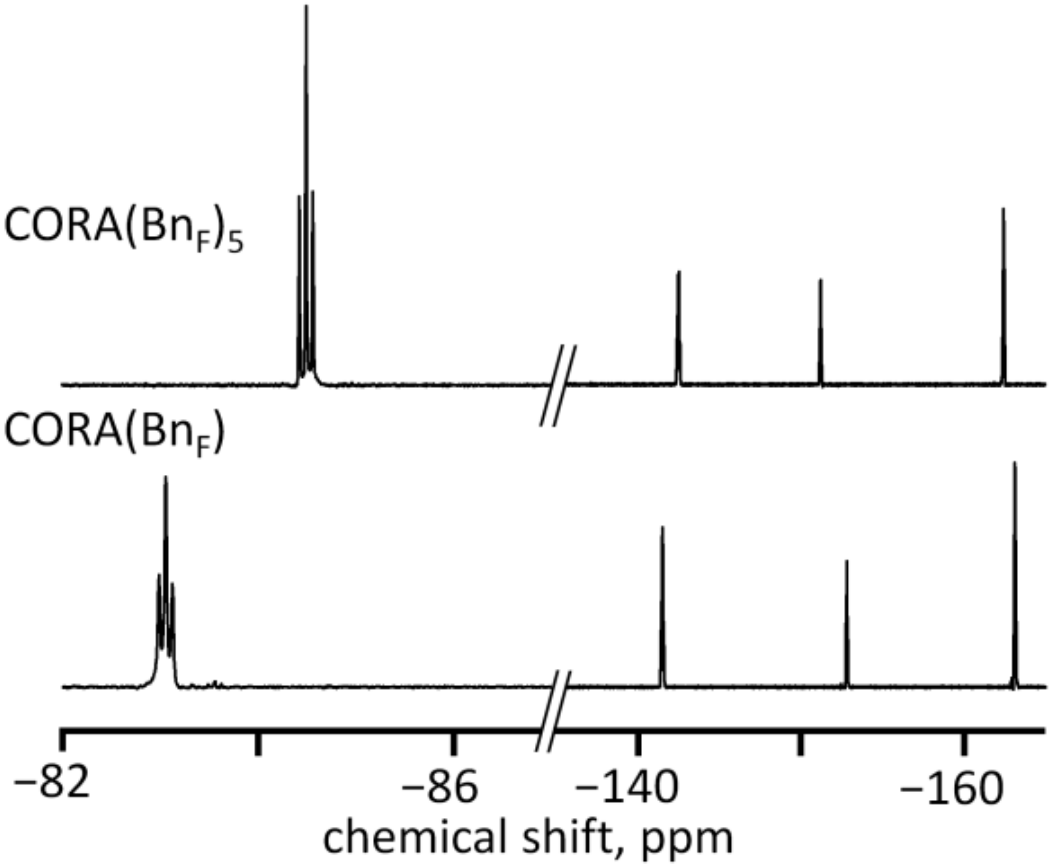

Figure 2.3.9. Fluorine-19 NMR spectra ($CDCl_3$, 376 MHz, δ(1,4-$C_6H_4(CF_3)_2$) = −66.35 ppm) of CORA(Bn_F)$_n$ compounds showing the CF_2 and Ar_F regions.

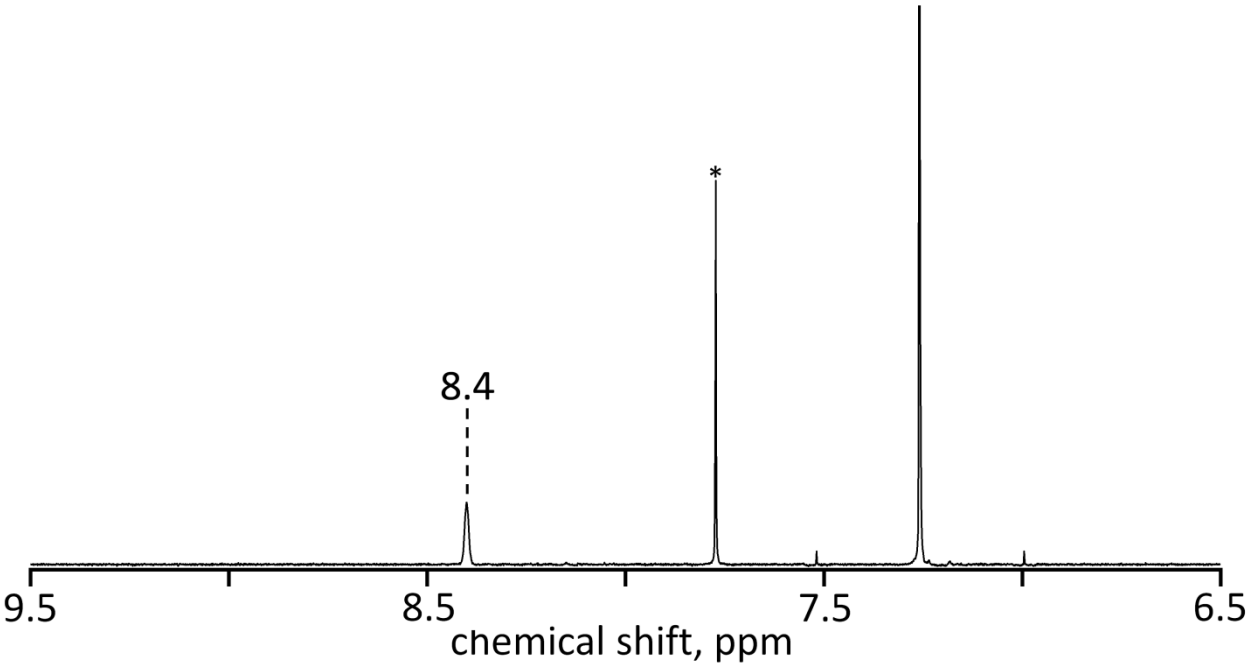

Figure 2.3.10. Proton NMR spectra ($CDCl_3$, 399 MHz) of **CORA(Bn_F)$_5$** showing the Ar_H region. The internal standard 1,4-$(CF_3)_2$-C_6H_4 (δ = 7.77 ppm) is marked by asterisk and the residual solvent ($CHCl_3$, δ = 7.26 ppm) are shown.

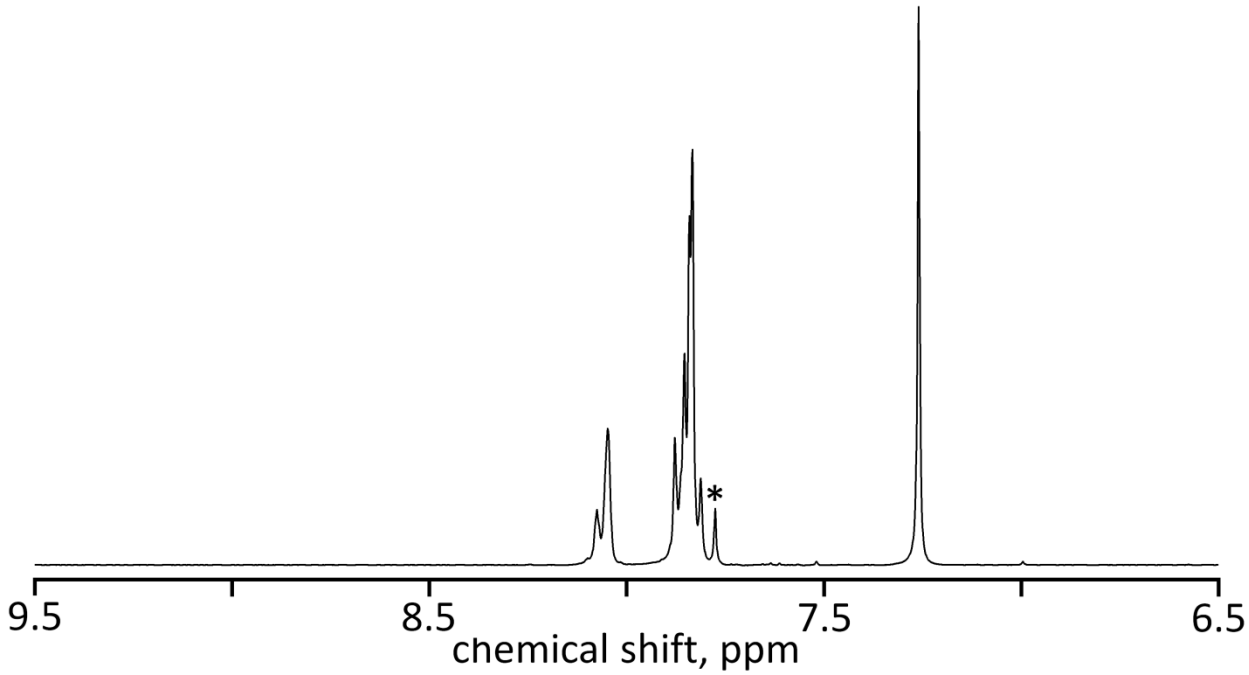

Figure 2.3.11. Proton NMR spectra ($CDCl_3$, 399 MHz) of **CORA(Bn_F)** compounds showing the Ar_H region. The internal standard 1,4-$(CF_3)_2$-C_6H_4 (δ = 7.77 ppm) is marked by asterisk and the residual solvent ($CHCl_3$, δ = 7.26 ppm) are shown.

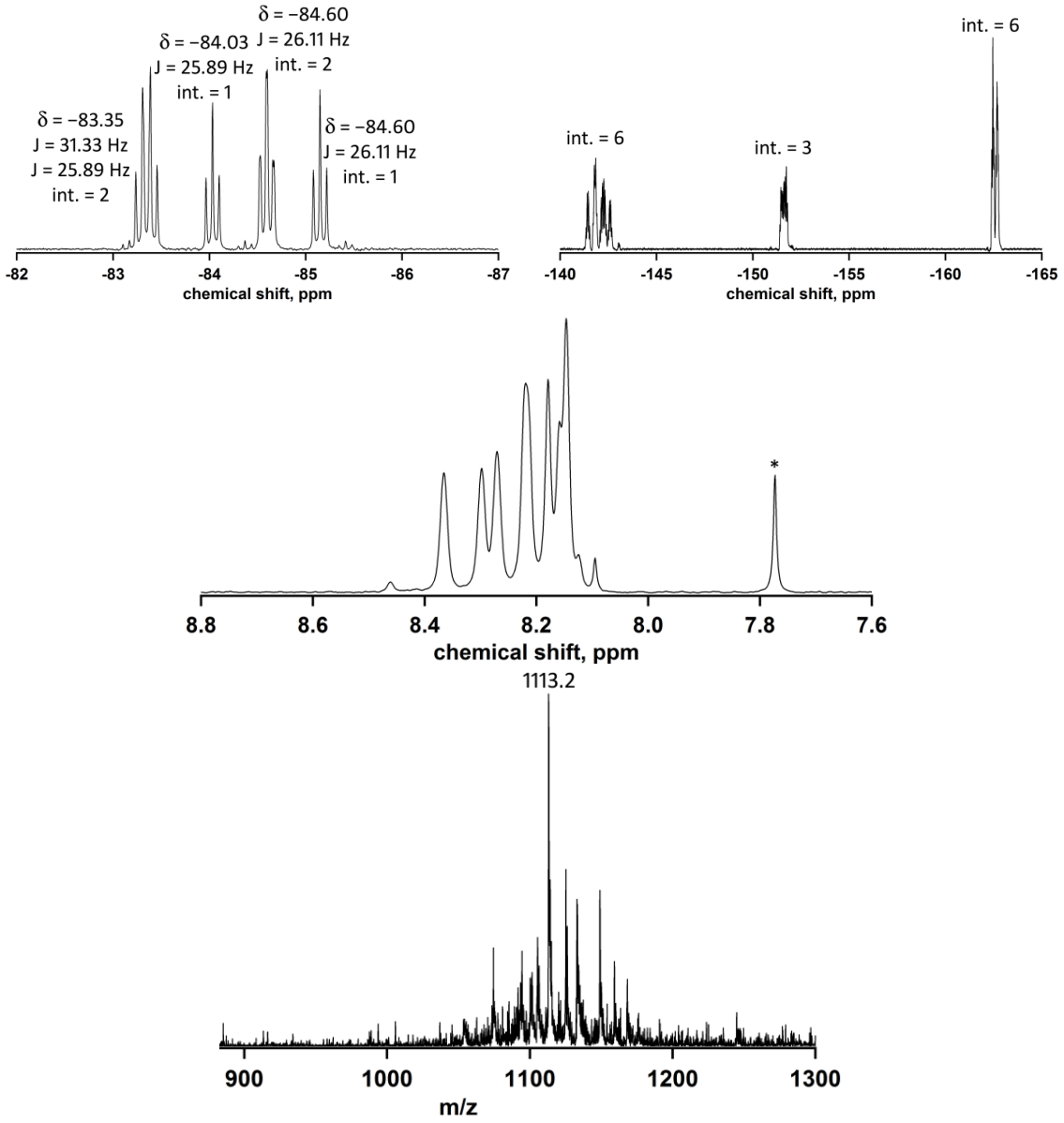

Figure 2.3.12. Characterization data for putative CORA(Bn_F)$_4$. From top to bottom: ^{19}F NMR spectra (379 MHz), ^{1}H NMR spectra (399 MHz), APCI-MS spectrum. NMR spectroscopy was performed in $CDCl_3$ with internal standard (* in ^{1}H NMR) 1,4-$C_6H_4(CF_3)_2$ (δ 7.77). It is tentatively concluded that this fraction contains a mixture of two CORA(Bn_F)$_4$ isomers, one symmetric and one asymmetric isomer. Attempts to further separate these two compounds have not yet succeeded.

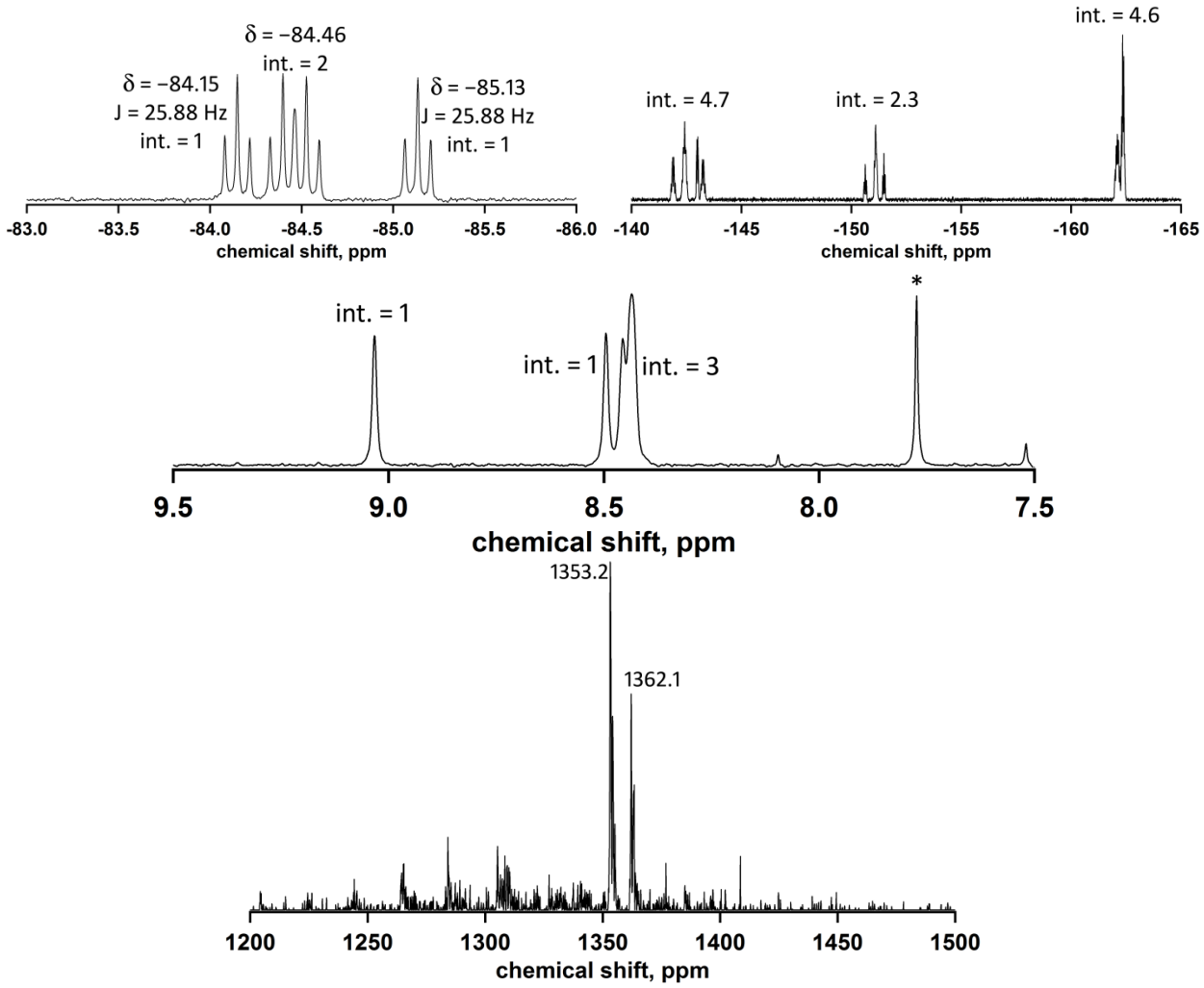

Figure 2.3.13. Characterization data for putative CORA(Bn_F)$_4$(C_6F_5). From top to bottom: ^{19}F NMR spectra (379 MHz), ^{1}H NMR spectra (399 MHz), APCI-MS spectrum. NMR spectroscopy was performed in $CDCl_3$ with internal standard (* in ^{1}H NMR) 1,4-$C_6H_4(CF_3)_2$ (δ 7.77). This compound appears to contain four Bn_F groups and one C_6F_5 group resulting in a formula of $C_{20}H_6(CF_2C_6F_5)_4(C_6F_5)$.

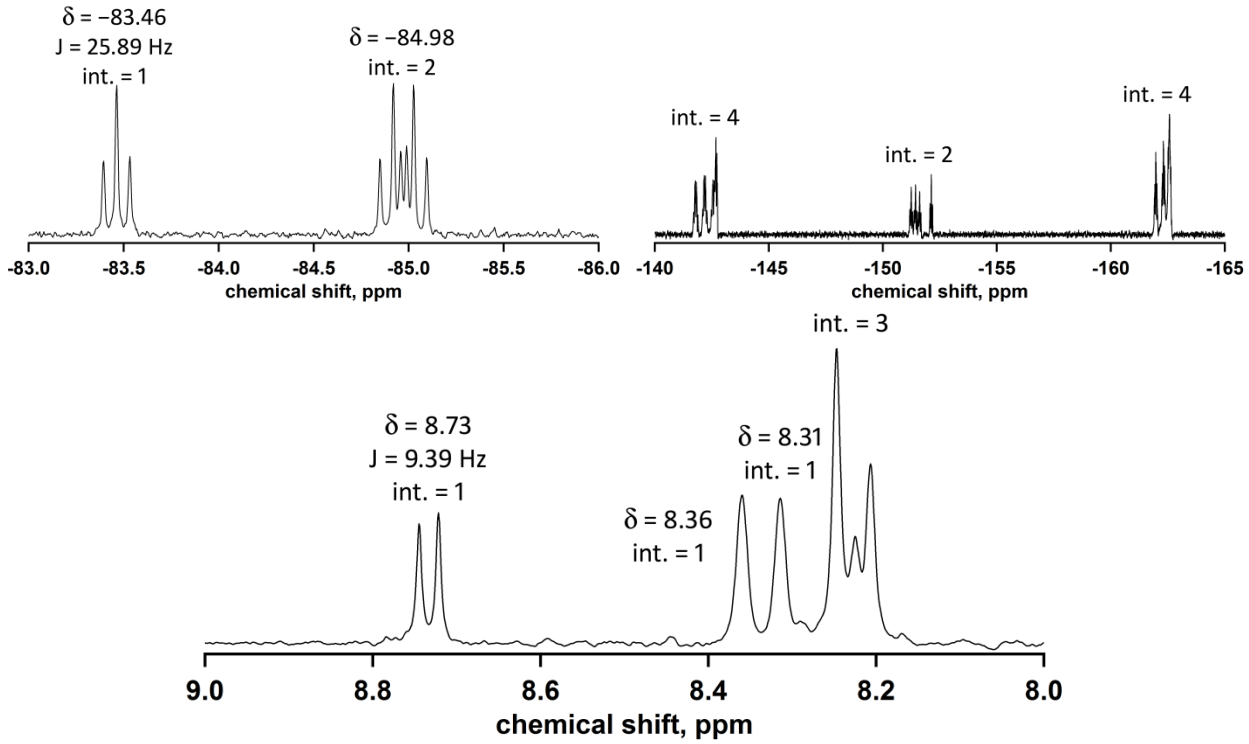

Figure 2.3.14. Characterization data for putative CORA(Bn_F)$_3$(C_6F_5). From top to bottom: ^{19}F NMR spectra (379 MHz) and ^{1}H NMR spectra (399 MHz). NMR spectroscopy was performed in $CDCl_3$ with internal standard (* in ^{1}H NMR) 1,4-$C_6H_4(CF_3)_2$ (δ 7.77). This compound appears to contain three Bn_F groups and one C_6F_5 resulting in a formula of $C_{20}H_6(CF_2C_6F_5)_3(C_6F_5)$. APCI Mass spectrum of this compound had low intensity and was not conclusive.

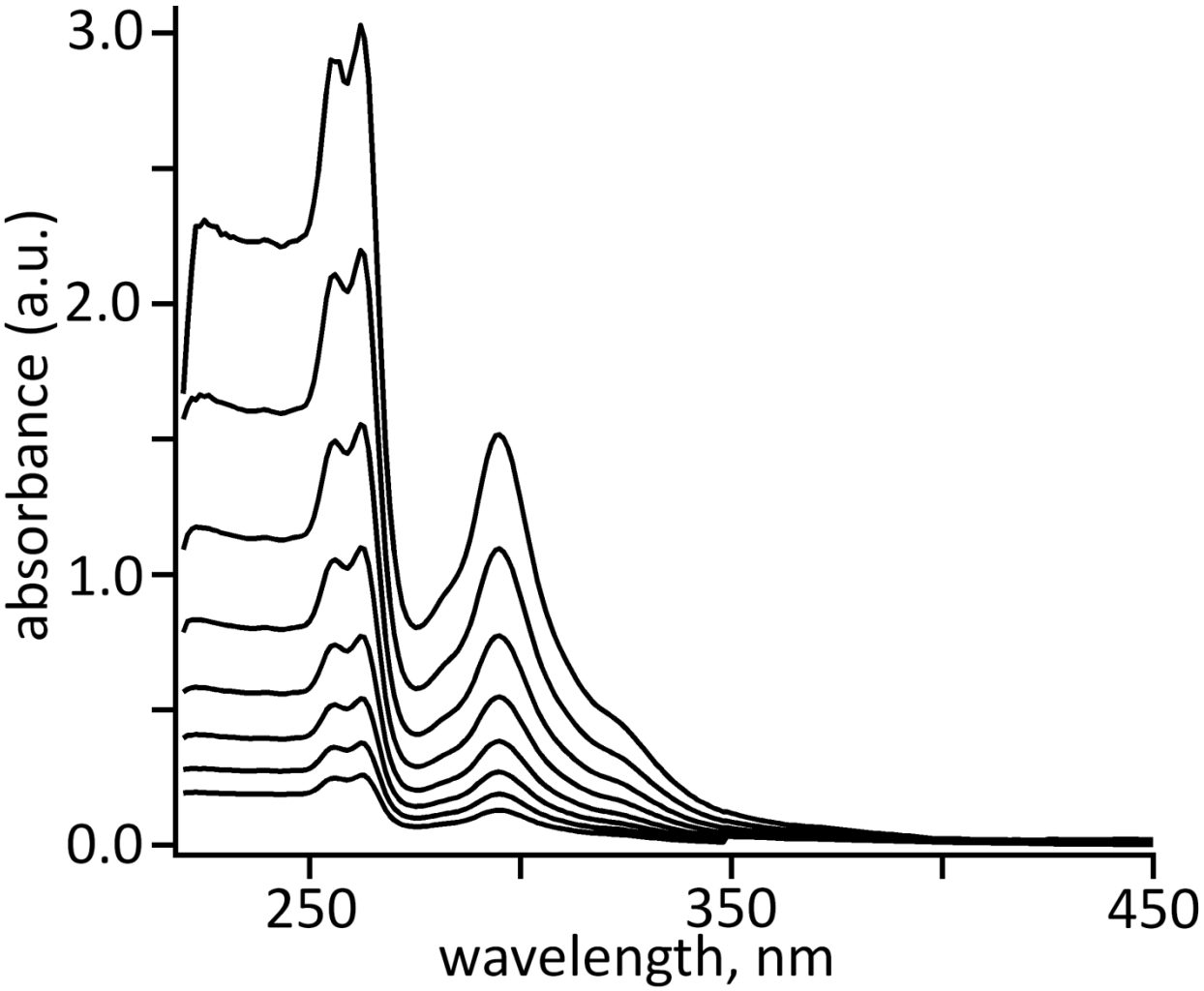

Figure 2.3.15. Absorption spectra of **CORA(Bn$_F$)$_5$** upon successive dilutions in CH_2Cl_2. Spectra between 1.1 and 0.13 absorbance were used to calculate log ε.
UV-vis (CH_2Cl_2, λ_{max} (log ε)): 256 (4.68), 262 (4.70), 295 (4.40).

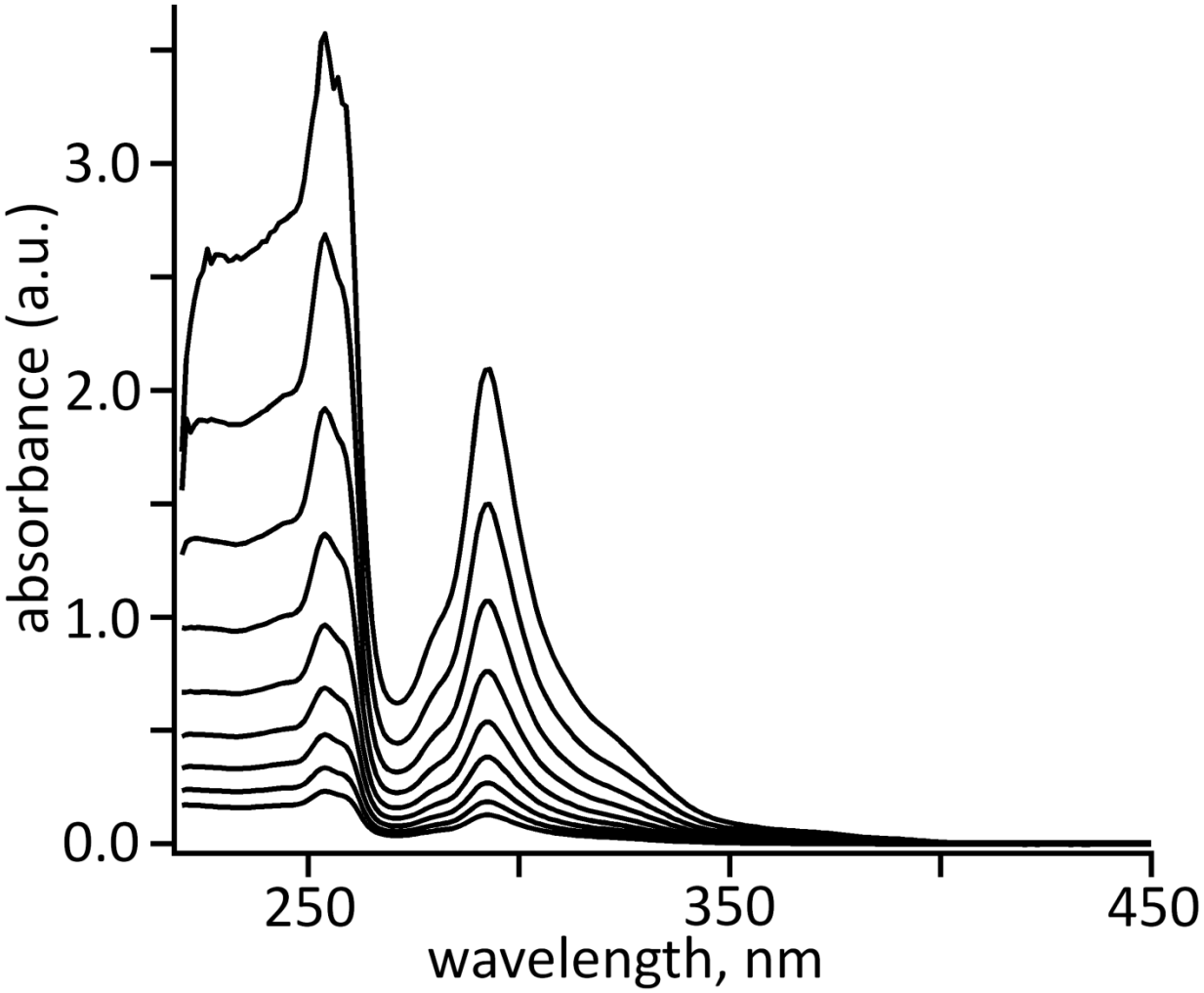

Figure 2.3.16. Absorption spectra of Fraction F1 of successive dilution in CH_2Cl_2.
Spectra between 0.97 and 0.13 absorbance were used to calculate log ε.
UV-vis (CH_2Cl_2, λ_{max} (log ε)): 254 (4.76), 258 (4.72), 293 (4.50).

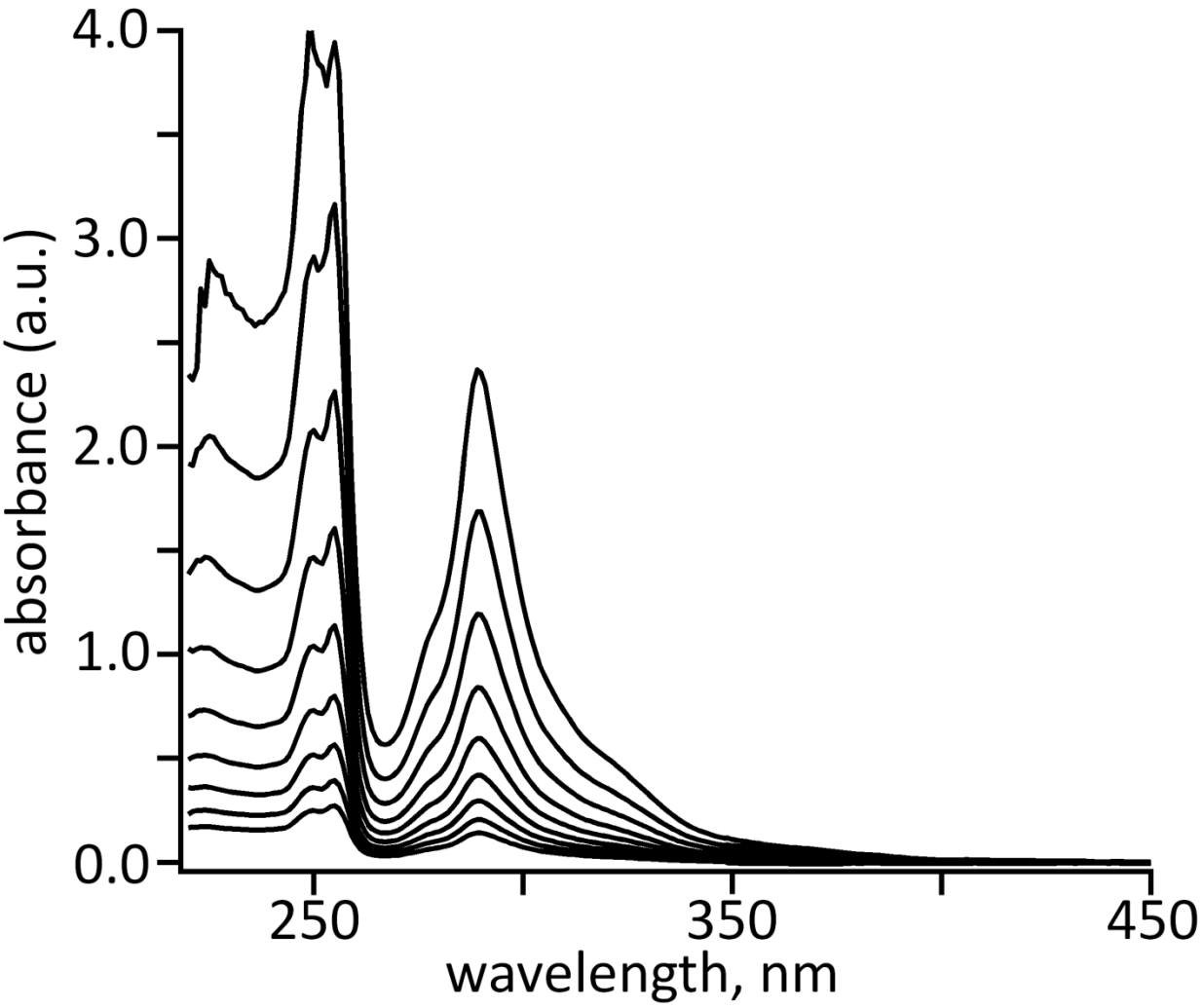

Figure 2.3.17. Absorption spectra of **CORA(Bn$_F$)** of successive dilution in CH_2Cl_2.
Spectra between 1.1 and 0.14 absorbance were used to calculate log ε.
UV-vis (CH_2Cl_2, λ_{max} (log ε)): 225 (4.27), 250 (4.42), 255 (4.46), 289 (4.18).

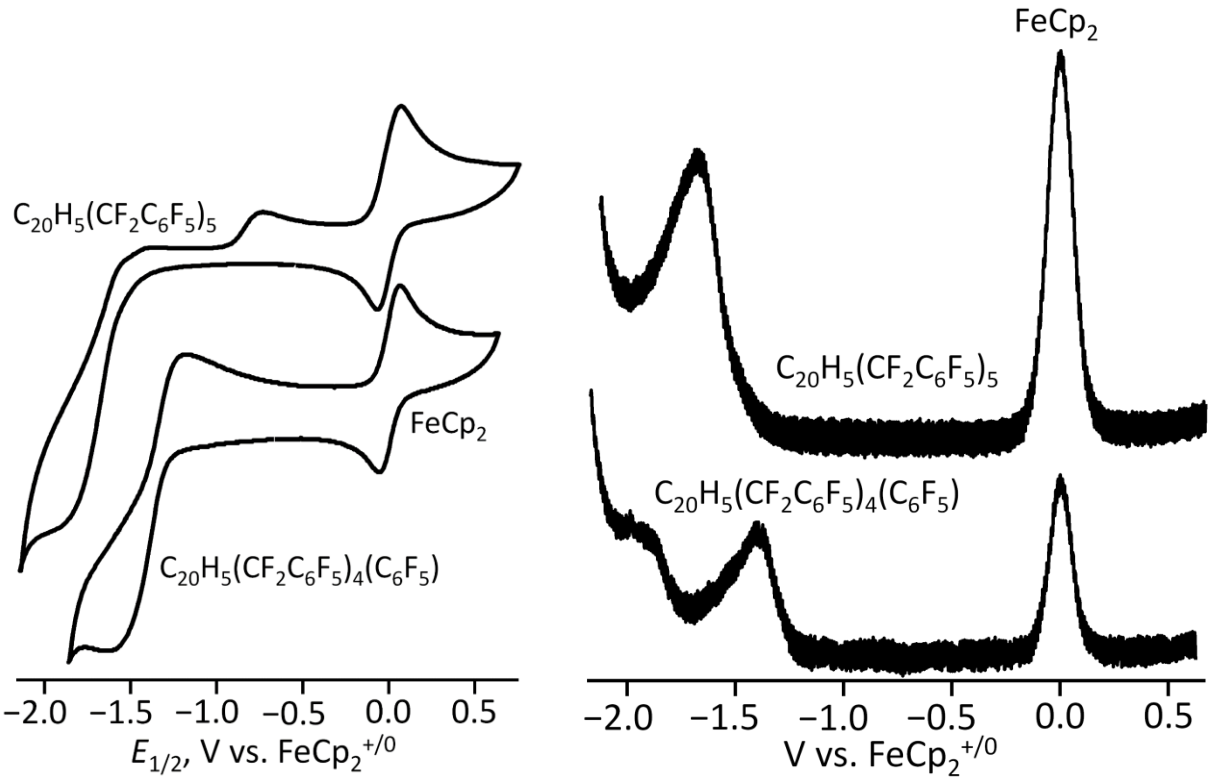

Figure 2.3.18. Cyclic voltammetry (left) and square wave voltammetry (right) of **CORA(Bn$_F$)$_5$** and **CORA(Bn$_F$)$_4$(C$_6$F$_5$)**.

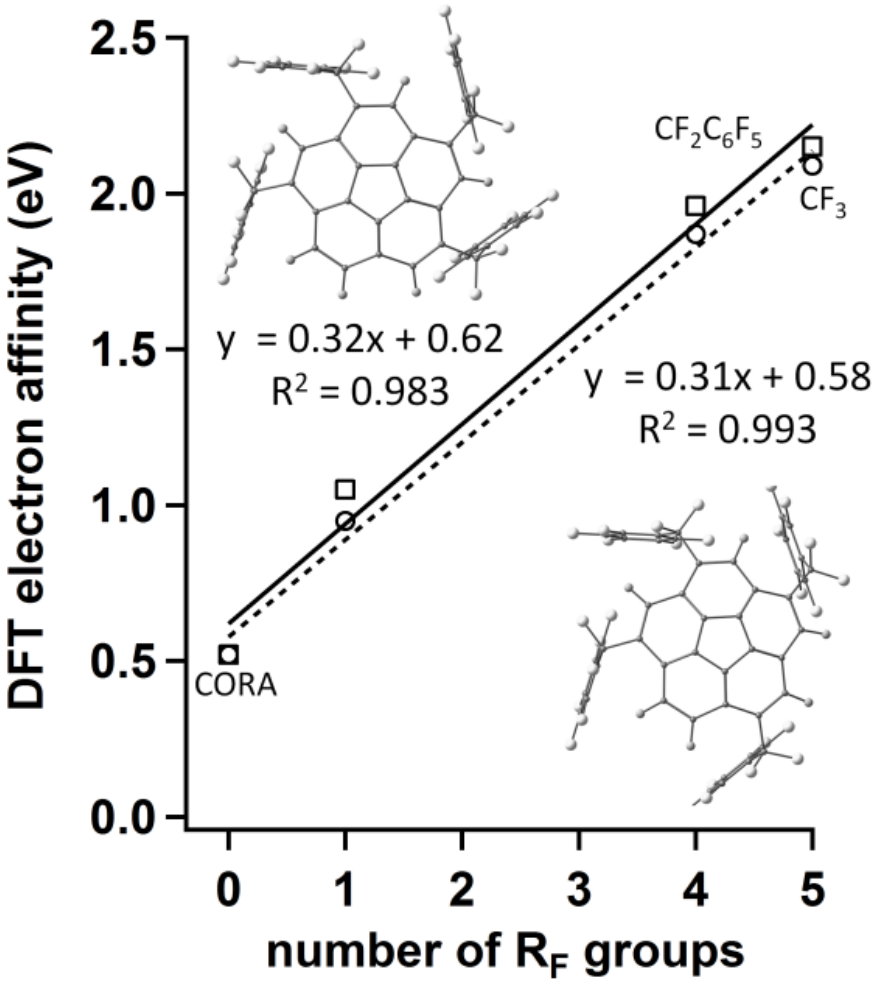

Figure 2.3.19. DFT-predicted electron affinity for CORA$(R_F)_n$ where R_F = CF_3 (○, dashed line) or $CF_2C_6F_5$ (□, solid line). The two DFT isomers of CORA$(Bn_F)_4$ are shown.

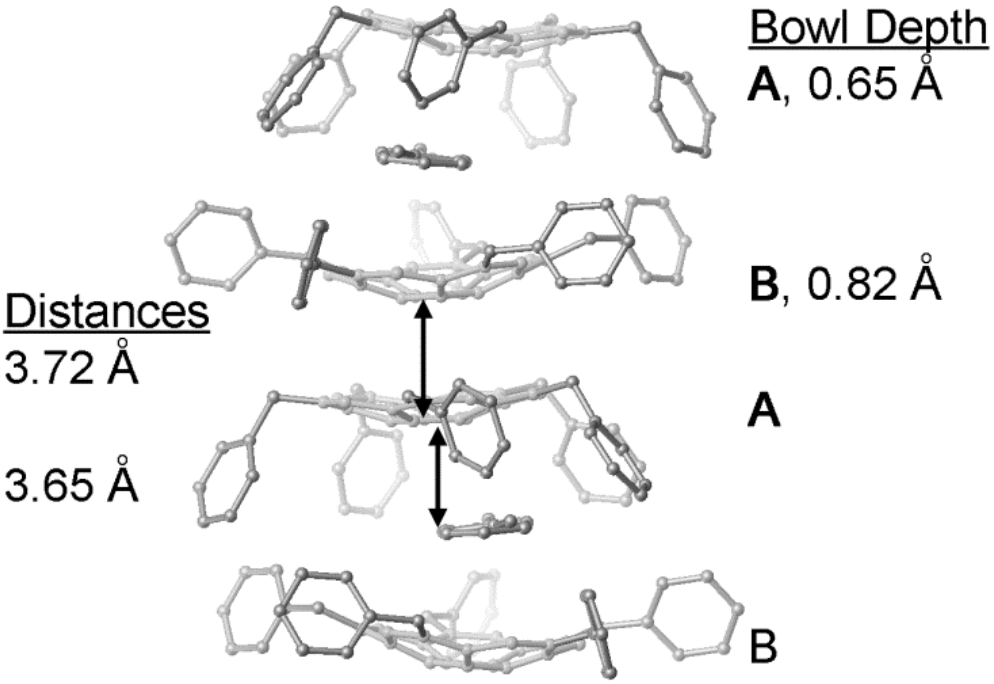

Figure 2.3.20. Crystal packing of one column of **CORA(Bn$_F$)$_5$** viewed along the *a* axis. Conformer names, selected distances, and bowl depths are given. Orange represents the CORA core carbon atoms. Fluorine and hydrogen atoms and the second toluene molecule are removed for clarity.

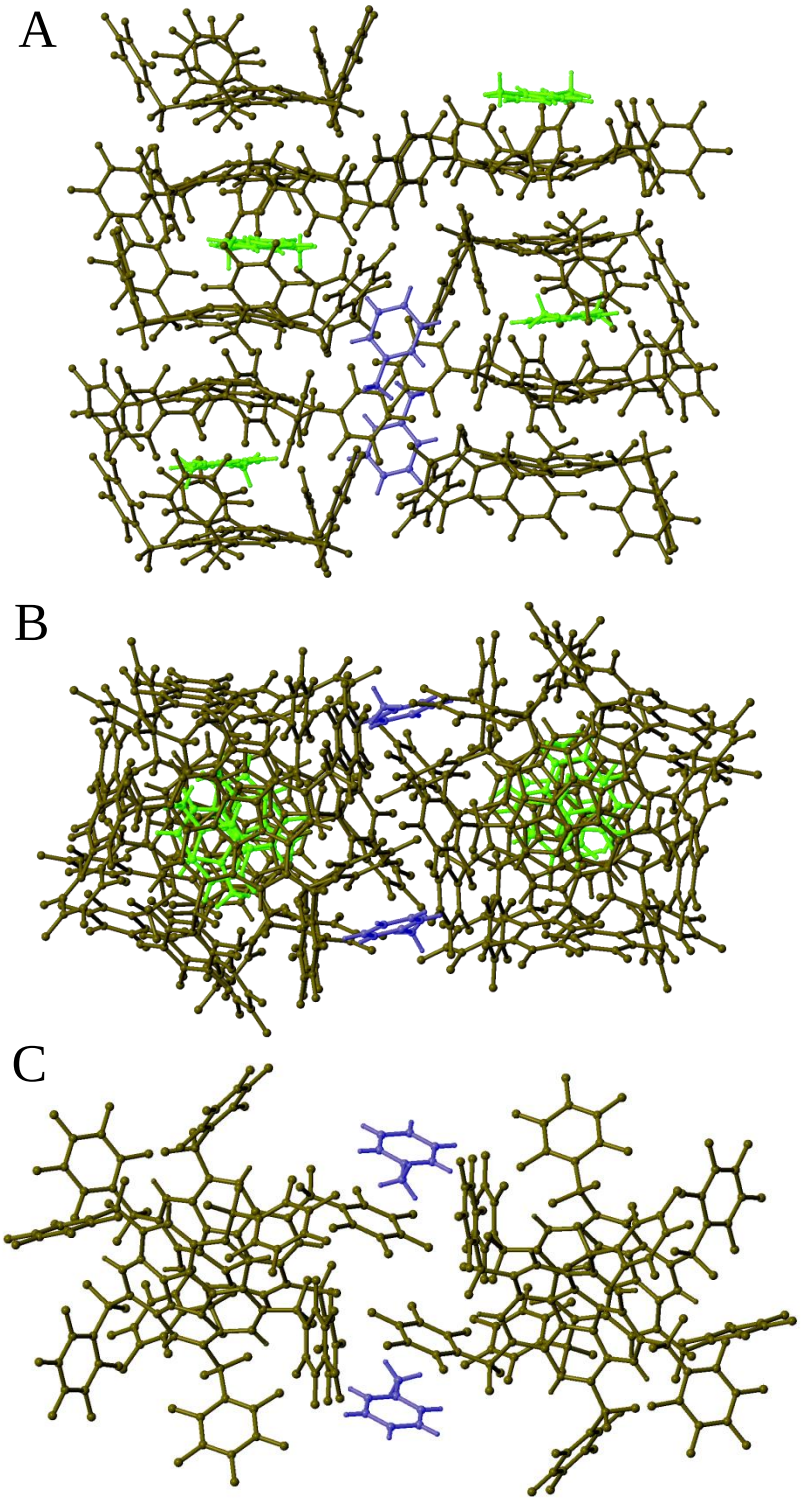

Figure 2.3.21. Three additional solid-state packing diagrams for **CORA(Bn$_F$)$_5$**. Molecules in black are **CORA(Bn$_F$)$_5$**, molecules in green are the disordered toluene sandwiched between **CORA(Bn$_F$)$_5$** molecules along the *c* axis, and molecules in blue are toluene molecules between columns.

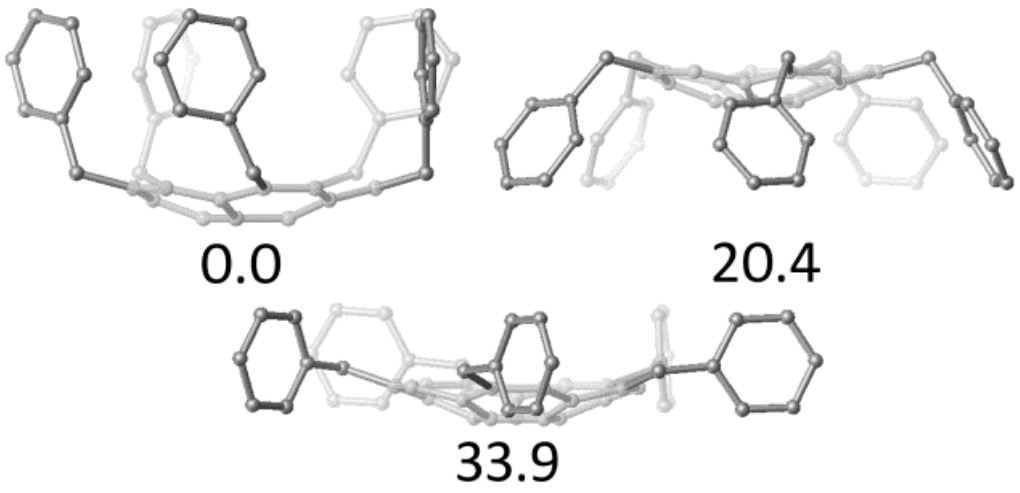

Figure 2.3.22. DFT optimized structures and relative energies (kJ/mol) of **CORA(Bn_F)$_5$** conformers with perfluorobenzyl blades "down" (upper left), "up" (upper right) and "parallel" (bottom). Fluorine and hydrogen atoms are removed for clarity.

Table 2.3.1. Molar fluorine/proton atom ratio based on ^{19}F and ^{1}H NMR spectroscopy. The internal standard 1,4-$C_6H_4(CF_3)_2$ (δ 7.77) was used.

HPLC fraction	chemical formula	F/H mol ratio (theo.)	F/H mol ratio (expt.)	relaxation delay (s)
F3	**$C_{20}H_5(CF_2C_6F_5)_5$**	7.0	7.4	1
F1	$C_{20}H_6(CF_2C_6F_5)_4$	4.7	4.1	1
F4	$C_{20}H_5(CF_2C_6F_5)_4(C_6F_5)$	6.6	6.3	3
F2	$C_{20}H_6(CF_2C_6F_5)_3(C_6F_5)$	4.3	3.6	2
CORA(Bn_F)	**$C_{20}H_9(CF_2C_6F_5)$**	0.8	0.8	3

Bold font is used to highlight compositions determined unambiguously in this work. The other molecular compositions are preliminary.

Table 2.3.2. Additional electrochemical experiments for **CORA(Bn$_F$)$_5$**.

compound	0.1M N(*n*-Bu)$_4$ClO$_4$ in CH_3CN[a]	0.1M N(*n*-Bu)$_4$ClO$_4$ in 1,2-$C_6H_4F_2$[b]
$C_{20}H_{10}^{0/-}$	0.0 (0.0)[c]	0.0 (0.0)
$Fe(Cp^*)_2^{+/0}$	1.80	1.95 (1.97)
$Fe(Cp)_2^{+/0}$	2.31	2.49 (2.50)
***C*$_5$-CORA(Bn$_F$)$_5^{0/-}$**	– (0.84)	– (0.75)

[a] Scan rate of 100 mV·s^{-1} was used.
[b] Scan rate of 500 mV·s^{-1} was used.
[c] The numbers in parentheses were measured by square-wave voltammetry (figures not shown; same experimental conditions were used as for cyclic voltammetry measurements).

Table 2.3.3. DFT–calculated relative energies (ΔE), electron affinity (*EA*s), $E_{1/2}$ (vs. CORA) and solvation energies of selected $C_{20}H_{10-x}(R_F)_x$.[a]

$C_{20}H_{10-x}(R_F)_x$	*EA* eV	$\Delta E_{1/2}$ V	ΔE_{solv} eV	$E_{solv}(0)$ eV	$E_{solv}(-1)$ eV
CORA	0.52	0.0	1.67	−0.24	−1.91
x = 1					
CF_3	0.95				
$CF_2C_6F_5$	**1.05**	**0.02**	**1.16**	**−0.27**	**−1.43**
x = 4					
CF_3	1.87	0.68	1.01	−0.22	−1.22
$CF_2C_6F_5$-I	**1.96**	**0.61**	**0.84**	**−0.44**	**−1.28**
$CF_2C_6F_5$-II	**1.96**	**0.58**	**0.83**	**−0.46**	**−1.29**
x = 5					
CF_3	2.09	0.82	0.92	−0.21	−1.13
$CF_2C_6F_5$	**2.15**	**0.74**	**0.79**	**−0.46**	**−1.25**

[a] The values are computed at the B3LYP-D3/def-TZVPP level using PBE/TZ2P optimized coordinates.

Table 2.3.4. Full DFT-calculated relative energies (ΔE), electron affinity (*EA*s), $E_{1/2}$ (vs. CORA) and solvation energies of selected CORA$(R_F)_xH_{10-x}$.

$C_{20}H_{10-x}(R_F)_x$	Conf.	ΔE, kJ/mol	*EA*, eV	$\Delta E_{1/2}$, V	ΔE_{solv}, eV	$E_{solv}(0)$, eV	$E_{solv}(-1)$, eV
CORA			0.52	0.0	1.67	−0.24	−1.91
***x* = 1**							
CF_3			0.95				
$CF_2C_6F_5$	a	0.6	1.08	0.04	1.16	−0.27	−1.43
	b	4.2	1.01	0.07	1.25	−0.30	−1.55
	c	0.0	1.05	0.02	1.16	−0.27	−1.43
***x* = 4**							
CF_3			1.87	0.68	1.01	−0.22	−1.22
$CF_2C_6F_5$-I	**a**	**0.0**	**1.96**	**0.61**	**0.84**	**−0.44**	**−1.28**
	b	23.6	1.94	0.62	0.87	−0.49	−1.36
	c	11.3	1.93	0.56	0.83	−0.48	−1.31
						–	–
$CF_2C_6F_5$-II	**down**	**0.0**	**1.96**	**0.58**	**0.83**	**−0.46**	**−1.29**
	parallel	22.4	1.96	0.62	0.86	−0.54	−1.40
	up	7.4	1.94	0.56	0.82	−0.49	−1.30
***x* = 5**						–	–
CF_3			2.09	0.82	0.92	−0.21	−1.13
$CF_2C_6F_5$	**down**	**0.0**	**2.15**	**0.74**	**0.79**	**−0.46**	**−1.25**
	up	20.4	2.13	0.69	0.75	−0.55	−1.30
	X-ray-a	17.8	2.14	0.70	0.76	−0.54	−1.29
	X-ray-b	33.9	2.15	0.76	0.81	−0.50	−1.31

Table 2.3.5. Selected crystallographic and data-collection parameters for **CORA(Bn_F)$_5$**.

Data were collected on The Advanced Photon Source synchrotron instrument at Argonne National Laboratory, Argonne IL, on beamline 15ID-B with a wavelength of 0.41328 Å, employing a diamond 1 1 1 monochromator and Bruker D8 goniometer. Unit cell parameters were obtained from least-squares fits to the angular coordinates of all reflections, and intensities were integrated from a series of frames ω and ϕ rotation scans. The structure was solved using direct methods and refined (on F^2, using all data) by a full-matrix, weighted least-squares process. Standard Bruker control and integration software (APEX II) was employed [1], and Bruker SHELXTL software was used with Olex 2 for structure solution, refinement, and molecular graphics [2,3].

compound	pentakis(perfluorobenzyl)corannulene
empirical formula	$C_{62}H_{13}F_{35}$
formula weight	1422.72
habit, color	needle, yellow
crystal size, mm	–
space group	$P2_1/c$
a (Å)	18.1806(14)
b (Å)	25.501(2)
c (Å)	22.0827(16)
α (°)	90.00
β (°)	90.9790(10)
γ (°)	90.00
V (Å^3)	10236.5(13)
Z	8
radiation type	Synchrotron
absorption coefficient, μ/mm^{-1}	0.065
R_{int}	0.0789
T (K)	106(2)
ρ_{calc} (g cm^{-3})	1.846
$R(F)$ ($I>2\sigma(I)$)[a]	0.0507
$wR(F^2)$ [all data][a]	0.1244
residual electron ρ max, min (Å^3)	0.383, −0.374

[a] $R(F) = \Sigma \left| |F_o|-|F_c| \right| / \Sigma|F_o|$; $wR(F^2) = (\Sigma[w(F_o^2 - F_c^2)^2 / \Sigma[w(F_o^2)^2])^{1/2}$

References:
1. G. M. Sheldrick, Crystallography Program APEX2, v. 2.0-2, Bruker AXS, Madison,WI, 2006.
2. G. M. Sheldrick, Crystallography Software Package SHELXTL, v. 6.12 UNIX, Bruker AXS, Madison, WI, 2001.
3. O. V. Dolomanov, L. J. Bourhis, R. J. Gildea, J. A. K. Howard, H. Puschmann *J. Appl. Cryst*. **2009**, *42*, 339-341.

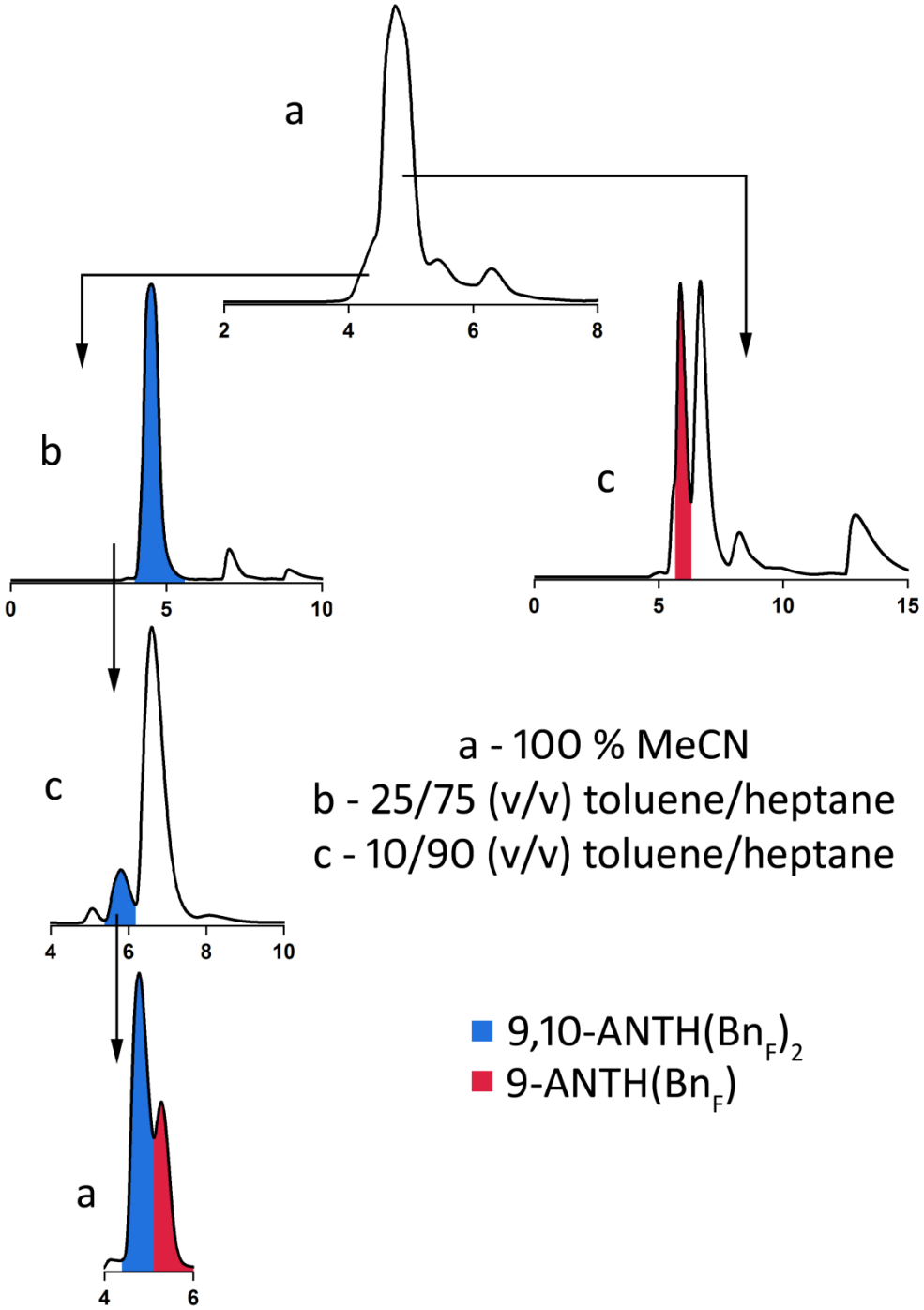

Figure 2.4.1. HPLC chromatograms for the separation of 9,10-ANTH(Bn$_F$)$_2$ and 9-ANTH(Bn$_F$). The conditions are listed next to the chromatograms. All traces collected used a COSMOSIL Buckyprep semi-preparative stationary phase at a flow rate of 5 mL min^{-1} and observed at 300 nm detection wavelength. The peaks in color are those collected and further separated in a subsequent separation stage. The blue color corresponds to 9,10-ANTH(Bn$_F$)$_2$ and the magenta color corresponds to 9-ANTH(Bn$_F$). The x-axis for all chromatograms is the t_R in minutes. Chromatogram a is of the crude product mixture.

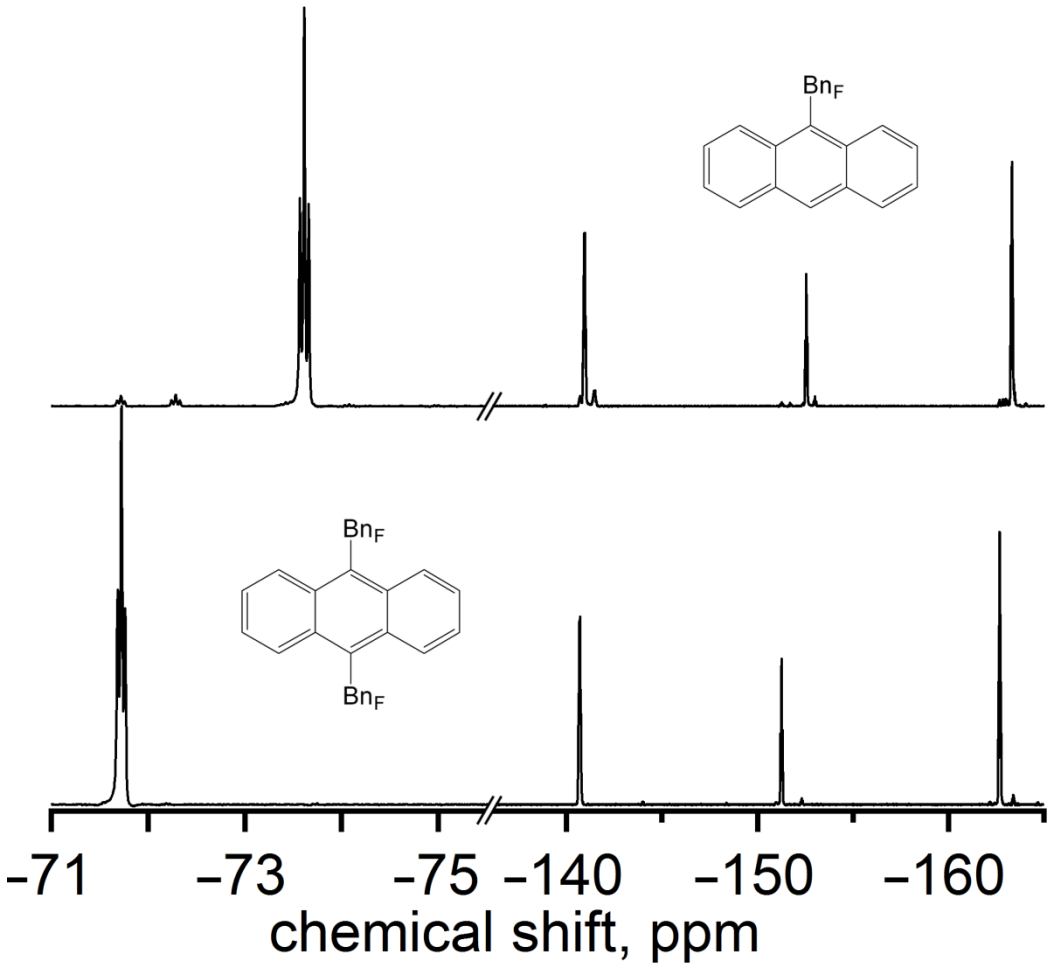

Figure 2.4.2. Condensed ^{19}F NMR spectra (379 MHz) of 9-ANTH(Bn_F) (top) and 9,10-ANTH(Bn_F)$_2$ (bottom) in $CDCl_3$.

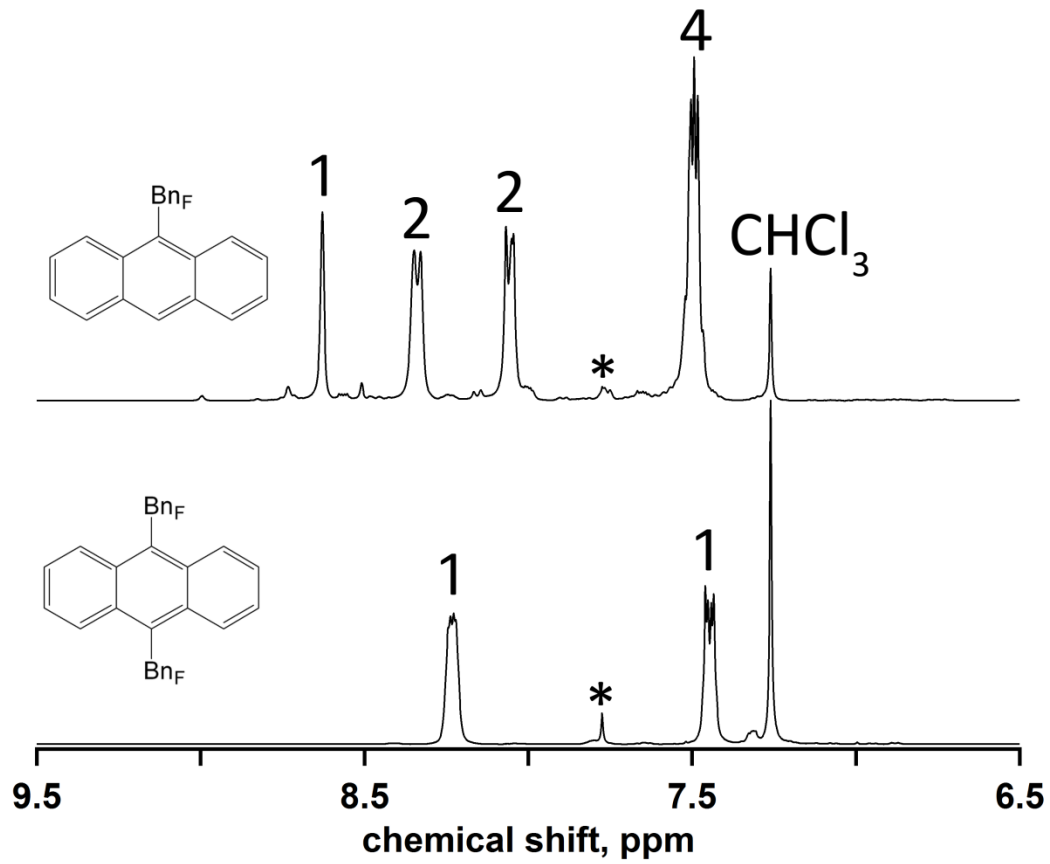

Figure 2.4.3. Proton NMR spectra (399 MHz) of 9-ANTH(Bn_F) and 9,10-ANTH(Bn_F)$_2$ in $CDCl_3$ (residual resonance δ 7.26 ppm). The internal standard 1,4-bis(trifluoromethyl)benzene is marked by an asterisk at δ 7.77 ppm).

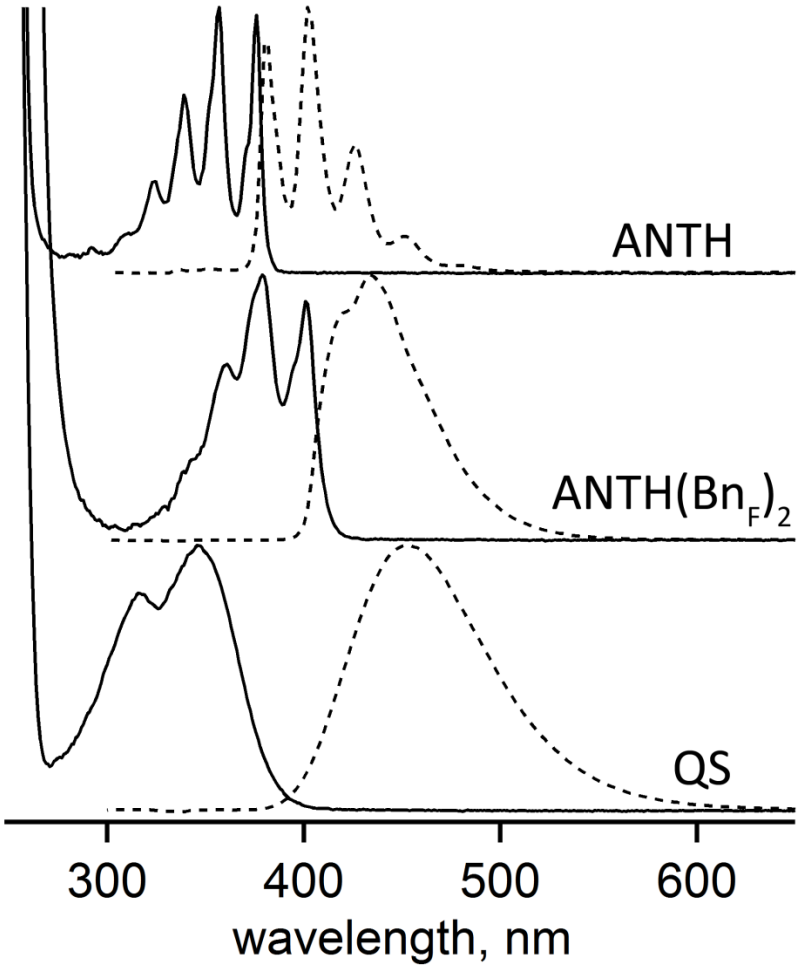

Figure 2.4.4. Absorption and emission spectra of ANTH and 9,10-ANTH(Bn_F)$_2$ in cyclohexane, and quinine sulfate (QS) in 0.1 M aqueous H_2SO_4. Samples were under aerobic (absorption, solid line) and anaerobic (emission, dashed line) conditions.

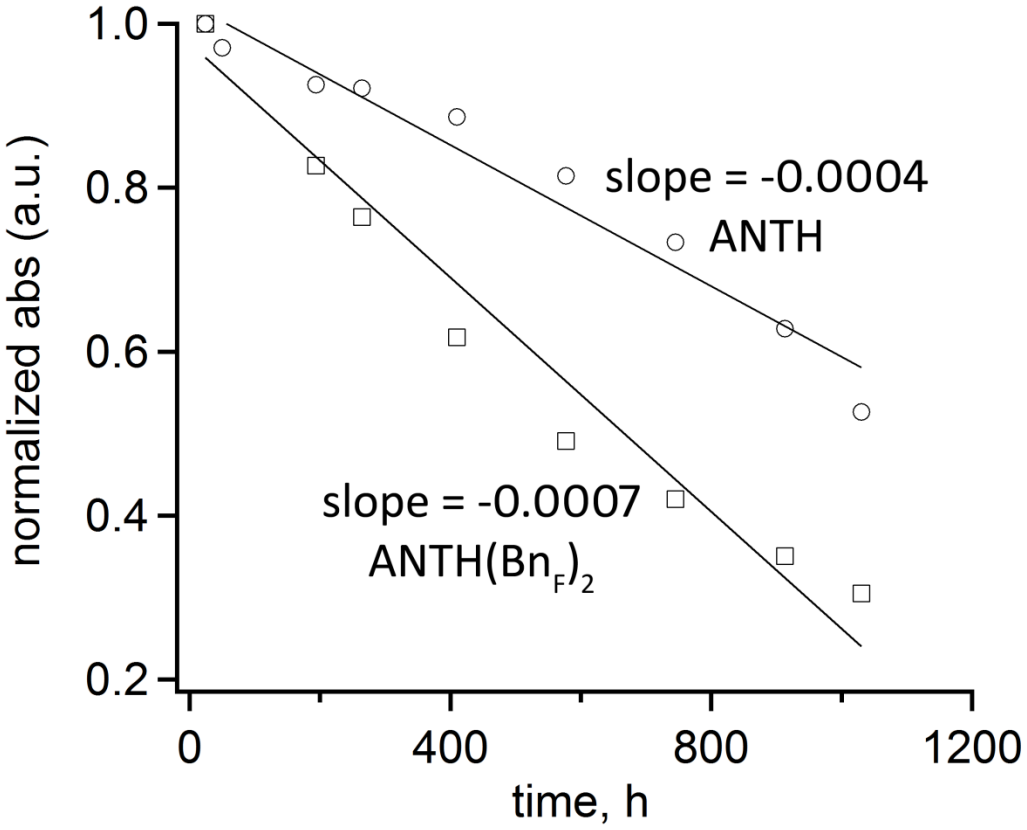

Figure 2.4.5. Normalized absorbance decay over time for ANTH and 9,10-ANTH(Bn_F)$_2$ under aerobic conditions and irradiated with 34 W ambient fume hood light bulb. Samples were dissolved in dichloromethane and placed into a quartz sample holder.

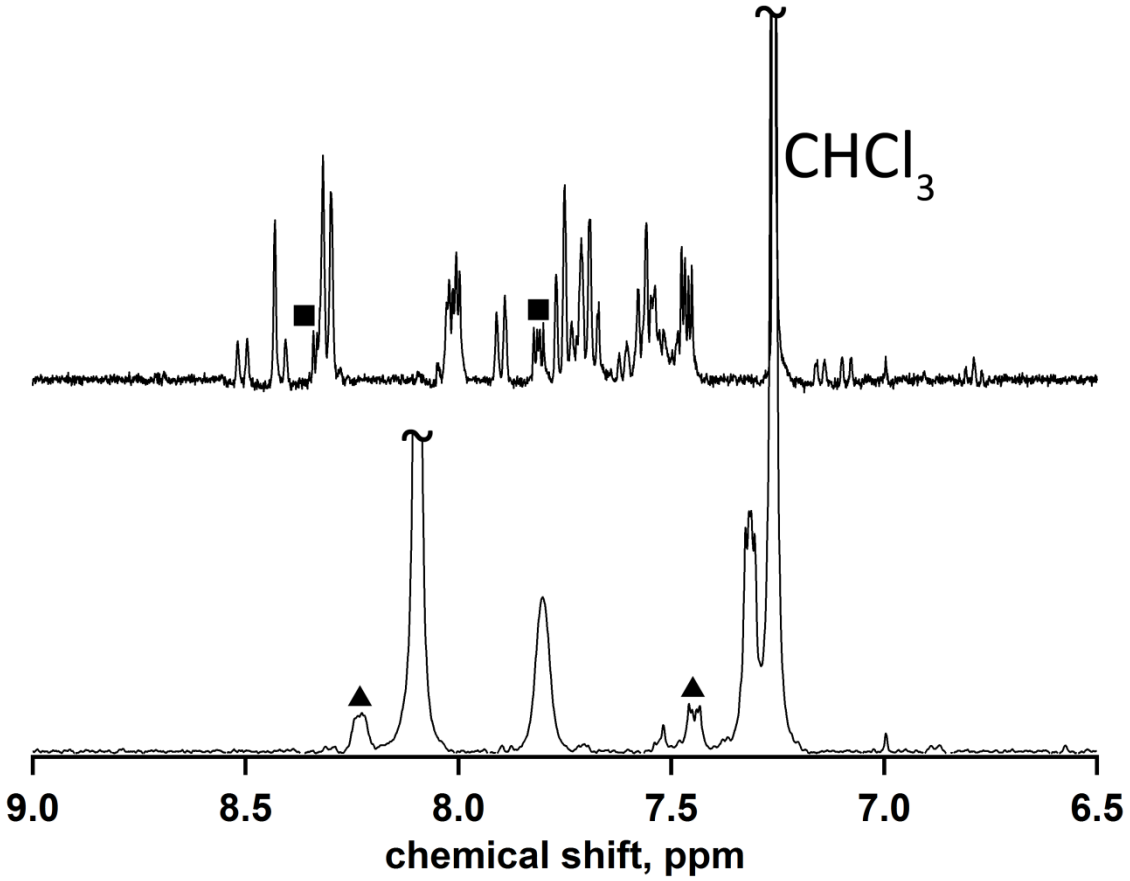

Figure 2.4.6. Proton NMR spectra (399 MHz) of ANTH (top) and 9,10-ANTH(Bn_F)$_2$ (bottom) post aerobic photostability in $CDCl_3$ (residual resonance δ 7.26 ppm). The black squares represent resonances corresponding to anthraquinone and the black triangles represent resonances corresponding to 9,10-ANTH(Bn_F)$_2$. Unidentified solvent impurity at δ 8.1 ppm.

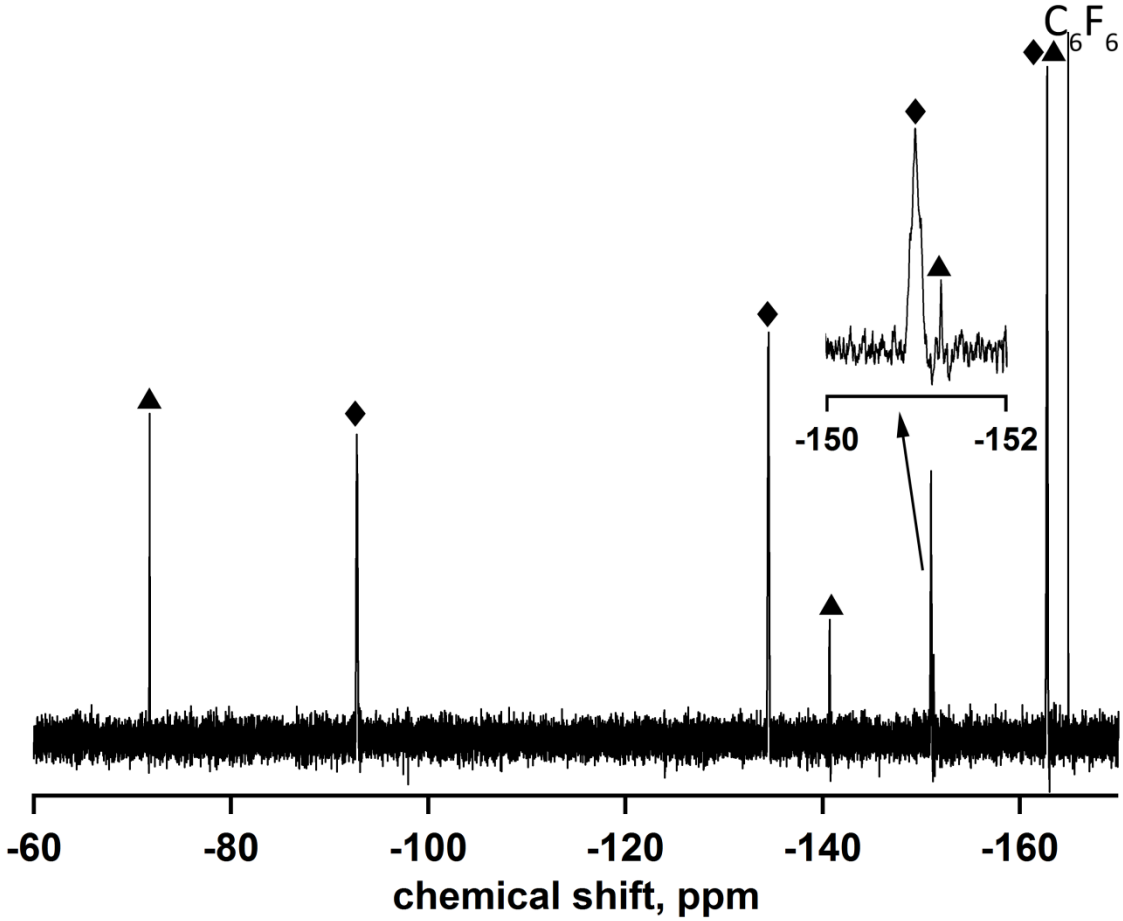

Figure 2.4.7. Fluorine-19 NMR spectrum (379 MHz) of 9,10-ANTH(Bn_F)$_2$ post aerobic photostability in $CDCl_3$. The resonance for the internal standard C_6F_6 (δ −164.9 ppm) is shown. The black triangles represent resonances corresponding to 9,10-ANTH(Bn_F)$_2$ and the black diamonds represent resonances corresponding to the new symmetric compound.

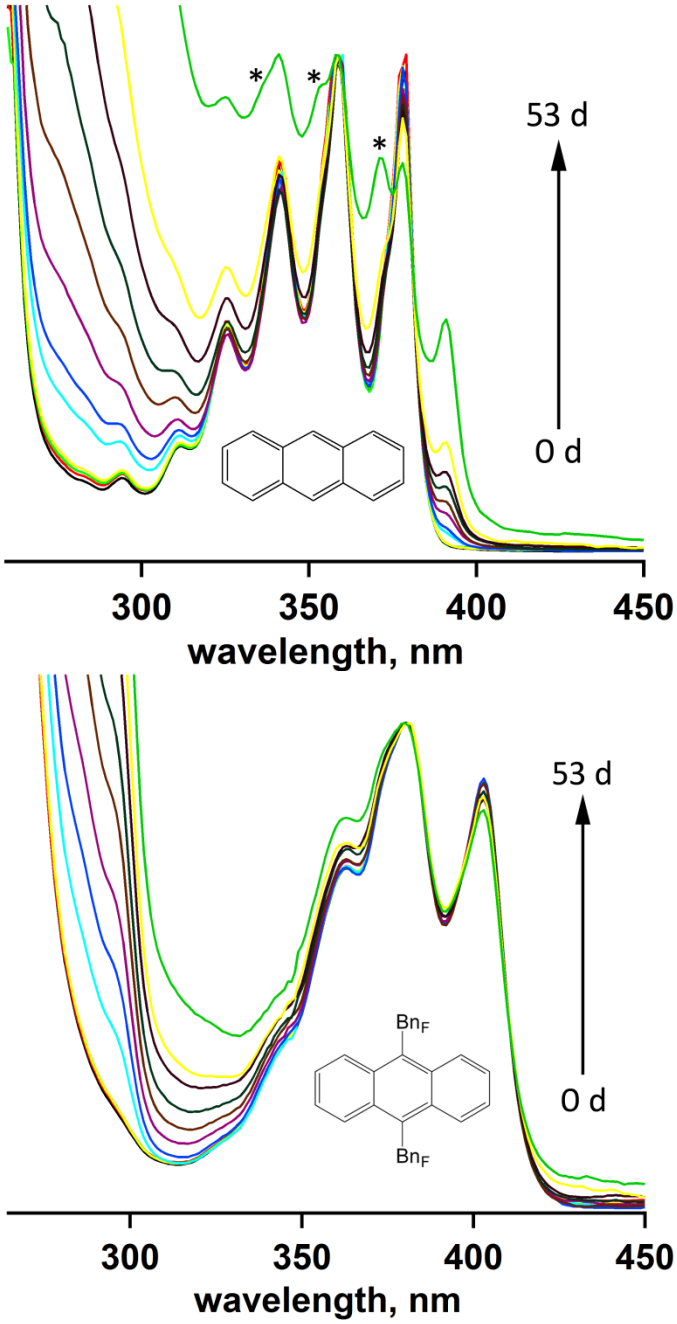

Figure 2.4.8. Normalized UV-vis absorption spectra of ANTH and 9,10-ANTH(Bn_F)$_2$ in dichloromethane monitored over time. New peaks growing in are marked with an asterisk.

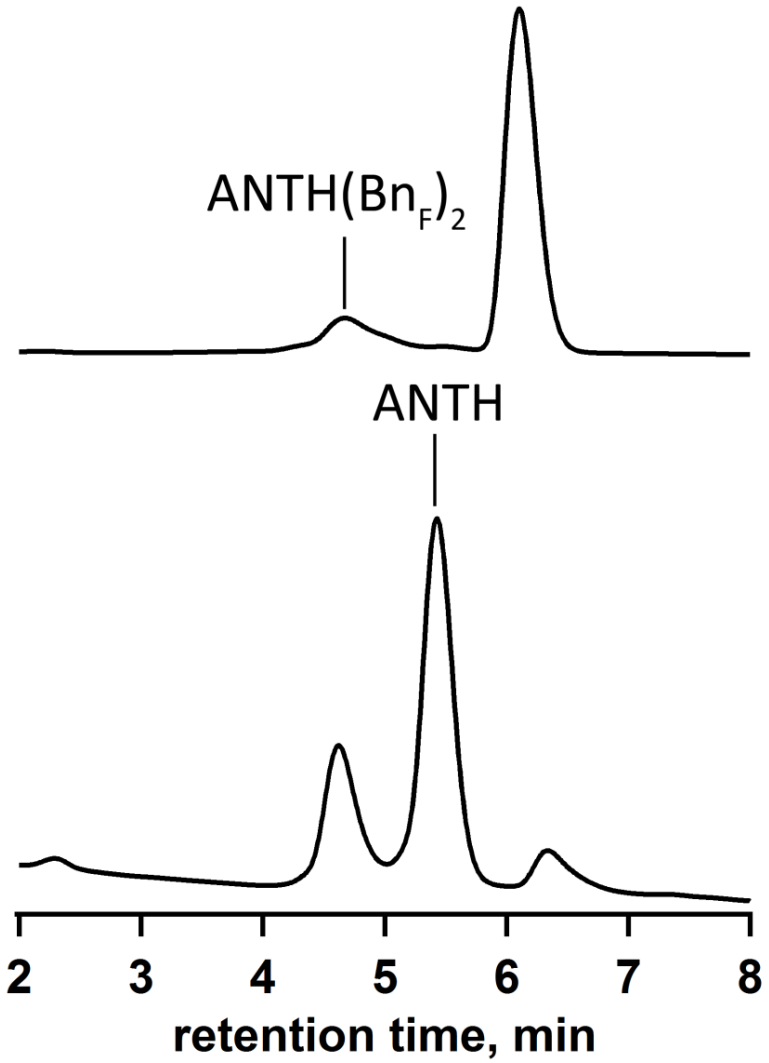

Figure 2.4.9. HPLC chromatograms of ANTH and 9,10-ANTH(Bn_F)$_2$ post aerobic photostability in in 100% MeCN at a flow rate of 5 mL min^{-1}. The compounds ANTH and 9,10-ANTH(Bn_F)$_2$ are shown at their retention times. Note: ANTH co-elutes with anthraquinone (major peak in bottom chromatogram).

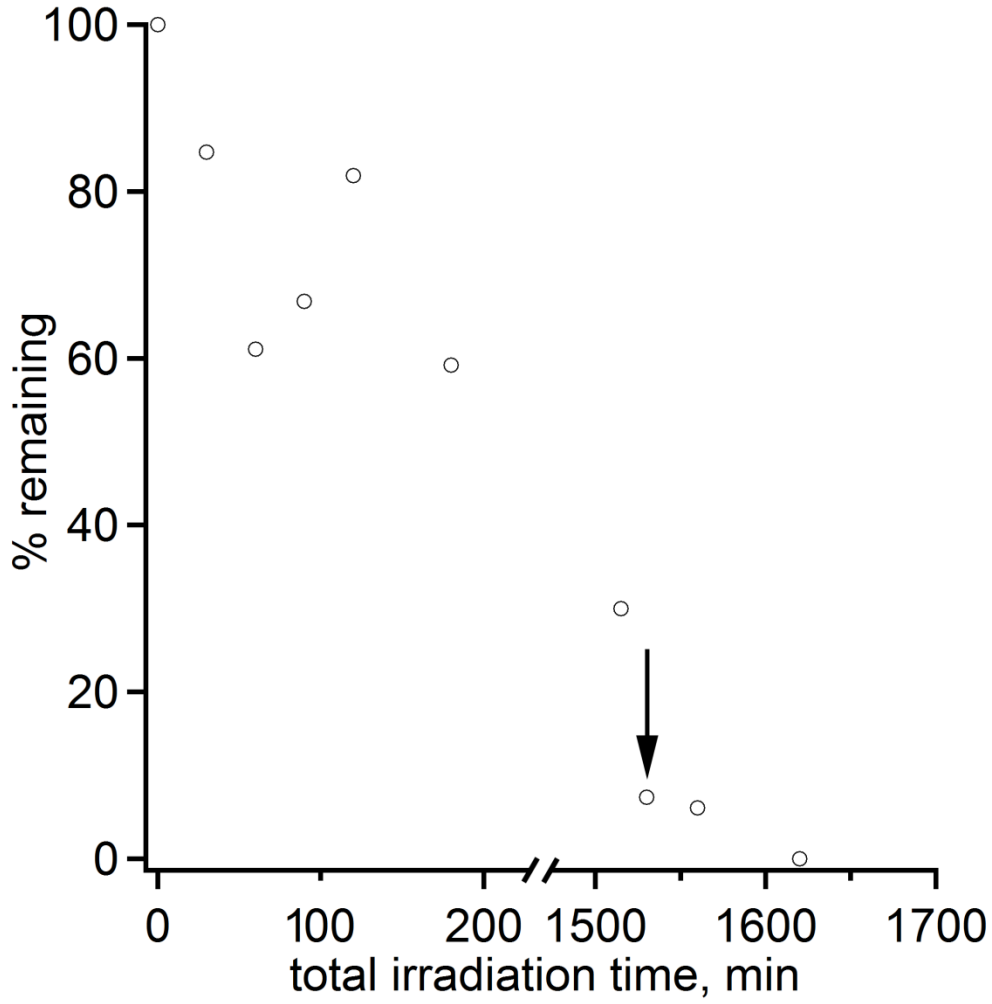

Figure 2.4.10. Relationship between % 9,10-ANTH(Bn_F)$_2$ remaining and total irradiation time of 9,10-ANTH(Bn_F)$_2$. Sample was irradiated 50 mm from a high-pressure mercury arc lamp. The arrow point towards the sample which was exposed to air and irradiated for 0.5 h.

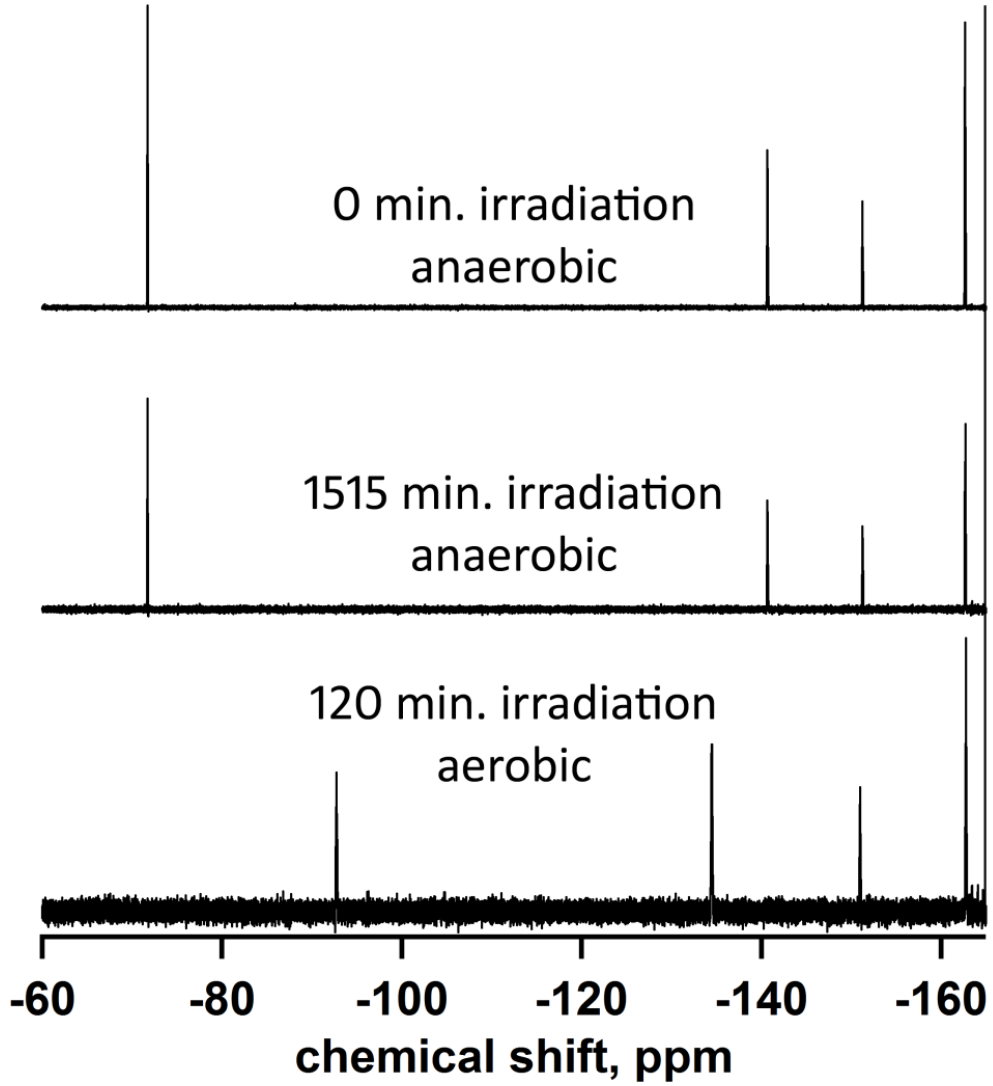

Figure 2.4.11. Fluorine-19 NMR spectra (379 MHz) of 9,10-ANTH(Bn_F)$_2$ irradiated for 0 min. (top), 1515 min. (middle), and after exposure to air with additional 120 min. irradiation (bottom). Internal standard C_6F_6 shown at δ −164.9 ppm.

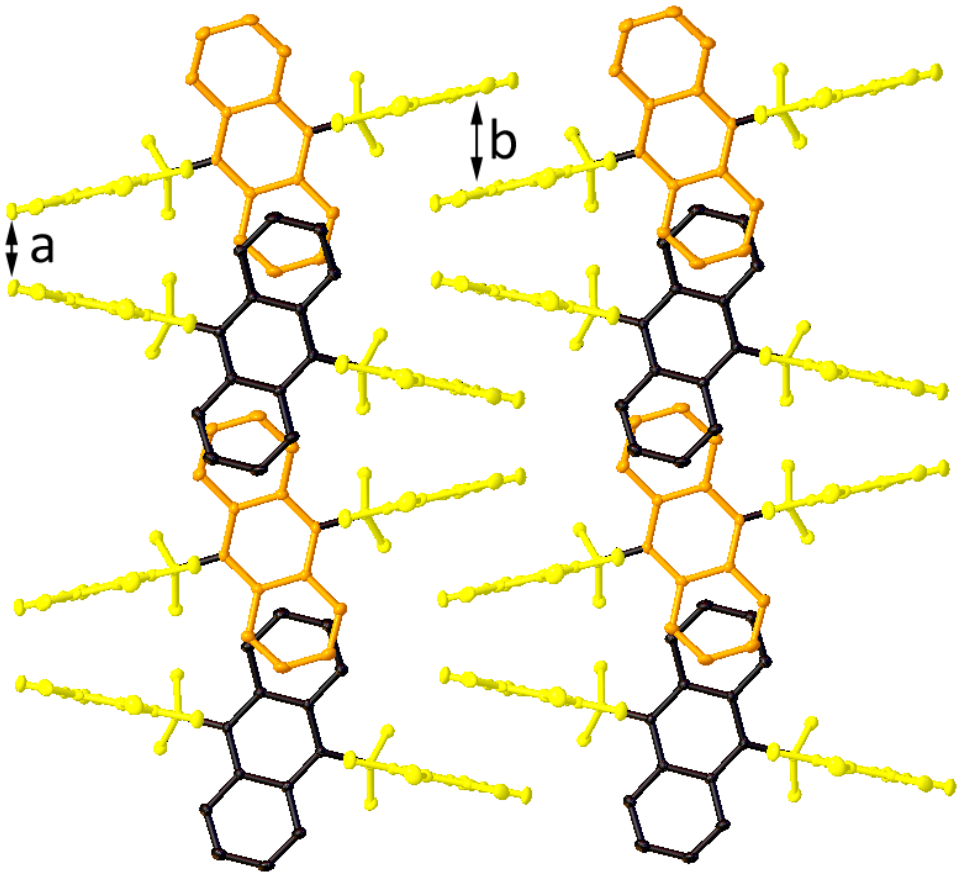

Figure 2.4.12. Top view of the solid-state packing of 9,10-ANTH(Bn_F)$_2$. Two different stacked columns are colored in orange and black, and the Bn_F groups are colored in yellow. Distances of a = 2.822 Å and b = 3.056 Å. Hydrogen atoms are omitted for clarity.

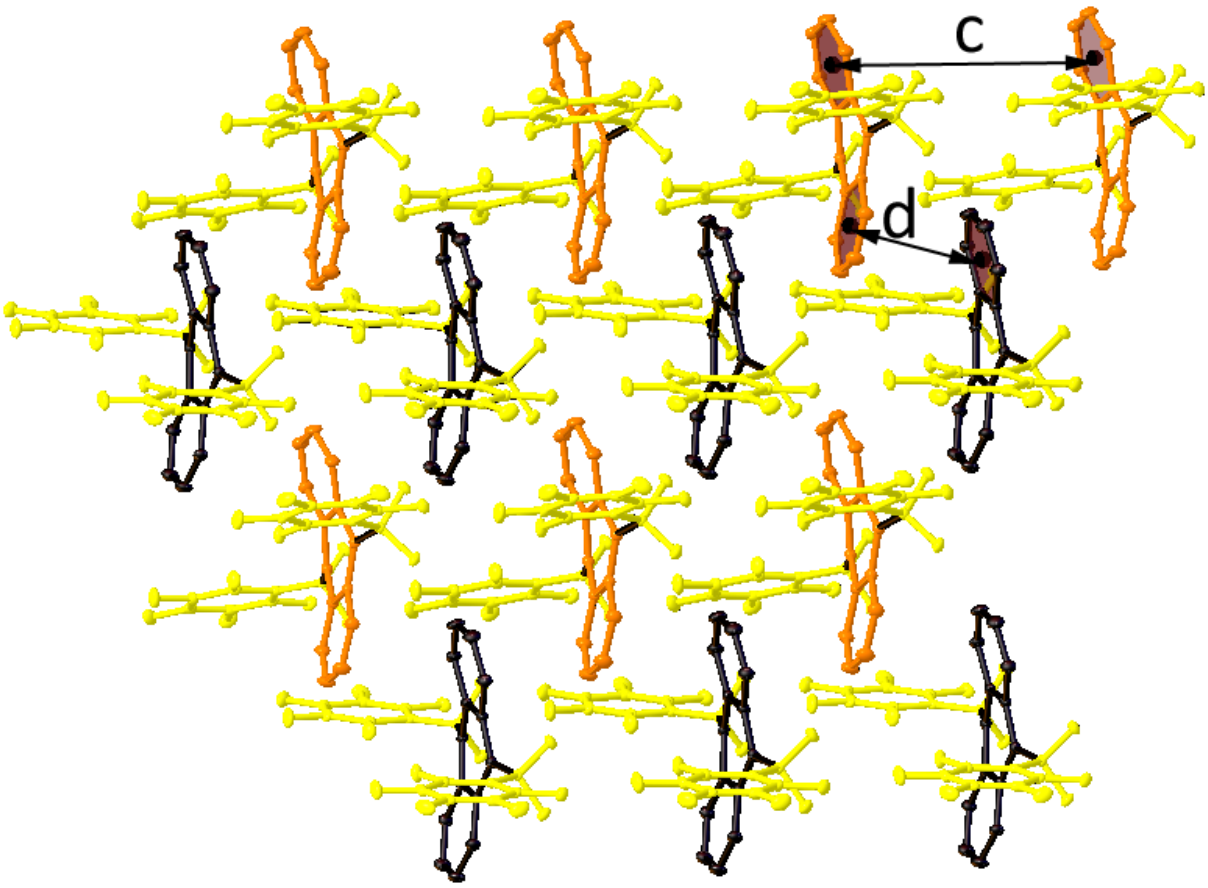

Figure 2.4.13. Side view of the solid-state packing of 9,10-ANTH(Bn_F)$_2$. Two different stacked columns are colored in orange and black, and the Bn_F groups are colored in yellow. Distances between centroids c = 8.028 Å and d = 4.154 Å. Hydrogen atoms are omitted for clarity.

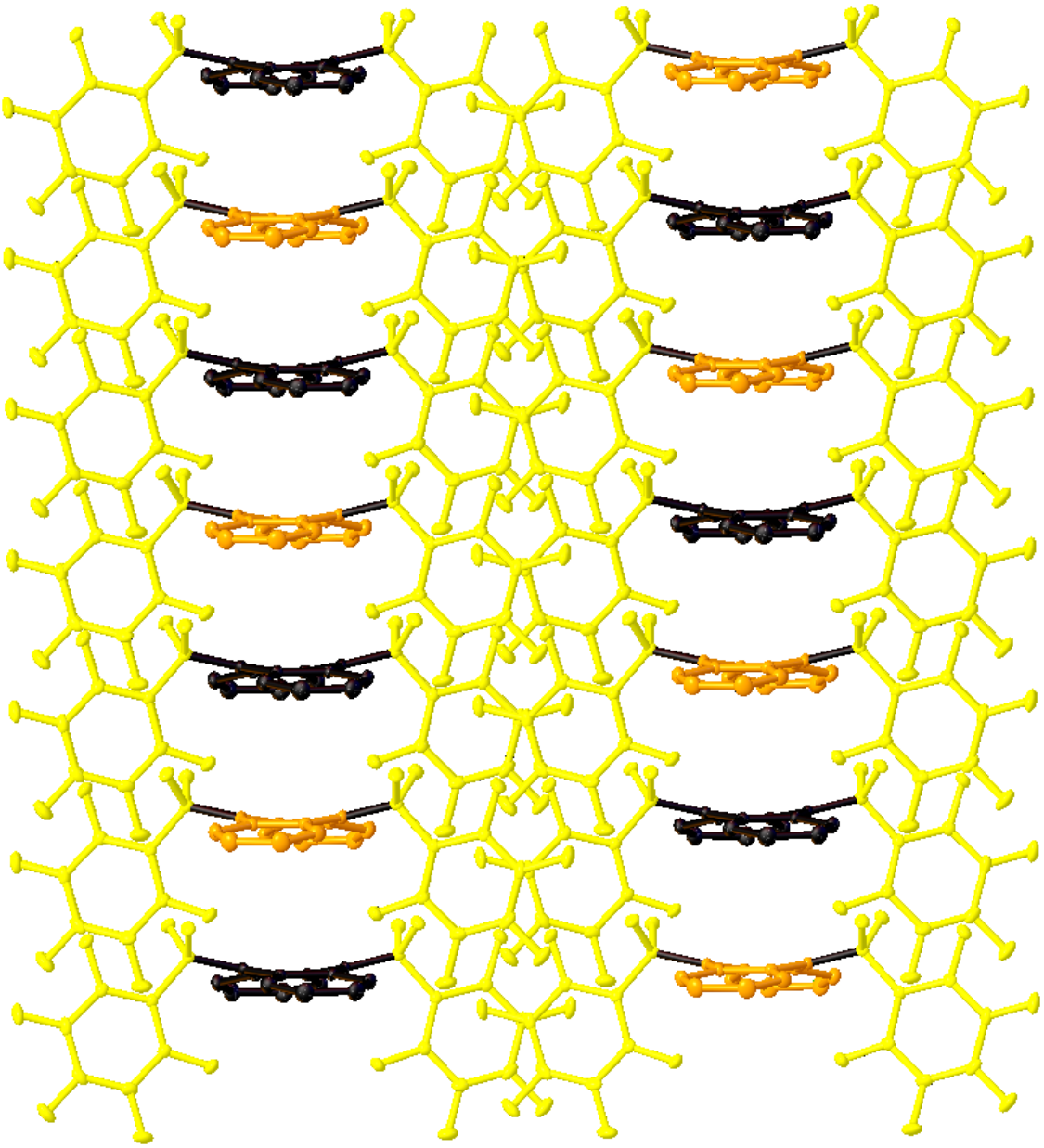

Figure 2.4.14. Solid-state packing of 9,10-ANTH(Bn_F)$_2$ viewed along the major axis of ANTH core. Two different stacked columns are colored in orange and black, and the Bn_F groups are colored in yellow. The Bn_F groups are shown to insult the ANTH core. Hydrogen atoms are omitted for clarity.

Figure 2.4.15. The fluorescence of 9,10-ANTH(Bn_F)$_2$ in DCM under a 405 nm illumination.

Table 2.4.1. Relative quantum yield, absorption and emission maxima, Stokes' shifts, and band gaps in cyclohexane. Quantum yields were referenced to quinine sulfate in 0.1 M H_2SO_4 (Φ_f = 0.55).

compound	Φ_f	λ_{abs} (nm)	λ_{em} (nm)	$\Delta\lambda$ (cm^{-1})	E_g (eV)
ANTH	0.40	376	381	349	3.28
$ANTH(Bn_F)_2$	0.85	402	416	837	3.05

Chapter 2 References

(1) Kroto, H. W.; Heath, J. R.; O'Brien, S. C.; Curl, R. F.; Smalley, R. E. *Nature* **1985**, *318*, 162.

(2) Heath, J. R.; O'Brien, S. C.; Zhang, Q.; Liu, Y.; Curl, R. F.; Kroto, H. W.; Tittel, F. K.; Smalley, R. E. *J. Am. Chem. Soc.* **1985**, *107*, 7779.

(3) Zade, S. S.; Bendikov, M. *J. Phys. Org. Chem.* **2011**, *25*, 452.

(4) Reyes-Reyes, M.; Kim, K.; Carroll, D. L. *Appl. Phys. Lett.* **2005**, *87*, 083506.

(5) Nardes, A. M.; Ferguson, A. J.; Whitaker, J. B.; Larson, B. W.; Larsen, R. E.; Maturová, K.; Graf, P. A.; Boltalina, O. V.; Strauss, S. H.; Kopidakis, N. *Adv. Funct. Mater.* **2012**, *22*, 4115.

(6) Yang, X.; Uddin, A. *Renew. Sust. Energy Rev.* **2014**, *30*, 324.

(7) Zhu, M.; Yang, C. *Chem. Soc. Rev.* **2012**, *42*, 4963.

(8) Yang, X.; Xu, X.; Zhou, G. *J. Mater. Chem. C.* **2015**, *3*, 913.

(9) Chang, Y.-C.; Kuo, M.-Y.; Chen, C.-P.; Lu, H.-F.; Chao, I. *J. Phys. Chem. C.* **2010**, *114*, 11595.

(10) Brabec, C. J.; Hauch, J. A.; Schilinsky, P.; Waldauf, C. *MRS Bull.* **2005**, *30*, 50.

(11) Brabec, C. J.; Durrant, J. R. *MRS Bull.* **2008**, *33*, 670.

(12) Figueria-Duarte, T. M.; Müllen, K. *Chem. Rev.* **2011**, *111*, 7260.

(13) Nelson, S. F.; Lin, Y.-Y.; Gundlach, D. J.; Jackson, T. N. *Appl. Phys. Lett.* **1998**, *72*, 1854.

(14) Tang, M. L.; Bao, Z. *Chem. Mater.* **2011**, *23*, 446.

(15) Hasegawa, T.; Takeya, J. *Sci. Technol. Adv. Mater.* **2009**, *10*, 024314.

(16) Sun, H.; Putta, A.; Billion, M. *J. Phys. Chem. A.* **2012**, *116*, 8015.

(17) Kuvychko, I. V.; Castro, K. P.; Deng, S. H. M.; Wang, X.-B.; Strauss, S. H.; Boltalina, O. V. *Angew. Chem. Int. Ed.* **2013**, *52*, 4871.

(18) Sun, H.; Putta, A.; Kloster, J. P.; Tottempudi, U. K. *Chem. Commun.* **2012**, *48*, 12085.

(19) Matsubara, Y.; Kimura, A.; Yamaguchi, Y.; Yoshida, Z. *Org. Lett.* **2008**, *10*, 5541.

(20) Filler, R.; Saha, R. *Future Med. Chem.* **2009**, *1*, 777.

(21) Gaye, B.; Adejare, A. *Future Med. Chem.* **2009**, *1*, 821.

(22) Purser, S.; Moore, P. R.; Swallow, S.; Gouverneur, V. *Chem. Soc. Rev.* **2008**, *37*, 320.

(23) Isanbor, C.; O'Hagan, D. *J. Fluorine Chem.* **2006**, *127*, 303.

(24) Kirk, K. L. *J. Fluorine Chem.* **2006**, *127*, 1013.

(25) Parisi, M. T. *Pediatr. Radiol.* **2011**, *41*, 803.

(26) Le Bars, D. *J. Fluorine Chem.* **2006**, *127*, 1488.

(27) Wong, D. T.; Bymaster, F. P.; Engleman, E. A. *Life Sci.* **1995**, *57*, 411.

(28) Schlosser, M. *Angew. Chem. Int. Ed.* **2006**, *45*, 5432.

(29) Chen, M.; Buchwald, S. L. *Angew. Chem. Int. Ed.* **2013**, *52*, 11628.

(30) Garcia, J. J.; Sierra, C.; Torrens, H. *Tetrahedron Lett.* **1996**, *37*, 6097.

(31) Brown, H. C.; Genwanter, H. L.; White, D. M.; Woods, W. G. *J. Org. Chem.* **1960**, *25*, 634.

(32) Mirsaleh-Kohan, N.; Robertson, W. D.; Lambert, J.; Compton, R.; Krasnokutski, S. A.; Yang, D.-S. *Intern. J. Mass Spectrom.* **2011**, *304*, 57.
(33) Roy, S.; Gregg, B. T.; Gribble, G. W.; Le, V.-D.; Roy, S. *Tetrahedron* **2011**, *67*, 2161.
(34) Bailly, F.; Cottet, F.; Schlosser, M. *Synthesis* **2005**, 791.
(35) Hosokawa, K.; Inukai, K. *Nippon Kagaku Kaishi* **1972**, 383.
(36) Hosokawa, K.; Inukai, K. *Nippon Kagaku Kaishi* **1976**, 1791.
(37) Hosokawa, K.; Fujii, S.; Inukai, K. *Nippon Kagaku Kaishi* **1979**, 294.
(38) Hosokawa, K.; Inukai, K. *Nippon Kagaku Kaishi* **1977**, 1163.
(39) Klebach, T. C.; Turkenburg, L. A. M.; Bickelhaupt, F. *Tetrahedron Lett.* **1978**, *19*, 1099.
(40) Krespan, C. G.; McKusic, B. C.; Cairns, T. L. *J. Am. Chem. Soc.* **1961**, *83*, 3428.
(41) Bonnet-Delpon, D.; Charpentier-Morize, M.; Jacquot, R. *J. Org. Chem.* **1988**, *53*, 759.
(42) Mellor, J. M.; El-Sagheer, A. H.; Salem, E. E.-D. M. *Tetrahedron Lett.* **2000**, *41*, 7383.
(43) Kuroboshi, M.; Hiyama, T. *Chem. Lett.* **1992**, *21*, 827.
(44) Le, V. P.; Wells, P. R. *Aust. J. Chem.* **1992**, *45*, 1057.
(45) Urata, H.; Fuchikami, T. *Tetrahedron Lett.* **1991**, *32*, 91.
(46) Zhang, X. L., Q., Ingels, J. B., Simmonett, A. C., Wheeler,S. E. Xie,Y.,; King, R. B., Schaefer III, H. F., Cotton, F. A. *Chem. Commun.* **2006**, 758.
(47) Dunyashev, V. S.; Polenov, E. A.; Minina, N. E.; Kazakova, V. M.; Grigorev, G. A.; Yagupolskii, L. M. *Zhurnal Obshchei Khimii* **1988**, *58*, 200.
(48) Freskos, J. N. *Synth. Commun.* **1988**, *18*, 965.
(49) Kuvychko, I. V.; Whitaker, J. B.; Larson, B. W.; Folsom, T. C.; Shustova, N. B.; Avdoshenko, S. M.; Chen, Y.; Wen, H.; Wang, X.; Dunsch, L.; Popov, A. A.; Boltalina, O. V.; Strauss, S. H. *Chem. Sci.* **2012**, *3*, 1399.
(50) Li, Y.; Li, C.; Yue, W.; Jiang, W.; Kopecek, R.; Qu, J.; Wang, Z. *Org. Lett.* **2010**, *12*, 2374.
(51) Combellas, C.; Kanoufi, F.; Thiebault, A. *Journal of Physical Chemistry B* **2003**, *107*, 10894.
(52) Popov, A. A.; Kareev, I. E.; Shustova, N. B.; Stukalin, E. B.; Lebedkin, S. F.; Seppelt, K.; Strauss, S. H.; Boltalina, O. V.; Dunsch, L. *J. Am. Chem. Soc.* **2007**, *129*, 11551.
(53) Chang, Y. C.; Kuo, M. Y.; Chen, C. P.; Lu, H. F.; Chao, I. *J. Phys. Chem. C* **2010**, *114*, 11595.
(54) Jian, H.; Tour, J. M. *J. Org. Chem.* **2005**, *70*, 3396.
(55) Luo, Z.; Zhang, Q.; Oderaotoshi, Y.; Curran, D. P. *Science* **2001**, *291*, 1766.
(56) Gosetti, F.; Mazzucco, E.; Zampieri, D.; Gennaro, M. C. *J. Chromatogr. A* **2010**, *1217*, 3929.
(57) Annesley, T. M. *Clinical chem.* **2003**, *49*, 1041.
(58) King, R.; Bonfiglio, R.; Fernandez-Metzler, C.; Miller-Stein, C.; Olah, T. *J. Amer. Soc. Mass Spectrom.* **2000**, *11*, 942.
(59) Wang, X.-B.; Wang, L.-S. *Rev. Sci. Instrum.* **2008**, *79*, 073108.
(60) Capelli, S. C. *J. Phys. Chem. A.* **2006**, *110*, 11695.
(61) Laikov, D. N.; Ustynuk, Y. A. *Russ. Chem. Bull.* **2005**, *54*, 820.
(62) Neese, F. *WIREs Comput. Mol. Sci.* **2012**, *2*, 73.

(63) Barth, W. E.; Lawton, R. G. *J. Am. Chem. Soc.* **1966**, *88*, 380.
(64) Scott, L. T.; Hashemi, M. M.; Meyer, D. T.; Warren, H. B. *J. Am. Chem. Soc.* **1991**, *113*, 7082.
(65) Scott, L. T.; Cheng, P.-C.; Hashemi, M. M.; Bratcher, M. S.; Meyer, D. T.; Warren, H. B. *J. Am. Chem. Soc.* **1997**, *119*, 10963.
(66) Butterfield, A. M.; Gilomen, B.; Siegel, J. S. *Org. Process Res. Dev.* **2012**, *16*, 664.
(67) Barth, W. E.; Lawton, R. G. *J. Am. Chem. Soc.* **1971**, *93*, 1730.
(68) Zabula, A. V.; Filatov, A. S.; Spisak, S. N.; Rogachev, A. Y.; Petrukhina, M. A. *Science* **2011**, *333*, 1008.
(69) Wu, Y.-L.; Stuparu, M. C.; Boudon, C.; Gisselbrecht, J.-P.; Schweizer, W. B.; Baldridge, K. K.; Siegel, J. S.; Diederich, F. *J. Org. Chem.* **2012**, *77*, 11014.
(70) Zoppi, L.; Martin-Samos, L.; Baldridge, K. K. *J. Am. Chem. Soc.* **2011**, *133*, 14002.
(71) Mack, J.; Vogel, P.; Jones, D.; Kaval, N.; Sutton, A. *Org. Biomol. Chem* **2007**, *5*, 2448.
(72) Valenti, G.; Bruno, C.; Rapino, S.; Fiorani, A.; Jackson, E. A.; Scott, L. T.; Paolucci, F.; Marcaccio, M. *J. Phys. Chem. C* **2010**, *114*, 19467.
(73) Dey, J.; Will, A. Y.; Agbaria, R. A.; Rabideau, P. W.; Abdourazak, A. H.; Sygula, R.; Warner, I. M. *J. Fluoresc.* **1997**, *7*, 231.
(74) Scott, L. T. *Angew. Chem. Int. Ed.* **2004**, *43*, 4994.
(75) Amsharov, K. Y.; Kabdulov, M. A.; Jansen, M. *Angew. Chem. Int. Ed.* **2012**, *51*, 4594.
(76) Grill, L.; Rieder, K.-H.; Moresco, F.; Rapenne, G.; Stojkovic, S.; Bouju, X.; Joachim, C. *Nat. Nanotechnol.* **2007**, *2*, 95.
(77) Gao, L.; Du, S.-X.; Gao, H.-J. *Int. J. Mol. Sci.* **2010**, *11*, 656.
(78) Mizyed, S.; Georghiou, P. E.; Bancu, M.; Cuadra, B.; Rai, A. K.; Cheng, P.; Scott, L. T. *J. Am. Chem. Soc.* **2001**, *123*, 12770.
(79) Scott, L. T. *Pure Appl. Chem.* **1996**, *68*, 291.
(80) Xu, G.; Sygula, A.; Marcinow, Z.; Rabideau, P. W. *Tetrahedron Lett.* **2000**, *41*, 9931.
(81) Schmidt, B. M.; Topolinski, B.; Yamada, M.; Higashibayashi, S.; Shionoya, M.; Sakurai, H.; Lentz, D. *Chem. Eur. J.* **2013**, *19*, 13872.
(82) Schmidt, B. M.; Seki, S.; Topolinski, B.; Ohkubo, K.; Fukuzumi, S.; Sakurai, H.; Lentz, D. *Angew. Chem. Int. Ed.* **2012**, *51*, 11385.
(83) Kuvychko, I. V.; Spisak, S. N.; Chen, Y.-S.; Popov, A. A.; Petrukhina, M. A.; Strauss, S. H.; Boltalina, O. V. *Angew. Chem. Int. Ed.* **2012**, *51*, 4939.
(84) Schmidt, B. M.; Lentz, D. *Chem. Lett.* **2014**, *43*, 171.
(85) Kuvychko, I. V.; Dubceac, C.; Deng, S. H. M.; Wang, X.-B.; Granovsky, A. A.; Popov, A. A.; Petrukhina, M. A.; Strauss, S. H.; Boltalina, O. V. *Angew. Chem. Int. Ed.* **2013**, *52*, 7505.
(86) San, L. K.; Bukovsky, E. V.; Kuvychko, I. V.; Popov, A. A.; Strauss, S. H.; Boltalina, O. V. *Chem. Eur. J.* **2014**, *20*, 4373.
(87) Clikeman, T. T.; Bukovsky, E. V.; Kuvychko, I. V.; San, L. K.; Deng, S. H. M.; Wang, X.-B.; Chen, Y.-S.; Strauss, S. H.; Boltalina, O. V. *Chem. Commun.* **2014**, *50*, 6263.

(88) Li, Y.; Li, C.; Yue, W.; Jiang, W.; Kopecek, R.; Qu, J.; Wang, Z. *Org. Lett.* **2010**, *12*, 2374.

(89) Chen, G.; Cooks, R. G.; Corpuz, E.; Scott, L. T. *J. Am. Soc. Mass Spectrom.* **1996**, *7*, 619.

(90) Wu, D.; Shao, T.; Men, J.; Chen, X.; Gao, G. *Dalton Trans.* **2014**, *43*, 1753.

(91) Baldridge, K. K.; Hardcastle, K. I.; Seiders, T. J.; Siegel, J. S. *Org. Biomol. Chem* **2010**, *8*, 53.

(92) pCrystal data for C62H13F35: Mr=1422.72 g mol−1; monoclinic; P21/c; a=18.1806(14).

(93) Steinberg, B. D.; Jackson, E. A.; Filatov, A. S.; Wakamiya, A.; Petrukhina, M. A.; Scott, L. T. *J. Am. Chem. Soc.* **2009**, *131*, 10537.

(94) Shi, K.; Lei, T.; Wang, X.-Y.; Wang, J.-Y.; Pei, J. *Chemical Science* **2014**, *5*, 1041.

(95) Seiders, T. J.; Baldridge, K. K.; Grube, G. H.; Siegel, J. S. *J. Am. Chem. Soc.* **2001**, *123*, 517.

(96) Zhang, Q.; Kawasumi, K.; Segawa, Y.; Itami, K.; Scott, L. T. *J. Am. Chem. Soc.* **2012**, *134*, 15664.

(97) Sevryugina, Y.; Rogachev, A. Y.; Jackson, E. A.; Scott, L. T.; Petrukhina, M. A. *J. Org. Chem.* **2006**, *71*, 6615.

(98) Filatov, A. S.; Zabula, A. V.; Spisak, S. N.; Rogachev, A. Y.; Petrukhina, M. A. *Angew. Chem. Int. Ed.* **2014**, *53*, 140.

(99) Sygula, A. *Eur. J. Org. Chem.* **2011**, 1611.

(100) Helfrich, W.; Schneider, W. G. *J. Appl. Phys.* **1966**, *44*, 2902.

(101) Helfrich, W.; Schneider, W. G. *Phys. Rev. Lett.* **1965**, *14*, 229.

(102) Adachi, C.; Tsutsui, T.; Saito, S. *Appl. Phys. Lett.* **1990**, *56*, 799.

(103) Shi, J.; Tang, C. W. *Appl. Phys. Lett.* **2002**, *80*, 3201.

(104) Lee, M.-T.; Chen, H.-H.; Liao, C.-H.; Tsai, C.-H.; Chen, C. H. *Appl. Phys. Lett.* **2004**, *85*, 3301.

(105) Hamal, S.; Hirayama, F. *J. Phys. Chem.* **1983**, *87*, 83.

(106) Melhuish, W. H. *J. Phys. Chem.* **1961**, *65*.

(107) Vincett, P. S.; Barlow, W. A.; Hann, R. A.; Roberts, G. G. *Thin Solid Films* **1982**, *94*, 171.

(108) San, L. K.; Clikeman, T. T.; Dubceac, C.; Popov, A. A.; Chen, Y.-S.; Petrukhina, M. A.; Strauss, S. H.; Boltalina, O. V. *Chem. Eur. J.* **2015**.

(109) Natarajan, P.; Schmittel, M. *J. Org. Chem.* **2012**, *77*, 8669.

(110) Duerr, B. F.; Chung, Y.-S.; Czarnik, A. W. *J. Org. Chem.* **1988**, *53*, 2120.

(111) Yamada, S.; Kinoshita, K.; Iwama, S.; Yamazaki, T.; Kubota, T.; Yajima, T. *RSC Adv.* **2013**, *3*, 6803.

(112) San, L. K.; Bukovsky, E. V.; Larson, B. W.; Whitaker, J. B.; Deng, S. H. M.; Kopidakis, N.; Rumbles, G.; Popov, A. A.; Chen, Y.-S.; Wang, X.-B.; Boltalina, O. V.; Strauss, S. H. *Chem. Sci.* **2014**, *6*, 1801.

(113) Levitus, M.; Garcia-Garibay, M. A. *J. Phys. Chem. A.* **2000**, *104*, 8632.

(114) Daele, I. V.; Bomholt, N.; Filichev, V. V.; Calenbergh, S. V.; Pedersen, E. B. *ChemBioChem* **2008**, *9*, 791.

(115) Kemp, T. J.; Roberts, J. P. *Trans. Faraday Soc.* **1969**, *65*, 725.

(116) Berlman, I. B. *Handbook of Fluorescence Spectra of Aromatic Molecules*; Academic Press, Inc.: New York, 1971.

Chapter 3.

Exploratory Chemistry with Fullerenes, Fullerene Derivatives, and PAHs

Section 3.1 describes the direct hydrogenation of fullerenes and fullerene derivatives. During the work described in Chapter 1, one of the control experiments indicated that the reagent (*n*-Bu)$_3$SnH can be used to hydrogenate the fullerene C_{60} at elevated temperatures. This, in turn, prompted the investigation of reactions with C_{70}. Indeed, hydrogenation of C_{70} can also occur at elevated temperatures. Later, the hydrogenation of trifluoromethylfullerenes (TMFs) was studied. The author of this dissertation performed all of the synthetic reactions, all of the HPLC analyses, and all of the spectroscopic measurements.

Section 3.2 describes the trifluoromethylated heterocycles, acridine (ACRD) and phenothiazine (PHTZ). This study is based on the application of the solvent-, catalyst-, and promotor-free synthesis used in Chapter 2 towards heterocyclic compounds containing nitrogen and sulfur atoms. In general, reactivity of PAHs and heterocycles appear to be similar. For instance, formation of (poly)trifluoromethyl heterocyclic derivatives with 4-6 CF_3 groups was observed with several isomers within each composition. The author of this dissertation performed all of the HPLC chromatography, spectroscopy, and grew crystals of compound **vii** suitable for X-ray diffraction studies. Single crystals of other compounds were grown by Dr. Olga V. Boltalina. Dr. Igor V. Kuvychko performed both of the syntheses.

Section 3.3 reports the solution-phase perfluorobenzylation and gas-phase perfluoroarylation of tetracene (TETR). Two isolated compounds bearing a perfluorobenzyl and a hydroxyl or hydrogen atom on the same carbon atom, resulting in the broken aromaticity of the TETR core,

were confirmed by X-ray crystallography. A separate study of the perfluoroarylation of TETR was performed in an attempt to realize a perfluorinated analogue of rubrene. Rubrene is a well characterized and studied *p*-type semiconductor known for its high charge carrier mobility. The author of this dissertation performed all of the synthesis, HPLC chromatography, spectroscopy, and grew crystals suitable for X-ray diffraction studies. Eric V. Bukovsky solved and refined the crystallographic data.

Project supervision by Prof. Steven H. Strauss and Dr. Olga V. Boltalina.

3.1. Hydrogenation of trifluoromethylfullerenes (TMFs), C_{60}, and C_{70}.

Recent progress in the applied science of fullerenes that includes optoelectronics[1,2] and biomedical[3] fields has been based on their uniquely versatile chemical reactivity which allows one to design and prepare derivatives with the required set of physical, electronic and chemical properties. Among numerous chemical reactions reported for the fullerenes in the past two decades, hydrogenation has been historically one of the first, along with fluorination, and the simplest functionalization method. Hydrofullerenes, i.e., fullerenes containing hydrogen atoms, have been of interest to the researchers both from the fundamental point of view and as promising materials for hydrogen storage.[4]

Furthermore, hydrofullerenes have been utilized effectively as synthons for further modifications of the fullerene cage by C–H activation (via deprotonation) followed by the electrophilic attack with the desired functional groups.[5] For example, the introduction of imine groups to deprotonated $C_{60}RH$ produced 1-imino-4-organo[60]fullerenes.[6] The deprotonation of 1,9-$C_{60}(CF_2C_6F_5)H$, discussed in Chapter 1, afforded a novel perfluoroaryl[60]fullerene which was shown as a viable alternative for the commonly used fullerene acceptor PCBM in organic photovoltaics applications.[7]

The recent study of chemical reactions with perfluoroalkylfullerenes revealed that the location of reactive sites can be quite reliably predicted by analyzing their molecular structures and DFT-calculated frontier orbitals. For instance, the sequential addition of cyano nucleophile followed by an electrophile attack to the most reactive bonds was supported both experimentally and theoretically.[8]

The reaction of organotin hydride with trifluoromethylfullerenes (TMFs) studied in this work resulted in the addition of two hydrogen atoms to the cage. Room-temperature reactions of organotin hydride with TMFs C_s-$C_{60}(CF_3)_4$ and C_1-$C_{60}(CF_3)_6$ yielded single-isomer bis-hydrogenated products with high yield within minutes. Reactions with other TMFs occur rapidly, but less selectively. In contrast, analogous reactions with parent fullerenes C_{60} and C_{70} required high temperatures and longer times, affording either single-isomer dihydrofullerenes, $C_{60}H_2$ and $C_{70}H_2$, respectively or mixtures of di- and tetra-hydrofullerenes.

3.1.1. General remarks. The TMF substrates studied in this section were chosen to test the reactivity of molecules with different number of CF_3 groups (i.e., $C_{60}(CF_3)_{2,4,6,10}$) and different addition patterns within the same composition (i.e., two compositional isomers of $C_{60}(CF_3)_4$ and three compositional isomers of $C_{60}(CF_3)_{10}$). This way, we were able to probe the chemical reactivity and selectivity based on the differences in their chemical structures. The Schlegel diagrams, 2D representations of the 3D fullerene molecules, of the selected TMFs for this work are shown in Figure 3.1.1. The notation follows a three number format in which the first value represents the size of the fullerene cage, the second value represents the number of CF_3 groups, and the third value represents the isomer number. For example, 60-4-2 describes the C_{60} fullerene with four CF_3 groups addends, and it is isomer number 2. The preparation of TMFs has been reported elsewhere.[9-11]

There are a few examples in the literature of further derivatization of TMFs. For instance, the epoxidation of 60-4-2, forming $C_{60}(CF_3)_4O$, shows high regioselectivity producing one major product that is far greater in air stability than the parent 60-4-2.[12] In another example, the cyanation of 60-4-2 produced one major product.[13] These results suggest that 60-4-2 can be used as an effective synthon for highly regiospecific chemical reactions due to the presence of the highly reactive double bond in the fulvene-like moiety.

Although the literature on hydrofullerenes is abundant, hydrofullerenes containing perfluoroalkyl(aryl) groups have been barely explored.[7,14,15] There are two examples of the hydrogenation of TMFs which was reported to occur during mass spectrometry measurements resulting in multiple additions of hydrogen atoms;[16] however, such a technique does not produce bulk samples for additional study or provide insight their structures. In another example, the crude product of trifluoromethylation of fullerenes with silver trifluoroacetate produced partially hydrogenated TMFs, but they were removed from the product via sublimation.[17,18]

3.1.2. Reactions with C_s-$C_{60}(CF_3)_4$ (III). The hydrogenation of compound **III** is worthwhile to explore due to the remarkable reactivity of the fulvene π-system.[12] The addition of two bulky substituents to compound **III**, is expected to occur onto the shortest double bond in the fullerene fulvene moiety to form the skew-pentagonal-pyramid (SPP) addition pattern due to the presence of the two largest DFT-predicted LUMO contributions on compound **III**.[10] For example, $C_{60}(CF_3)_6$-2 contains six CF_3 groups with the SPP addition pattern which gives rise to the C_s-symmetric nature of the compound despite the sterics of two CF_3 groups in the *ortho*- position in this structure.[10,19] On the other hand, if the sixth addend happens to be a hydrogen atom, the SPP addition pattern was not formed as observed for compounds $C_{60}(CF_3)_4(CN)H$[13] (due to the SPP-$C_{60}(CF_3)_4(CN)H$ isomer being ca. 5 kJ mol^{-1} higher in energy based on DFT calculations) and

$C_{60}(CH_2Ph)_2(Ph)_3H$.[20] Although, it is possible that the hydrogen atom results in the SPP addition pattern as observed for C_s-$C_{60}(C_2F_5)_5H$.[21] The addition of two small substituents, e.g., hydrogen atoms, to compound **III** is expected to most likely form the SPP addition pattern.

When 5 equiv. of (n-Bu)$_3$SnH was added to an *o*-DCB solution containing compound **III**, the color changed immediately from a dark orange color to a light orange color. The ^{19}F NMR spectrum (Figure 3.1.2) of the crude reaction products showed one major product with two apparent septets (δ −69.86 and −73.11 ppm) and two quartets (δ −71.22 and −71.65 ppm) indicating C_1 symmetry of the product. The septet is indicative of one CF_3 group coupled to two other CF_3 groups. The quartet is indicative of a terminal CF_3 group coupled to only one CF_3 group. In the ^{1}H NMR spectrum, two doublets were observed at δ 5.58 and 5.21 ppm with coupling constants of 3.5 Hz suggesting two inequivalent proton atoms that are in close proximity to each other. The same results were observed when using cyclohexane, benzene or toluene as the reaction solvents indicating that facile hydrogenation occurred in non-polar solvents as well yielding the same products. Note, a minor impurity (ca 4% based on NMR integration) with two quartets (δ_F −71.53 and −73.99 ppm) and two multiplets (δ_F −70.9 and −71.0 ppm) was formed as observed by ^{19}F NMR spectroscopy. The fact that the major hydrogenation product of compound **III** is not symmetric based on ^{19}F NMR (Figure 3.1.2), the SPP-addition pattern was not formed, which suggests that sterics have no role in directing the reaction despite the small size of the hydrogen atoms and presence of the reactive short double bond in the structure.

3.1.3. Reactions with C_1-$C_{60}(CF_3)_4$ (II). Compound **II** has a different arrangement of the CF_3 groups on the cage than compound **III**. Its four CF_3 groups form a *para*-, *meta*-, *para*- (*pmp*) addition pattern; therefore, the reactivity toward hydrogen atoms was expected to be different.

When 5 equiv. of (n-Bu)$_3$SnH was added to a $CDCl_3$ solution containing compound **II** under aerobic conditions, slow consumption of compound **II** was observed (Figure 3.1.3B). Upon successive addition of 25 equiv. (Figure 3.1.3C) and 55 equiv. (Figure 3.1.3D) of (n-Bu)$_3$SnH, one major product was formed with two septets (δ_F −68.03 and −73.01 ppm) and two quartets (δ_F −71.96 and −72.80 ppm) along with other unidentified impurities. The ^{1}H NMR exhibits two doublets at δ 5.45 and 4.94 ppm with coupling constants of 4.70 Hz. The ESI-MS analysis of this product showed two abundant ions at m/z of 997 and 1993 corresponding to $C_{60}(CF_3)_4H^-$ and $[C_{60}(CF_3)_4H]_2^-$, respectively, with the latter being a likely product of dimerization during the mass spectrometry experiment.

Interestingly, when 10 equiv. of (n-Bu)$_3$SnH was added to compound **II** under anaerobic conditions, the ^{19}F spectrum (Figure 3.1.4B) observed after 17 h was similar to the ^{19}F spectrum (Figure 3.1.3D) from the aerobic reaction with 55 equiv. of (n-Bu)$_3$SnH. When this anaerobic reaction sample was exposed to air, the major product converted into a more stable and isolable product (Figure 3.1.4C) exhibiting an apparent septet at δ −68.84, a septet at δ −73.55, and two quartets at δ −72.75 and −73.15 ppm in the ^{19}F NMR spectrum and two doublets at δ 5.30 and 5.19 ppm in the ^{1}H NMR spectrum with coupling constants of 9.78 Hz.

One explanation for this transformation is that the hydrogenation initially results in the kinetically favored isomer of $C_{60}(CF_3)_4H_2$. Upon exposure to air, the thermodynamically favored isomer of $C_{60}(CF_3)_4H_2$ or its hydroxide derivative is formed. The addition of two hydrogen atoms occurs albeit at a much slower rate (hours instead of minutes) in comparison to compound **III** highlighting the differences in reactivity even though both compounds have the same number of CF_3 groups and reactions were carried out under the same conditions.

3.1.4. Reactions with C_1-$C_{60}(CF_3)_6$ (IV). If two more CF_3 groups are added to compound **III** continuing the ribbon-like pattern, an isomer of $C_{60}(CF_3)_6$ (compound **IV,** see Figure 3.1.1 for the Schlegel diagram) can be derived. When 10 equiv. of (*n*-Bu)$_3$SnH was added to a $CDCl_3$ solution of compound **IV** under aerobic conditions, one major product was formed within minutes and persisted for at least 6 h (Figure 3.1.5). In the ^{19}F NMR spectrum, there are three septets (δ_F δ −69.44, −69.86, and −72.55 ppm), one multiplet (δ_F −71.93 ppm), and two quartets (δ_F −71.10 and −71.21 ppm). At the same time, two doublets (δ 4.82 and 4.75 ppm) are observed in the ^{1}H NMR spectrum. The NMR spectra are consistent with the formation of $C_{60}(CF_3)_6H_2$.

When the same reaction was performed under anaerobic conditions, the same major product was formed immediately. Upon further monitoring of the reaction, the resonances due to this product slowly decreased over 45 h until no CF_3 resonances were observed in the ^{19}F NMR. One explanation for the disappearance of the CF_3 signals could be due to multiple isomers of $C_{60}(CF_3)_6H_2$ forming attenuating the fluorine signals or the hydrogenated compound **IV** converted into a less soluble product. Remarkably, the instantaneous hydrogenation of compound **IV** was highly selective and forms one major product.

3.1.5. Reactions with C_1-$C_{60}(CF_3)_2$ (I). Compound **I** was explored because it is the simplest TMF containing only two CF_3 groups. When 20 equiv. of (*n*-Bu)$_3$SnH was added to compound **I** (99%+ purity) dissolved in $CDCl_3$ at room temperature under aerobic conditions, no change was observed in the ^{19}F NMR spectrum after 30 minutes. Only after an additional 20 equiv. of (*n*-Bu)$_3$SnH was added, an asymmetric product began to form within minutes. Over the course of 91 h, the formation of at least 4 products was observed, which were subsequently consumed. At the end of 91 h, a single symmetric compound exhibiting a singlet at δ_F −73.63 ppm persisted. The

slow rates and low selectivity of this reaction turned our attention towards reactions at elevated temperatures.

When compound **I** was heated at 105 °C for 24 h in the presence of 2 equiv. of (n-Bu)$_3$SnH under anaerobic conditions, one asymmetric, one symmetric, and a mixture of asymmetric compounds in a 1:10:3 ratio were formed as determined by HPLC which indicated that 71% of the product was constituted by a single symmetric product. The C_6D_6 ^{19}F NMR spectra of the isolated compounds are shown in Figure 3.1.6 where the isolated asymmetric compound exhibits two quartets at δ_F −70.53 and −73.19 ppm and the symmetric compound exhibits a singlet at δ_F −72.32 ppm. Interestingly, both isolated compounds exhibit a singlet at δ 4.72 and 5.08, respectively, in the ^{1}H NMR spectra. The fact that a singlet is observed in the ^{1}H NMR spectrum for the asymmetric compound is not fully understood. The current hypotheses are that either the two proton signals are isochronous resulting in the same chemical shift or another substituent other than hydrogen, such as hydroxide, was added. The latter may be a broad signal due to hydrogen bonding with an adjacent fullerene molecule. On the other hand, the symmetric compound formed in the high temperature reaction is the same symmetric compound formed after 91 h under anaerobic conditions from the previously discussed reaction. The fact that only one major compound was formed under two different reaction conditions suggests that this compound is both kinetically and thermodynamically favored.

3.1.6. Reactions with C_1-$C_{60}(CF_3)_{10}$-2,3,6 (V, VI, VII). Three isomers of $C_{60}(CF_3)_{10}$ (compounds **V**, **VI**, and **VII**) were chosen as fullerenes with 10 CF_3 groups to study. When 5 equiv. of (n-Bu)$_3$SnH was added to a benzene solution of compound **V** under aerobic conditions at room temperature, the fluorine resonances due to compound **V** immediately decreased, and after 24 h, no fluorine resonances were observed in the ^{19}F NMR spectra. The same results were observed

when the same reaction conditions were applied to compound **VII**. We propose that over time, multiple hydrogenated products are formed in low concentrations that cannot be detected by NMR spectroscopy. In sharp contrast, compound **VI** forms one product upon the room temperature addition of 5 equiv. of $(n\text{-Bu})_3\text{SnH}$ under aerobic conditions. This new compound persists for over 2 h when monitored by ^{19}F NMR spectroscopy (Figure 3.1.7), but diminishes overtime similarly to compounds **V** and **VII**. The fluorine resonances completely disappear after 21 h based on the ^{19}F NMR spectra analysis; thus, the selectivity of the hydrogenation reactions with compounds **V** and **VII** was not observed whereas compound **VI** reacted with $(n\text{-Bu})_3\text{SnH}$ with high selectivity. These results suggest that the addition pattern of the ten CF_3 groups greatly affects the selectivity of the hydrogenation.

3.1.7. Hydrogenation of C_{60} and C_{70}. To explore further room temperature fullerene hydrogenation, reactions between C_{60} and $(n\text{-Bu})_3\text{SnH}$ were investigated. When 24 equiv. of $(n\text{-Bu})_3\text{SnH}$ was added to a toluene solution of C_{60} at room temperature under aerobic conditions, the hydrofullerene $C_{60}H_2$ was formed exclusively but in low conversion. The rate of reaction was extremely slow (days) in comparison to the hydrogenation of the TMFs (minutes); thus, reactions were performed at higher temperatures. Hirsch *et al.* first reported that the treatment of C_{60} with $(n\text{-Bu})_3\text{SnH}$ in refluxing benzene for 24 h formed 1,9-$C_{60}(\text{SnBu}_3)\text{H}$ in 59% yield.[22] A more recent example showed that formation of $C_{60}(\text{BuH})_{1-3}$ was observed after refluxing in toluene for 6 h, but the formation of the hydrostannylated fullerene product was not reported.[23]

To compare the reactivity between C_{60} and compound **I** under the same reaction conditions, 2 equiv. of $(n\text{-Bu})_3\text{SnH}$ was added to C_{60} dissolved in *o*-DCB and heated at 105 °C for 24 h. The conversion of C_{60} was low (in comparison to the conversion of compound **I**), but the reaction produced mostly $C_{60}H_2$ and small amounts of $C_{60}H_4$ which were confirmed by NMR

spectroscopy. When the reaction was repeated under refluxing *o*-DCB, $C_{60}H_2$ and $C_{60}H_4$ were also the major products formed. The hydrostannation[22] or hydroalkylation[23] products previously reported for reactions of organotin hydride with bare-cage fullerenes were not observed. It could very well be under the applied reaction conditions that 1,9-$C_{60}(SnBu_3)H$ observed by Hirsch *et al.* is not thermally stable and would not withstand higher reaction temperatures due to the higher boiling point of *o*-DCB than the boiling point of benzene.

When C_{60} dissolved in *o*-DCB was heated under anaerobic conditions at 100(5) °C for 24 h in the presence of 2 equiv. of $(n\text{-Bu})_3SnH$, the major product isolated by HPLC (Figure 3.1.8) and characterized by ^1H NMR and mass spectrometry was $C_{60}H_2$ and small amounts of $C_{60}H_4$ were detected. The ^1H NMR of the isolated compounds are in agreement with the literature reported spectra.[24,25] If the reaction time is increased from 24 h to 48 h, higher conversion of C_{60} was observed, and a small peak at shorter retention times appears which was attributed to $C_{60}H_6$. When more equiv. of $(n\text{-Bu})_3SnH$ were used, as expected, further hydrogenation occurred to produce more $C_{60}H_4$ with possible formation of $C_{60}H_6$ (Figure 3.1.8).

When the reaction was performed at a higher reaction temperature of 140 °C for 2 h with 2 equiv. (dashed line) and 24 equiv. (solid line) of $(n\text{-Bu})_3SnH$, mostly $C_{60}H_2$ and $C_{60}H_4$ was produced as seen in the HPLC chromatogram (Figure 3.1.9). The conditions for the highest yield of $C_{60}H_2$ (57% yield based on converted C_{60}) were achieved when the reaction temperature was 160 °C with 24 equiv. of $(n\text{-Bu})_3SnH$ and heated for 2 h.

When C_{70} was used instead of C_{60} with 24 equiv. of $(n\text{-Bu})_3SnH$ and heated for 2 h, $C_{70}H_2$ was formed in 61% yield based on converted C_{70} with the other 39% constituting $C_{70}H_4$ (HPLC chromatogram not shown). The ^1H NMR of the isolated $C_{70}H_2$ is in agreement with the literature reported spectrum with δ_H at 4.82 and 5.30 ppm for the 1,2-$C_{70}H_2$ isomer.[26] The advantage of

this direct hydrogenation methodology is that it circumvents the use of fullerene based intermediates[27,28] and transition metal complexes.[29]

3.1.8. Summary and conclusions. The use of (n-Bu)$_3$SnH as a hydrogenation reagent was investigated for bare fullerenes and TMFs. Surprisingly, the hydrogenation of some TMFs can occur selectively, in high yields, and within seconds/minutes at room temperature. Due to the decrease in reactivity, elevated temperatures are required for bare-cage C_{60} and C_{70} fullerenes. No correlation was found between the number of CF_3 groups present on the fullerene cage and rates or selectivity of hydrogenation. For example, high selectivity was observed for the hydrogenation of $C_{60}(CF_3)_6$ (compound **IV**), while multiple products were formed during the hydrogenation of the other two selected $C_{60}(CF_3)_{10}$ isomers. With this, the selectivity of the fullerene compounds investigated in this work is as follows: compound **III, IV, VI** > **I** > **II** > **V**, **VII** based on the number of compounds formed during the reaction. The hydro-TMFs presented here can be useful synthons for further chemical elaborations enhancing desirable functionality, e.g., solubility in certain polar solvents or their electronic properties by introducing various electron withdrawing or electron donating groups, which can lead to molecular engineered materials as potent electron acceptors. Additional studies to be performed include DFT calculations of the localized HOMO and LUMO orbitals to predict the most stable isomers and deprotonation experiments of the TMF hydrides followed by subsequent addition electrophiles are of particular interest.

3.1.9. Experimental.

Solvents and reagents. The following reagents and solvents were used as received unless otherwise indicated: C_{60} (MTR Ltd., 99.5+%); C_{70} (Term USA, >98%); tri-n-butyltin hydride ((n-Bu)$_3$SnH, Strem Chemicals, 95+%, stored under N_2), 1,2-dichlorobenzene (o-DCB, Acros

Organics, 99%); chloroform-d ($CDCl_3$, Cambridge Isotope Labs, 99.8%); benzene (EMD Chemical, ACS grade); toluene (Fisher Scientific, ACS grade, dried over Na and stored under N_2); hexafluorobenzene (Oakwood Products); cyclohexane. For HPLC separations: toluene (Fisher Scientific, ACS grade); acetonitrile (Fisher Scientific, ACS grade); heptane (Fisher Scientific, HPLC grade).

Instrumentation. HPLC analysis and separations were carried out using a Shimadzu LC-6AD system with a SPD-201A UV-vis detector, a SPD-M20A diode array detector set at 300 nm and 370 nm, and a CBM-20A communication bus module. The columns used were a semi-preparative COSMOSIL Buckyprep column (10 × 250 mm, Nacalai Tesque) and a semi-preparative COSMOSIL Buckyprep-M column (10 × 250 mm, Nacalai Tesque). APCI mass spectra were recorded on a 2000 Finnigan LCQ-DUO mass spectrometer (CH_3CN carrier solvent, 0.3 mL min^{-1} flow rate). Fluorine-19 (376 MHz) and ^1H (399 MHz) NMR spectra were recorded using a Varian INOVA 400 instrument with trace amount of C_6F_6 ($\delta(^{19}F)$ −164.9) added as the internal standard.

Hydrogenation of $C_{60}(CF_3)_n$ [n = 0,2,4,6,10] and C_{70}. For anaerobic reactions, samples were either prepared in a N_2 glovebox or degassed at least three times using the freeze-pump-thaw technique (for elevated temperature reactions). A typical reaction consists of the addition of (n-Bu)$_3$SnH with a syringe to a sonicated solution containing the fullerene and allowed to sit for at least five minutes prior to the addition of $CDCl_3$ for NMR analysis.

3.2. Trifluoromethylated acridine (ACRD) and phenothiazine (PHTZ).

Potential applications of acridine (ACRD) and phenothiazine (PHTZ) based compounds have been investigated in pharmacotherapeutics for prion diseases,[30] antibacterial reagents,[31] and other medicinal uses.[32-35] More recently, research of heterocycles and their derivatives has begun to

include applications in organic electronics.[36-38] The trifluoromethylation of heterocycles has been demonstrated elsewhere.[39,40] Most importantly, the reactions typically involve a regiospecific mono-trifluoromethylation via catalytic substitution routes. Adding electron withdrawing CF_3 groups has profound effects on the physical, chemical, and biological properties which can be tailored for various applications.

ACRD and PHTZ are heterocyclic analogues of ANTH. For ACRD, one of the central carbon atoms of the ANTH core is replaced with a nitrogen atom. For PHTZ, both central carbon atoms of the ANTH core are replaced with a sulfur atom and an NH group; thus, product distribution for both substrates will most likely be different than ANTH substituted with CF_3 groups.[41] Such replacement of the carbon atom core with a nitrogen or sulfur group will be of interest from an electronic property standpoint to understand the effects of heteroatoms on the relevant characteristics such as electron affinity, redox potentials, and solid-state packing. It is known that for parent PAHs, the electron affinity values increase upon the introduction of nitrogen in the carbon framework of PAHs. For example, the electron affinity increases by 0.366 eV from ANTH (0.530 eV[42]) to ACRD (0.896 eV[43]).

Dr. Igor V. Kuvychko investigated, as part of his post-doctoral work, the trifluoromethylation of two heterocyclic compounds: acridine (ACRD) and phenothiazine (PHTZ). The developed solvent-, catalyst-, and promoter-free synthesis for trifluoromethylation of PAHs was used to modify these heterocyclic substrates.[41,44-47] For instance, nine equiv. of CF_3I heated at 330 °C for 8.5 h or ten equiv. of CF_3I heated at 330 °C for 7.5 h were performed for ACRD and PHTZ, respectively. A typical work up consisted of the removal of I_2 by reduced pressures or by $Na_2S_2O_3$ aqueous wash.

3.2.1. HPLC separation and characterization of ACRD(CF_3)$_n$. The separation scheme in Figure 3.2.1 shows how the 11 ACRD(CF_3)$_n$ compounds isolated and characterized from the crude product material. Note that two detection wavelengths (300 and 370 nm) were used for HPLC trace peak analysis; however, only one wavelength was used for the collection of compounds. The different detection wavelengths are of importance due to the different molar absorptivity of the various ACRD(CF_3)$_n$ compounds. The structural assignments are based on the ^{19}F NMR (Figure 3.2.2), ^{1}H NMR (Figure 3.2.3), and X-ray crystallographic analysis. The majority of the ACRD compounds isolated contain three to five CF_3 groups.

Single crystals of compounds **iii**, **vii**, and **x** were grown from MeCN solutions and were found suitable for X-ray diffraction studies. Their confirmed molecular structures along with the ACRD numbering scheme are shown in Figure 3.2.4. There are some interesting NMR spectra characteristics concerning these three ACRD(CF_3)$_n$ compounds. When compounds **iii** and **x** are compared, one resonance has δ(^{19}F) chemical shifts between −50 and −55 ppm whereas compound **vii** does not have a resonance in its ^{19}F NMR spectra. This range of chemical shifts was also observed for ANTH-6-1 which has a chemical shift of ca. −51 ppm.[41] The difference in the structures arises from the fact that there is a CF_3 group attached to the 9 position in compounds **iii**, **x** and ANTH-6-1, whereas it is not the case for compound **vii**. When analyzing the ^{1}H NMR spectra of compound **vii**, one resonance has a δ(^{1}H) chemical shift of ca. 9.5 ppm which is absent in compounds **iii** and **x**. Again, this difference arises from the fact that there is a proton attached to the 9 position as in the case for compound **vii**. The observed trend of the downfield chemical shift for substituents (i.e., CF_3 groups or hydrogen atoms) attached to the 9 position can be used to predict the molecular structures of the other ACRD(CF_3)$_n$ compounds.

The nitrogen atom in the *para*- positions to the 9 position most likely influences this trend. For example, the proton on the 9 position in ANTH has a chemical shift of ca. 8.4 ppm where it has a chemical shift of ca. 8.8 ppm in ACRD suggesting that substituents *para*- to the nitrogen atom will have more deshielded chemical shifts.

3.2.2. HPLC separation and characterization of PHTZ(CF_3)$_n$. From the reaction between PHTZ and CF_3I gas, only one derivative has so far been isolated in sufficient purity and yield for characterization. The separation scheme and ^{19}F and ^{1}H NMR spectra are shown in Figure 3.2.5. The two quartets and two singlets observed in the ^{19}F NMR spectrum indicate two coupled CF_3 and two isolated CF_3 groups, respectively. The NH group gives rise to the broad singlet at $\delta(^{1}H)$ 6.67. Further experiments to improve selectivity and yield are currently underway in our laboratory and will be reported in the future.

3.2.3. Summary and conclusions. Preliminary work on the trifluoromethylation of ACRD and PHTZ shows that the developed solvent-, catalyst-, and promotor-free synthesis was applicable to heterocycles that contain nitrogen and/or sulfur atoms and can be separated in high purity by HPLC. For the isolated ACRD(CF_3)$_n$ compounds for which X-ray data are not known, the molecular structures can be predicted based on the NMR trends observed for compounds **iii**, **vii**, and **x**. In the case of PHTZ(CF_3)$_n$, only one compound has been characterized so far and does not appear to substitute the hydrogen atom on the NH group with a CF_3 group. Additional experimentations to be performed are the measurement of the solution reduction potentials by cyclic voltammetry of the highly purified compounds, gas-phase electron affinity measurements, and electron paramagnetic resonance spectra. Comparisons will be made between PAHs and heterocycles and will be used to foster fundamental knowledge on the effects of various heterocycles.

3.2.4. Experimental.

Methods, reagents and solvents. Acridine (Sigma Aldrich, 97%), phenothiazine (Sigma Aldrich, 98%), iodotrifluoromethane (CF_3I. SynQuest Labs), sodium thiosulfate ($Na_2S_2O_3$, Fisher Scientific, ACS grade), chloroform-*d* ($CDCl_3$, Cambridge Isotopes), hexafluorobenzene (Oakwood Products), dichloromethane (Fisher Scientific, ACS grade), and acetonitrile (Fisher Scientific, ACS grade) were used as received. Deionized distilled water was purified by a Barnstead NANOpure Ultrapure Water system (final resistance 18 MΩ).

Instrumentation. HPLC analysis and separation were carried on a Shimadzu instrument (composed of Shimadzu LC-6AD pump, a Shimadzu UV detector SPD-20A, and a communication bus module Shimadzu CBM-20A). The columns used were COSMOSIL Bucky-prep (Nacalai Tesque, 10 × 250 mm) and FluoroFlash (Fluorous Technologies, Inc., PF-C8, 5 μm). Proton (399 MHz) and ^{19}F (376 MHz) NMR spectra were recorded on a Varian INOVA instrument in $CDCl_3$ solution using C_6F_6 ($\delta(^{19}F) = -164.9$) as the internal standard.

3.3. Perfluorobenzylation of tetracene (TETR).

Tetracene, composed of four fused benzene rings, is typically used as a *p*-type semiconductor, and it is well known for its singlet fission phenomenon in crystalline form.[48-53] Singlet fission, the production of two excited triplet states from a singlet excited state, has been predicted to improve power conversion efficiencies of OPVs if charge collection is efficient. This has led to the development of organic solar cells based on singlet fission.[54] Rubrene, a tetracene derivative bearing four phenyl groups, also contains similar singlet fission characteristics[55] and considered as the benchmark for very high charge mobility.[56] To further improve the charge carrier mobility, partially fluorinated analogous of rubrene-like structures were investigated and shown to improve charge carrier characteristics.[57,58] A complete

perfluoroaryl rubrene analog has not been realized experimentally. The introduction of perfluorobenzyl groups is an attractive alternative to perfluoroaryl groups due to the stronger electron withdrawing strength and the additional conformational flexibility observed in pentakis(perfluorobenzyl)corannulene.[59]

3.3.1. Synthesis and characterization of TETR(Bn_F)$_n$. The temperatures required to sublime TETR were too high for reactions with $C_6F_5CF_2I$ in gas-phase reactions typically carried out in sealed glass ampoules as observed for reactions between 330 °C to 360 °C. The dimerization of $C_6F_5CF_2I$ was observed as the major product and significant insoluble carbonaceous products were formed. Reaction temperatures at 200 °C were not sufficient to sublime TETR into the gas-phase; thus, the solution-phase reactions described in Section 2.3 and Section 2.4 of Chapter 2 were adapted for the perfluorobenzylation of TETR. A DMSO solution containing TETR (0.087 mmol) was charged with copper powder (0.26 mmol) and perfluorobenzyliodide (0.18 mmol) and degassed three times by a freeze-pump-thaw technique. The reaction mixture was heated for 24 h in a ca. 160 °C oil bath. Single crystals of compounds **a** ($C_{25}H_{11}F_7O_2$), compound **b** ($C_{25}H_{11}F_7O$), and compound **c** ($C_{25}H_9F_7O$) were grown and found suitable for X-ray diffraction studies after HPLC separations (see Figure 3.3.1). In each compound, the aromaticity of the TETR core was broken resulting in the formation of dihydro-TETR (H_2-TETR) derivatives such that each derivative contains at least one sp^3 carbon atom as confirmed by X-ray crystallography.

For example, in compounds **a** and **b,** two substituents ($CF_2C_6F_5$, OH and $CF_2C_6F_5$, H, respectively) are attached to the same sp^3 carbon atom. Their molecular drawings are shown in Figure 3.3.2 and Figure 3.3.3. A ketone is found to be in the *para*- position from the sp^3 carbon atom in both compounds. At the same time, compound **c** also contains a ketone with a *cyclo*-CFC_6F_4 substituent in the *para*- position. This type of *cyclo*-adduct resulted from the loss of an

aromatic fluorine atom (as described in Chapter 1) of the perfluorobenzyl functional group. Most strikingly was the loss of a fluorine atom from the $–CF_2$ methylene bridge resulting in a double bond connecting the fluoro-substituent and the H_2-TETR core.

In the ^{19}F NMR spectrum of compound **a** (Figure 3.3.5), the expected resonances of the perfluorobenzyl moiety are observed; however, the resonance for the CF_2 group changes from a triplet in compound **a** to a complex multiplet in compound **b** (Figure 3.3.7), which suggests geminal coupling with the hydrogen atom in compound **b**. In fact, the chemical shift of the hydrogen atom is deshielded from δ 3.20 ppm in compound **a** to δ 5.04 ppm in compound **b** as seen in the ^1H NMR spectra (Figure 3.3.6 and Figure 3.3.8, respectively). Interestingly, the multiplicity of this resonance changes from a singlet in compound **a** to a triplet in compound **b** further confirming geminal coupling with the CF_2 group.

Figure 3.3.2 and Figure 3.3.3 show the solid-state packing for compounds **a** and **b**, respectively. As shown for compound **a** in Figure 3.3.2, no π-π overlap between the H_2-TETR cores was observed; however, the Bn_F groups form an insulating layer between H_2-TETR cores and exhibits some π-π overlap separated by 4.14 Å. In comparison, compound **b** exhibit no π-π overlap between the H_2-TETR cores or between the Bn_F groups (Figure 3.3.3). The solid-state packing for compound **c** is currently being investigated.

3.3.2. Perfluoroarylation of TETR. An attempt to synthesize a perfluoroaryl analogue of rubrene involved reacting TETR (0.22 mmol) and pentafluorophenyliodide (3.5 mmol) in the gas phase at 375 °C for 2 h and in the presence of copper powder (3.8 mmol).[41,44-46] The crude product was placed under dynamic vacuum to remove any volatiles after it was cooled to room temperature, extracted with dichloromethane and filtered. The HPLC analysis of the crude product mixture revealed upon further separation and characterizations that the unproductive reaction forms

decafluorobiphenyl and unreacted TETR (Figure 3.3.9). Two compounds identified as **α** and **§** require further characterizations, but are believed to be TETR(Ph_F) and the dimer $[TETR]_2$, respectively, based on ^{19}F and ^{1}H NMR spectroscopy. Solution-phase reactions will be investigated in the future.

3.3.3. Summary and conclusions. The perfluorobenzylation of TETR was shown to occur in the solution based reactions. The NMR characterization showed that only one Bn_F group was attached to H_2-TETR core. The HPLC separation of H_2-TETR$(Bn_F)_n$ derivatives show that multiple products are formed within the reaction; thus, synthetic approaches towards higher selectivity will be investigated. More importantly, the origin of the oxygen atoms in the X-ray determined structures requires further investigation. Do they come from post reaction workup or during the reaction with trace amount of water? It is also possible that the origin of the oxygen atoms comes from the reaction solvent DMSO. Additionally, the intramolecular cyclization of compound **c** (which still needs to be analyzed by NMR spectroscopy) resembles that of the intramolecular cyclization of 1,9-$C_{60}(CF_2C_6F_5)H$[7] described in Chapter 1 and needs to be further explored. Although the loss of HF occurred from sp^2 and sp^3 bearing carbon atoms in 1,9-$C_{60}(CF_2C_6F_5)H$, in compound **c**, the loss of HF would occur from only sp^2 carbon atoms; thus, the reactivity and mechanism will most certainly be different. Rearomatization of dihydrotetracene derivatives will be interesting to explore to form molecules with stronger acceptor properties and improved π-π overlap.

3.3.4. Experimental.

Methods, reagents and solvents. Tetracene (Acros Organics, 98%), perfluorobenzyl iodide ($C_6F_5CF_2I$, SynQuest), 1,4-bis-(trifluoromethyl)benzene (Sigma Aldrich), chloroform-*d* ($CDCl_3$,

Cambridge Isotopes), Cu powder (Strem Chemicals, 99%), dichloromethane (Fisher Scientific, ACS grade), and acetonitrile (Fisher Scientific, ACS grade) were used as received.

Instrumentation. HPLC analysis and separation were carried on a Shimadzu instrument (composed of Shimadzu LC-6AD pump, a Shimadzu UV detector SPD-20A, and a communication bus module Shimadzu CBM-20A). The columns used were COSMOSIL Bucky-prep (Nacalai Tesque, 10 × 250 mm). Proton (399 MHz) and ^{19}F (376 MHz) NMR spectra were recorded on a Varian INOVA instrument in $CDCl_3$ solution using 1,4-bis-(trifluoromethyl)benzene ($\delta(^{19}F) = -66.35$; $\delta(^{1}H) = 7.77$) as the internal standard.

Reaction workup. After the reaction mixture was cooled to room temperature, liquid-liquid extraction (water:ether) was used to extract the TETR$(Bn_F)_n$ compounds into the organic layer. The organic layer was washed several times with deionized water, dried over anhydrous $MgSO_4$ and passed through a silica gel column. The resulting filtrate was concentrated down to dryness.

3.4. Chapter Summary and Conclusions.

In Chapter 3, three on-going projects were described. First, the room temperature instantaneous hydrogenation of TMFs and elevated temperature reactions of C_{60} and C_{70} using $(n\text{-Bu})_3SnH$ were discussed. The products from the crude reaction mixture are separated by HPLC and were characterized by NMR spectroscopy. In general, there was no correlation found between the number of CF_3 groups and the selectivity of hydrogenation. Secondly, the gas-phase trifluoromethylation developed previously by our group was not only applicable to PAHs, but to heterocycles such as ACRD and PHTZ. Finally, the perfluoro- benzylation and arylation of TETR was investigated. It was shown that the aromaticity of the TETR core can be broken forming dihydro-TETR derivatives. Also, the intramolecular cyclization of the perfluorobenzyl moiety, as seen in Chapter 1, still needs to be further investigated.

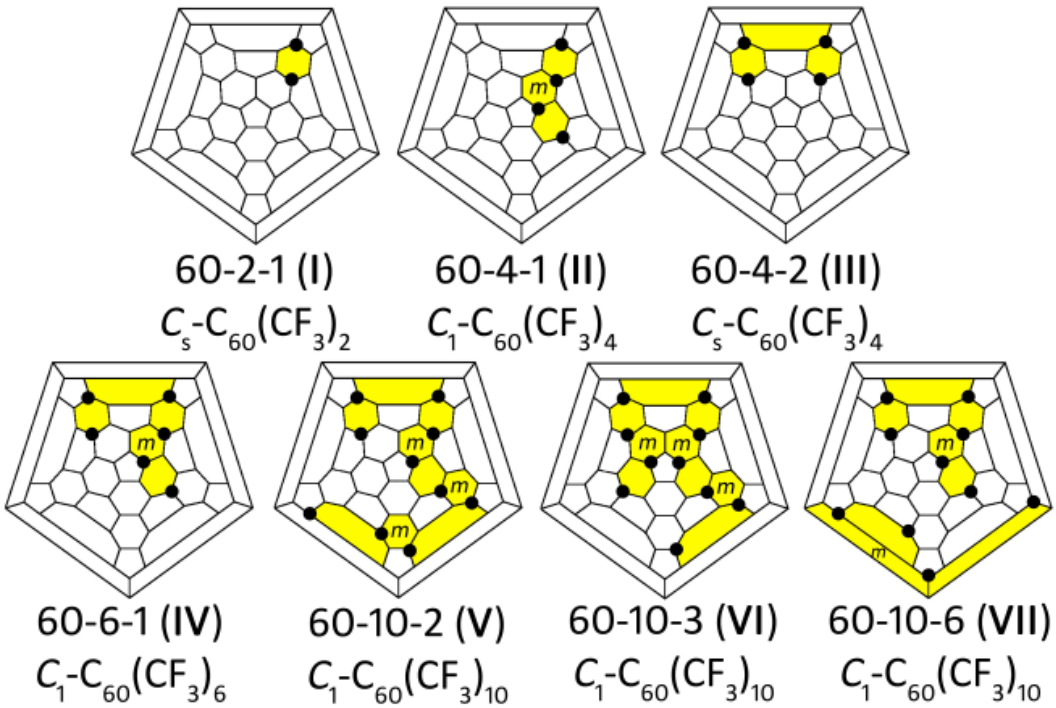

Figure 3.1.1. Schlegel diagrams of TMFs used for this work with notations from ref [10]. The first digit describes the fullerene cage size, the second digit describes the number of CF_3 groups, and the third digit describes the isomer number. For example, 60-2-1 refers to C_{60} with two CF_3 groups isomer number one. The Roman numeral denotes corresponding compound number. Black circles represent CF_3 groups and the yellow highlights edge sharing hexagons connecting in a *para*- or *meta*- (*m*) addition pattern.

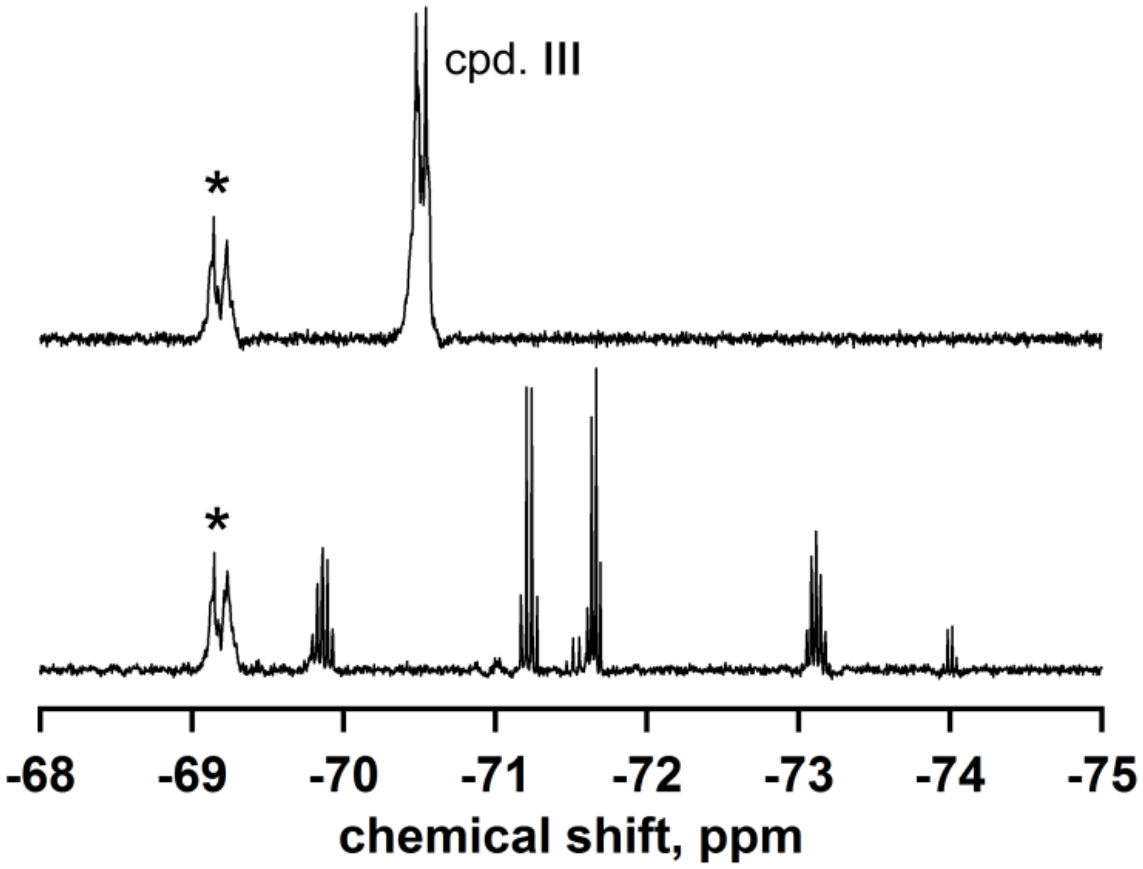

Figure 3.1.2. The before (top) and after (bottom) ^{19}F NMR spectra of compound **III** and 5 equiv. $(n\text{-Bu})_3SnH$. The compound $C_s\text{-}C_{60}(CF_3)_4O$ is marked with an asterisk.

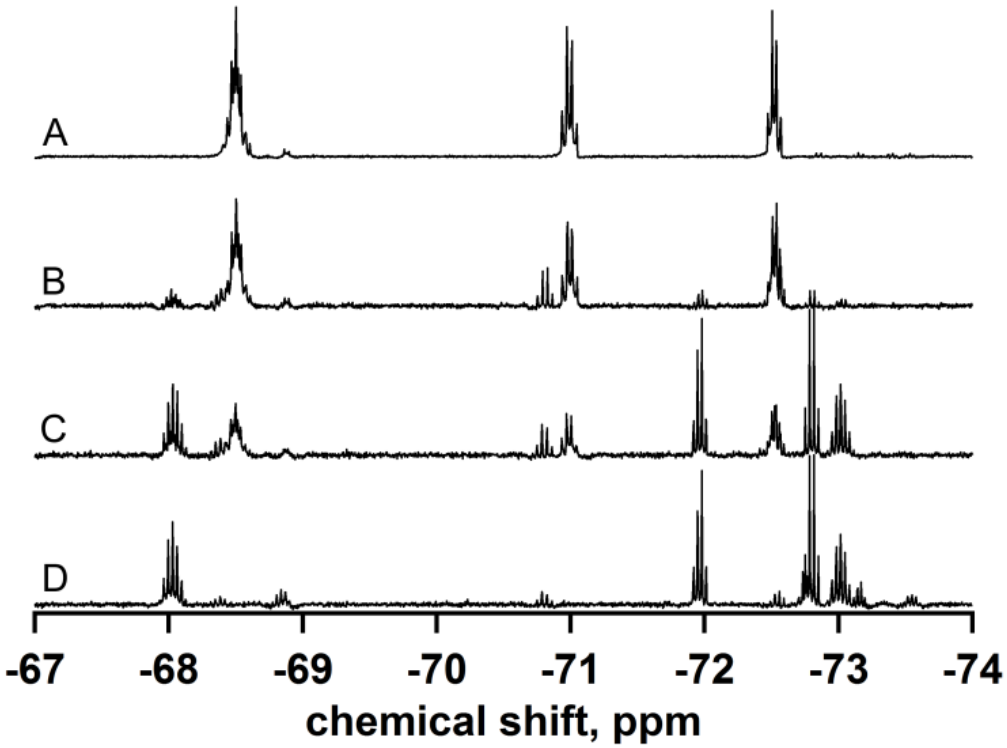

Figure 3.1.3. The ^{19}F NMR spectra after the addition of (n-Bu)$_3$SnH to compound **II** under aerobic conditions. A: starting compound **II**; B: after 5 equiv. (n-Bu)$_3$SnH and 20 min.; C: after 25 equiv. (n-Bu)$_3$SnH and additional 30 min.; D: after 55 equiv. (n-Bu)$_3$SnH and additional 110 min.

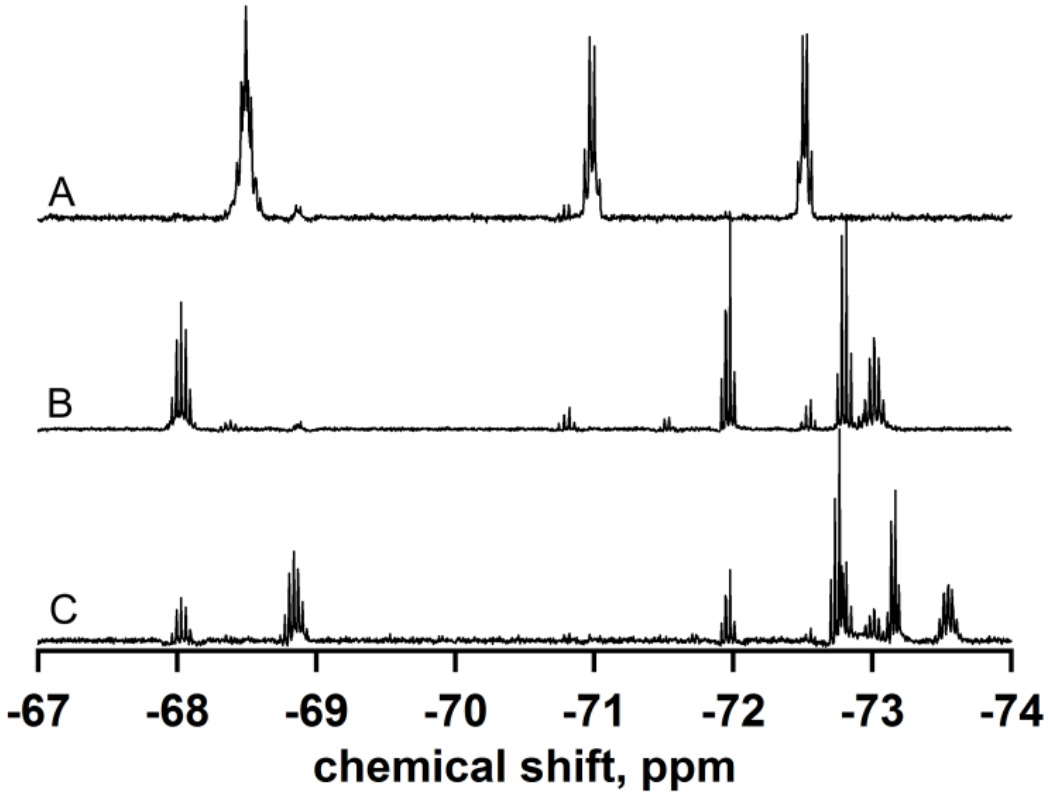

Figure 3.1.4. The ^{19}F NMR spectra after the addition of (n-Bu)$_3$SnH to compound **II** under anaerobic conditions. A: starting compound **II**; B: after 10 equiv. (n-Bu)$_3$SnH and 17 h; C: after 27 h exposed to air.

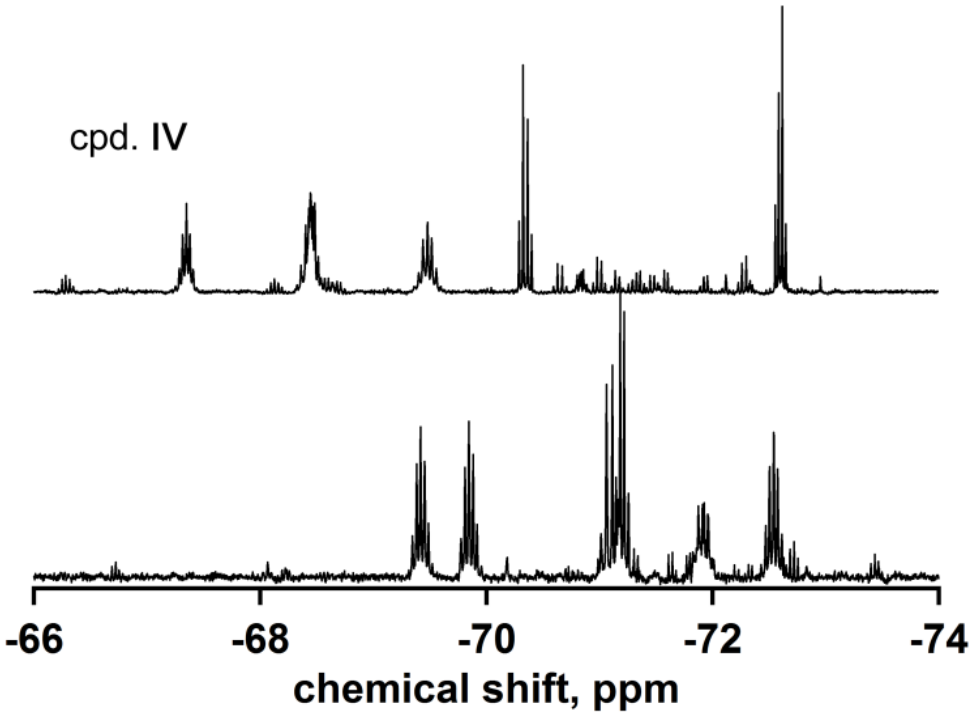

Figure 3.1.5. The ^{19}F NMR spectra of starting compound **IV** (90% purity, top) and after the addition of 10 equiv. of (n-Bu)$_3$SnH (bottom).

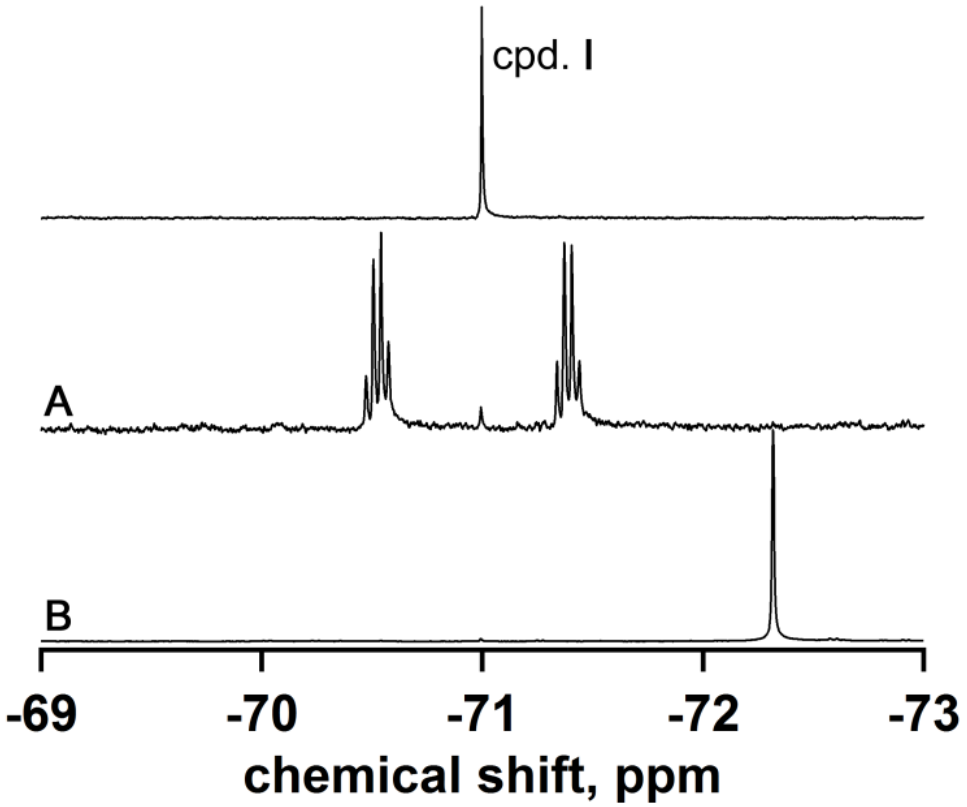

Figure 3.1.6. The ^{19}F NMR spectra of compound **I**, the asymmetric and the symmetric compounds.

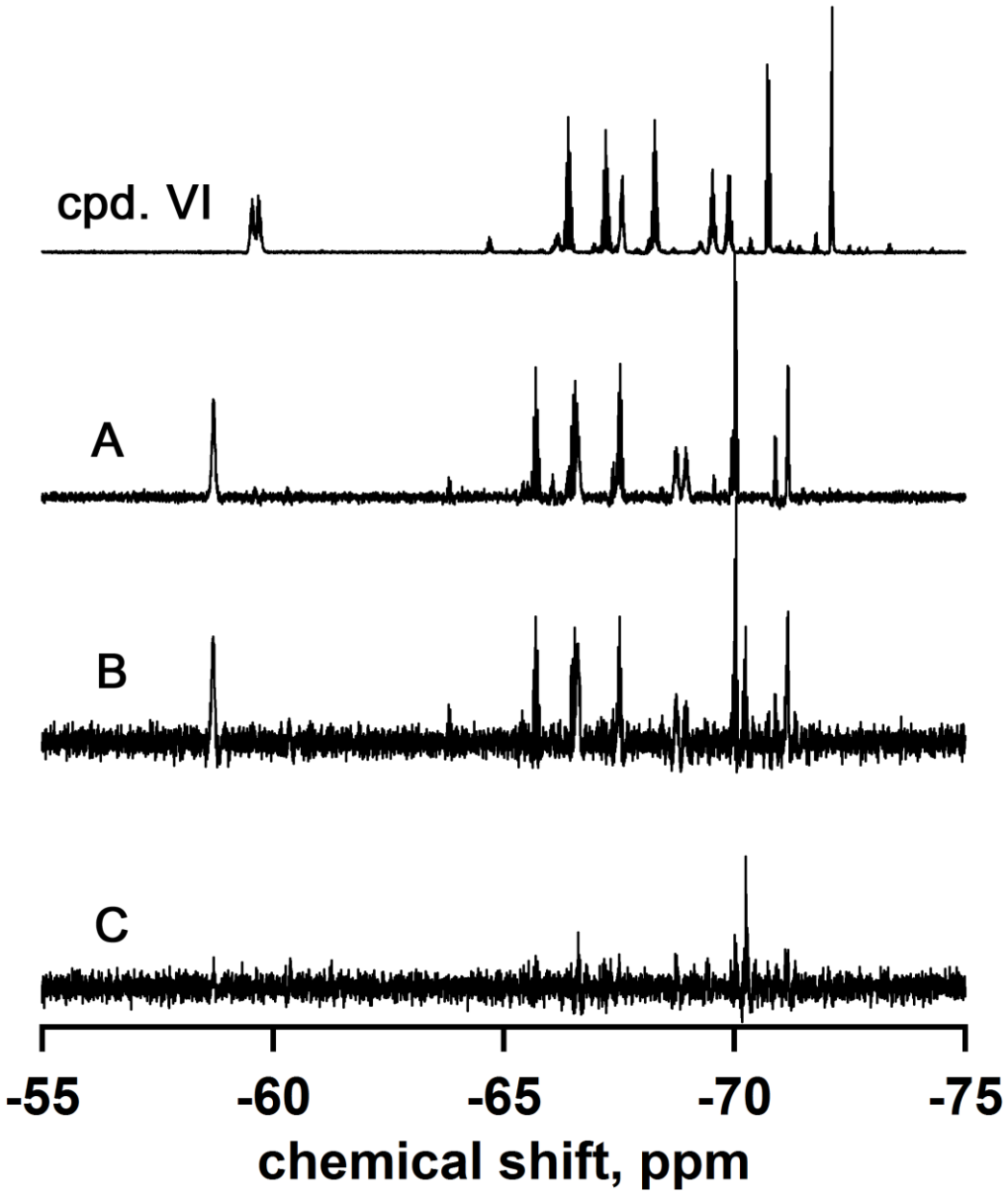

Figure 3.1.7. Fluorine-19 NMR spectra (379 MHz) of starting compound **VI** (top), minutes after the addition of 5 equiv. of $(n\text{-Bu})_3\text{SnH}$ (A), after 2 h (B), and after 21 h (C).

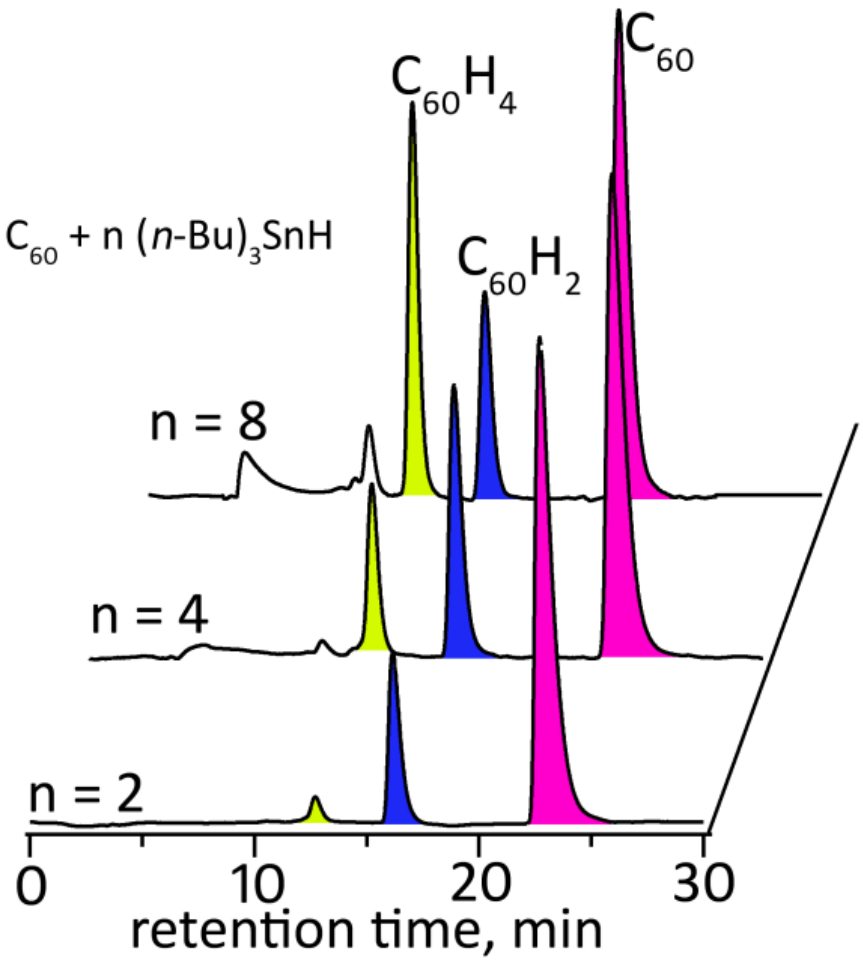

Figure 3.1.8. HPLC chromatograms of the reaction product mixture between C_{60} and n equiv. of (n-Bu)$_3$SnH are used. Note: shift in retention time for C_{60} due to slight deviation in mobile phase composition. Stationary phase: COSMOSIL Buckyprep semi-preparative column; mobile phase: 70/30 (v/v) toluene/acetonitrile at a flow rate of 5 mL min^{-1}.

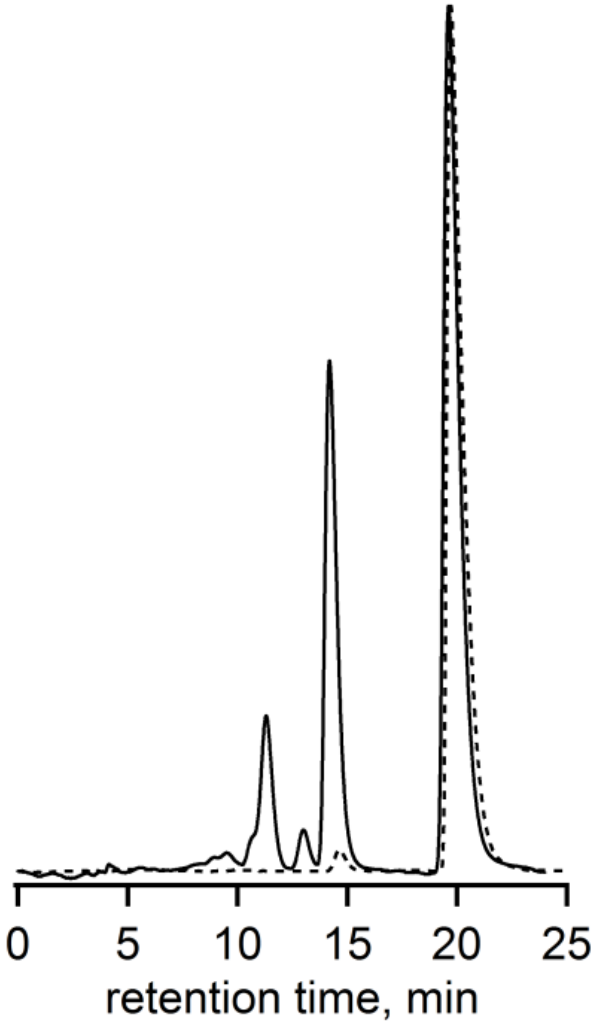

Figure 3.1.9. HPLC chromatogram for 2 equiv. (dashed lined) and 24 equiv. (solid line) of (*n*-Bu)$_3$SnH. Stationary phase: COSMOSIL Buckyprep semi-preparative column; mobile phase: 70/30 (v/v) toluene/acetonitrile at a flow rate 5 mL min^{-1}.

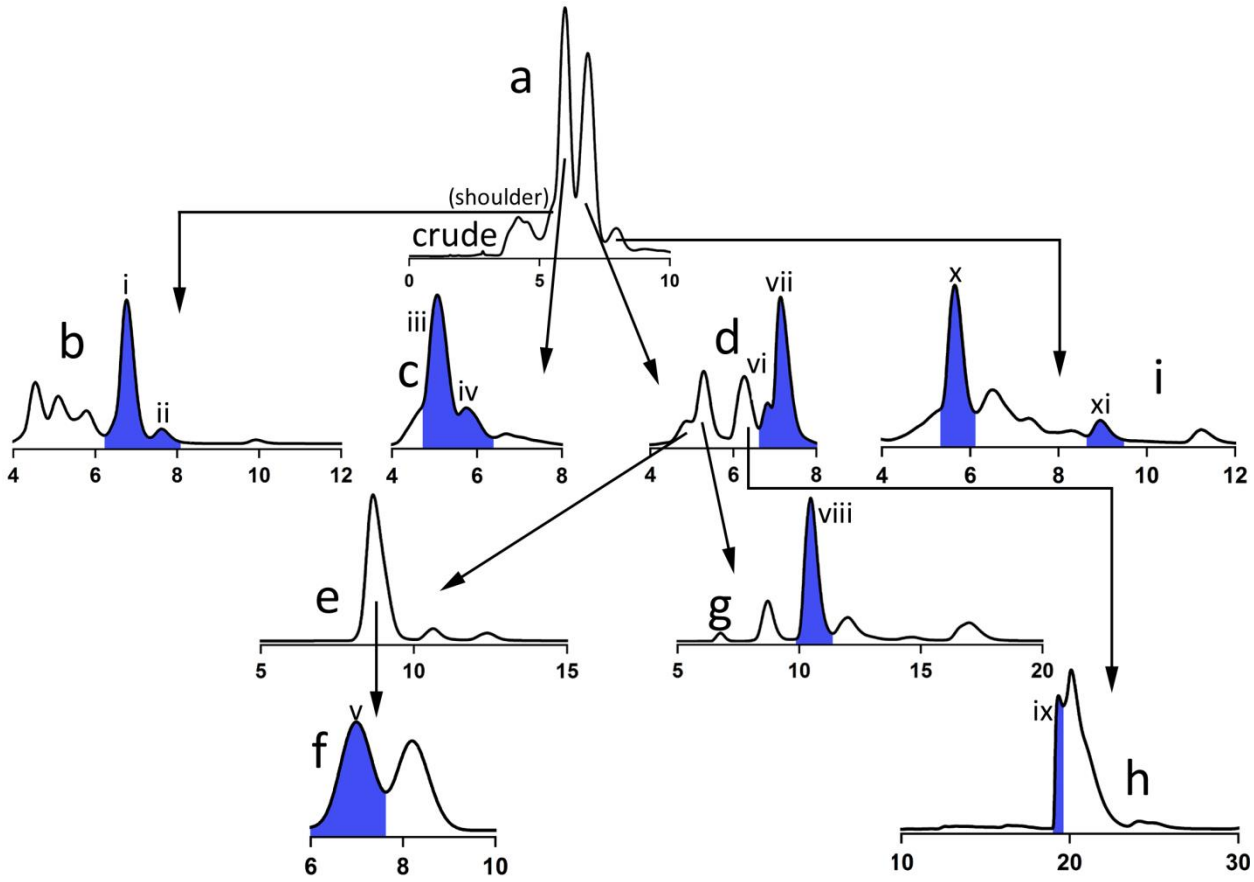

Figure 3.2.1. HPLC separation scheme for ACRD$(CF_3)_n$. Each arrow indicates which peaks were collected and used for the next stage of separation. The peaks colored in blue are compounds that were characterized by ^{19}F and ^{1}H NMR and are labeled with corresponding roman numerals. Each chromatogram used a COSMOSIL Buckyprep semi-preparative column at a flow rate of 5 mL min^{-1} except for chromatogram f, which used the FluoroFlash column at a flow rate of 1 mL min^{-1}. a: 100% MeCN 370 nm; b: 25/75 (v/v) toluene/heptane 370 nm; c: 25/75 (v/v) toluene/heptane 300 nm; d: 25/75 (v/v) toluene/heptane 300 nm; e: 100% heptane 370 nm; f: 100% MeCN 300 nm; g: 100% heptane 300 nm; h: 100% heptane 300 nm; i: 25/75 (v/v) toluene/heptane 300 nm. The x axis is retention time (minutes).

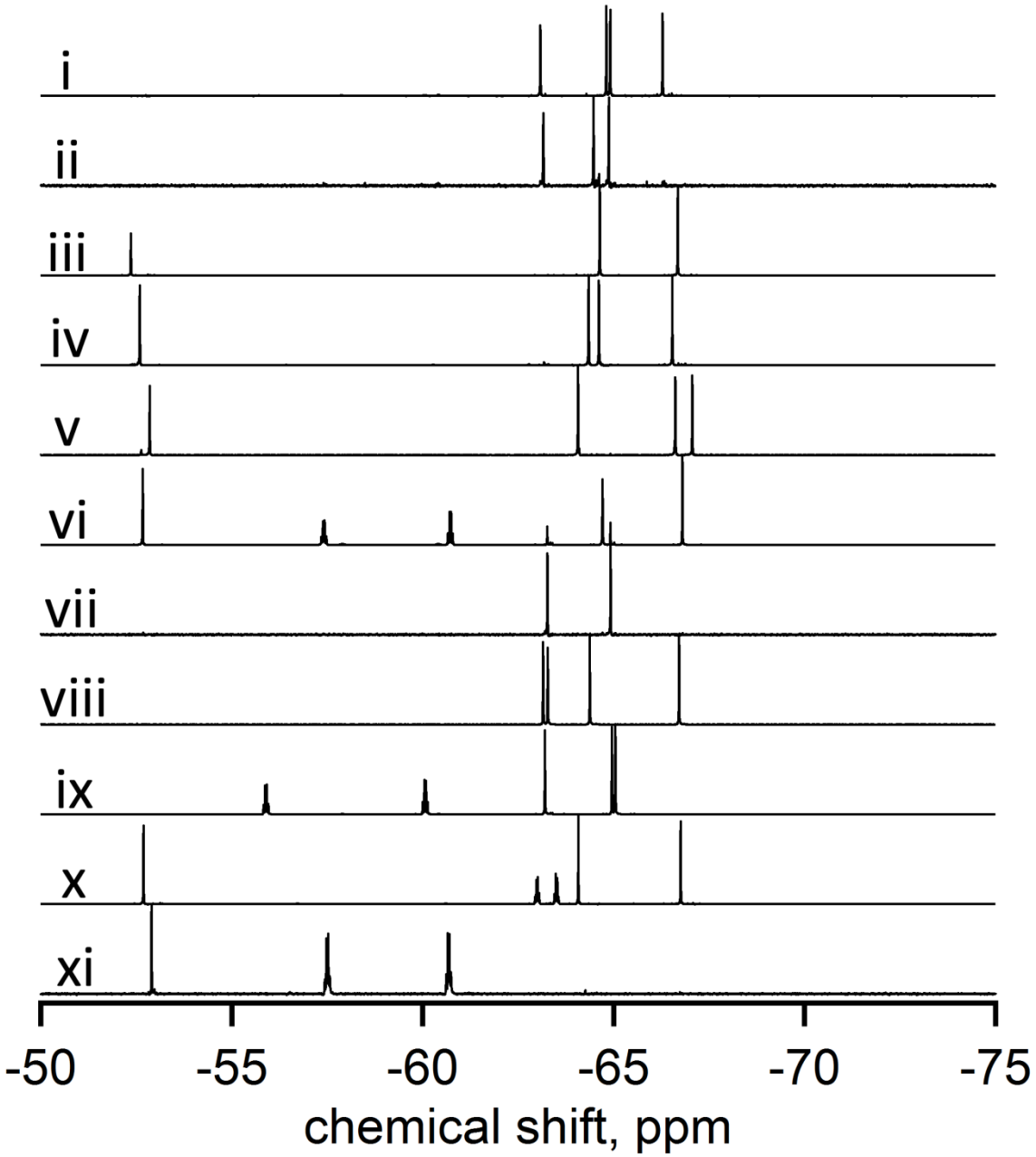

Figure 3.2.2. Fluorine-19 NMR spectra ($CDCl_3$, 379 MHz) of the isolated ACRD$(CF_3)_n$ compounds shown in Figure 3.2.1 with corresponding roman numerals. Note: no peaks overlap into an adjacent spectrum.

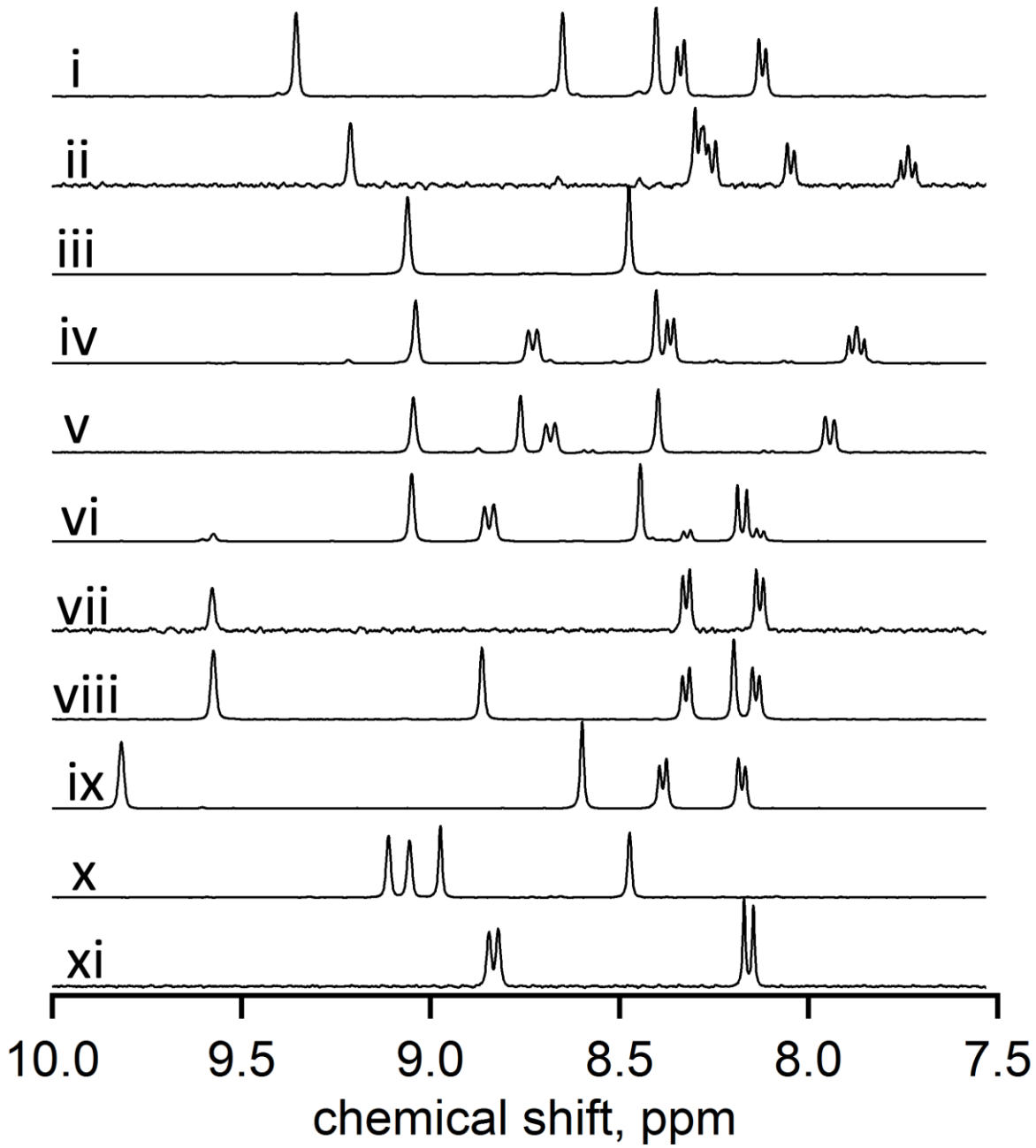

Figure 3.2.3. Proton NMR spectra of the isolated ACRD$(CF_3)_n$ compounds shown in Figure 3.2.1 with corresponding roman numerals. Residual $CHCl_3$ solvent and satellite peaks were truncated.

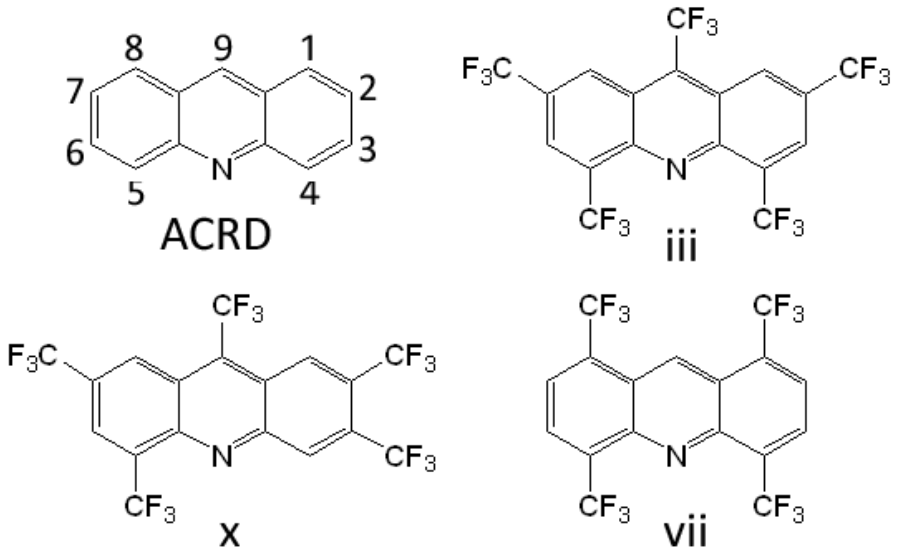

Figure 3.2.4. ACRD numbering scheme and the molecular structures confirmed by X-ray diffraction.

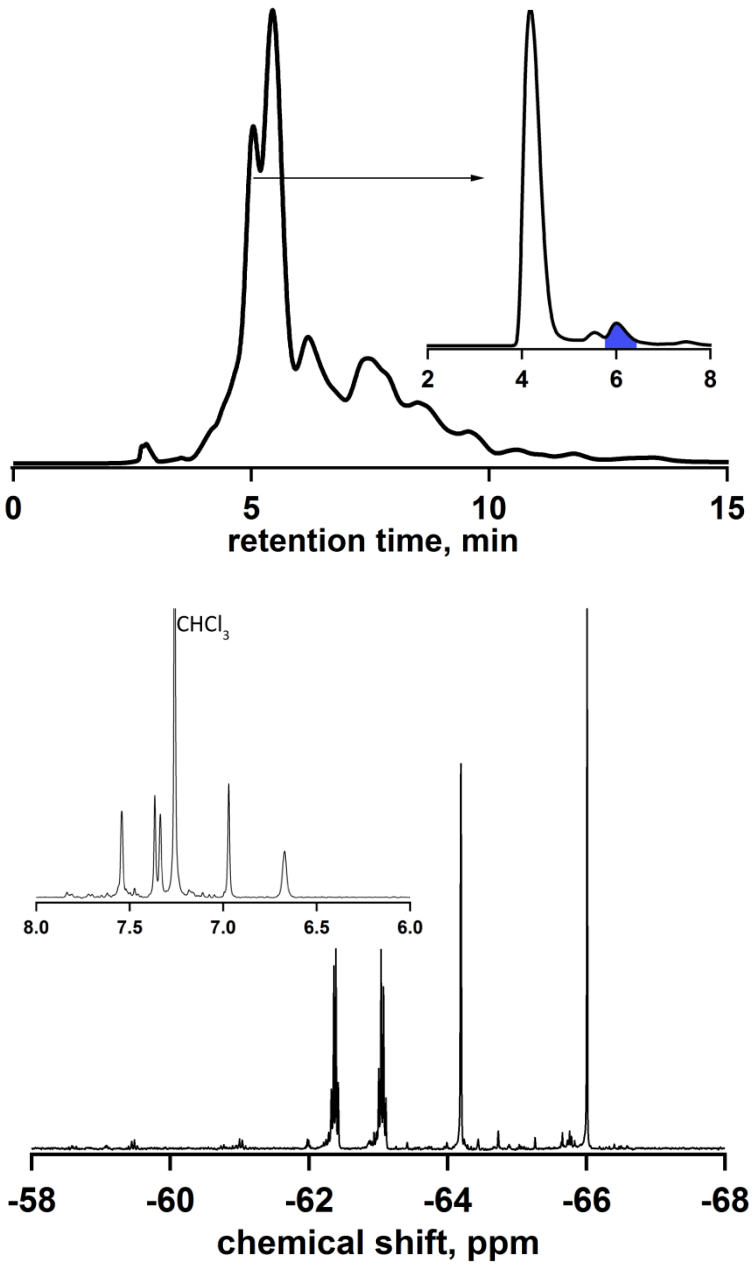

Figure 3.2.5. HPLC separation scheme of PHTZ$(CF_3)_n$ (top) with second state separation shown in the inset. COSMOSIL Buckyprep semi-preparative column at a flow rate of 5 mL min^{-1} for both stages and 100% MeCN (25/75 (v/v) toluene/heptane for inset) mobile phases. Fluorine-19 NMR spectrum (379 MHz, bottom) and ^1H NMR (399 MHz, bottom inset) with residual $CHCl_3$ solvent represents the peak highlight blue in the chromatogram.

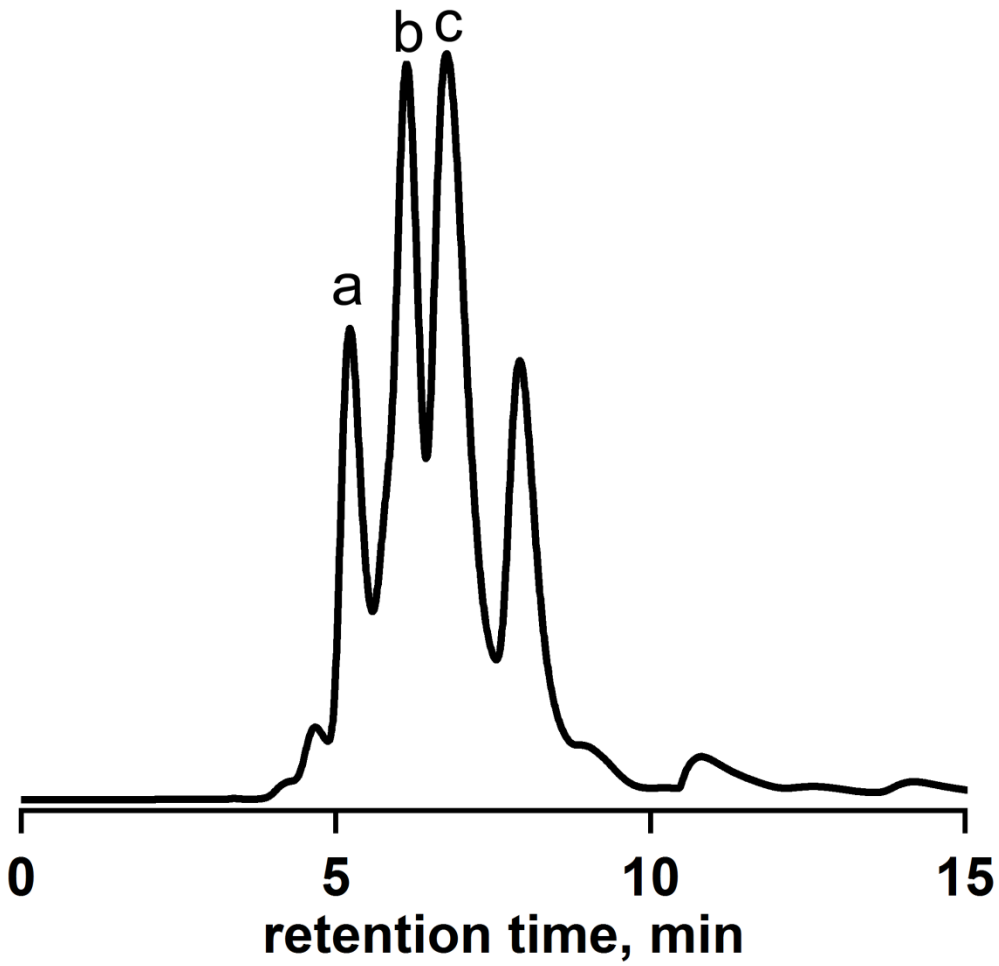

Figure 3.3.1. HPLC separation scheme of TETR(Bn_F)$_n$. COSMOSIL Buckyprep semi-preparative column at a flow rate of 5 mL min^{-1} and 100% MeCN mobile phase. The retention time of compounds a, b, and c are shown; however, additional stages of separation are required for pure product.

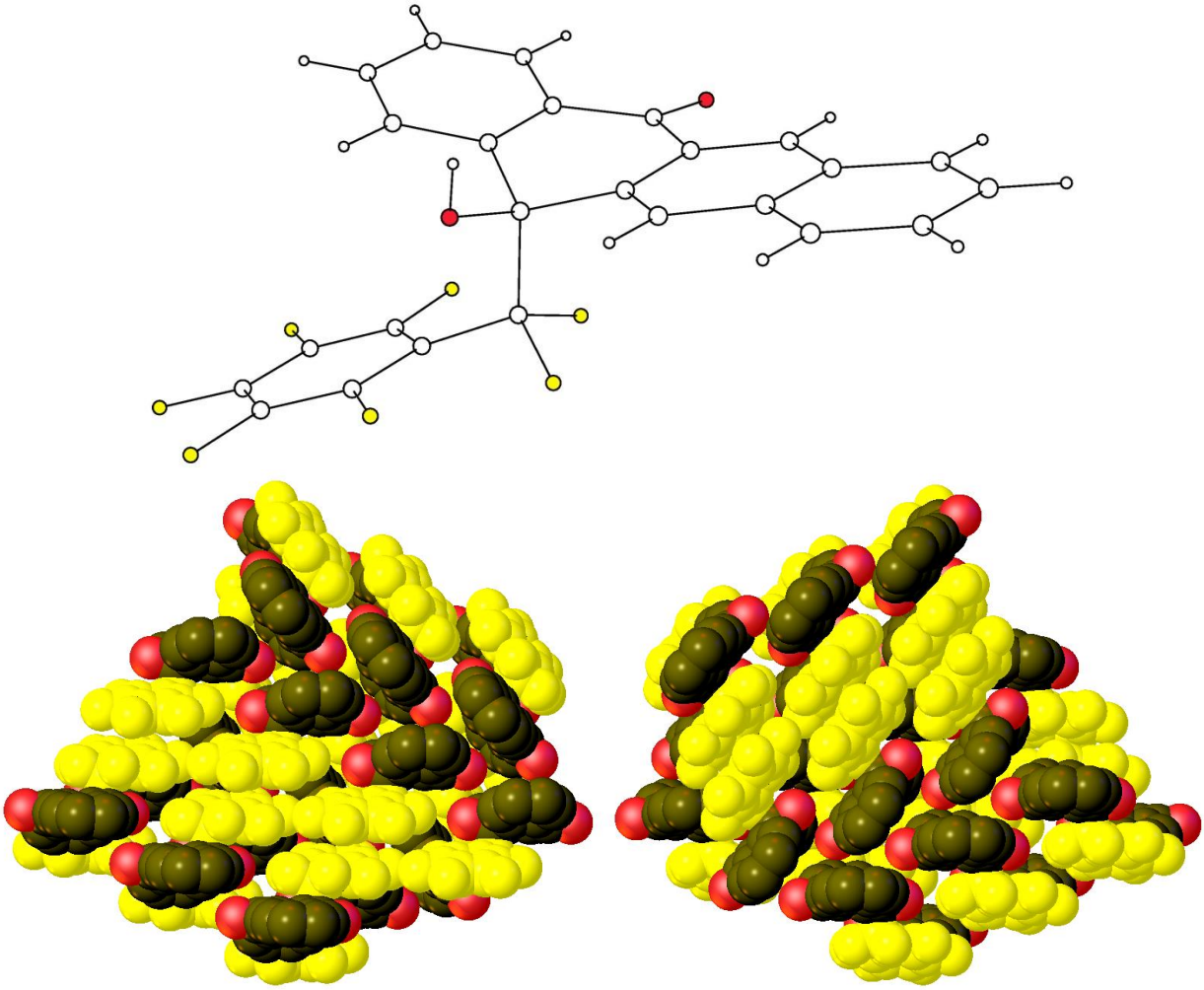

Figure 3.3.2. Molecular drawing (top) and space filled solid state packing of compound **a** (bottom). The TETR cores are represented by the black colored atoms, oxygen by the red colored atoms, and the $CF_2C_6F_5$ group by the yellow colored atoms. Hydrogen atoms are omitted for clarity.

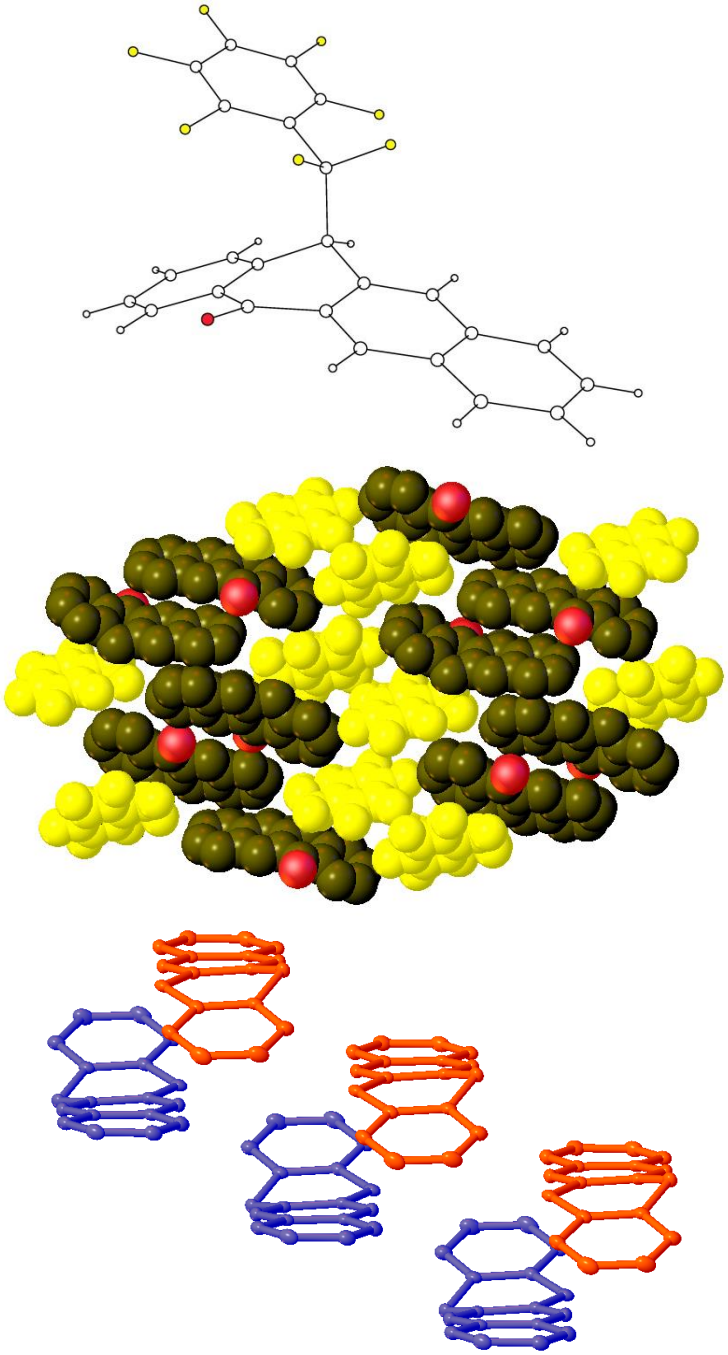

Figure 3.3.3. Molecular drawing (top) and space filled solid state packing (middle), and TETR core overlap (bottom) of compound **b**. The TETR cores are represented by the black colored atoms (or by orange and blue in bottom panel), oxygen by the red colored atoms, and the $CF_2C_6F_5$ group by the yellow colored atoms. Hydrogen atoms are omitted for clarity.

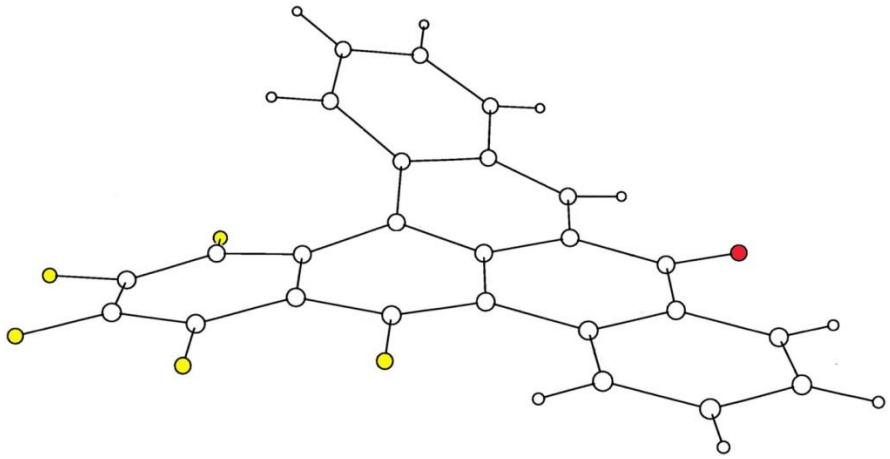

Figure 3.3.4. Molecular drawing of compound **c**. The white (hydrogen), red (oxygen), and yellow (fluorine) atoms are shown.

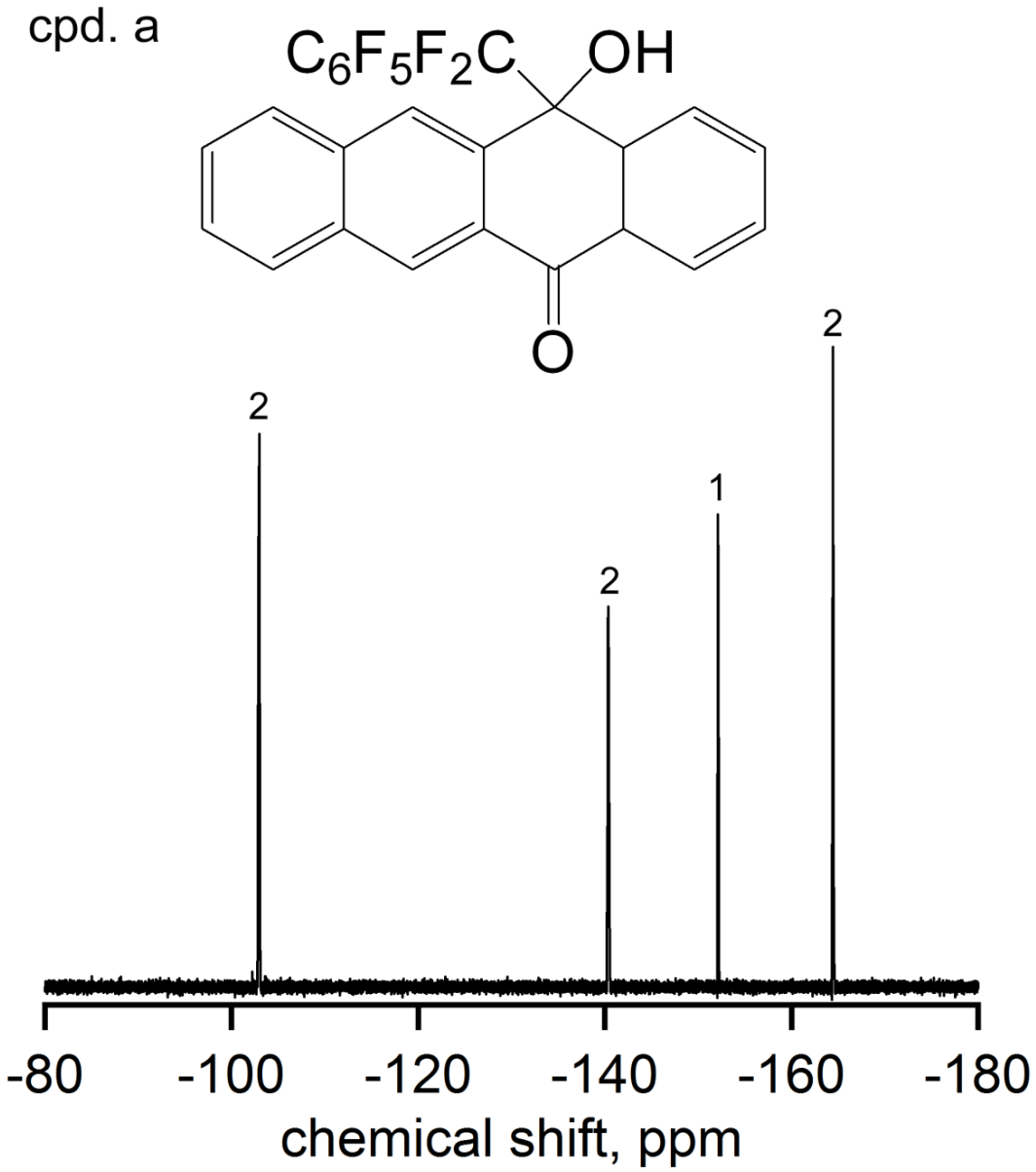

Figure 3.3.5. Fluorine-19 NMR spectrum (379 MHz) in $CDCl_3$ and molecular drawing of compound **a**. Internal standard used 1,4-$(CF_3)_2$-C_6H_4 (δ −66.35). Integration values are shown above resonances.

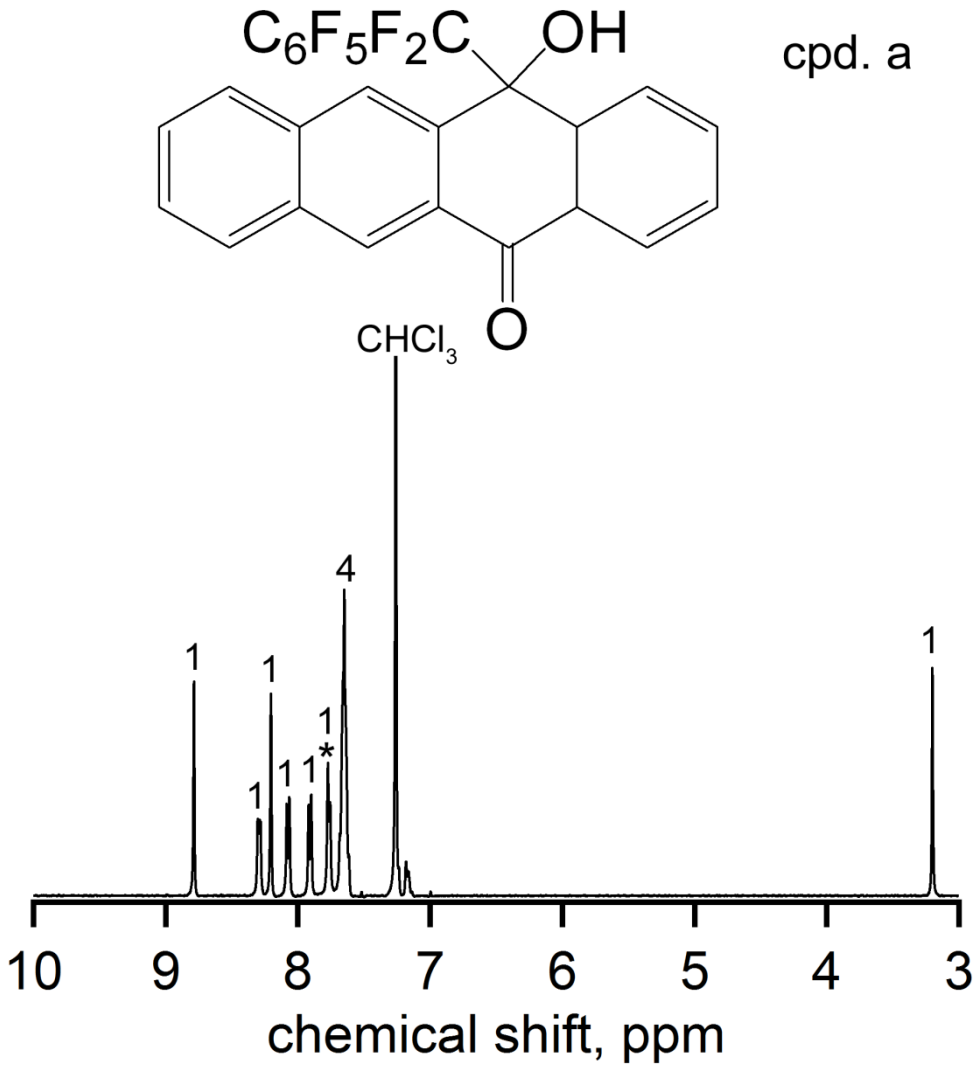

Figure 3.3.6. Proton NMR spectrum (399 MHz) in $CDCl_3$ and molecular drawing of compound **a**. Internal standard used 1,4-$C_6H_4(CF_3)_2$ (δ 7.77) marked by an asterisk. Integration values are shown above resonances.

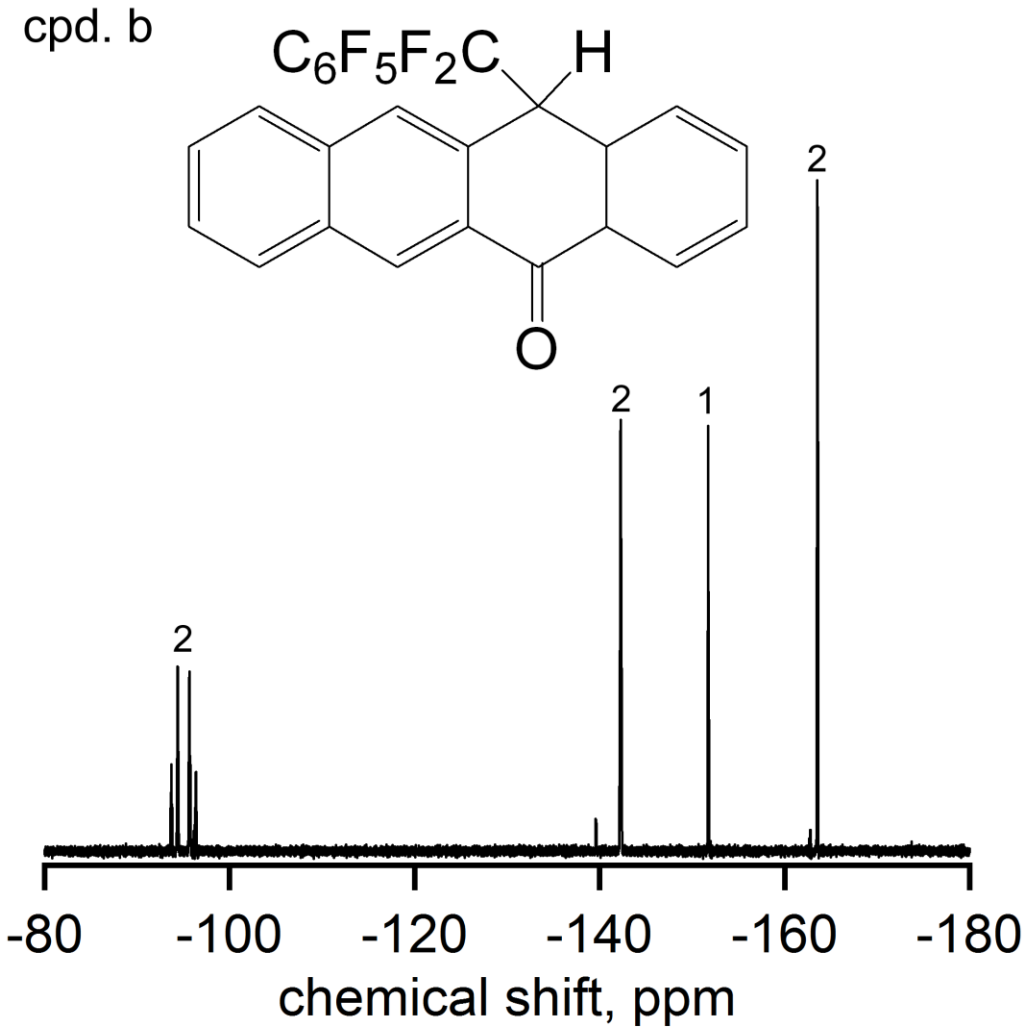

Figure 3.3.7. Fluorine-19 NMR spectrum(379 MHz) in $CDCl_3$ and molecular drawing of compound **b**. Internal standard used 1,4-$(CF_3)_2$-C_6H_4 (δ −66.35). Integration values are shown above resonances.

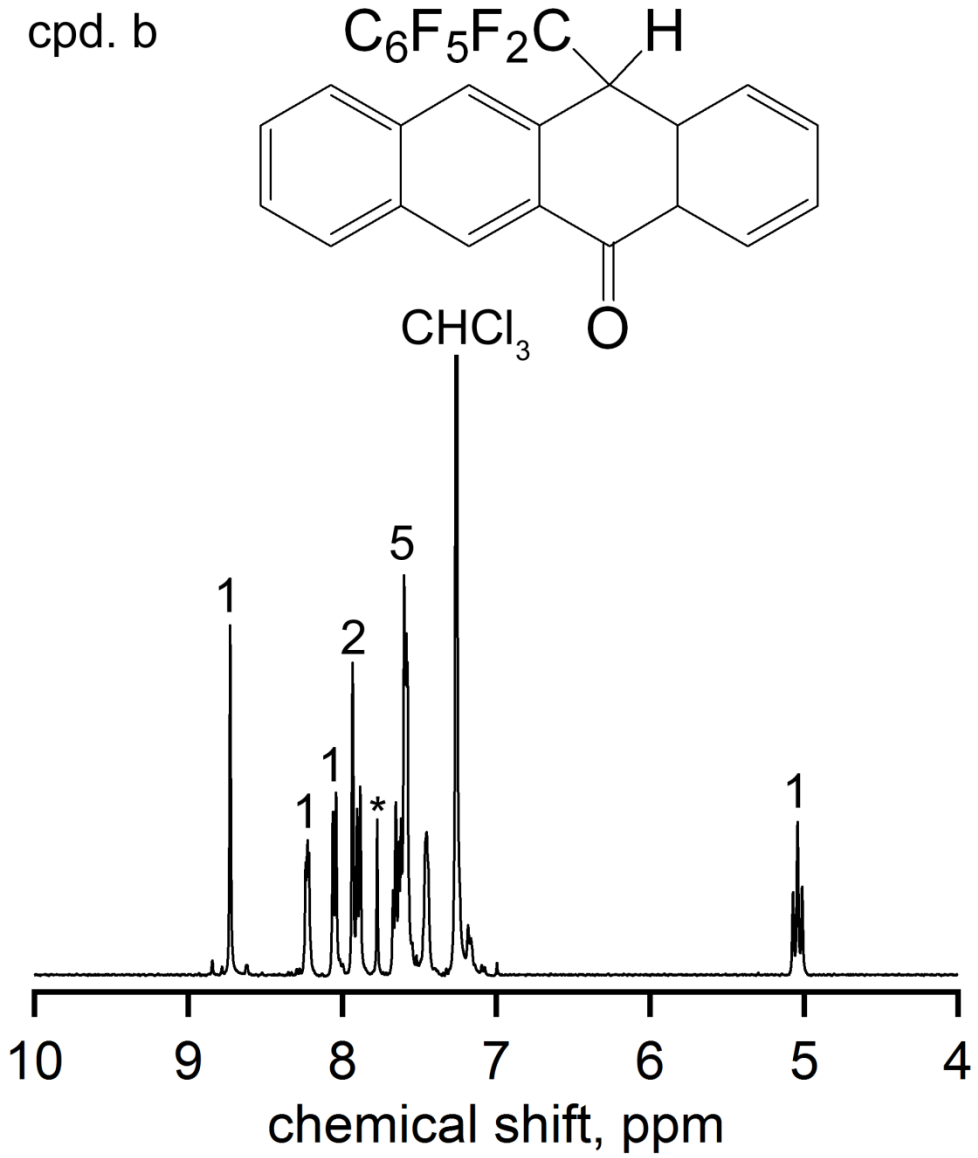

Figure 3.3.8. Proton NMR spectrum (399 MHz) in $CDCl_3$ and molecular drawing of compound **b**. Internal standard used 1,4-$C_6H_4(CF_3)_2$ (δ 7.77) marked by an asterisk. Integration values are shown above resonances.

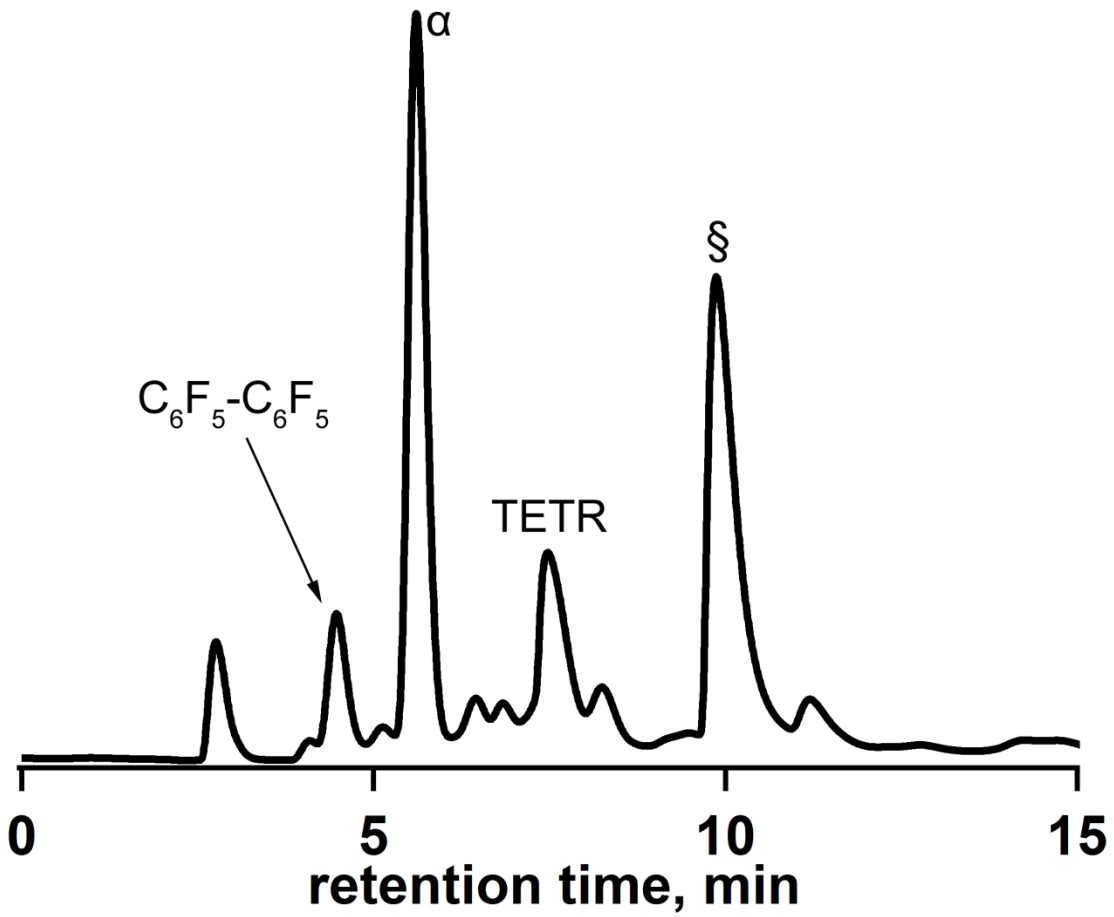

Figure 3.3.9. HPLC chromatogram of the reaction mixture of TETR and C_6F_5I. COSMOSIL Buckyprep semi-preparative column at a flow rate of 5 mL min^{-1} and 100% MeCN mobile phase. The peak marked α corresponds to predicted TETR(Bn_F), and the peak marked § corresponds to predicted $[TETR]_2$ dimer.

Chapter 3 References

(1) Abe, Y.; Hata, R.; Matsuo, Y. *Chem. Lett.* **2013**, *42*, 1525.

(2) Matsumoto, F.; Iwai, T.; Moriwaki, K.; Takao, Y.; Ito, T.; Mizuno, T.; Ohno, T. *J. Org. Chem.* **2012**, *77*, 9038.

(3) Partha, R.; Conyers, J. L. *Int. J. Nanomedicine* **2009**, *4*, 261.

(4) Schur, D. V.; Zaginaichenko, S. Y.; Savenko, A. F.; Bogolepov, V. A.; Anikina, N. S.; Zolotarenko, A. D.; Matysina, Z. A.; Veziroglu, T. N.; Skryabina, N. E. *Int. J. Hydrogen Energy* **2011**, *36*, 1143.

(5) Allard, E.; Cheng, F.; Chopin, S.; Delaunay, J.; Rondeau, D.; Cousseau, J. *New J. Chem.* **2003**, *27*, 188.

(6) Matsuo, K.; Matsuo, Y.; Iwashita, A.; Nakamura, E. *Org. Lett.* **2009**, *11*, 4192.

(7) San, L. K.; Bukovsky, E. V.; Larson, B. W.; Whitaker, J. B.; Deng, S. H. M.; Kopidakis, N.; Rumbles, G.; Popov, A. A.; Chen, Y.-S.; Wang, X.-B.; Boltalina, O. V.; Strauss, S. H. *Chem. Sci.* **2014**, *6*, 1801.

(8) Clikeman, T. T.; Kuvychko, I. V.; Shustova, N. B.; Chen, Y.-S.; Popov, A. A.; Boltalina, O. V.; Strauss, S. H. *Chem. Eur. J.* **2013**, *19*, 5070.

(9) Kareev, I. E.; Kuvychko, I. V.; Lebedkin, S. F.; Miller, S. M.; Anderson, O. P.; Seppelt, K.; Strauss, S. H.; Boltalina, O. V. *J. Am. Chem. Soc.* **2005**, *127*, 8362.

(10) Popov, A. A.; Kareev, I. E.; Shustova, N. B.; Stukalin, E. B.; Lebedkin, S. F.; Seppelt, K.; Strauss, S. H.; Boltalina, O. V.; Dunsch, L. *J. Am. Chem. Soc.* **2007**, *129*, 11551.

(11) Kuvychko, I. V.; Whitaker, J. B.; Larson, B. W.; Raguindin, R. S.; Suhr, K. J.; Strauss, S. H.; Boltalina, O. V. *J. Fluorine Chem.* **2011**, *132*, 679.

(12) Whitaker, J. B.; Kuvychko, I. V.; Shustova, N. B.; Chen, Y.-S.; Strauss, S. H.; Boltalina, O. V. *Chem. Commun.* **2014**, *50*, 1205.

(13) Clikeman, T. T.; Deng, S. H. M.; Avdoshenko, S. M.; Wang, X.-B.; Popov, A. A.; Strauss, S. H.; Boltalina, O. V. *Chem. Eur. J.* **2013**, *19*, 15404.

(14) Yoshida, M.; Suzuki, D.; Iyoda, M. *Chem. Lett.* **1996**, 1097.

(15) Yoshida, M.; Morishima, A.; Morinaga, Y.; Iyoda, M. *Tetrahedron Lett.* **1994**, *35*, 9045.

(16) Tuktarov, R. F.; Khatymov, R. V.; Muftakhov, M. V. *High Energy Chem.* **2008**, *42*, 472.

(17) Dorozhkin, E. I.; Ignat'eva, D. V.; Tamm, N. B.; Goryunkov, A. A.; Khavrel, P. A.; Ioffe, I. N.; Popov, A. A.; Kuvychko, I. V.; Streletskiy, A. V.; Markov, V. Y.; Spandl, J.; Strauss, S. H.; Boltalina, O. V. *Chem. Eur. J.* **2006**, *12*, 3876.

(18) Goryunkov, A. A.; Kuvychko, I. V.; Ioffe, I. N.; Dick, D. L.; Sidorov, L. N.; Strauss, S. H.; Boltalina, O. V. *J. Fluorine Chem.* **2003**, *124*, 61.

(19) Matsuo, Y.; Nakamura, E. *Chem. Rev.* **2008**, *108*, 3016.

(20) Sawamura, M.; Toganoh, M.; Suzuki, K.; Hirai, A.; Likura, H.; Nakamura, E. *Org. Lett.* **2000**, *2*, 1919.

(21) Kuvychko, I. V.; Shustova, N. B.; Avdoshenko, S. M.; Popov, A. A.; Strauss, S. H.; Boltalina, O. V. *Chem. Eur. J.* **2011**, *17*, 8799.

(22) Hirsch, A.; Grösser, T.; Skiebe, A.; Soi, A. *Chem. Ber.* **1993**, *126*, 1061.

(23) She, Y.-M.; Guo, X.-H.; Liu, Z.-Y.; Liu, S.-Y.; Fu, F.-X.; Qian, M.-X. *Chem. J. Chin. Univ.* **1996**, *17*, 303.

(24) Nossal, J.; Saini, R. K.; Alemany, L. B.; Meier, M.; Billups, W. E. *Eur. J. Org. Chem.* **2001**, 4167.

(25) Henderson, C. C.; Rohlfing, C. M.; Assink, R. A.; Cahill, P. A. *Angew. Chem. Int. Ed. Engl.* **1994**, *33*, 786.

(26) Spielmann, H. P.; Wang, G.-W.; Meier, M. S.; Weedon, B. R. *J. Org. Chem.* **1998**, *63*, 9865.

(27) Tzirakis, M. D.; Alberti, M. N.; Nye, L. C.; Drewello, T.; Orfanopoulos, M. *J. Org. Chem.* **2009**, *74*, 5746.

(28) Henderson, C. C.; Cahill, P. A. *Science* **1993**, *259*, 1885.

(29) Ballenweg, S.; Gleiter, R.; Krätschmer, W. *Tetrahedron Lett.* **1993**, *34*, 3737.

(30) Korth, C.; May, B. C. H.; Cohen, F. E.; Prusiner, S. B. *Proc. Natl. Acad. Sci. U. S. A.* **2001**, *98*, 9836.

(31) Wainwright, M. *J. Antimicrob. Chemother.* **2001**, *47*, 1.

(32) Ames, B. N.; Sims, P.; Grover, P. L. *Science* **1972**, *176*, 47.

(33) Brennan, S. T.; Colbry, N. L.; Leeds, R. L.; Leja, B.; Priebe, S. R.; Reily, M. D.; Showalter, H. D. H.; Uhlendor, S. E. *J. Heterocyclic Chem.* **1989**, *26*, 1469.

(34) Dunn, E. A.; Roxburgh, M.; Larsen, L.; Smith, R. A. J.; McLellan, A. D.; Heikal, A.; Murphy, M. P.; Cook, G. M. *Bioorg. Med. Chem.* **2014**, *22*, 5320.

(35) Wampler, G. *Drugs* **1983**, *25*, 35.

(36) Shinamura, S.; Osaka, I.; Miyazaki, E.; Takimiya, K. *Heterocycles* **2011**, *83*, 1187.

(37) Kojima, T.; Nishida, J.-i.; Tokito, S.; Yamashita, Y. *Chem. Lett.* **2008**, *37*, 1122.

(38) Takimiya, K.; Osaka, I.; Nakano, M. *Chem. Mater.* **2014**, *26*, 587.

(39) Schlosser, M. *Angew. Chem. Int. Ed.* **2006**, *45*, 5432.

(40) Chen, M.; Buchwald, S. L. *Angew. Chem. Int. Ed.* **2013**, *52*, 11628.

(41) Kuvychko, I. V.; Castro, K. P.; Deng, S. H. M.; Wang, X.-B.; Strauss, S. H.; Boltalina, O. V. *Angew. Chem. Int. Ed.* **2013**, *52*, 4871.

(42) Ando, N.; Mitsui, M.; Nakajima, A. *J. Chem. Phys.* **2007**, *127*, 234305.

(43) Kokubo, S.; Ando, N.; Koyasu, K.; Mitsui, M.; Nakajima, A. *J. Chem. Phys.* **2004**, *121*.

(44) San, L. K.; Bukovsky, E. V.; Kuvychko, I. V.; Popov, A. A.; Strauss, S. H.; Boltalina, O. V. *Chem. Eur. J.* **2014**, *20*, 4373.

(45) Clikeman, T. T.; Bukovsky, E. V.; Kuvychko, I. V.; San, L. K.; Deng, S. H. M.; Wang, X.-B.; Chen, Y.-S.; Strauss, S. H.; Boltalina, O. V. *Chem. Commun.* **2014**, *50*, 6263.

(46) Kuvychko, I. V.; Spisak, S. N.; Chen, Y.-S.; Popov, A. A.; Petrukhina, M. A.; Strauss, S. H.; Boltalina, O. V. *Angew. Chem. Int. Ed.* **2012**, *51*, 4939.

(47) Kuvychko, I. V.; Dubceac, C.; Deng, S. H. M.; Wang, X.-B.; Granovsky, A. A.; Popov, A. A.; Petrukhina, M. A.; Strauss, S. H.; Boltalina, O. V. *Angew. Chem. Int. Ed.* **2013**, *52*, 7505.

(48) Swenberg, C. E.; Stacy, W. T. *Chem. Phys. Lett.* **1968**, *2*, 327.

(49) Smith, M. B.; Michl, J. *Chem. Rev.* **2010**, *110*, 6891.

(50) Smith, M. B.; Michl, J. *Annu. Rev. Phys. Chem.* **2013**, *64*, 361.

(51) Burdett, J. J.; Gosztola, D.; Bardeen, C. J. *J. Chem. Phys.* **2011**, *135*, 214508.

(52) Grumstrup, E. M.; Johnson, J. C.; Damrauer, N. H. *Phys. Rev. Lett.* **2010**, *105*, 257403.
(53) Burdett, J. J.; Müller, A. M.; Gosztola, D.; Bardeen, C. J. *J. Chem. Phys.* **2010**, *133*, 114506.
(54) Jadhav, P. J.; Mohanty, A.; Sussman, J.; Lee, J.; Baldo, M. A. *Nano Lett.* **2011**, *11*, 1495.
(55) Ma, L.; Zhang, K.; Kloc, C.; Sun, H.; Michel-Beyerle, M. E.; Gurzadyan, G. G. *Phys. Chem. Chem. Phys.* **2012**, *14*, 8307.
(56) Hasegawa, T.; Takeya, J. *Sci. Technol. Adv. Mater.* **2009**, *10*, 024314.
(57) Zhang, B.; Kan, Y.-H.; Geng, Y.; Duan, Y.-A.; Li, H.-B.; Hua, J.; Su, Z.-M. *Org. Electron.* **2013**, *14*, 1359.
(58) Okamoto, T.; Nakahara, K.; Saeki, A.; Seki, S.; Oh, J. H.; Akkerman, H. B.; Bao, Z.; Matsuo, Y. *Chem. Mater.* **2011**, *23*, 1646.
(59) San, L. K.; Clikeman, T. T.; Dubceac, C.; Popov, A. A.; Chen, Y.-S.; Petrukhina, M. A.; Strauss, S. H.; Boltalina, O. V. *Chem. Eur. J.* **2015**.

Dissertation Summary/Conclusions and Future Outlook

The research described in this dissertation focused on the synthesis of novel electron acceptors (based on fullerenes and polycyclic aromatic hydrocarbons substrates) with fluorinated electron-withdrawing substituents for the potential use in organic electronics such as organic photovoltaics and organic light emitting diodes. The ability to tune electronic properties (i.e., solution redox potentials and gas-phase electron affinity) and physical properties (i.e., solubility and photoluminescence) of *n*-type semiconductors by the decoration with various fluorine-containing substituents was demonstrated in this dissertation. The need to expand the library of *n*-type semiconductors to include moisture- and air-stable and fluorinated compounds is one alternative way towards realizing highly stable, highly performing and highly efficient organic electronics. Fluorinated compounds open the potential for the molecular engineering of novel compounds, to tune the electronic properties and to control the morphology present within the organic electronics.

For the first time, a novel fullerene containing a perfluorinated cycloadduct was synthesized and characterized in Chapter 1. Also, a S_N2 *intra*molecular fullerene carbanion reaction mechanism was observed for the first time with fullerenes. This new chemistry may provide means for synthetic routes towards expanding the π system of various organic semiconductors. In some aspects, the superiority of 1,9-C_{60}(*cyclo*-CF_2(2-C_6F_4)) (**2**) over PCBM shows promise as a potential OPV electron acceptor.

The introduction of the perfluorobenzyl ($CF_2C_6F_5$) functional group to various polycyclic aromatic hydrocarbons was demonstrated. In fact, it was shown that the perfluorobenzyl functional group is a stronger electron-withdrawing group than the trifluoromethyl (CF_3)

functional group when CORA(Bn_F)$_5$ and CORA(CF_3)$_5$ were compared in Chapter 2. The additional –CF_2 linker provides structural flexibility as observed in CORA(Bn_F)$_5$ and 9,10-ANTH(Bn_F)$_2$. Also in Chapter 2, the polyperfluoroalkylation of NAPH produced highly substituted compounds which show a linear increase in the gas-phase electron affinity values with longer perfluoroalkyl chain length.

In Chapter 3, some on-going projects were presented. The hydrogenation of various trifluoromethylfullerenes showed remarkable, in some cases, selectivity and instantaneity at room temperature; however, no correlation was found between the number of CF_3 groups on C_{60} and reaction rates/selectivity. Also in Chapter 3, the trifluoromethylation of two different heterocycles was explored. It appears that the reactivity of these heterocycles towards CF_3 radicals is similar to previously explored polycyclic aromatic hydrocarbons. Finally, the perfluorobenzylation of TETR produced interesting compounds revealing unusual chemistry including the formation of ketones and hydroxides. Surprisingly, a similar *intra*molecular cyclization was observed, similar to the observation made in Chapter 1.

These fundamental studies have provided a gateway towards the better understanding of fullerene and polycyclic aromatic hydrocarbon incorporation into organic electronics; however, there are many questions that need to be addressed. The control of the morphology in organic electronics is an important aspect for improving efficiency.[1] One premise is to develop new deposition methodologies that might provide better ways to control the morphology. One emerging deposition methodology is based on sequentially processing[2,3] the electron donor and electron acceptor from orthogonal solvents in organic photovoltaics. It has been demonstrated that active layer blends deposited this way have comparable performances to that of the bulk heterojunction device architecture.[4] One aspect to also explore is the use of fluorine-containing

n-type semiconductors and traditional organic solvents (i.e., toluene, *o*-DCB, etc.). The concept of "like-dissolves-like" with fluorinated and non-fluorinated molecules may achieve similar results to the use of orthogonal solvents. Sequentially processing of polycyclic aromatic hydrocarbons has yet to be explored. X-ray[5] and neutron[6] scattering techniques will aid in the characterization of the morphology produced from the sequential processing of these materials.

Dissertation Summary/Conclusions and Future Outlook References

(1) Jackson, N. E.; Savoie, B. M.; Marks, T. J.; Chen, L. X.; Ratner, M. A. *J. Phys. Chem. Lett.* **2015**, *6*, 77.

(2) Ayzner, A. L.; Tassone, C. J.; Tolbert, S. H.; Schwartz, B. J. *J. Phys. Chem. C* **2009**, *113*, 20050.

(3) Wang, D. H.; Moon, J. S.; Sieifter, J.; Jo, J.; Park, J. H.; Park, O. O.; Heeger, A. J. *Nano Lett.* **2011**, *11*, 3163.

(4) Liu, Y.; Liu, F.; Wang, H.-W.; Nordlund, D.; Sun, Z.; Ferdous, S.; Russell, T. P. *ACS Appl. Mater. Interfaces* **2015**, *7*, 653.

(5) Buchaca-Domingo, E.; Ferguson, A. J.; Jamieson, F. C.; McCarthy-Ward, T.; Shoaee, S.; Tumbleston, J. R.; Reid, O. G.; Yu, L.; Madec, M.-B.; Pfannmöller, M.; Hermerschmidt, F.; Schröder, R. R.; Watkins, S. E.; Kopidakis, N.; Portale, G.; Amassian, A.; Heeney, M.; Ade, H.; Rumbles, G.; Durrant, J. R.; Stingelin, N. *Mater. Horiz.* **2014**, *1*, 270.

(6) Lee, K. H.; Schwenn, P. E.; Smith, A. R. G.; Cavaye, H.; Shaw, P. E.; James, M.; Krueger, K. B.; Gentle, I. R.; Meredith, P.; Burn, P. L. *Adv. Mater.* **2011**, *23*, 766.